TU
WIEN

DISSERTATION

Microscopic Simulation of Particle Detectors

ausgeführt zum Zwecke der Erlangung des akademischen Grades eines

Doktors der technischen Wissenschaften unter der Leitung von

Univ. Prof. Dipl.-Ing. Dr. Christian Fabjan

E 141

Atominstitut der österreichischen Universitäten

eingereicht an der Technischen Universität Wien

Fakultät für Physik

von

Dipl.-Ing. Heinrich Schindler

Matrikel-Nr. 0225800

Mechtlerstr. 17, 2100 Korneuburg

Wien, im Oktober 2012

Abstract

Detailed computer simulations are indispensable tools for the development and optimization of modern particle detectors. The interaction of particles with the sensitive medium, giving rise to ionization or excitation of atoms, is stochastic by its nature. The transport of the resulting photons and charge carriers, which eventually generate the observed signal, is also subject to statistical fluctuations. Together with the readout electronics, these processes – which are ultimately governed by the atomic cross-sections for the respective interactions – pose a fundamental limit to the achievable detector performance.

Conventional methods for calculating electron drift lines based on macroscopic transport coefficients used to provide an adequate description for traditional gas-based particle detectors such as wire chambers. However, they are not suitable for small-scale devices such as micropattern gas detectors, which have significantly gained importance in recent years. In this thesis, a novel approach, based on semi-classical ("microscopic") Monte Carlo simulation, is presented.

As a first application, the simulation of avalanche fluctuations is discussed. It is shown that the microscopic electron transport method allows, for the first time, a quantitative prediction of gas gain spectra. Further, it is shown that the shape of avalanche size distributions in uniform fields can be understood intuitively in terms of a toy model extracted from the simulation.

Stochastic variations in the number of electrons produced along a charged particle track are another determining factor for the resolution and efficiency of a detector. It is shown that the parameters characterizing primary ionization fluctuations, more specifically the so-called W value and the Fano factor, can be calculated accurately using microscopic techniques such that they need no longer be treated as free variables in the simulation.

Profiting from recent progress in the determination of Penning transfer probabilities, the influence of excitation transfer on both primary ionization fluctuations and avalanche statistics is examined and a model for the microscopic calculation of Penning effects is proposed.

"Garfield" is a widely used program for the simulation of gas-based particle detectors. In the context of this thesis work, an object-oriented version (Garfield++) of this software package was developed which includes the above-mentioned microscopic methods. The integration of semiconductor detectors in Garfield++, comprising the adaptation of algorithms, modelling of material properties and validation against measurements, constitutes a further topic of the thesis.

Kurzfassung

Detailgenaue Computersimulationen sind unverzichtbare Werkzeuge für die Entwicklung und Optimierung moderner Teilchendetektoren. Die Wechselwirkung von Teilchen mit dem sensitiven Medium, die typischerweise zur Ionisierung oder Anregung von Atomen führt, ist von stochastischer Natur. Ebenso ist der Transport der produzierten Photonen und Ladungsträger, welche das beobachtete Signal erzeugen, statistischen Fluktuationen unterworfen. Gemeinsam mit der Ausleseelektronik stellen diese Prozesse – die letztlich von den zugrundeliegenden atomaren Wirkungsquerschnitten bestimmt werden – fundamentale Beschränkungen der erzielbaren Detektorauflösung dar.

Herkömmliche Methoden zur Berechnung von Elektronendrift auf der Basis von makroskopischen Transportkoeffizienten liefern eine adäquate Beschreibung für traditionelle Gasdetektoren wie beispielsweise Drahtkammern. Sie sind jedoch ungeeignet für sogenannte "Micropattern" Gasdetektoren, die in den letzten Jahren stark an Bedeutung gewonnen haben. In der vorliegenden Arbeit wird ein neuartiger Zugang zu Elektronentransportberechnungen in Gasdetektoren vorgestellt, der auf semi-klassischer ("mikroskopischer") Monte-Carlo-Simulation beruht.

Als erste Anwendung wird die Simulation von Lawinenfluktuationen diskutiert. Es wird gezeigt, dass die mikroskopische Elektrontransportmethode erstmalig eine quantitative Voraussage der Verteilung des Gasverstärkungsfaktors erlaubt. Weiters wird gezeigt, dass die Lawinenverteilung in ebenen Feldern mittels eines aus der Simulation gewonnenen Toy-Modells intuitiv verstanden werden kann.

Stochastische Schwankungen in der Anzahl der entlang einer Primärteilchen-Trajektorie produzierten Elektronen stellen einen weiteren ausschlaggebenden Faktor für die Auflösung und Effizienz eines Detektors dar. Es wird gezeigt, dass die charakteristischen Größen für Primärionisationsfluktuationen, insbesonders der sog. W-Wert und der Fano-Faktor, mittels mikroskopischer Techniken berechnet werden können, sodass diese Parameter nicht länger als freie Variablen in der Simulation behandelt werden müssen.

Auf kürzlich erfolgten Arbeiten zur Bestimmung von Penningtransfer-Wahrscheinlichkeiten aufbauend wird der Einfluss von Anregungstransfer auf Primärionisationsfluktuationen und Elektronenlawinenstatistik untersucht und ein Modell zur mikroskopischen Berechnung von Penningeffekten wird vorgeschlagen.

"Garfield" ist ein weitverbreitetes Programm zur Simulation von gasbasierten Teilchendetektoren. Im Rahmen dieser Arbeit wurde eine objektorientierte Version (Garfield++) dieses Programmpakets erarbeitet, die die oben genannten mikroskopischen Methoden beinhaltet. Die Integration von Halbleiterdetektorsimulation in Garfield++, einschließlich der Anpassung von Algorithmen, Modellierung von Materialeigenschaften und Vergleich mit Messdaten, bildet ein weiteres Thema der Arbeit.

Acknowledgments

Contents

1. Introduction

Broadly speaking, particle physics experiments require two kinds of tools: a source of particles (e. g. colliders) and instruments (detectors) which measure the properties of these particles. Particle detectors – the physics of which is the subject of the present thesis – can be classified according to the purpose they serve in an experiment or, in other words, the type of information they are meant to provide about a particle.

- Tracking detectors record the path of a charged particle. By immersing the detector in a magnetic field, the particle momentum can be inferred from the track curvature.

- Calorimeters measure the energy of charged and neutral particles.

- Particle identification detectors help discriminate between different types of particles. Phenomena like the emission of Cherenkov or transition radiation are often exploited for this purpose.

From a technological viewpoint, one can characterize detectors according to the type of particle interaction with matter on which they are based (ionization, excitation followed by emission of scintillation light, Cherenkov radiation etc.) and the type of sensitive medium (gas, semiconductor, noble liquid, scintillator crystal etc.). The present thesis deals primarily with devices for tracking and photon detection which are based on ionization measurement in gases or semiconductors. These detectors work according to the same fundamental principles:

- a charged particle traversing the detector ionizes the medium along its track;

- the electrons and ions (or holes) released in the primary ionization process are separated by means of an electric field and are observed through the current their motion induces on the readout electrodes.

In gases, the amount of primary ionization is usually too small to be detected directly. Internal charge amplification, achieved by electron multiplication in a strong electric field, is necessary to obtain a good signal-to-noise ratio. The characteristics of a gas-based detector are to a large extent determined by the shape of the amplification field. Due to the $1/r$ dependence of the electric field in their vicinity, metal wires represent convenient structures for generating a localized high field region in which electron avalanches can develop. This concept, dating back to the Geiger counter, was revolutionized with the invention of the multiwire proportional counter (MWPC) by G. Charpak in the 1960s [1] and has been subject to continuous improvement ever since. MWPCs, drift chambers, straw tubes and other wire-based detectors are still widely used today, for instance in the muon systems of the LHC experiments. A comprehensive introduction to wire chambers is given in Ref. [2].

The limited rate capability of wire chambers (a consequence of space charge accumulation due to slow ion evacuation) motivated the development of detectors with alternative electrode layouts. Profiting from manufacturing techniques developed for microelectronics, a new generation of gas-based detectors with cell sizes of the order of 100 μm has emerged in the last two decades. Two main "families" of so-called Micropattern Gas Detectors (MPGDs) have established themselves:

GEMs[1], developed in 1997 by F. Sauli [3], and Micromegas[2], introduced by Y. Giomataris [4] in 1996. A concise, up-to-date description of these detectors can be found in Ref. [5]. MPGDs, which are already in operation in several experiments, are candidates for LHC detector upgrades and are also being considered to be used as readout chambers in future time projection chambers (TPCs) [6].

While gas detectors continue to be the technology of choice for instrumenting large areas, precision tracking near the vertex has become the domain of silicon sensors. In ATLAS, CMS and ALICE, for example, silicon pixel detectors constitute the innermost layers of instrumentation around the beam pipe, followed by silicon strip sensors at larger radii. In order to cope with the challenges in terms of radiation hardness associated with the planned luminosity upgrade of the LHC, strong R&D efforts are underway aimed at exploring new materials and detector layouts which promise to be less prone to radiation damage than current technologies [7]. Monolithic detectors, which integrate sensor and readout electronics on the same substrate, are another active line of research. Excellent textbooks [8, 9] discussing the physics and technology of semiconductor detectors are available.

Monte Carlo simulations are indispensable and ubiquitous tools in modern high-energy physics. Event generators like Pythia [10] are used for sampling the final state particles produced in a collision. The trajectories of these particles (including their decay and interaction with matter) through the experiment surrounding the interaction point can subsequently be calculated by detector simulation programs like Geant4 [11, 12]. Such "virtual experiments" are used e. g. for optimizing the layout of an experiment during the design phase, for calibrating detectors, and for discriminating new phenomena against the "background" of known physics as implemented in event generators.

On a smaller scale, but in a conceptually similar manner, simulations also play a vital role in the development of particle detectors. A necessary prerequisite for the successful operation of a detector is a profound understanding of its response. In other words, it has to be known how the passage of a particle through the sensitive region of the device translates into a signal observed in the readout electronics (and vice versa). For this purpose, it is useful to estimate the expected detector response by means of a calculation and to compare the result against measurements. Good agreement between measurement and calculation can be taken as an indication that the detector is fully understood. Moreover, given sufficient confidence in the reliability of a calculation, one can try to optimize a detector "on the drawing-board" by varying, for instance, the field configuration or, in case of gas-based detectors, the composition of the gas mixture.

Order-of-magnitude (and occasionally even more accurate) estimates can often be obtained by analytic, "back of the envelope" calculations. For refined calculations it has become common practice to resort to computer programs, though. For instance, numerical methods are often necessary to evaluate the electric field inside the detector (Sec. 2.2). Other key elements of detector physics such as the inelastic interaction of relativistic charged particles with the detection medium (Sec. 2.1) or the transport of electrons (and holes/ions) under the influence of an electric field are stochastic processes and can thus be modelled conveniently in terms of Monte Carlo simulation. A central theme of the present thesis is the simulation of particle (in particular: electron) transport using semi-classical ("microscopic") Monte Carlo techniques. Being based on atomic cross-sections, this approach represents a close approximation to the "true" detector processes.

---

[1] **G**as **E**lectron **M**ultiplier
[2] **Microme**sh **gas**eous structure

In the Magboltz program [13, 14], such a technique has been used for several years for calculating electron transport coefficients such as drift velocity or diffusion coefficients in gas mixtures. Using the same set of input data (i. e. the cross-sections for electron scattering by gas atoms/molecules) and adapting the algorithm to arbitrary, inhomogeneous field configurations, a broad range of topics – beyond the conventional scope of Magboltz – can be investigated. This is the basis of the microscopic tracking method presented in Sec. 2.3.2. While the development of this technique was initiated within the context of MPGD R&D (more specifically, within the framework of the RD51 collaboration), its use is not limited to micropattern gas detectors. A more generic application is the study of fluctuations in ionization processes, which constitutes the core of this thesis work. In Chapter 3, the microscopic technique is used for the calculation of electron avalanche size statistics. Chapter 4 addresses fluctuations in the primary ionization process. In Chapter 5 an extended model (including radiative and collisional excitation transfer) for the Monte Carlo simulation of electron avalanches is presented.

In order to simulate the overall behaviour of a detector, it is necessary to "glue" different modules such as field calculation and charge transport simulation together. Garfield [15], written by R. Veenhof, is a widely used program for the detailed simulation of gas-based detectors. It is interfaced with various field solvers, programs for the simulation of primary ionization, and Magboltz for the computation of electron transport properties. Unless explicitly indicated otherwise, the simulation results presented in this work were obtained using Garfield++ [16], an object-oriented version of Garfield developed within the context of this thesis, which is intended to provide a common framework for the simulation of both gas and semiconductor detectors. The implementation of silicon detector simulation in Garfield++ is discussed in Chapter 6.

2. Concepts and Techniques

In this introductory chapter, an overview of the building blocks constituting a typical detector simulation program is given. Basic concepts, definitions and calculation methods used and referred to in subsequent chapters are reviewed.

2.1. Primary Ionization

2.1.1. Photons

Photoelectric absorption is the dominant interaction process of photons in the VUV and X-ray energy range. It is described by the photoabsorption cross-section σ_γ (shown in Fig. 2.1a for the case of argon). At high energies, i. e. above the respective absorption edges, photons interact preferentially with inner shell electrons. As an example, we consider the absorption of a 5.9 keV photon[1] by an argon atom. With a probability of about 80% the photon liberates an electron from the K shell [18]. The vacancy in the K shell gives rise to a relaxation chain proceeding either radiatively, i. e. by emission of a fluorescence photon, or radiation-less (Auger effect), resulting in the emission of an Auger electron. The fluorescence photon can in turn ionize another atom in the gas or, with a probability depending on the geometry of the device, escape from the detector. The ejected photoelectrons and (most of) the Auger electrons have kinetic energies well above the ionization threshold of the gas and are thus able to release further electrons along their path. The resulting ionization pattern provides information about the primary photon, in particular its energy ϵ_γ.

The average number of electron-ion pairs $\overline{n}$ is expressed in terms of the mean energy W required to form an electron-ion pair [19]:

$$\overline{n} = \frac{\epsilon_\gamma}{W}. \tag{2.1}$$

The energy resolution is limited by fluctuations in the relaxation cascade and in the electron degradation process. The variance σ^2 of the number of electron-ion pairs n is characterized by the Fano factor F,

$$\sigma^2 = \overline{(n - \overline{n})^2} = F\overline{n}. \tag{2.2}$$

Similarly as for photons, a W value and Fano factor describing the secondary electron spectrum produced by a high energy electron (δ-electron) can be defined. The calculation of these parameters is the subject of Section 4.3.

As discussed in Section 2.1.3, the photoabsorption cross-section (more generally: the optical dielectric function) is not only relevant for the simulation of photon transport but also serves as an ingredient for constructing models for charged particle interaction.

---

[1] This energy corresponds to the main X-ray emission line of ^{55}Fe sources, which are often used for calibration purposes.
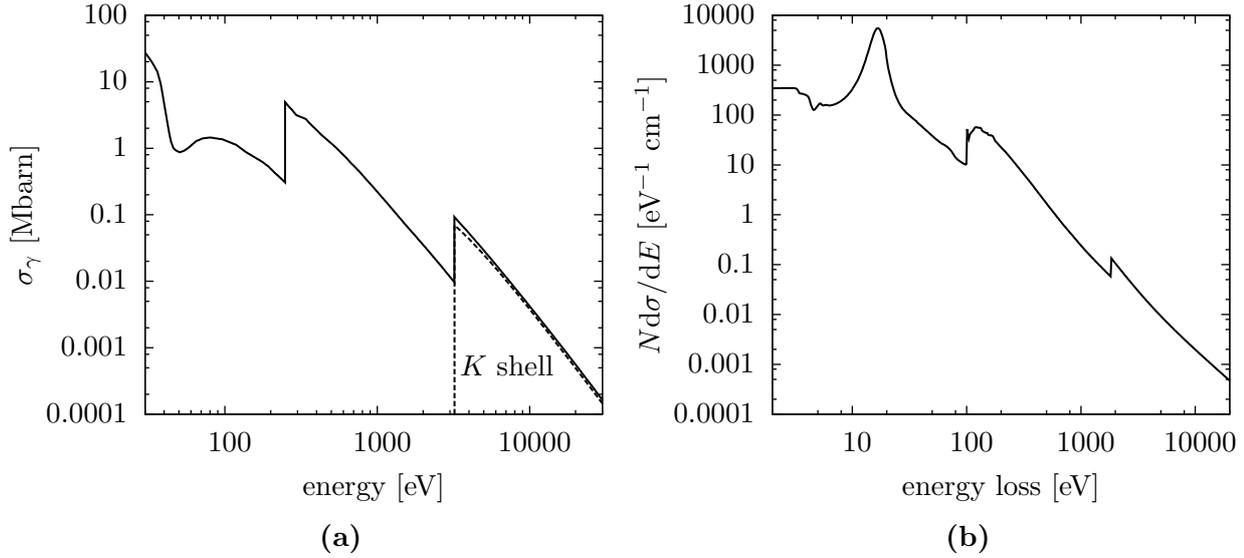
Figure 2.1. Left: total photoabsorption cross-section of argon [17] (solid curve) and cross-section for photoabsorption by K shell electrons [18] (dashed curve). Right: differential inverse inelastic mean free path (differential cross-section $d\sigma/dE$ multiplied by the atomic density) for minimum-ionizing pions ($\beta\gamma = 4$) in silicon, calculated using the PAI model implementation discussed in Section 6.1.

2.1.2. Charged Particles

The energy loss of a fast charged particle due to electromagnetic interaction with the matter it traverses is described by the differential cross-section $d\sigma/dE$, where E denotes the energy transferred in a collision. An example (for pions in silicon) is shown in Fig. 2.1b.

Important average quantities determined by $d\sigma/dE$ are:

- the total cross-section σ and thus the inverse inelastic mean free path λ^{-1},

$$\lambda^{-1} = N\sigma = N \int\limits_{0}^{E_{\max}} dE \frac{d\sigma}{dE},$$

  where N is the number of scattering centres per unit volume (i. e. the atomic density of the medium);

- the so-called stopping power dE/dx, i. e. the mean energy loss per track length,

$$\frac{dE}{dx} = N \int\limits_{0}^{E_{\max}} dE\, E \frac{d\sigma}{dE}.$$

In combination with a measurement of the particle momentum, the dependence of the stopping power on $\beta\gamma$, as described by the Bethe-Bloch formula (A.12), can be used for particle identification.

Fluctuations of the energy loss play an important role. Due to the long tail of $d\sigma/dE$ towards large energy transfers, the distribution of the energy loss over a short[2] track segment has an

---

[2] In this context, "short" means that the energy loss of the charged particle over this distance is small compared to the kinetic energy.

asymmetric shape. As a consequence, the mean energy loss corresponding to $\mathrm{d}E/\mathrm{d}x$ is typically higher than the most probable energy loss. An approximate representation of energy loss spectra is given by the Landau distribution (A.13), which is based on a simplified differential cross-section of the form $\mathrm{d}\sigma/\mathrm{d}E \propto 1/E^2$. For accurate calculations of energy loss distributions and simulations of ionization patterns however, a more detailed description of the differential cross-section is required. A convenient framework for calculating $\mathrm{d}\sigma/\mathrm{d}E$ is provided by the so-called dielectric theory of energy loss [20–22] outlined in the following section. In this formalism, the response of the medium to an incident particle is described by the dielectric function $\varepsilon\left(k,\omega\right)$.

2.1.3. Dielectric Theory

We start with a macroscopic derivation of the stopping power (see e. g. Ref. [23]). The electric field of a particle with mass M, charge ze, and velocity $\boldsymbol{\beta}c$ traversing a non-magnetic medium is determined by Maxwell's equations (cgs system)

$$\nabla \cdot \mathbf{B} = 0 \quad , \qquad \nabla \times \mathbf{E} = -\frac{1}{c}\frac{\partial \mathbf{B}}{\partial t},$$

$$\nabla \times \mathbf{B} = \frac{1}{c}\frac{\partial \mathbf{D}}{\partial t} + \frac{4\pi}{c}\mathbf{j} \quad , \qquad \nabla \cdot \mathbf{D} = 4\pi\rho,$$

with source terms $\rho = ze\delta^3\left(\mathbf{r} - \boldsymbol{\beta}ct\right)$, $\mathbf{j} = \boldsymbol{\beta}c\rho$.

Within the domain of linear response, the displacement field $\mathbf{D}$ in an isotropic medium is (in Fourier space) related to the electric field $\mathbf{E}$ by

$$\mathbf{D}\left(\mathbf{k},\omega\right) = \varepsilon\left(\mathbf{k},\omega\right)\mathbf{E}\left(\mathbf{k},\omega\right), \qquad \varepsilon\left(\mathbf{k},\omega\right) = \varepsilon'\left(\mathbf{k},\omega\right) + \mathrm{i}\varepsilon''\left(\mathbf{k},\omega\right). \tag{2.3}$$

In order to find a solution of the inhomogeneous Maxwell equations, the fields are written in terms of Fourier integrals

$$\mathbf{D}\left(\mathbf{r},t\right) = \frac{1}{\left(2\pi\right)^2}\int \mathrm{d}^3k \int \mathrm{d}\omega\,\varepsilon\left(\mathbf{k},\omega\right)\mathbf{E}\left(\mathbf{k},\omega\right)\mathrm{e}^{\mathrm{i}\left(\mathbf{k}\cdot\mathbf{r}-\omega t\right)},$$

$$\mathbf{B}\left(\mathbf{r},t\right) = \frac{1}{\left(2\pi\right)^2}\int \mathrm{d}^3k \int \mathrm{d}\omega\,\mathbf{B}\left(\mathbf{k},\omega\right)\mathrm{e}^{\mathrm{i}\left(\mathbf{k}\cdot\mathbf{r}-\omega t\right)}.$$

We obtain for the Fourier components of the fields

$$\mathrm{i}\varepsilon\left(\mathbf{k},\omega\right)\mathbf{k}\cdot\mathbf{E}\left(\mathbf{k},\omega\right) = 2ze\delta\left(\omega - \mathbf{k}\cdot\boldsymbol{\beta}c\right),$$

$$\mathrm{i}\mathbf{k}\times\mathbf{B}\left(\mathbf{k},\omega\right) = -\frac{\mathrm{i}\omega\varepsilon\left(\mathbf{k},\omega\right)}{c}\mathbf{E}\left(\mathbf{k},\omega\right) + 2ze\boldsymbol{\beta}\delta\left(\omega - \mathbf{k}\cdot\boldsymbol{\beta}c\right),$$

and, adopting the Coulomb gauge $\mathbf{k}\cdot\mathbf{A}\left(\mathbf{k},\omega\right) = 0$, for the Fourier components of the potentials

$$\phi\left(\mathbf{k},\omega\right) = \frac{1}{\varepsilon\left(\mathbf{k},\omega\right)k^2}2ze\delta\left(\omega - \mathbf{k}\cdot\boldsymbol{\beta}c\right),$$

$$\mathbf{A}\left(\mathbf{k},\omega\right) = \frac{\frac{-\omega\mathbf{k}}{k^2c} + \boldsymbol{\beta}}{k^2 - \varepsilon\left(\mathbf{k},\omega\right)\frac{\omega^2}{c^2}}2ze\delta\left(\omega - \mathbf{k}\cdot\boldsymbol{\beta}c\right).$$

The moving particle gives rise to an electric field

$$\mathbf{E}(\mathbf{r},t) = \frac{1}{\left(2\pi\right)^2}\int \mathrm{d}^3k \int \mathrm{d}\omega\,\mathrm{e}^{\mathrm{i}\left(\mathbf{k}\cdot\mathbf{r}-\omega t\right)}\left[\frac{\mathrm{i}\omega}{c}\mathbf{A}\left(\mathbf{k},\omega\right) - \mathrm{i}\mathbf{k}\phi\left(\mathbf{k},\omega\right)\right]$$

$$= \frac{\mathrm{i}ze}{2\pi^2}\int \mathrm{d}^3k \int \mathrm{d}\omega\,\mathrm{e}^{\mathrm{i}\left(\mathbf{k}\cdot\mathbf{r}-\omega t\right)}\delta\left(\omega - \mathbf{k}\cdot\boldsymbol{\beta}c\right)\left[\frac{\frac{\omega^2}{k^2c^2}\mathbf{k} - \frac{\omega}{c}\boldsymbol{\beta}}{-k^2 + \varepsilon\left(\mathbf{k},\omega\right)\frac{\omega^2}{c^2}} - \frac{\mathbf{k}}{k^2\varepsilon\left(\mathbf{k},\omega\right)}\right].$$

At $\mathbf{r} = \boldsymbol{\beta} ct$, the particle experiences a force $ze\mathbf{E}(\boldsymbol{\beta} ct, t)$. The stopping power $\mathrm{d}E/\mathrm{d}x$ is given by the component of this force along the direction of the particle,

$$\frac{\mathrm{d}E}{\mathrm{d}x} = ze\mathbf{E}\left(\boldsymbol{\beta} ct, t\right) \cdot \frac{\boldsymbol{\beta}}{\beta}. \tag{2.4}$$

The magnetic field $\mathbf{B}$ does not affect the energy of the particle. Inserting the above expression for the electric field, one obtains

$$\frac{\mathrm{d}E}{\mathrm{d}x} = \frac{\mathrm{i}z^2e^2}{\beta 2\pi^2} \int \mathrm{d}^3k \int \mathrm{d}\omega \, \mathrm{e}^{\mathrm{i}(\mathbf{k}\cdot\boldsymbol{\beta} ct - \omega t)} \delta\left(\omega - \mathbf{k}\cdot\boldsymbol{\beta} c\right) \left[\frac{\frac{\omega^2 \mathbf{k}\cdot\boldsymbol{\beta}}{k^2c^2} - \frac{\omega\beta^2}{c}}{-k^2 + \varepsilon\left(\mathbf{k},\omega\right)\frac{\omega^2}{c^2}} - \frac{\mathbf{k}\cdot\boldsymbol{\beta}}{k^2\varepsilon\left(\mathbf{k},\omega\right)} \right].$$

Transforming to spherical coordinates and integrating over the angles yields

$$\frac{\mathrm{d}E}{\mathrm{d}x} = \frac{\mathrm{i}z^2e^2}{\beta^2\pi} \int\limits_{-\infty}^{\infty} \mathrm{d}\omega \int\limits_{\frac{\omega}{\beta c}}^{\infty} \mathrm{d}k \left[\frac{k\omega\left(\beta^2 - \frac{\omega^2}{k^2c^2}\right)}{-k^2c^2 + \varepsilon\left(k,\omega\right)\omega^2} - \frac{\omega}{kc^2\varepsilon\left(k,\omega\right)} \right].$$

Using $\varepsilon(-\omega) = \varepsilon^*(\omega)$ the integration over ω can be limited to positive frequencies,

$$\frac{\mathrm{d}E}{\mathrm{d}x} = -\frac{2z^2e^2}{\beta^2\pi} \int\limits_{0}^{\infty} \mathrm{d}\omega \int\limits_{\frac{\omega}{\beta c}}^{\infty} \mathrm{d}k \left[\omega k \left(\beta^2 - \frac{\omega^2}{k^2c^2}\right) \mathrm{Im}\left(\frac{1}{-k^2c^2 + \varepsilon\left(k,\omega\right)\omega^2} \right) + \frac{\omega}{kc^2}\mathrm{Im}\left(\frac{-1}{\varepsilon\left(k,\omega\right)} \right) \right].$$

$$\tag{2.5}$$

The second term in the integrand represents the non-relativistic contribution to the energy loss which we would have obtained by considering only the scalar potential ϕ (Coulomb interaction). It is often referred to as the longitudinal term. The first term (transverse term) originates from the vector potential $\mathbf{A}$; it incorporates relativistic effects.

Up to this point, the interaction of the incident particle with the medium has been treated in an entirely classical framework. We reinterpret (2.5) now in a quantum mechanical picture: the incident particle is not slowed down continuously but loses energy in collisions with energy transfer $E = \hbar\omega$ and momentum transfer $\hbar k$. With N being the atomic density in the medium, we can write the stopping power as

$$\frac{\mathrm{d}E}{\mathrm{d}x} = -\int\limits_{0}^{\omega_{\mathrm{max}}} \mathrm{d}\omega \int\limits_{\frac{\omega}{\beta c}}^{\infty} \mathrm{d}k \, N\hbar\omega \frac{\mathrm{d}^2\sigma}{\mathrm{d}k\mathrm{d}\omega}. \tag{2.6}$$

The limits of the integration over k in (2.6) can be understood from kinematic considerations. With p^μ and p'^μ being the four-momenta of the incident particle before and after a collision, respectively, we have

$$\frac{p^2 - p'^2}{2\gamma M} = \hbar\omega\left(1 - \frac{\hbar\omega}{2\gamma Mc^2}\right) - \hbar c\boldsymbol{\beta}\cdot\mathbf{k} + \frac{\hbar^2 k^2}{2\gamma M} = 0,$$

which in the limit of small energy and momentum transfers ($\hbar\omega \ll \gamma Mc^2, \hbar k \ll \beta\gamma Mc$) reduces to $\omega = \beta kc\cos\theta$. At fixed ω, the lower bound of k is thus $k_{\mathrm{min}} = \omega/\beta c$.

The upper limit of the integration over ω is also determined by kinematic constraints, as the maximum energy a particle (other than an electron) can transfer to an electron in a single collision is given by [24]

$$E_{\mathrm{max}} = 2m_ec^2\beta^2\gamma^2 \left[1 + \left(\frac{m_e}{M}\right)^2 + 2\gamma\frac{m_e}{M}\right]^{-1}. \tag{2.7}$$

By comparison of (2.5) and (2.6), one sees that the doubly differential cross-section $\mathrm{d}^2\sigma/(\mathrm{d}k\mathrm{d}\omega)$ is fully determined by the dielectric function $\varepsilon(k,\omega)$. As a next step we, therefore, have to specify $\varepsilon(k,\omega)$, in particular the so-called loss function $\mathrm{Im}\left(-1/\varepsilon\left(k,\omega\right)\right)$.

Dielectric Function

In order to find a quantum-mechanical expression for the dielectric function $\varepsilon\left(\mathbf{k},\omega\right)$, we follow the approach outlined in Ref. [25]. We consider the response of a system of electrons to a weak perturbation induced by an external test charge density $\rho_{\mathrm{ext}}\left(\mathbf{r},t\right)$. In particular, we want to calculate the expectation value of the induced electron density ρ_{ind}. Using

$$
\begin{aligned}
\mathrm{i}\mathbf{k}\cdot\mathbf{D}\left(\mathbf{k},\omega\right) &= \mathrm{i}\mathbf{k}\cdot\varepsilon\left(\mathbf{k},\omega\right)\mathbf{E}\left(\mathbf{k},\omega\right) = 4\pi\rho_{\mathrm{ext}}\left(\mathbf{k},\omega\right), \\
\mathrm{i}\mathbf{k}\cdot\mathbf{E} &= 4\pi\left(\rho_{\mathrm{ind}}\left(\mathbf{k},\omega\right)+\rho_{\mathrm{ext}}\left(\mathbf{k},\omega\right)\right)
\end{aligned}
$$

we can then obtain the dielectric function $\varepsilon\left(\mathbf{k},\omega\right)$ from

$$
\frac{1}{\varepsilon\left(\mathbf{k},\omega\right)} = 1 + \frac{\rho_{\mathrm{ind}}\left(\mathbf{k},\omega\right)}{\rho_{\mathrm{ext}}\left(\mathbf{k},\omega\right)}.
$$

The Hamiltonian of the system, $H = H_0 + U$, consists of the Hamiltonian H_0 of the unperturbed system and a perturbation term U due to the external test charge,

$$
U(\mathbf{r}_i,t) = \frac{1}{(2\pi)^2}\int\mathrm{d}^3\mathbf{k}\int\mathrm{d}\omega\, e\phi_{\mathrm{ext}}\left(\mathbf{k},\omega\right)\sum_i \mathrm{e}^{\mathrm{i}\mathbf{k}\cdot\mathbf{r}_i}\mathrm{e}^{-\mathrm{i}\omega t+\Gamma t},
$$

where

$$
\phi_{\mathrm{ext}}\left(\mathbf{k},\omega\right) = \frac{4\pi}{k^2}\rho_{\mathrm{ext}}\left(\mathbf{k},\omega\right)
$$

is the Fourier component of the test charge potential ϕ_{ext}. The damping constant Γ is inserted to ensure that the perturbation vanishes at $t = -\infty$. The many-body wave function of the electron system can be expanded as

$$
|\psi(t)\rangle = \sum_j c_j(t)\mathrm{e}^{-\mathrm{i}(\epsilon_j/\hbar)t}|j\rangle,
$$

where $|j\rangle$, ϵ_j are the eigenstates and eigenvalues of H_0. It is assumed that the electron system was initially, that is at $t = -\infty$, in its ground state $|0\rangle$. In first order time dependent perturbation theory the coefficients c_j are given by

$$
c_j(t) = c_j^{(0)}(t) + c_j^{(1)}(t) = \delta_{j0} + \frac{1}{\mathrm{i}\hbar}\int_{-\infty}^{t}\mathrm{d}t'\mathrm{e}^{\mathrm{i}\omega_{j0}t'}\langle j|U\left(t'\right)|0\rangle; \qquad \omega_j = \frac{\epsilon_j-\epsilon_0}{\hbar}.
$$

Inserting the expression for U from above we find for the first order coefficient

$$
\begin{aligned}
c_j^{(1)}(t) &= \frac{e}{\mathrm{i}\hbar}\frac{1}{(2\pi)^2}\int\mathrm{d}^3k\int\mathrm{d}\omega\int_{-\infty}^{t}\mathrm{d}t'\mathrm{e}^{\mathrm{i}\omega_{j0}t'}\mathrm{e}^{-\mathrm{i}\omega t'}\mathrm{e}^{\Gamma t'}\phi_{\mathrm{ext}}\left(\mathbf{k},\omega\right)F_{j0}\left(\mathbf{k}\right) \\
&= \frac{e}{\hbar}\frac{1}{(2\pi)^2}\int\mathrm{d}^3k\int\mathrm{d}\omega\,\frac{\mathrm{e}^{\mathrm{i}(\omega_{j0}-\omega)t}\mathrm{e}^{\Gamma t}}{-\omega_{j0}+\omega+\mathrm{i}\Gamma}\phi_{\mathrm{ext}}\left(\mathbf{k},\omega\right)F_{j0}\left(\mathbf{k}\right)
\end{aligned}
$$

where F_{j0} denotes the so-called form factor

$$
F_{j0}\left(\mathbf{k}\right) = \langle j|\sum_i \mathrm{e}^{\mathrm{i}\mathbf{k}\cdot\mathbf{r}_i}|0\rangle.
$$

Since the charge density of the electron system is given by

$$\rho\left(\mathbf{r}\right) = e \sum_i \delta\left(\mathbf{r} - \mathbf{r}_i\right), \qquad \rho\left(\mathbf{k}\right) = \frac{e}{(2\pi)^{3/2}} \sum_i e^{-i\mathbf{k}\cdot\mathbf{r}_i},$$

the matrix elements of $\rho\left(\mathbf{k}\right)$ are

$$\langle 0 | \rho\left(\mathbf{k}\right) | j \rangle = \frac{e}{(2\pi)^{3/2}} F_{0j}\left(-\mathbf{k}\right).$$

To linear order we obtain for the expectation value of the induced charge density

$$
\begin{aligned}
\rho_{\text{ind}}\left(\mathbf{k}\right) &\approx \langle \psi | \rho\left(\mathbf{k}\right) | \psi \rangle - \langle 0 | \rho\left(\mathbf{k}\right) | 0 \rangle \\
&= \sum_j \left[c_j^{(1)\,*}(t)\, e^{i\omega_{j0}t}\, \langle j | \rho\left(\mathbf{k}\right) | 0 \rangle + c_j^{(1)}(t)\, e^{-i\omega_{j0}t}\, \langle 0 | \rho\left(\mathbf{k}\right) | j \rangle \right].
\end{aligned}
$$

Inserting the expression for $c_j^{(1)}$ and using $\phi^*\left(\mathbf{k}, \omega\right) = \phi\left(-\mathbf{k}, -\omega\right)$ yields

$$\rho_{\text{ind}}\left(\mathbf{k}, \omega\right) = - \int d^3 k' \sum_j \phi\left(\mathbf{k}', \omega\right) \left[\frac{F_{j0}\left(\mathbf{k}'\right) F_{0j}\left(-\mathbf{k}\right)}{\omega_{j0} - (\omega + i\Gamma)} + \frac{F_{0j}\left(\mathbf{k}'\right) F_{j0}\left(-\mathbf{k}\right)}{\omega_{j0} + (\omega + i\Gamma)} \right].$$

Neglecting coupling between different components $\mathbf{k}$ of the density fluctuation, i. e. considering only the Fourier component $\mathbf{k}' = \mathbf{k}$ of the potential, one finally obtains the result

$$\frac{1}{\varepsilon\left(\mathbf{k}, \omega\right)} = 1 - \frac{4\pi e^2}{\hbar k^2} \sum_j |F_{j0}\left(\mathbf{k}\right)|^2 \left[\frac{1}{\omega_{j0} - (\omega + i\Gamma)} + \frac{1}{\omega_{j0} + (\omega + i\Gamma)} \right]. \tag{2.8}$$

Using[3]

$$\lim_{\Gamma \to 0} \frac{1}{\omega - y + i\Gamma} = \mathsf{P}\frac{1}{\omega - y} - i\pi\delta\left(\omega - y\right),$$

where P denotes the Cauchy principal value, one obtains for the loss function in the limit of small Γ

$$\text{Im}\left(\frac{-1}{\varepsilon\left(k, \omega\right)} \right) = \frac{4\pi^2 e^2}{\hbar k^2} \sum_j |F_{j0}\left(\mathbf{k}\right)|^2 \left[\delta\left(\omega - \omega_{j0}\right) - \delta\left(\omega + \omega_{j0}\right) \right].$$

A closed-form expression for (2.8) can only be obtained for special cases such as the hydrogen atom and the Fermi gas.

Atomic Hydrogen

In atomic physics, the coupling between a charged particle and an atom is usually described in terms of the so-called generalized oscillator strength density (GOS)

$$\frac{df\left(k, \omega\right)}{d\omega} = \frac{2m_e}{\hbar k^2} \sum_j \omega_{j0} |F_{j0}\left(\mathbf{k}\right)|^2 \delta\left(\omega - \omega_{j0}\right),$$

which is related to the loss function by

$$\text{Im}\left(\frac{-1}{\varepsilon\left(k, \omega\right)} \right) = \frac{2\pi^2 e^2 N}{m_e \omega} \frac{df\left(k, \omega\right)}{d\omega}.$$

---

[3] Strictly speaking, this relation holds only under the integral.

(a) Hydrogen   **(b)** Fermi Gas
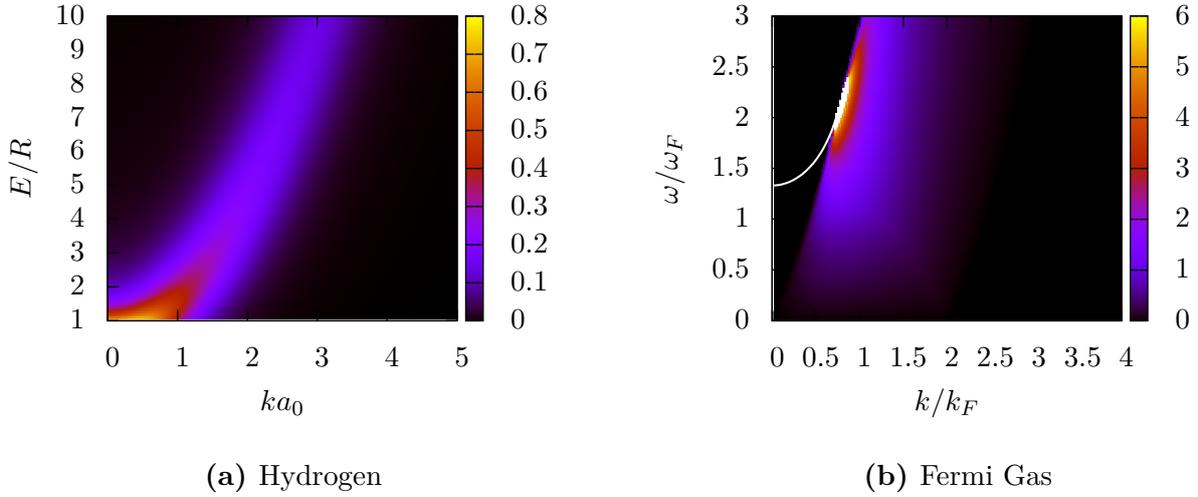
Figure 2.2. Left: generalized oscillator strength density $\frac{\mathrm{d}f}{\mathrm{d}(E/R)}$ of atomic hydrogen for transitions
to the continuum according to formula (3.10) in Ref. [27] (R is the binding energy of hydrogen,
a_0 is the Bohr radius). Right: loss function $\mathrm{Im}\left(-1/\varepsilon_L\left(k,\omega\right)\right)$ of a degenerate Fermi gas
(Lindhard function).

The form factors $F_{j0}\left(\mathbf{k}\right)$ of the hydrogen atom were calculated in 1930 by Bethe [26]. Figure 2.2a
shows a plot of the corresponding generalized oscillator strength density for transitions to the
continuum.

At large energy and momentum transfers, $\mathrm{d}f\left(k,\omega\right)/\mathrm{d}\omega$ is concentrated along the free electron
line $\omega = \hbar k^2/2m_e$. At low k the exponential in the form factor can be approximated by an
expansion to linear order (dipole approximation). The generalized oscillator strength then reduces
to the dipole (or optical) oscillator strength (see Appendix A.1.1) describing the photon-atom
interaction. A comprehensive review of the generalized oscillator strength concept can be found
in Ref. [27].

Fermi Gas

For free electrons,

$$\phi_j\left(\mathbf{r}\right) = \frac{1}{\sqrt{V}}\mathrm{e}^{\mathrm{i}\mathbf{k}_j\cdot\mathbf{r}},$$

the form factor reduces to [28]

$$F_{j0}\left(\mathbf{k}\right) = \frac{\left(2\pi\right)^3}{V}\delta\left(\mathbf{k} - \mathbf{k}_j + \mathbf{k}_0\right),$$

and the excitation frequencies become

$$\omega_{j0} = \frac{\hbar k^2}{2m_e} + \frac{\hbar}{m_e}\mathbf{k}\cdot\mathbf{k}_0 = \omega_k + \frac{\hbar}{m_e}\mathbf{k}\cdot\mathbf{k}_0.$$

As we are dealing with continuous quantum numbers $\mathbf{k}_j$, the sum over the states j is transformed
into an integral,

$$\sum_j \rightarrow \frac{V}{\left(2\pi\right)^3}\int\mathrm{d}^3\mathbf{k}_j.$$

The occupation probability of the initial state $\mathbf{k}_0$ is given by the Fermi-Dirac distribution $g_{\mathrm{FD}}(k_0)$. For the ensemble average of $\varepsilon(k,\omega)$ one obtains

$$\varepsilon(k,\omega) = 1 + \frac{\omega_p^2}{2\omega_k}\frac{3}{4\pi k_F^3}\int \mathrm{d}^3 k_0\, g_{\mathrm{FD}}(k_0)\left[\frac{1}{\omega_k + \frac{\hbar}{m_e}\mathbf{k}\cdot\mathbf{k}_0 - (\omega + \mathrm{i}\Gamma)} + \frac{1}{\omega_k + \frac{\hbar}{m_e}\mathbf{k}\cdot\mathbf{k}_0 + (\omega + \mathrm{i}\Gamma)}\right],$$

where we have introduced the plasma frequency

$$\omega_p = \sqrt{\frac{4\pi e^2 N_e}{m_e}}, \tag{2.9}$$

with N_e being the electron density of the medium. Considering the limit of low momentum transfer, we perform a Taylor expansion of the integrand to fourth order

$$\frac{1}{\omega_{j0}-\omega} + \frac{1}{\omega_{j0}+\omega} = -\frac{2\hbar k_0 \cos\theta}{m_e\omega^2}k - \frac{\hbar}{m_e\omega^2}k^2 - \frac{2\hbar^3 k_0^3\cos^3\theta}{m_e^3\omega^4}k^3 - \frac{3\hbar^3 k_0^2\cos^2\theta}{m_e^3\omega^4}k^4 + ...$$

The linear and the cubic term contain odd powers of $\cos\theta$ and thus vanish upon integration. Retaining only the quadratic term yields

$$\varepsilon(k,\omega) \approx 1 - \frac{\omega_p^2}{\omega^2}.$$

In the regime of low momentum transfer, the loss function thus exhibits a singularity at the plasma frequency ω_p. In a simple, classical picture this resonance can be interpreted as follows [29]: the external perturbation causes a displacement of the electrons by $\mathbf{r}$ leading to a polarization $\mathbf{P} = N_e e\mathbf{r}$ and an electric field $\mathbf{E} = -4\pi\mathbf{P}$. The resulting equation of motion

$$m_e\frac{\mathrm{d}^2}{\mathrm{d}t^2}\mathbf{r} = e\mathbf{E} = -4\pi N_e e^2\mathbf{r},$$

describes a harmonic oscillation with frequency ω_p. Collective oscillations of the electron density are indeed a predominant feature of the loss function of solids, in particular of simple metals and semiconductors. The quanta of such plasma oscillations are called plasmons. Inserting the fourth-order expansion term yields

$$\varepsilon(k,\omega) \approx 1 - \frac{\omega_p^2}{\omega^2}\left(1 + \frac{3}{5}\frac{k^2 v_F^2}{\omega^2}\right).$$

From the resonance condition, $\varepsilon(k,\omega) = 0$, one obtains the plasmon dispersion relation

$$\omega^2 \approx \omega_p^2 + \frac{3}{5}\frac{k^2 v_F^2}{\omega_p^2}.$$

Lindhard [30, 31] found a closed-form solution for the dielectric function of a Fermi gas at zero temperature. The Lindhard loss function $\mathrm{Im}\left(-1/\varepsilon_L(k,\omega)\right)$ is plotted in Fig. 2.2b. Two distinct features of the loss function can be identified: the continuum of single-electron excitations in the region

$$\frac{\hbar k^2}{2m_e} - \frac{\hbar k k_F}{m_e} < \omega < \frac{\hbar k^2}{2m_e} + \frac{\hbar k k_F}{m_e},$$

and the plasmon line determined by $\varepsilon(k,\omega) = 0$. As in the case of hydrogen, with increasing momentum transfer the loss function is concentrated around the free electron line $\omega = \omega_k$. The plasmon line joins the single-electron excitation region at a critical wave-vector $k = k_c$, beyond which plasmons decay by transferring their energy to one of the electrons. The critical wave-vector can roughly be approximated as $k_c \approx \omega_p/v_F$.

Equivalence with Born Approximation

As outlined in Appendix A.1, the non-relativistic expression for the stopping power according to the first Born approximation is given by

$$\frac{\mathrm{d}E}{\mathrm{d}x} = -\frac{8\pi z^2 e^4 M^2 N}{\hbar^4 K^2} \sum_j \int\limits_{k_{\min}}^{k_{\max}} \mathrm{d}k \frac{|F_{j0}|^2}{k^3} \left(\epsilon_j - \epsilon_0\right). \tag{2.10}$$

From the macroscopic derivation we obtained for the longitudinal part of the stopping power

$$\frac{\mathrm{d}E}{\mathrm{d}x} = -\frac{2z^2 e^2}{\beta^2 c^2 \pi} \int\limits_0^\infty \mathrm{d}\omega \int\limits_{k_{\min}}^{k_{\max}} \mathrm{d}k \frac{\omega}{k} \mathrm{Im}\left(\frac{-1}{\varepsilon\left(k, \omega\right)}\right).$$

Inserting the expression for the loss function (for small damping constants) derived above,

$$\mathrm{Im}\left(\frac{-1}{\varepsilon\left(k, \omega\right)}\right) = \frac{4\pi^2 e^2 N}{\hbar k^2} \sum_j |F_{j0}\left(\mathbf{k}\right)|^2 \left[\delta\left(\omega - \omega_{j0}\right) - \delta\left(\omega + \omega_{j0}\right)\right], \qquad \omega_{j0} = \frac{1}{\hbar}\left(\epsilon_j - \epsilon_0\right),$$
$$\tag{2.11}$$

one sees that the macroscopic expression for the longitudinal contribution to the stopping power in combination with an appropriate microscopic expression for the dielectric function is equivalent to the first-order non-relativistic quantum-mechanical result.

Optical Data Models

The dielectric formalism described above can easily be implemented in a computer simulation, provided that the generalized dielectric function is known. First-principles calculations of $\varepsilon\left(\mathbf{k}, \omega\right)$ – or, equivalently, the generalized oscillator strength – for many-electron atoms, molecules or solids are quite complicated however. On the other hand, for calculating the energy loss of a particle, one is primarily interested in the (singly) differential cross-section $\mathrm{d}\sigma/\mathrm{d}E$, in which the dependence on k is "averaged out". While measurements of the loss function over the full range of k seem to be very scarce, optical data are more abundant. A common approach is, therefore, to rely on measured data in the optical regime, and to use a physically motivated algorithm for the extrapolation of the optical dielectric function $\varepsilon\left(\omega\right)$ to larger k. Model dielectric functions of a gas or solid are typically constructed in such a way that key features of the respective paradigmatic examples (hydrogen atom, Fermi gas) such as the Bethe ridge or the plasmon dispersion relation are preserved.

Numerous optical data based models exist. In the following we describe the so-called photoabsorption ionization (PAI) model, which is often used in calculations for gas-based detectors.

Photoabsorption Ionization (PAI) Model

The PAI model was introduced in 1980 by Allison and Cobb [23]. A similar model had been described before by Chechin et al. [32] and had been used by Lapique and Piuz for simulating ionization patterns in argon [33]. The model was used for solid state detectors for the first time by Hall [34].

Let us first consider the longitudinal term of the integrand in Eq. (2.5). In the PAI model, the dipole approximation, that is the approximation of $\varepsilon\left(k, \omega\right)$ by its optical limit $\varepsilon\left(\omega\right)$, is

extended to the whole domain $\hbar k < \sqrt{2 m_e \hbar \omega}$. Inspired by the shape of the hydrogenic oscillator strength, the remaining contribution to $\mathrm{Im}(-1/\varepsilon(k,\omega))$ required to satisfy the Bethe sum rule (cf. Appendix A.1.1),

$$\int_0^\infty \omega \mathrm{Im}\left(\frac{-1}{\varepsilon(k,\omega)}\right) \mathrm{d}\omega = \frac{\pi}{2}\omega_p^2, \tag{2.12}$$

is attributed to the scattering by free electrons ("close collisions"). This term is thus of the form $C\delta(\omega - \hbar k^2/2m_e)$. The factor C is determined by the normalization (2.12),

$$C = \frac{1}{\omega}\int_0^\omega \omega' \mathrm{Im}\left(\frac{-1}{\varepsilon(\omega')}\right) \mathrm{d}\omega'.$$

Combining the two terms, the longitudinal loss function becomes

$$\mathrm{Im}\left(\frac{-1}{\varepsilon(k,\omega)}\right) = \mathrm{Im}\left(\frac{-1}{\varepsilon(\omega)}\right)\Theta\left(\omega - \frac{\hbar k^2}{2m_e}\right) + \frac{\delta\left(\omega - \frac{\hbar k^2}{2m_e}\right)}{\omega}\int_0^\omega \omega'\mathrm{Im}\left(\frac{-1}{\varepsilon(\omega')}\right)\mathrm{d}\omega'.$$

After integration over k we obtain

$$\left(\frac{\mathrm{d}E}{\mathrm{d}x}\right)_{\mathrm{long}} = -\frac{z^2 e^2}{\beta^2 c^2 \pi}\int_0^{\omega_{\max}} \omega \left[\mathrm{Im}\left(\frac{-1}{\varepsilon(\omega)}\right)\ln\frac{2m_e\beta^2 c^2}{\hbar\omega} + \frac{1}{\omega^2}\int_0^\omega \omega'\mathrm{Im}\left(\frac{-1}{\varepsilon(\omega')}\right)\mathrm{d}\omega'\right]\mathrm{d}\omega. \tag{2.13}$$

As for the transverse term, i. e. the first term of the integrand in Eq. (2.5), the largest contribution to the integral comes from the vicinity of the real photon line $\omega = kc/\sqrt{\varepsilon}$. In the transverse term one consequently sets $\varepsilon(k,\omega) = \varepsilon(\omega)$ throughout. Substituting $u = k^2 c^2$ one obtains

$$\left(\frac{\mathrm{d}E}{\mathrm{d}x}\right)_{\mathrm{trans}} = \frac{z^2 e^2}{\beta^2 c^2 \pi}\int_0^{\omega_{\max}}\mathrm{d}\omega\,\varepsilon''(\omega)\omega^3\int_{\omega^2/\beta^2}^\infty \mathrm{d}u\left(\beta^2 - \frac{\omega^2}{u}\right)\frac{1}{u^2 - 2u\varepsilon'(\omega)\omega^2 + \omega^4\left|\varepsilon(\omega)\right|^2}.$$

Integrating over u yields

$$\left(\frac{\mathrm{d}E}{\mathrm{d}x}\right)_{\mathrm{trans}} = -\frac{z^2 e^2}{\beta^2 c^2 \pi}\int_0^{\omega_{\max}}\omega\left[\mathrm{Im}\left(\frac{-1}{\varepsilon(\omega)}\right)\ln\frac{1}{\sqrt{(1 - 2\varepsilon'(\omega)\beta^2)^2 + \varepsilon''(\omega)^2\beta^4}}\right.$$
$$\left. + \left(\beta^2 - \frac{\varepsilon'(\omega)}{\left|\varepsilon(\omega)\right|^2}\right)\left(\frac{\pi}{2} - \arctan\frac{1 - \beta^2\varepsilon'(\omega)}{\beta^2\varepsilon''(\omega)}\right)\right]\mathrm{d}\omega.$$

By comparison with

$$\frac{\mathrm{d}E}{\mathrm{d}x} = -\int_0^{E_{\max}} NE\frac{\mathrm{d}\sigma}{\mathrm{d}E}\mathrm{d}E, \qquad E = \hbar\omega,$$

we obtain for the differential cross-section $\mathrm{d}\sigma/\mathrm{d}E$

$$N\frac{\mathrm{d}\sigma}{\mathrm{d}E} = \frac{z^2\alpha_f}{\beta^2\pi\hbar c}\mathrm{Im}\left(\frac{-1}{\varepsilon(E)}\right)\ln\frac{2m_e\beta^2 c^2}{E}$$
$$+ \frac{z^2\alpha_f}{\beta^2\pi\hbar c}\mathrm{Im}\left(\frac{-1}{\varepsilon(E)}\right)\ln\frac{1}{\left|1 - \beta^2\varepsilon(E)\right|}$$
$$+ \frac{z^2\alpha_f}{\beta^2\pi\hbar c}\left(\beta^2 - \frac{\varepsilon'(E)}{\left|\varepsilon(E)\right|^2}\right)\left(\frac{\pi}{2} - \arctan\frac{1 - \beta^2\varepsilon'(E)}{\beta^2\varepsilon''(E)}\right)$$
$$+ \frac{z^2\alpha_f}{\beta^2\pi\hbar c}\frac{1}{E^2}\int_0^E E'\mathrm{Im}\left(\frac{-1}{\varepsilon(E')}\right)\mathrm{d}E', \tag{2.14}$$

with $\alpha_f = e^2 / (\hbar c) \approx 1/137$ being the fine structure constant.

Since the model is based on dielectric theory, the density effect is naturally included (in the second term) and does not need to be added a posteriori as a correction term. In the transparency region ($\varepsilon''(\omega) = 0$), the third term can be identified with the cross-section for the emission of Cherenkov photons. It vanishes for $\beta < 1/\sqrt{\varepsilon}$; above threshold it becomes

$$\left(\frac{\mathrm{d}\sigma}{\mathrm{d}E} \right)_{\text{Čer}} = \frac{\alpha_f}{N\hbar c} \left(1 - \frac{1}{\beta^2 \varepsilon} \right) \approx \frac{\alpha_f}{N\hbar c} \sin^2 \theta_{\text{Čer}},$$

where

$$\cos \theta_{\text{Čer}} = \frac{1}{\beta \sqrt{\varepsilon}}.$$

The last term describes the scattering by quasi-free electrons. For large energy transfers it approaches the Rutherford cross-section (A.3).

In the formulation of the PAI model by Allison and Cobb, the imaginary part ε'' of the dielectric function is approximated by the photoabsorption cross-section σ_γ,

$$\varepsilon''(E) \approx \frac{N\hbar c}{E} \sigma_\gamma(E) \tag{2.15}$$

and the real part ε' is calculated from the Kramers-Kronig relation

$$\varepsilon'(E) - 1 = \frac{2}{\pi} \mathsf{P} \int\limits_0^\infty \frac{E' \varepsilon''(E')}{E'^2 - E^2} \mathrm{d}E'.$$

In addition, the approximation $|\varepsilon(E)|^2 \approx 1$ is used. These are valid approximations if the refractive index is close to one ($\mathsf{n} \approx 1$) and the attenuation coefficient k is small. For gases, this requirement is usually fulfilled in the practically relevant energy range, that is above the ionization potential. Whether this approximation is appropriate for solid media as well is discussed in Section 6.1.

2.2. Electric Fields

With rare exceptions, calculation techniques providing closed-form expressions of the electrostatic potential are limited to two-dimensional problems. A number of conventional detector geometries (e. g. wire chambers and drift tubes) do exhibit - to good approximation - translational invariance in one direction such that a two-dimensional treatment is adequate. Semi-analytical calculation techniques – based essentially on the capacitance matrix method[4] – for the arrangements of wires and equipotential planes (with or without periodicities) which can be handled by Garfield are described in Ref. [35].

An elegant method for solving the two-dimensional Laplace equation is based on the use of conformal mappings. In Section 2.2.1 this method is illustrated with the help of an example to be used later for the weighting field in a strip detector.

For truly three-dimensional devices (e. g. GEMs), one has to resort to numerical techniques such as the finite element method (FEM) or the boundary element method (BEM).

---

[4] Using the Green's function for the electrostatic potential of a wire under the given boundary conditions, the capacitance matrix of the system is established and numerically inverted to calculate the charges on the wires corresponding to the respective potentials. This method is conceptually similar to the neBEM approach discussed in Section 2.2.2.

Figure 2.3 Geometry discussed in Section 2.2.1: two infinite parallel planes (y = const.), separated by a distance $\Delta y = d$.
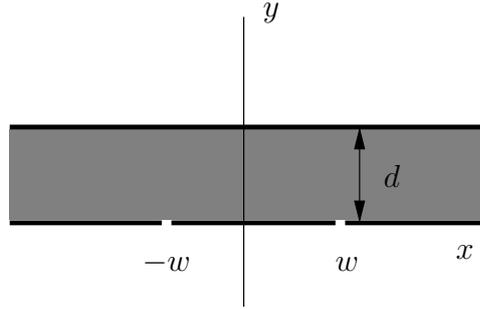
The finite element approach affords great flexibility in that virtually arbitrarily shaped geometries can be modelled. Powerful commercial software packages (e. g. Ansys [36]) are available. A crucial step in FEM-based calculations is the subdivision (meshing) of the physical domain into discrete elements. In this respect, geometries involving feature sizes which are small compared to the overall dimensions of the region to be meshed (e. g. 50 µm wire diameter vs. 1 cm tube radius in a drift tube, 1 µm grid thickness vs. 1 mm drift gap in a GOSSIP) are particularly challenging. In such cases, a fine mesh is necessary to obtain good accuracy for the potential, which comes at the price of a large field map and thus slow interpolation, though. Other adverse aspects of finite element field calculations are discontinuities of the electric field between elements and the approximation of the field by low order polynomials [37].

These deficiencies are largely overcome in BEM-based field solvers, where only the boundary of the domain and not its interior need to be meshed. With regard to micropattern gas detectors, a novel BEM-variant called "nearly exact Boundary Element Method" (neBEM) has been developed by S. Mukhopadhyay and coworkers [38, 39] and integrated into Garfield (Fortran version) by R. Veenhof. A two-dimensional neBEM-version, which was implemented in the context of this thesis, is described in Section 2.2.2.

2.2.1. Conformal Mapping

A conformal mapping is a transformation $\zeta = f(z)$ ($z, \zeta \in \mathbb{C}$) which preserves local angles. If $f(z)$ is analytic, the mapping $\zeta = f(z)$ is conformal at any point where $f'(z) \neq 0$ [40, 41].

As an example, we consider two infinite parallel plates separated by distance d (Fig. 2.3). For the boundary conditions applied to the lower plane ($y = 0$), we choose

$$\phi(x, y = 0) = \begin{cases} \phi_0, & -w < x < w \\ 0, & \text{else} \end{cases}.$$

The plane at $y = d$ is assumed to be grounded. With $\phi_0 = 1$, this corresponds to the weighting field of a parallel-plate chamber with a segmented readout electrode (pitch $2w$). By means of the transformation

$$z = x + \mathrm{i}y \rightarrow \zeta = \xi + \mathrm{i}\eta = \mathrm{e}^{\pi z/d},$$

the shaded region of the z plane is mapped conformally on the upper half of the ζ plane [40].

The solution for the Laplace equation in the upper half plane

$$\left(\frac{\partial^2}{\partial \xi^2} + \frac{\partial^2}{\partial \eta^2}\right)\phi(\xi, \eta) = 0, \qquad \eta > 0,$$
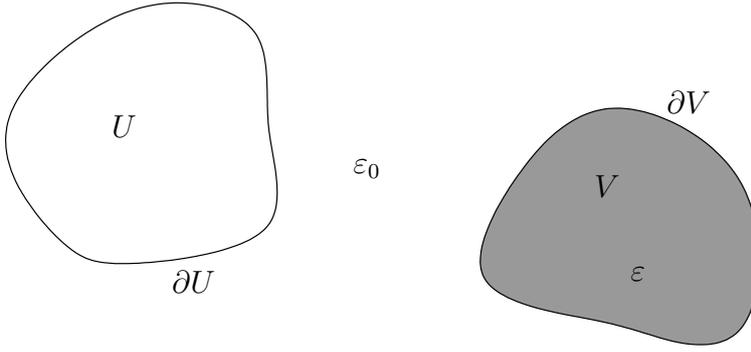
Figure 2.4 Elementary configuration for an electrostatic problem to be solved by neBEM: a conductor U with boundary ∂U at fixed potential and a dielectric body V (boundary ∂V) with relative dielectric constant ε.

satisfying the boundary condition $\phi(\xi, 0) = g(\xi)$ on the ξ axis is given by Poisson's formula for the half plane [40]

$$\phi(\xi, \eta) = \frac{1}{\pi} \int_{-\infty}^{\infty} ds \frac{\eta g(s)}{\eta^2 + (\xi - s)^2}. \tag{2.16}$$

With

$$g(\xi) = \begin{cases} \phi_0, & e^{-\pi w/d} < \xi < e^{\pi w/d} \\ 0, & \text{else} \end{cases}$$

Eq. (2.16) yields

$$\phi(\xi, \eta) = \frac{\phi_0}{\pi} \left[\arctan\left(\frac{\xi - e^{-\pi w/d}}{\eta}\right) - \arctan\left(\frac{\xi - e^{\pi w/d}}{\eta}\right) \right].$$

After transformation back to the z domain one obtains

$$\phi(x, y) = \frac{\phi_0}{\pi} \arctan\left(\frac{\sin(\pi y/d)\sinh(\pi w/d)}{\cosh(\pi x/d) - \cos(\pi y/d)\cosh(\pi w/d)}\right). \tag{2.17}$$

2.2.2. Nearly Exact Boundary Element Method (2D)

We consider the system depicted in Fig. 2.4 consisting of a conductor U at fixed potential ϕ and a dielectric V with relative dielectric constant ε. The generalization of this basic configuration to an arbitrary number of conducting and dielectric bodies is straightforward. Our goal is to compute the electric field $\mathbf{E}$ and the potential ϕ at any point $\mathbf{r}$ outside the conductor. In addition to a possible contribution from a space charge distribution $\rho(\mathbf{r})$, ϕ and $\mathbf{E}$ are in part due to charges residing on the surface ∂U of the conductor, and in part due to the polarisation of the dielectric. For a linear, homogeneous dielectric, the effect of the latter can be described in terms of a polarization charge density σ_p on the boundary ∂V of the dielectric. In the absence of space charge, the potential and field are thus given by the boundary integrals (cf. Chapter 3 in Ref. [42])

$$\phi(\mathbf{r}) = \int_{\partial U} dl' \sigma(\mathbf{r}') G(\mathbf{r}, \mathbf{r}') + \int_{\partial V} dl' \sigma_p(\mathbf{r}') G(\mathbf{r}, \mathbf{r}'),$$

$$\mathbf{E}(\mathbf{r}) = -\int_{\partial U} dl' \sigma(\mathbf{r}') \nabla G(\mathbf{r}, \mathbf{r}') - \int_{\partial V} dl' \sigma_p(\mathbf{r}') \nabla G(\mathbf{r}, \mathbf{r}'),$$

$$\tag{2.18}$$

where $G(\mathbf{r}, \mathbf{r}')$ is the two-dimensional free-space Green's function

$$G(\mathbf{r}, \mathbf{r}') = -\frac{1}{2\pi\varepsilon_0} \ln|\mathbf{r} - \mathbf{r}'|.$$

The problem consists now in determining the charge density distributions $\sigma\left(\mathbf{r}\right)$ and $\sigma_p\left(\mathbf{r}\right)$ corresponding to the applied boundary conditions. As a first step towards the numerical solution, the boundary curves are approximated by straight line segments with constant charge densities,

$$\int \mathrm{d}l'\sigma\left(\mathbf{r}'\right)G\left(\mathbf{r},\mathbf{r}'\right) \to \sum_i \sigma_i \int_{C_i} \mathrm{d}l' G\left(\mathbf{r},\mathbf{r}'\right).$$

The integration of the Green's function $G\left(\mathbf{r},\mathbf{r}'\right)$ and its derivative, respectively, over a line element C_i can easily be carried out. For a uniformly charged line element of length $2a$ along the x axis (centered at $x = 0$), the potential is given by

$$
\begin{aligned}
\phi\left(x,y\right) &= -\frac{1}{2\pi\varepsilon_0}\int_{-a}^{a}\mathrm{d}x'\ln\sqrt{\left(x-x'\right)^2+y^2}\\
&= \frac{1}{2\pi\varepsilon_0}\left[2a-y\left(\arctan\left(\frac{a-x}{y}\right)+\arctan\left(\frac{a+x}{y}\right)\right)\right.\\
&\quad \left.- \left(a-x\right)\ln\sqrt{\left(a-x\right)^2+y^2}-\left(a+x\right)\ln\sqrt{\left(a+x\right)^2+y^2}\right],
\end{aligned}
$$

and the components of the electric field are given by

$$
\begin{aligned}
E_x\left(x,y\right) &= \frac{1}{2\pi\varepsilon_0}\ln\sqrt{\frac{\left(a+x\right)^2+y^2}{\left(a-x\right)^2+y^2}},\\
E_y\left(x,y\right) &= \frac{1}{2\pi\varepsilon_0}\left[\arctan\left(\frac{a-x}{y}\right)+\arctan\left(\frac{a+x}{y}\right)\right].
\end{aligned}
$$

These expressions are simple compared to the three-dimensional case where the Green's function is integrated over rectangular or triangular boundary elements.

As a next step, we establish the equations linking the surface charge densities to the boundary conditions of the problem.

Conductor-dielectric interface (Dirichlet boundary conditions) According to (2.18), the potential ϕ_i applied to a conducting boundary element i can be expressed in terms of the (unknown) charge densities on the boundary elements:

$$\phi_i = \sum_j \sigma_j \underbrace{\int_{C_j}\mathrm{d}l' G\left(\mathbf{r}_i,\mathbf{r}'\right)}_{A_{ij}}. \tag{2.19}$$

Dielectric-dielectric interface (Neumann boundary conditions) In the absence of free surface charges, the normal component of the displacement field $\mathbf{D} = \varepsilon\mathbf{E}$ at the boundary of a dielectric is continuous,

$$\mathbf{n}_i\cdot\left(\varepsilon_i^+\mathbf{E}_i^+ - \varepsilon_i^-\mathbf{E}_i^-\right) = 0,$$

where $\mathbf{E}^\pm$ and $\varepsilon^\pm$ denote the electric field and the relative dielectric constant on the inside $(-)$ and outside $(+)$ of the dielectric. The electric fields $\mathbf{E}^\pm$ are given by

$$\mathbf{E}_i^\pm = -\sum_{j\neq i}\sigma_j\int_{C_j}\mathrm{d}l'\nabla G\left(\mathbf{r}_i,\mathbf{r}'\right)\pm\mathbf{n}_i\frac{\sigma_i}{2\varepsilon_0}.$$

One thus obtains the equation

$$0 = \underbrace{\frac{\varepsilon_i^+ + \varepsilon_i^-}{2\varepsilon_0\left(\varepsilon_i^+ - \varepsilon_i^-\right)}}_{B_{ii}}\sigma_i + \sum_{j\neq i}\sigma_j\,\mathbf{n}_i\cdot\underbrace{\int_{C_j}\mathrm{d}l'\left(-\nabla G\left(\mathbf{r}_i,\mathbf{r}'\right)\right)}_{B_{ij}}. \tag{2.20}$$
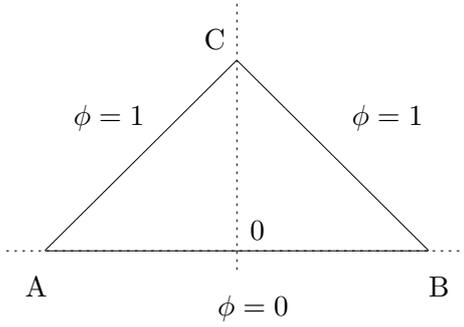
Figure 2.5 Test configuration for neBEM validation: right-angled triangle $\overline{\mathrm{ABC}}$, with boundary conditions $\phi = 1$ V on the legs and $\phi = 0$ V on the hypotenuse.

Based on (2.19) and (2.20) one can set up a system of equations determining the charge densities σ_i. Written in matrix form, we have

$$K\boldsymbol{\sigma} = \mathbf{b}.$$

For a system broken down into n conducting line elements and m line elements along a dielectric-dielectric interface, the so-called influence matrix K is given by

$$K = \begin{pmatrix} A_{1,1} & \dots & A_{1,n+m} \\ \vdots & \ddots & \vdots \\ A_{n,1} & \dots & A_{n,n+m} \\ B_{n+1,1} & \dots & B_{n+1,n+m} \\ \vdots & \ddots & \vdots \\ B_{n+m,1} & \dots & B_{n+m,n+m} \end{pmatrix}.$$

The right-hand-side vector $\mathbf{b}$ reflecting the boundary conditions is given by

$$\mathbf{b} = (\phi_1, \dots, \phi_n, 0, \dots, 0)^T.$$

In the presence of a space charge distribution $\rho(\mathbf{r})$, we have to add the terms

$$\phi^{(0)}(\mathbf{r}) = \int \mathrm{d}^2 r' \rho(\mathbf{r}') G(\mathbf{r}, \mathbf{r}'), \qquad \mathbf{E}^{(0)}(\mathbf{r}) = -\int \mathrm{d}^2 r' \rho(\mathbf{r}') \nabla G(\mathbf{r}, \mathbf{r}')$$

to the right hand sides of (2.18). Consequently, the vector $\mathbf{b}$ becomes

$$\mathbf{b} = \left(\phi_1 - \phi_1^{(0)}, \dots, \phi_n - \phi_n^{(0)}, -\mathbf{n}_{n+1} \cdot \mathbf{E}_{n+1}^{(0)}, \dots, -\mathbf{n}_{n+m} \cdot \mathbf{E}_{n+m}^{(0)} \right)^T.$$

After inverting the influence matrix, one can obtain the charge densities from

$$\sigma_i = K_{ij}^{-1} b_j.$$

From the computational point of view, the matrix inversion is the most time consuming part in this algorithm. Once the influence matrix has been inverted, though, solutions for different sets of boundary conditions (i. e. different potentials or space charge distributions) can be calculated relatively fast provided that the geometry remains unaltered.

y [cm]	ϕ [V] (exact)	ϕ [V] (neBEM)	$|\Delta\phi|$ $[10^{-9}$ V]
0.1	0.165973895	0.165973895	—
0.2	0.326353080	0.326353080	—
0.3	0.476078222	0.476078222	—
0.4	0.611014157	0.611014158	1
0.5	0.728113328	0.728113330	2
0.6	0.825364529	0.825364532	3
0.7	0.901598676	0.901598682	6
0.8	0.956238103	0.956238116	13
0.9	0.989057910	0.989057963	53

Table 2.1. Potential along the y-axis in the interior of the right-angled triangle $\overline{\text{ABC}}$ shown in Fig. 2.5. The values in the third column are neBEM calculations with each side of the triangle split into 1000 line elements. For comparison, the exact numerical values (Chapter 5, Section 1.1.6 in Ref. [41]) obtained from a series expansion are given in the second column. The difference between the two results is shown in the fourth column.

The solution depends to some extent on the choice of the so-called collocation points, i. e. the points at which the potential and field are evaluated when calculating the matrix elements. For the examples discussed below, one collocation point located in the centre of the line element was used.

In order to test the numerical accuracy of the two-dimensional neBEM technique and the correctness of the implementation, we consider the configuration shown in Fig. 2.5. This example (including the reference values given in Table 2.1) was taken from Chapter 5 of Ref. [41]. On the legs of the right-angled triangle, the potential is set to $\phi = 1$ V, on the hypotenuse it is set to $\phi = 0$ V. The side lengths are $\overline{0\text{A}} = \overline{0\text{B}} = \overline{0\text{C}} = 1$ cm. A comparison between the results from a neBEM calculation with 1000 elements per side and the exact numerical values is given in Table 2.1. At all test points, the neBEM results agree with the exact solution to at least 7 decimal places. The agreement deteriorates towards the corner, which is a general deficiency of the neBEM approach.

As a test example involving both conducting and dielectric interfaces, we consider two parallel conducting plates at voltages V_1 and V_2 separated by a distance $3w$ and a dielectric slab of width w midway between the plates (Fig. 2.6a). In order to avoid edge effects, the length of the plates and the slab should be large compared to w. For an infinitely long capacitor, the x-components of the electric fields are given by [42]

$$E_x^{(1)} = E_x^{(3)} = \frac{\Delta V}{w\left(2 + \frac{1}{\varepsilon}\right)}, \qquad E_x^{(2)} = \frac{E_x^{(1)}}{\varepsilon}. \tag{2.21}$$

For the calculation, the length was set to 20 cm and the width of the slab to $w = 1$ cm. In the vicinity of the y-axis (more precisely, for $|y| < w$), the boundaries were discretized by elements with a size of 2 mm. For $|y| > w$, an element size of 1 cm was chosen. As can be seen from Fig. 2.6b, the electric field calculated using neBEM is consistent with the behaviour expected from (2.21).
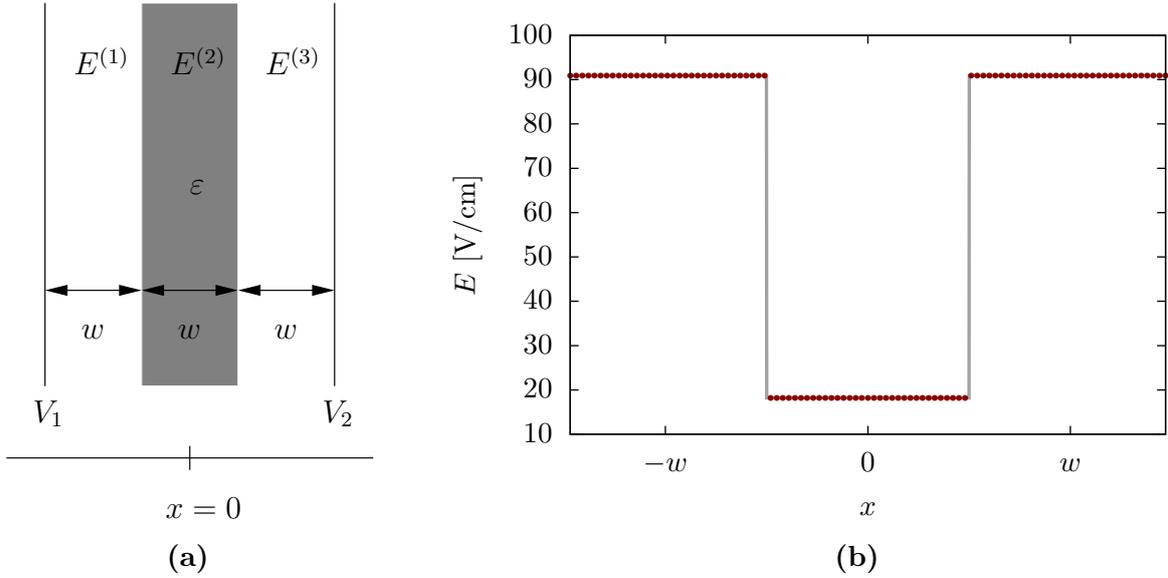
Figure 2.6. Left: dielectric slab with relative dielectric constant ε and width w inside a parallel-plate capacitor. Right: electric field calculated by means of neBEM (dots); the solid curve corresponds to the asymptotic solution (2.21). For the calculation, the values $\Delta V = V_1 - V_2 = 200$ V, $w = 1$ cm, $\varepsilon = 5$ were used.

2.3. Charge Transport

On a phenomenological level, the drift of electrons and ions in gases – and electrons and holes in semiconductors – under the influence of an electric field $\mathbf{E}$ and a magnetic field $\mathbf{B}$ can be described in terms of macroscopic transport parameters.

- Given the drift velocity $\mathbf{v}_{\mathrm{d}}\left(\mathbf{E}, \mathbf{B}\right)$, the average path of charge carriers can be calculated using

$$\dot{\mathbf{r}} = \mathbf{v}_{\mathrm{d}}\big(\mathbf{E}\left(\mathbf{r}\right), \mathbf{B}\left(\mathbf{r}\right)\big). \tag{2.22}$$

- Due to the random nature of the scattering processes, the trajectories of individual charges deviate from the average. In a constant field the lateral spread over a mean drift distance d follows a Gaussian distribution with standard deviation $\sigma = D_{\mathrm{T}}\sqrt{d}$, where D_{T} is the transverse diffusion coefficient. The longitudinal diffusion coefficient D_{L} describes the spread in the direction of $\mathbf{v}_{\mathrm{d}}$.

- In strong electric fields, electrons in gases (and electrons and holes in semiconductors) can attain sufficient energy to ionize and start an avalanche. In electronegative gases, on the other hand, electrons can be absorbed by gas molecules. Similarly, electrons and holes in semiconductors can be captured ("trapped") by defects. Phenomenologically, multiplication and attachment of electrons can be described by the Townsend coefficient $\alpha\left(\mathbf{E}\right)$ and the attachment coefficient $\eta\left(\mathbf{E}\right)$, respectively. In terms of these coefficients, the average change $\mathrm{d}n$ of the number of drift electrons over a distance $\mathrm{d}x$ ($\mathrm{d}x \ll \alpha^{-1}$, $\mathrm{d}x \ll \eta^{-1}$) can be expressed as

$$\mathrm{d}n = (\alpha - \eta)\,\mathrm{d}x.$$

In the rest of this section, we shall focus on the transport properties of electrons in gases[5]. From a microscopic viewpoint, the above parameters are determined by the cross-sections for scattering of electrons by atoms or molecules. Typical collision mechanisms are

1. elastic scattering,

2. excitation of molecular vibrations and rotations,

3. atomic excitations,

4. attachment, and

5. ionization.

As can be seen from Fig. 2.7, in atomic gases like argon only elastic, exciting (i. e. process 3 in the above list), and ionizing collisions play a role, while molecular gases like carbon dioxide generally exhibit a larger variety of inelastic scattering processes. Mixtures of Ar and CO_2 are used in many of the calculations presented below.

2.3.1. Magboltz

Magboltz[6] [13, 14], written by S. Biagi, is a widely used program for computing electron transport coefficients in detector gas mixtures by means of semi-classical Monte Carlo simulation. The results are time average values obtained by following an electron over a large number of collisions (typically $10^7 - 10^9$) with the gas atoms/molecules.

Transport Algorithm

The Monte Carlo algorithm which is used in Magboltz (and which serves as a basis for the calculations using microscopic electron tracking discussed below) proceeds as follows.

- For each available scattering process i in the selected gas mixture, the collision rate $\tau_i^{-1}(\epsilon)$ as a function of the electron energy is calculated:

$$\tau_i^{-1}(\epsilon) = N\sigma_i(\epsilon) v(\epsilon),$$

where N is the partial density of the respective atom/molecule, σ_i is the cross-section for the scattering process under consideration, and $v = \sqrt{2\epsilon/m_e}$ is the electron velocity.

- Between collisions an electron (described by its coordinates $\mathbf{r}$, energy ϵ, and velocity[7] vector $\mathbf{v}$) is traced on a classical vacuum trajectory according to the electric and magnetic field specified by the user. Arbitrary relative orientations of $\mathbf{E}$ and $\mathbf{B}$ are allowed.

- The duration Δt of a free flight step is controlled by the total collision rate

$$\tau^{-1}(\epsilon) = \sum_i \tau_i^{-1}(\epsilon).$$

Let us first consider the sampling of Δt in a "field-free" situation. If the electron energy ϵ and thus the collision rate were constant, the time step Δt would follow an exponential distribution and, given a uniform random variate $u \in (0, 1]$, could be sampled according to

$$\Delta t = -\tau \ln u. \tag{2.23}$$

---

[5] Scattering mechanisms of electrons in semiconductors are discussed in Chapter 6.

[6] The name refers to an earlier version of the program [43] which was based on the Boltzmann equation.

[7] The microscopic velocity $\mathbf{v}$ is to be distinguished from the effective, macroscopic drift velocity $\mathbf{v}_d$.

(a)

(b)
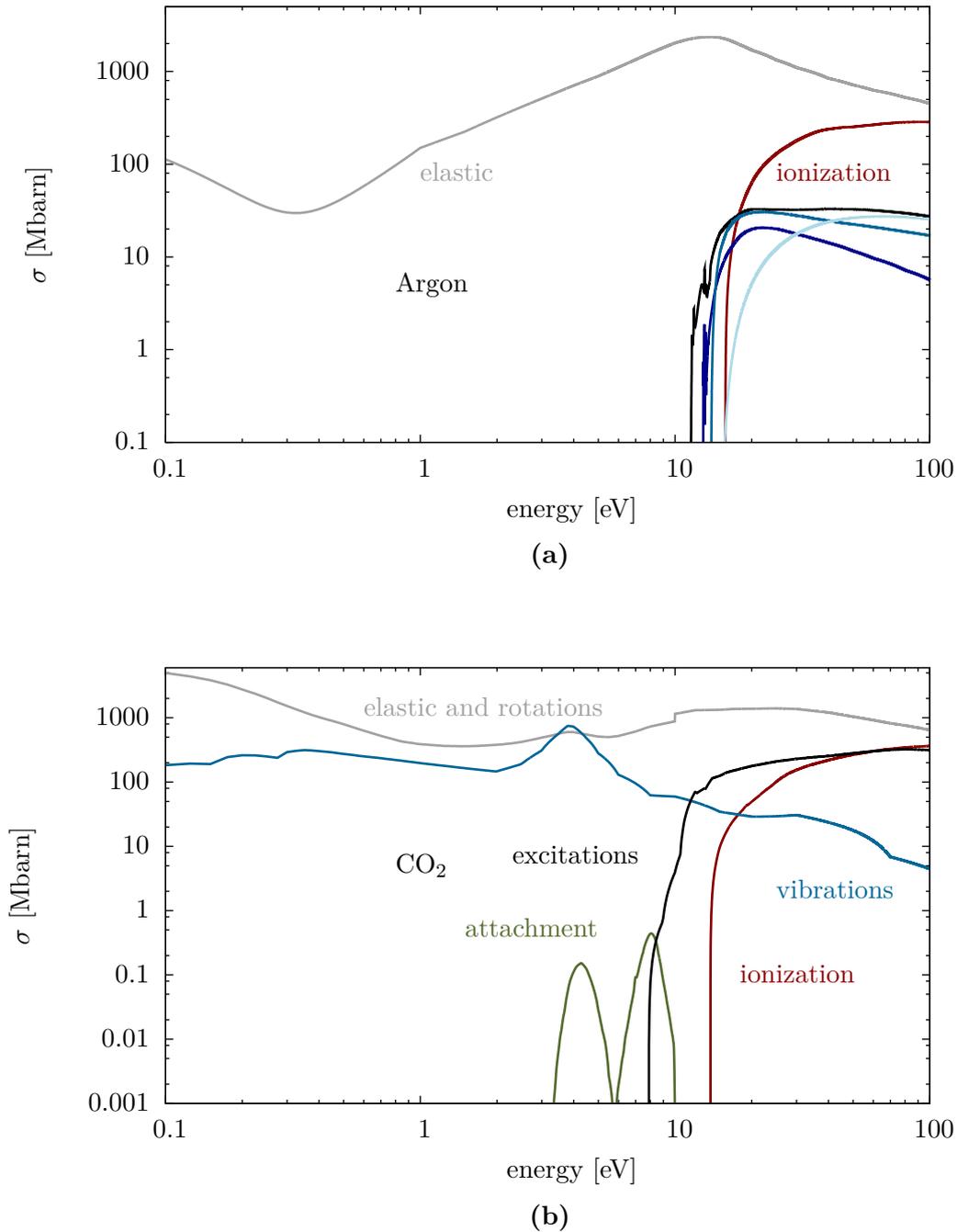
Figure 2.7. Cross-sections for scattering of electrons by Ar (top) and CO_2 (bottom) as implemented in Magboltz 8.9 [14]. For the sake of clarity, the above plots involve a few simplifications with respect to the actual cross-sections in the Magboltz database: (1) the 44 excitation cross-section levels for Ar are combined to four groups; (2) the rotation terms for CO_2 (inelastic energy loss < 12 meV) are added to the elastic cross-section; (3) only the respective sums of the vibration, excitation and attachment cross-sections in CO_2 are plotted. The cross-section data included in Magboltz extend beyond the energy range shown here: elastic, excitation and ionization cross-sections in argon up to an electron energy of 10 MeV are shown in Fig. 4.1.

Because of the electric field, the electron energy and the collision rate do however vary during the free flight step. This can be taken into account using the so-called null-collision technique [44]. An artificial "null-collision" scattering rate $\tau_{\mathrm{null}}^{-1}$ is introduced which balances the energy dependence of the "real" scattering rate τ^{-1} such that their sum $\bar{\tau}^{-1}$ is constant,

$$\bar{\tau}^{-1} = \tau^{-1}\left(\epsilon\right) + \tau_{\mathrm{null}}^{-1}\left(\epsilon\right) = \mathrm{const.}$$

The sampling of Δt then proceeds as follows.

1. A trial time step is sampled using (2.23), but with $\bar{\tau}$ in lieu of τ.

2. The energy ϵ' after the trial step is calculated. In the absence of a magnetic field $\mathbf{B}$, ϵ' is given by

$$\epsilon' = \epsilon + q\mathbf{v} \cdot \mathbf{E}\Delta t + \frac{q^2}{2m_e}\mathbf{E}^2\Delta t^2. \tag{2.24}$$

3. Another random number $u \in [0, 1]$ is drawn. If $u < \tau^{-1}\left(\epsilon\right)/\bar{\tau}$, i. e. in case of a "real" collision (as opposed to a "null-collision"), the trial time step Δt is accepted. Otherwise, a new random trial step $\Delta t'$, offset by Δt, is sampled:

$$\Delta t' = \Delta t - \bar{\tau}\ln u.$$

The steps 2 and 3 are repeated until a "real" collision occurs.

- The velocity $\mathbf{v}'$ and position $\mathbf{r}'$ after the free flight are calculated. For $\mathbf{B} = 0$:

$$\mathbf{v}' = \mathbf{v} + \frac{q}{m_e}\mathbf{E}\Delta t, \tag{2.25}$$

$$\mathbf{r}' = \mathbf{r} + \mathbf{v}\Delta t + \frac{q}{2m_e}\mathbf{E}\Delta t^2. \tag{2.26}$$

- Based on the relative collision rates at the new energy ϵ', the scattering process to take place is selected and the energy and direction of the electron are updated according to the type of collision. The scattering angle is calculated based on the algorithm described in Ref. [45].

- After the collision, stepping is continued with the new energy and direction.

Cross-Section Database

Magboltz includes at present (version 8.9.7) cross-sections for 54 counting gases. Where available, the cross-sections used in the program are taken from measurements and adjusted within the experimental error to obtain agreement with measured transport coefficients [46].

The estimated reliability of the implemented cross-sections for each gas is specified in terms of "stars". A rating of "2*" corresponds to a coarse description of the cross-sections, while a rating of "5*" corresponds to a detailed, carefully validated description of the cross-sections.

In the last few years[8], a number of major cross-section updates were made.

---

[8] More precisely, the above list describes changes with respect to version 7.1 of Magboltz (the version currently interfaced to Fortran Garfield)

- A detailed description of the excitation cross-sections for the noble gases was implemented. The database now includes 44 excitation levels for Ar which were previously modelled by three lumped cross-section terms. The excitation cross-section descriptions of He, Ne, Kr, and Xe were also upgraded to the same level of detail. This opens up the possibility to simulate light emission [47] and allows a refined modelling of deexcitation processes (Chapter 5).

- An improved algorithm for angular scattering was introduced (in particular with regard to δ-electron transport calculations).

- For a number of gases, the cross-section description was extended up to MeV energies (see Section 4.2).

2.3.2. Microscopic Tracking

In Garfield, the first-order equation of motion (2.22) is traditionally solved by means of Runge-Kutta integration. This approach is well suited for tracking electrons over large distances (like in a TPC) or for calculations in detectors where transverse diffusion does not have significant impact on the induced signal (e. g. drift tubes). A downside is that stochastic variations of drift paths are not taken into account (for $\mathbf{B} = 0$, electrons follow strictly the electric field lines). In order to randomize electron drift lines which start from the same initial coordinates on an event-by-event basis, (2.22) can be integrated in a stochastic manner [15]:

- a step of length $\Delta s = v_{\mathrm{d}} \Delta t$ in the direction of the drift velocity $\mathbf{v}_{\mathrm{d}}$ at the local field is calculated (based on a time step[9] Δt specified by the user);

- a random diffusion step is sampled from three uncorrelated Gaussian distributions with standard deviation $\sigma_L = D_L \sqrt{\Delta s}$ for the component parallel to the drift velocity and standard deviation $\sigma_T = D_T \sqrt{\Delta s}$ for the two transverse components;

- the two steps are added vectorially and the location is updated.

For accurate simulations of electron trajectories in small-scale structures (with characteristic dimensions comparable to the electron mean free path), and also for detailed calculations of ionization and excitation processes (see Chapters 3 and 4), transporting electrons on a microscopic level – i. e. based on the second-order equation of motion – is the method of choice. Such a simulation technique was implemented in Garfield/Garfield++ based on the algorithm used in Magboltz, with the stepping procedure being adapted such that it allows arbitrarily oriented fields to be handled.

The expressions (2.24), (2.25), and (2.26) are exact solutions for constant fields and good approximations if the electric field does not change significantly over distances of the order of the electron mean free path. The adequacy of this approach can be verified by comparing the results with those from a more refined method in which the electric field is updated after each null-collision step (instead of being updated only after "real" collisions). For the field configurations discussed below, no significant difference was found.

In the presence of a magnetic field $\mathbf{B}$, the equations of motion become more complicated. To simplify the solution, Magboltz uses a coordinate system where $\mathbf{B}$ is aligned with the x axis and $\mathbf{E}$ lies in the $x - z$ plane. For the microscopic tracking stepping algorithm, the same convention was adopted. Since the magnitude and orientation of $\mathbf{E}$ and $\mathbf{B}$ may vary from collision to collision

---

[9] Alternatively, the calculation can be done using fixed distance steps.

however, a rotation of the electron velocity vector $\mathbf{v}$ into this coordinate system and back to the global frame is required. The simulation is thus more time-consuming with respect to the situation without magnetic field.

In Magboltz, the energy ϵ' of the secondary electron produced in an ionizing collision is sampled according to a differential cross-section of the form

$$\frac{\mathrm{d}\sigma}{\mathrm{d}\epsilon'} \propto \frac{1}{\epsilon'^2 + w^2}. \tag{2.27}$$

In this parameterization of the secondary electron energy distribution, which was proposed by Opal, Beaty, and Peterson [48], w is a gas specific parameter ("splitting" parameter) which is of the order of the ionization potential. The normalization of (2.27) is chosen such that the integral over ϵ' from zero to the max. possible secondary energy $(\epsilon_p - \epsilon_{\mathrm{ion}})/2$ equals the total cross-section at the primary electron energy ϵ_p:

$$\int_0^{(\epsilon_p - \epsilon_{\mathrm{ion}})/2} \frac{\mathrm{d}\sigma}{\mathrm{d}\epsilon'} \mathrm{d}\epsilon' = \sigma\left(\epsilon_p\right).$$

By default, the "splitting" function (2.27) is also used in the microscopic tracking technique implemented in Garfield++. Alternatively, the secondary electron energy can be sampled according to the parameterization proposed by Green and Sawada [49],

$$\frac{\mathrm{d}\sigma}{\mathrm{d}\epsilon'} \propto \frac{1}{\left(\epsilon' - \epsilon_0\right)^2 + \Gamma^2}, \tag{2.28}$$

where ϵ_0 and Γ are functions of the primary electron energy.

In Magboltz, the collision rates τ_i (and other energy-dependent parameters) are stored on an equidistant energy grid. At energies below 1 keV, Garfield++ also uses a linear binning of the collision rate table. At higher electron energies, the collision rates are stored on a logarithmically spaced energy grid.

2.3.3. Penning Transfer

As can be seen from the cross-section plots in Fig. 2.7, excitations represent a significant scattering process at high electron energies. The deexcitation of an excited atom $A^\star$ can proceed via different channels.

- In pure noble gases at atmospheric pressure, the dominant process is excimer formation,

$$A^\star + 2A \rightarrow A_2^\star + A.$$
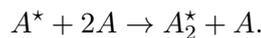
  The excimer $A_2^\star$ eventually decays to the dimer ground state A_2 under emission of a VUV photon. A recent simulation study of electroluminescence in pure noble gases using the microscopic tracking technique of Garfield++ can be found in Ref. [47].

- Detector gas mixtures often consist of a noble gas (in the following denoted by A) and a molecular component (B), the so-called quenching gas. If the excitation energy of an excited noble gas atom $A^\star$ exceeds the ionization threshold of the quencher, ionization of a molecule B due to energy transfer from the excited noble gas atom can occur. This process can be responsible for a sizeable fraction of the observed gain.
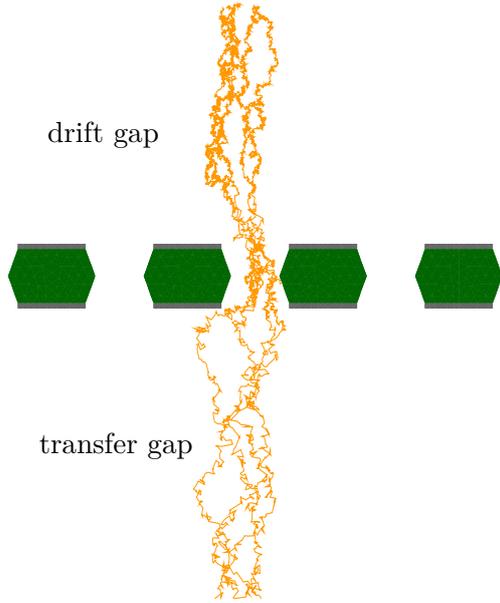
Figure 2.8 Electron trajectories in a GEM, calculated using microscopic tracking. The plot shows the positions of every 10th electron collision, connected by straight lines. The electric field configuration is characterized by the field E_D in the drift gap, the field E_T in the transfer gap, and the voltage difference U_{GEM} between the top and bottom metal layers (drawn in grey) on the kapton foil (drawn in green).

– If the excited level $A^\star$ has a dipole-allowed decay to the ground state (resonance transition), the excitation transfer can proceed via photon emission and subsequent absorption,

$$A^\star \to A + \gamma, \qquad B + \gamma \to B^+ + e^-. \tag{2.29}$$
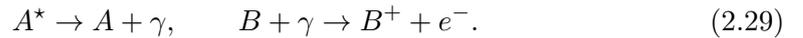
– Collision-induced excitation transfer,

$$A^\star + B \to A + B^+ + e^- \tag{2.30}$$
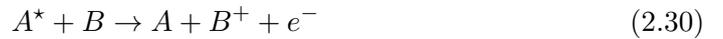
is possible for both resonant and non-resonant levels.

• The ionizing transfer processes (2.29) and (2.30) compete with neutral photoabsorption and collisional loss of excitation energy.

• Highly excited atoms $A^{\star\star}$ can also produce an electron by means of homonuclear associative ionization,

$$A^{\star\star} + A \to A_2^+ + e^-. \tag{2.31}$$

In the following, we subsume all excitation transfer channels leading to ionization under the term Penning transfer. Phenomenologically, Penning effects can be described in terms of transfer efficiencies. The transfer efficiency r_i of an excited state i (with excitation energy greater than the ionization potential of the admixture) expresses the probability that an ionization electron is produced eventually in the deexcitation process.

Transfer efficiencies for a number of Ar based gas mixtures have recently been determined by Şahin et al. [50] from gain curve fits, that is by comparing gain measurements against theoretical predictions according to the Townsend coefficient calculated by Magboltz.

In Chapters 3 and 4, these values are used for estimating the effects of Penning transfer on avalanche size fluctuations and ionization statistics.

2.3.4. Example: Electron Transparency

Typical applications of the microscopic tracking technique include calculations which require accurate modelling of diffusion effects in inhomogeneous fields.

K. Nikolopoulos et al. [51] showed recently that the Magboltz-based microscopic tracking technique – in combination with a realistic description of the electric field – allows an accurate calculation of the electron transparency in a Micromegas. A similar example is discussed here, namely the electron transmission properties of a GEM.

Figure 2.9a shows the measured [52] and calculated transparency of a standard[10] GEM operated in Ar/CO_2 (70:30) at a drift field[11] $E_D = 150$ V/cm as a function of the voltage difference U_{GEM} applied to the GEM electrodes, for two values of the transfer field, $E_T = 300$ V/cm and $E_T = 3000$ V/cm.

The simulation method is illustrated in Fig. 2.8. The electric field used in the calculation was computed using Ansys. Starting from 200 μm above the GEM, at randomized lateral positions, electrons are traced through the field map. The transparency is calculated by recording the number of electrons which pass through the GEM hole and arrive in the transfer gap. If multiplication occurs, the number of electrons in the transfer gap can exceed the number of primaries, giving rise to a transmission probability greater than 100%. Penning transfer was taken into account with a transfer efficiency $r = 0.57$ [50].

As can be seen from Fig. 2.9a, there is overall agreement between simulation and measurements with the exception of the data points at a transfer field of 3 kV/cm for $U_{GEM} < 60$ V. The deviation at high GEM voltages ($U_{GEM} \geq 160$ V for $E_T = 3$ kV/cm, $U_{GEM} \geq 260$ V for $E_T = 300$ V/cm) could be an indication that the Penning transfer efficiency was underestimated in the simulation. For the transmission efficiency at low GEM voltages ($U_{GEM} \leq 160$ V for $E_T = 300$ V/cm, $U_{GEM} \leq 100$ V for $E_T = 3$ kV/cm) Penning effects are negligible, though: the values obtained with and without Penning transfer agree within the statistical uncertainty. Another possible source of systematic bias is that charging up of the dielectric was not taken into account in the simulation.

The measurements reported in Ref. [52] were performed with a view to assessing the performance of GEMs as readout detectors of a TPC. In particular, the possibility of using the first GEM foil[12] for pulsed ion gating was discussed. For this application it is vital to consider the effect of a strong magnetic field (in which TPCs in collider experiments are immersed) on the transmission properties. While magnets providing a homogeneous field of a few Tesla are usually not readily available in a laboratory or beam test setup, $\mathbf{B}$ fields can easily be included in the simulation. The calculated transparency in the presence of a magnetic field of 4 T (as proposed for the linear collider TPC [6]) perpendicular to the GEM foil is shown in Fig. 2.9b. It can be seen that the overall transmission efficiency increases, but the transparency at low values of U_{GEM} is reduced. The latter effect can be made plausible by means of the Langevin formula for the drift velocity (see e. g. Chapter 2 in Ref. [2]),

$$\mathbf{v}_d = \mu \left| \mathbf{E} \right| \frac{1}{1 + \mu^2 B^2} \left(\hat{\mathbf{E}} + \mu B \left(\hat{\mathbf{E}} \times \hat{\mathbf{B}} \right) + \mu^2 B^2 \left(\hat{\mathbf{E}} \cdot \hat{\mathbf{B}} \right) \hat{\mathbf{B}} \right), \qquad (2.32)$$

---

[10] Outer hole diameter: 70 μm, pitch: 140 μm.

[11] The drift field E_D is the voltage difference between the cathode and the top metal layer of the GEM foil, divided by the length of the drift gap. Analogously, the transfer field E_T is the voltage difference between the bottom layer of the GEM and the top metal layer of the second GEM, divided by the length of the transfer gap.

[12] A typical configuration consists of three layers of GEM foils separated by a few mm (triple GEM).

(a) $B = 0$

(b) $B = 4$ T

Figure 2.9. Electron transparency of a standard GEM operated with Ar/CO_2 (70:30) at a drift field of $E_D = 150$ V/cm. Triangles are measurements [52], circles are calculations (at $U_{GEM} = 20$ V and $U_{GEM} = 40$ V the markers representing the measured values for $E_T = 300$ V/cm are hidden by the markers representing the calculations). The errorbars on the calculated values indicate the statistical error ($3\,\sigma$). For the experimental data in Fig. 2.9a an uncertainty of $\pm 5\%$ [53] is assumed.

where μ is the electron mobility[13], and $\hat{\mathbf{E}}, \hat{\mathbf{B}}$ are the unit vectors of the electric and magnetic field. With increasing magnetic field, the component of the drift velocity in the direction of $\mathbf{B}$ also increases (in the limit $B \rightarrow \infty$, $\mathbf{v}_d$ is aligned with $\mathbf{B}$). Electrons starting from an initial position which is off-centred with respect to the hole axis are thus more likely to end up on the top electrode of the GEM.

On the other hand, the same effect should help improve the extraction efficiency from the hole to the transfer region. In addition, the higher transparency in the presence of a $\mathbf{B}$ field can in part be attributed to the reduced transverse diffusion (see Fig. 2.10).

2.4. Induced Signals

Consider a point charge q moving along a trajectory $\mathbf{R}\,(t)$ in a volume bounded by n electrodes which are kept at fixed potentials ϕ_j $(j = 1, \ldots, n)$. The electrostatic potential $\phi\,(\mathbf{r})$ inside the volume is determined by the surface charge densities σ_j on the conductors and the space charge density

$$\rho\,(\mathbf{r}) = \rho_0\,(\mathbf{r}) + q\delta(\mathbf{r} - \mathbf{R}\,(t))$$

which, apart from a possible static charge density ρ_0, includes a time-dependent term due to the mobile charge q. As a consequence, the surface charge densities σ_j will also change with time.

In order to calculate the currents induced on the electrodes, we introduce a second (fictitious) set of charge distributions $\overline{\rho}$, $\overline{\sigma_k}$ giving rise to a potential $\overline{\phi}\,(\mathbf{r})$. Green's reciprocity theorem states

---

[13] The electron mobility is assumed to have a negative sign here.

Figure 2.10 Transverse diffusion in Ar/CO$_2$ (70:30) as a function of the electric field for $B = 0$ and $B = 4$ T ($\mathbf{E}\|\mathbf{B}$), calculated using Magboltz.

that [54]

$$\int \mathrm{d}^3 r\, \rho\,(\mathbf{r})\,\overline{\phi}\,(\mathbf{r}) + \sum_{j=1}^{n} \int \mathrm{d}^2 f_j\, \sigma_j\,(\mathbf{r})\,\overline{\phi}\,(\mathbf{r}) = \int \mathrm{d}^3 r\, \overline{\rho}\,(\mathbf{r})\, \phi\,(\mathbf{r}) + \sum_{j=1}^{n} \int \mathrm{d}^2 f_j\, \overline{\sigma}_j\,(\mathbf{r})\, \phi\,(\mathbf{r}). \quad (2.33)$$

By setting

$$\overline{\rho} = 0, \qquad \overline{\phi}_j = \begin{cases} 1, & j = k \\ 0, & \text{else} \end{cases}$$

we obtain for the time-dependent induced charge on electrode k

$$Q_k\,(t) = \int \mathrm{d}^2 f\, \sigma_k\,(t) = -q\overline{\phi}\,(\mathbf{R}\,(t))\,.$$

The induced current is given by

$$i_k\,(t) = -\frac{\mathrm{d}Q_k}{\mathrm{d}t} = -q\overline{\mathbf{E}}\,(\mathbf{R}\,(t)) \cdot \dot{\mathbf{R}}\,(t)\,. \quad (2.34)$$

This equation is known as the Shockley-Ramo theorem [55, 56] and $\overline{\phi}$, $\overline{\mathbf{E}}$ are usually called the weighting potential and weighting field, respectively. By time integration of (2.34) one obtains for the total charge ΔQ induced by a particle moving from an initial position $\mathbf{R}_0$ to a position $\mathbf{R}_1$

$$\Delta Q = q\left(\overline{\phi}\,(\mathbf{R}_1) - \overline{\phi}\,(\mathbf{R}_0)\right)\,.$$

2.5. Summary

The main components of a gas detector simulation program are

- simulation of the ionization pattern produced by a charged particle crossing the detector,

- computation of the electrostatic field inside the device,

- transport of electrons (including multiplication) and ions in electric and magnetic fields, and

- calculation of induced currents.

Elements discussed in this chapter which exceed common "textbook knowledge" or include own contributions from this thesis work are recapitulated below.

- The PAI model [23] is a popular semi-empirical scheme for calculating the differential cross-section $d\sigma/dE$ for the energy loss of fast charged particles in matter. It is based on dielectric theory, which – as demonstrated explicitly in Section 2.1.3 for the non-relativistic case – is equivalent to the first Born approximation.

- Boundary element methods are an attractive option for electric field calculations in gas detectors, particularly for devices with small feature sizes or dielectric elements as in case of micropattern gas detectors. A two-dimensional version of the so-called neBEM technique [39] was implemented and validated within the framework of this thesis.

- The microscopic tracking technique (derived from the Magboltz program) allows a "first-principle" simulation of electron transport in arbitrary field configurations based on the cross-sections for electron scattering by gas atoms/molecules. As an application of the method in the low-field domain (below the ionization threshold), the calculation of the electron transparency of a GEM foil in the presence of a magnetic field was discussed.

3. Avalanche Statistics

Due to the stochastic nature of the charge amplification process, the size of an electron avalanche in a gas-based detector is subject to fluctuations. In this chapter, the calculation of these fluctuations by means of the microscopic tracking technique is discussed.

3.1. Overview

3.1.1. Terminology

Gain fluctuations can quantitatively be described in terms of probabilities $P_n(\mathbf{r}_0, \mathbf{p}_0)$ that an electron with initial momentum $\mathbf{p}_0$ released at a position $\mathbf{r}_0$ initiates an avalanche comprising n electrons in the detector. Given P_n, one can calculate the avalanche size distribution for k primary electrons by $(k-1)$ fold convolution, provided that the k avalanches proceed independently of each other, and that P_n does not depend on the initial momentum. The latter criterion can be relaxed however, by redefining P_n as an average over a distribution of initial energies and directions.

Determining factors for the single electron avalanche size distribution P_n are

- properties of the gas mixture, in particular the electron-molecule scattering cross-sections as functions of the electron energy,

- macroscopic parameters such as the electric field $\mathbf{E}(\mathbf{r})$, the temperature T, and the gas pressure p, and

- the initial momentum and position of the electron.

In order to separate avalanche fluctuations from primary ionization statistics, we assume throughout this chapter that the initial electron energy is below the ionization potential of the gas. This is typically the case in detectors where the primary electrons are thermalized in a drift zone before entering the amplification region (e. g. wire chambers, GEMs, and Micromegas), and also in the experimental setups considered in Section 3.2.3 where single electrons were released from the cathode of a parallel-plate chamber by illumination with UV light.

In order to simplify the identification of the mechanisms at play, we first discuss the evolution of avalanches in a constant electric field, as realized in parallel-plate counters and, to good approximation, in Micromegas. Moreover, we focus on the proportional regime of amplification, i. e. we assume that distortions of the electric field caused by space charge can be neglected. Under these conditions, the mean avalanche size $\overline{n}$ grows exponentially with the gap size x,

$$\overline{n} = \mathrm{e}^{\alpha x}.$$

3.1.2. Motivation

Together with primary ionization statistics, gain fluctuations set a physical limit to the energy resolution of a detector. Of particular importance in this respect is the relative variance

$$f = \frac{\sigma^2}{\overline{n}^2}$$

of P_n.

Under convolutions, both $\overline{n}$ and σ^2 are additive. The relative variance f_m for m primary electrons is, therefore, given by

$$f_m = \frac{1}{m}f.$$

Let ϵ be the energy deposition in a charged particle collision (or the energy of a photon absorbed in the gas), $\overline{m} = \epsilon/W$ the mean number of electron-ion pairs produced in the collision, and $\sigma_m^2 = F\overline{m}$ the corresponding variance. Assuming that the measured signal is proportional to $k = mn$, the energy resolution is given by [57]

$$\frac{\sigma_\epsilon^2}{\epsilon^2} = \frac{\sigma_k^2}{\overline{k}^2} = \frac{\sigma_m^2}{\overline{m}^2} + \frac{1}{m}f = \frac{W}{\epsilon}\left(F + f\right).$$

The relative variance f also affects the so-called number of effective electrons N_{eff} characterizing the spatial resolution of a TPC [2, 58].

Another performance parameter determined by the avalanche size distribution is the detection efficiency κ, i. e. the probability for the avalanche size to exceed the detection threshold n_{t} of the readout electronics,

$$\kappa = \sum_{n=n_{\text{t}}}^{\infty} P_n. \tag{3.1}$$

Further, a low spread in avalanche size and thus low probability of large avalanches could be beneficial in terms of reducing the discharge rate.

3.1.3. Mathematical Description Of Gain Spectra

Measurements of gain spectra in uniform fields were first reported by L. Frommhold [59, 60], who observed that at low reduced fields E/p, the gain spectrum could be described by an exponential function

$$\overline{n}P_n \approx \mathrm{e}^{-n/\overline{n}} \tag{3.2}$$

with relative variance $f \approx 1$. This behaviour had been anticipated [61, 62] and could be explained [63] in terms of the so-called Yule-Furry model (see Section A.2.1). An exponential shape of the gain spectrum implies that the efficiency

$$\kappa = \mathrm{e}^{-n_{\text{t}}/\overline{n}} \tag{3.3}$$

falls exponentially with increasing threshold n_{t}.

At higher fields – yet moderate avalanche size, thus retaining exponential growth – the avalanche size distribution was found to depart from the monotonically falling shape in that it exhibits a peak at $n > 1$ [64]. It was further established that with increasing E/p, the relative variance f decreases and the most probable size approaches the mean.

(a) Pólya Distribution   **(b)** Detection Efficiency
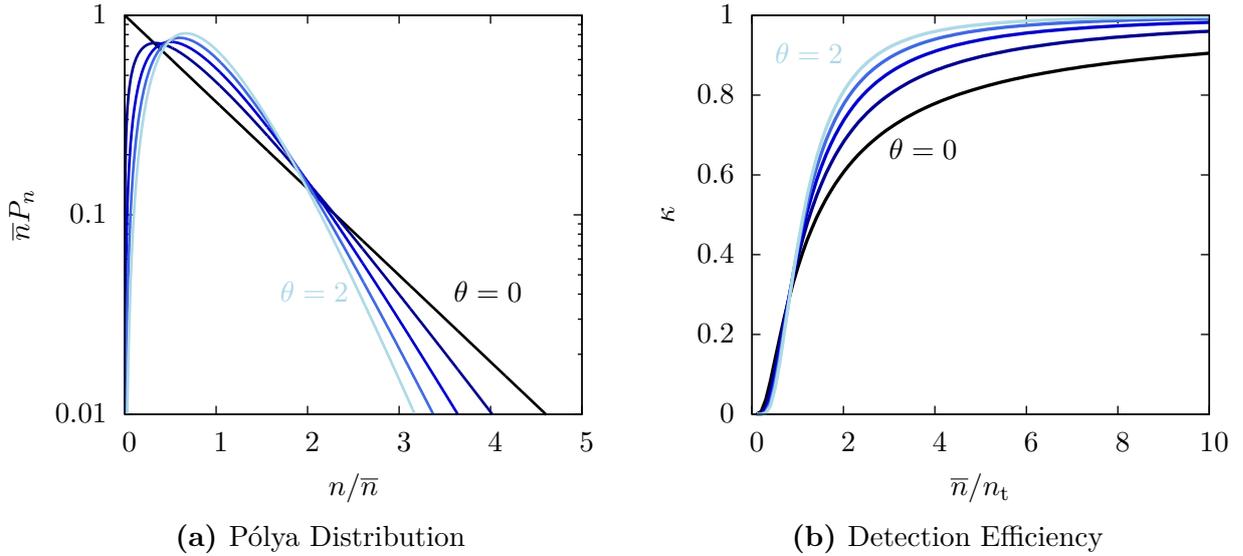
Figure 3.1. Pólya distribution (3.4) as a function of the normalized avalanche size $n/\overline{n}$ and detection efficiency κ (3.6) as a function of gain $\overline{n}$ over threshold n_t for shape parameters $\theta = 0$, $\theta = 0.5$, $\theta = 1$, $\theta = 1.5$, and $\theta = 2$.

Such spectra – which are clearly preferable with regard to detector performance – are not compatible with the Yule-Furry model or variants thereof which include attachment or double-ionization (see Section 3.2.2). In order to reproduce "rounded" avalanche size distributions, a more detailed description of the multiplication process is needed, which takes the energy dependence of the ionization mean free path (an aspect which is neglected in the Yule-Furry model), and the competition between ionization and other inelastic scattering processes into account. Such models are discussed in Section 3.2.2.

A popular function for describing non-monotonic, "rounded" spectra is the so-called Pólya distribution

$$\overline{n}P_n = \frac{(\theta + 1)^{\theta+1}}{\Gamma(\theta + 1)} \left(\frac{n}{\overline{n}}\right)^{\theta} \mathrm{e}^{-(\theta+1)n/\overline{n}}. \tag{3.4}$$

Pólya distributions for a number of shape parameters between $\theta = 0$ and $\theta = 2$ are plotted in Fig. 3.1a. For $\theta = 0$ one recovers the exponential distribution (3.2). With increasing θ, the relative variance

$$f = \frac{1}{1 + \theta} \tag{3.5}$$

decreases and the most probable size $n_\mathrm{mp} = \overline{n}\theta/(\theta + 1)$ shifts towards the mean. As can be seen from Fig. 3.1b, the efficiency associated to the Pólya distribution (3.4),

$$\kappa = \frac{\Gamma(\theta + 1, (\theta + 1)\, n_\mathrm{t}/\overline{n})}{\Gamma(\theta + 1)}, \tag{3.6}$$

can be significantly enhanced compared to (3.3).

The standard "derivation" of the Pólya distribution (see Appendix A.2.2), in particular the ansatz of modelling the energy dependence of the ionization probability in terms of the avalanche size alone, has been subject to criticism [65]. Despite its dubious physical foundation, the Pólya function is useful as a phenomenological fit function.

3.1.4. Implementation in Simulations

In simulations based on macroscopic transport coefficients, gain fluctuations can be taken into account by randomizing the number of electrons produced along a drift line according to a Pólya distribution (or any other suitable function). For this purpose, the shape parameter θ for the gas mixture and field configuration under consideration needs to be known. This is, in general, not the case however, such that one has to resort to an "educated guess".

Alternatively, a Yule-Furry like approach can be adopted. In the `Avalanche` procedure of Garfield [15], for instance, the number of electrons produced along a drift line is calculated in the following way:

- each drift step is subdivided such that the length Δx of a sub-step is small compared with the inverse Townsend coefficient α^{-1} at the local electric field;

- the probability for an electron to ionize during such a sub-step is thus given by $\alpha \Delta x$;

- a random number $u \in [0, 1]$ is drawn and a new electron is produced if $u < \alpha \Delta x$.

Since this is essentially a Monte Carlo implementation of the Yule-Furry process, the resulting avalanche size distribution is invariably exponential. Non-monotonic gain spectra are not reproducible with this method.

The Magboltz-based microscopic tracking technique (described in Section 2.3.2) allows one to calculate electron avalanches from "first principles", i. e. without additional tuning of shape parameters or the like. By comparison with gain spectra reported in the literature, we show in Section 3.2.3 that this is indeed a viable approach for quantitative predictions of the relative variance f in detection gases, provided that the electron-molecule scattering cross-sections are accurately known.

3.2. Uniform Fields

With respect to the calculation of avalanche size fluctuations, homogeneous fields have two particularly attractive aspects.

- As discussed in Section 3.2.1, the evolution of the relative variance f as a function of the gap size can be derived by means of general statistical considerations [66, 67]. It is thus possible to simulate an avalanche size distribution for a moderate mean avalanche size of the order of a few hundred electrons, and to extrapolate the corresponding relative variance to higher gains for comparison with experimental data.

- Toy models (Section 3.2.2) incorporating crucial aspects such as the existence of an ionization threshold and the interplay of ionizations and excitations can be constructed, and closed-form expressions for the relative variance according to these models can be derived. Such models can be useful for a qualitative understanding of the mechanisms at play.
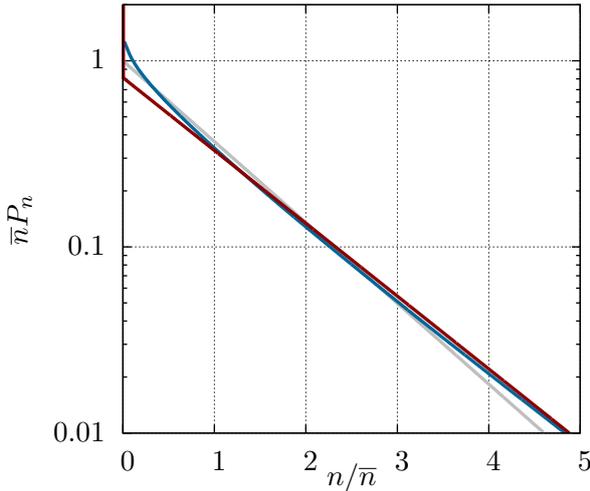
Figure 3.2 Avalanche size distributions for Yule-Furry type models including attachment or double-ionization as a function of the normalized avalanche size $n/\overline{n}$. The red curve was calculated using (3.9) with $\eta/\alpha = 0.1$. The blue curve shows a gain spectrum with a double-ionization coefficient $\beta = 0.1\alpha$ (calculated by Monte Carlo simulation).

3.2.1. Evolution of the Relative Width

Let $P_n^{(1)}$, with mean $\overline{n}_1$ and variance σ_1^2, be the avalanche size distribution after a distance x_1 along the electric field. The mean $\overline{n}_k$ after a distance $x_k = kx_1$ is given by

$$\overline{n}_k = \overline{n}_1{}^k.$$

Similarly, the variance after k steps is given by

$$\sigma_k^2 = \overline{n}_1{}^{k-1} \sum_{i=0}^{k-1} \overline{n}_1{}^i \sigma_1^2.$$

Combining these two expressions, we obtain for the relative variance after k steps [66, 67]

$$f_k = f_1 \frac{1 - 1/\overline{n}_k}{1 - 1/\overline{n}_1}.$$

The relative variance thus tends to an asymptotic value f_∞. Given the mean $\overline{n}_1$ over a certain step, the corresponding relative variance f_1 can be extrapolated to the asymptotic value using (cf. Eq. 49 in Ref. [68])

$$f_\infty = f_1 \frac{1}{1 - 1/\overline{n}_1}. \tag{3.7}$$

In the derivation of these expressions we have assumed mutual independence of the avalanches started by each new electron, and an equal avalanche size distribution for all of these sub-avalanches. These requirements are not met if e. g. space charge modifies the field in which later avalanches develop.

3.2.2. Toy Models

Variants of the Yule-Furry Model

We first discuss two straightforward extensions of the Yule-Furry model. Including an attachment coefficient η in analogy to the Townsend coefficient α, Eq. (A.15) becomes [2]

$$\frac{\mathrm{d}}{\mathrm{d}x} P_n(x) = \alpha(x)(n-1) P_{n-1}(x) + \eta(x)(n+1) P_{n+1}(x) - [\alpha(x) + \eta(x)] n P_n(x). \tag{3.8}$$

For a uniform electric field, i. e. constant α and η, W. Legler [69] showed that the solution of this equation is given by

$$P_n(x) = \begin{cases} \frac{\eta}{\alpha} \frac{\overline{n}-1}{\overline{n}-\eta/\alpha}, & n = 0 \\ \frac{}{\overline{n}} \left(\frac{1-\eta/\alpha}{\overline{n}-\eta/\alpha}\right)^2 \left(\frac{\overline{n}-1}{\overline{n}-\eta/\alpha}\right)^{n-1}, & n > 0 \end{cases}, \tag{3.9}$$

with mean and variance

$$\overline{n} = \mathrm{e}^{(\alpha-\eta)x}, \qquad \sigma^2 = \frac{\alpha+\eta}{\alpha-\eta}\overline{n}\,(\overline{n}-1).$$

For $\overline{n} \gg 1$, the probability of obtaining no electrons at all becomes $P_0 \approx \eta/\alpha$. The distribution for $n > 0$ remains exponential (Fig. 3.2). Detailed simulations confirm that in attaching gases values of $f > 1$ are possible (see e. g. Section 3.3.1).

One could also imagine that an electron occasionally releases two electrons within a step $\mathrm{d}x$ [70]. With the probability of such an event being described by a coefficient β, the corresponding differential equation reads

$$\frac{\mathrm{d}}{\mathrm{d}x}P_n(x) = \alpha\,(n-1)\,P_{n-1}(x) + \beta\,(n-2)\,P_{n-2}(x) - (\alpha+\beta)\,n P_n(x).$$

Although there is no analytic solution available, the size distribution can easily be calculated numerically for specific values of α and β. An example (for $\beta/\alpha = 0.1$) is shown in Fig. 3.2. Mean and variance are given by [70]

$$\overline{n} = \mathrm{e}^{(\alpha+2\beta)x}, \qquad \sigma^2 = \frac{\alpha+4\beta}{\alpha+2\beta}\overline{n}\,(\overline{n}-1).$$

Including attachment or double-ionization can thus be seen to increase the relative variance with respect to the original Yule-Furry model.

Legler-Alkhazov Theory

As already mentioned above, the energy dependence of the ionization mean free path has to be taken into account in order to explain spectra with $f < 1$. This was first pointed out by W. Legler [69] who emphasized that electrons need to travel a minimum distance along the electric field before they are able to ionize. A comprehensive catalog of avalanche models can be found in the classic paper by G. D. Alkhazov [68]. Before discussing specific models, let us briefly review the key elements of the theoretical framework on which they are based. In Legler's model and most of the other models discussed by Alkhazov, the energy dependence of the ionization process is taken into account in an indirect way by modelling the ionization probability as a function of the distance along the electric field travelled by an electron since its last ionizing collision. In this formalism, the avalanche evolution is controlled by the normalized distribution $\rho(\xi)$ of the distance ξ between successive ionizing collisions. If $\rho(\xi)$ is independent of the initial state of an electron, P_n satisfies [68]

$$P_n(x) = \int\limits_0^\infty \mathrm{d}\xi\,\rho(\xi) \sum_{n'=1}^{n-1} P_{n'}(x-\xi)\,P_{n-n'}(x-\xi). \tag{3.10}$$

Based on this expression, Alkhazov was able to derive a recursion relation for the moments of P_n. In the derivation it is assumed that $\overline{n}$ is proportional to $\exp(\alpha x)$, and that for $\overline{n} \gg 1$ the avalanche size distribution can be expressed as

$$P_n = \frac{1}{\overline{n}}\varphi(\nu),$$

(a) Legler's model   **(b)** Pólya "model"   **(c)** Stepwise evolution model
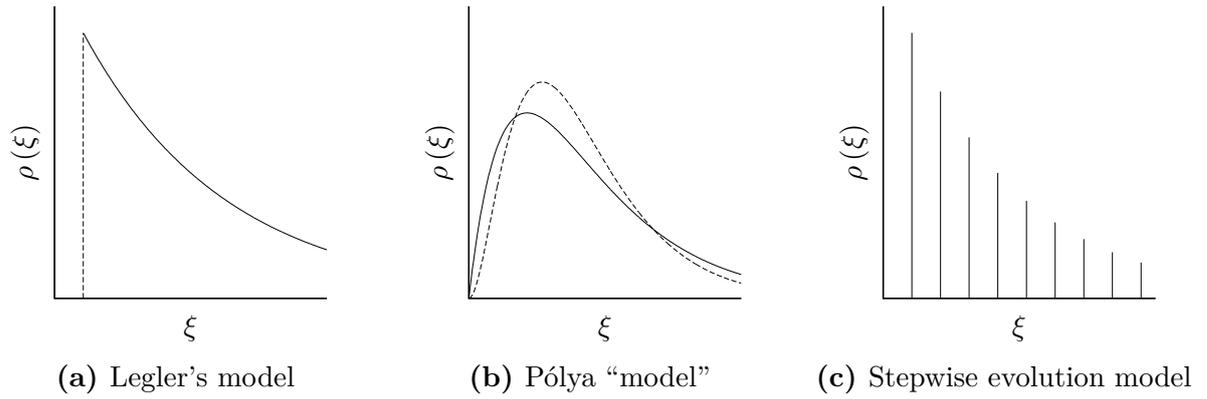
Figure 3.3. Ionization distance distribution $\rho(\xi)$ according to Legler's model (for $\alpha x_0 = 0.2$), the Pólya distribution for $\theta = 1$ (solid curve) and $\theta = 2$ (dashed curve), and the stepwise avalanche evolution model (for an ionization yield $p = 0.22$).

where φ is a continuous function which depends only on the normalized avalanche size $\nu = n/\overline{n}$. In other words, the shape of the avalanche size distribution is assumed to be independent of the distance x. This assumption is supported by experimental evidence [71] and is also plausible from a theoretical viewpoint, since according to (3.7) the relative variance barely changes once the avalanche has attained a size of a few hundred electrons. Equation (3.10) implies that [68]

$$\varphi(\nu) = \frac{1}{\alpha\nu} \int\limits_{\nu}^{\infty} \mathrm{d}\nu' \, \rho\left(\frac{1}{\alpha}\ln(\nu'/\nu)\right) \int\limits_{0}^{\nu'} \mathrm{d}\nu'' \, \varphi(\nu'') \, \varphi(\nu' - \nu''). \tag{3.11}$$

Closed-form solutions of this integral equation are available only for special cases. A "trivial" one is the Yule-Furry model where

$$\rho(\xi) = \alpha\mathrm{e}^{-\alpha\xi}.$$

This can be regarded as a coarse grain approximation valid at low fields where ionization is a comparatively rare event and an electron typically suffers many elastic and inelastic collisions before eventually ionizing. At strong fields, the ionization mean free path becomes comparable to the mean free paths for excitation and other inelastic processes such that a more refined modelling of $\rho(\xi)$ is necessary.

Legler's Model

In Legler's model [69], the energy dependence of the ionization mean free path is modelled in terms of a step function. The probability of ionization is zero below a characteristic distance $x_0 \approx U_{\mathrm{ion}}/E$, where U_{ion} is the ionization potential of the gas. For $\xi > x_0$, the ionization mean free path is assumed to be constant. The ionization distance distribution $\rho(\xi)$ is thus shifted with respect to the Yule-Furry model,

$$\rho(\xi) = \alpha\mathrm{e}^{-\alpha(\xi - x_0)}\Theta(\xi - x_0). \tag{3.12}$$

As shown by Alkhazov, the corresponding relative variance is given by

$$f = \frac{\left(2\mathrm{e}^{-\alpha x_0} - 1\right)^2}{4\mathrm{e}^{-\alpha x_0} - 2\mathrm{e}^{-2\alpha x_0} - 1}. \tag{3.13}$$

(a) Legler's Model   **(b)** Stepwise Evolution
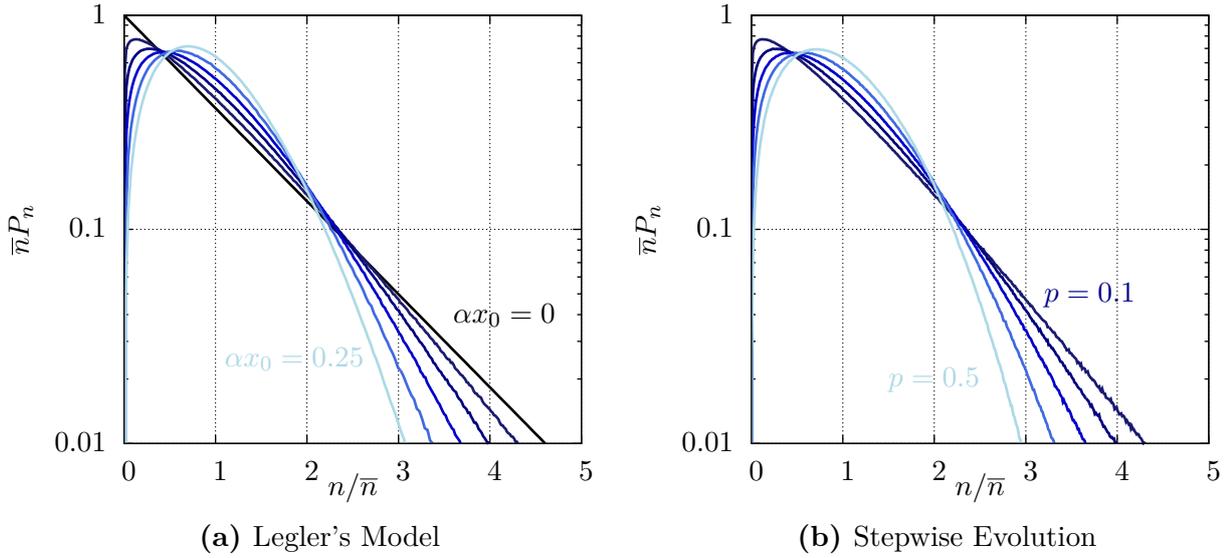
Figure 3.4. Toy model gain spectra evaluted by means of Monte Carlo integration. Left: avalanche size distribution according to Legler's model for $\alpha x_0 = 0$, $\alpha x_0 = 0.05$, $\alpha x_0 = 0.1$, $\alpha x_0 = 0.15$, $\alpha x_0 = 0.2$, and $\alpha x_0 = 0.25$. Right: avalanche size distribution according to the stepwise evolution model for $p = 0.1$, $p = 0.2$, $p = 0.3$, $p = 0.4$, and $p = 0.5$.

In Legler's "model gas", the size distribution is controlled by the parameter αx_0. Avalanche size distributions for some values of αx_0 are shown in Fig. 3.4a. By tuning the shape parameter αx_0, Legler was able to achieve good agreement with measured spectra [69]. On closer examination one notices a few problematic aspects of the model however.

- The parameter α appearing in (3.12) is neither identical to the Townsend coefficient as defined by $\ln{(\overline{n})}/x$, nor does its inverse correspond to the mean free path between ionizing collisions $\lambda_{\mathrm{ion}} = \alpha^{-1} + x_0$.

- The impact of scattering processes other than ionization (e. g. inelastic collisions) on the avalanche evolution is "hidden" in the dependence of α on the electric field.

- The explicit dependence of the ionization probability on the previous history of the electron renders the avalanche process non-Markovian.

Stepwise Evolution

Compared with Legler's model, the interplay of inelastic and ionizing collisions is reflected more clearly in "model 2" of Alkhazov's paper [68]. One views the multiplication process as proceeding in discrete steps of constant length x_0 along the electric field. After each step, an electron either ionizes with a probability p, or (with probability $1 - p$) it suffers a non-ionizing inelastic collision. Assuming that p has the same value for all steps, the probability ρ_k that an electron ionizes at a distance $k x_0$ with respect to the previous ionizing collision is given by

$$\rho_k = p \left(1 - p\right)^{k-1}. \tag{3.14}$$

The probability $P_n^{(k+1)}$ that the avalanche comprises n electrons after $k+1$ steps can be calculated recursively using

$$P_n^{(k+1)} = \left(1 - p\right) P_n^{(k)} + p \sum_{n'=1}^{n-1} P_{n'}^{(k)} P_{n-n'}^{(k)}. \tag{3.15}$$

For mean and variance one obtains

$$\overline{n} = (1 + p)^k, \qquad \sigma^2 = \frac{1 - p}{1 + p} \overline{n} (\overline{n} - 1).$$ (3.16)

The shape of the gain spectrum is determined by the "ionization yield" p. In the limit of small p the probability distribution tends to an exponential, whereas for $p = 1$ the distribution becomes a Dirac delta distribution. Avalanche size distributions in the range between $p = 0.1$ and $p = 0.5$ are shown in Fig. 3.4b.

It may be noted that p and x_0 should not be viewed as mutually independent parameters. Although the step size x_0 does not appear explicitly in (3.16), it does affect p in that it determines the gain in energy of an electron between successive steps. With the Townsend coefficient being given by

$$\alpha = \frac{1}{x_0} \ln (1 + p),$$

the relative variance can also be expressed as

$$f = 2\mathrm{e}^{-\alpha x_0} - 1.$$

Like in Legler's model, the shape of the distribution is characterized by a parameter $\alpha x_0 \in [0, \ln 2]$. Since α/p is, to good approximation, a function of E/p and x_0 is roughly proportional to $1/E$, this dependence suggests that the relative variance scales with the reduced electric field E/p.

Pólya Distribution Revisited

Alkhazov also discusses another category of models, in which a distinction between "slow" s-electrons and "fast" f-electrons is made. Only electrons of the latter class are supposed to be able to ionize while s-type electrons first have to come to equilibrium with the electric field by collisions with the gas molecules before they can multiply. Such a model was proposed by Byrne [72], who obtained a Pólya distribution as an approximative solution. This approximation was shown to be incompatible with the moments of the distribution calculated by means of the Alkhazov formalism [68] however.

On the other hand, the Pólya distribution can actually be reproduced by assuming an ionization distance distribution of the form

$$\rho (\xi) = \frac{\Gamma (2 (\theta + 1))}{\Gamma (\theta + 1)^2} \alpha \mathrm{e}^{-\alpha(\theta+1)\xi} \left(1 - \mathrm{e}^{-\alpha\xi}\right)^\theta.$$

This function (shown in Fig. 3.3) looks a bit like a "smeared out" version of its counterpart in the Legler model, but is not particularly instructive otherwise. The question how the shape parameter θ is to be interpreted from a physical viewpoint also remains unanswered in this "model".

Numerical Evaluation

While the moments

$$\mu_i = \int\limits_0^\infty \mathrm{d}\nu \varphi (\nu)$$

of the avalanche size distributions resulting from the toy models discussed above can be calculated efficiently by means of recurrence formulae, the numerical evaluation of the function $\varphi (\nu)$ itself
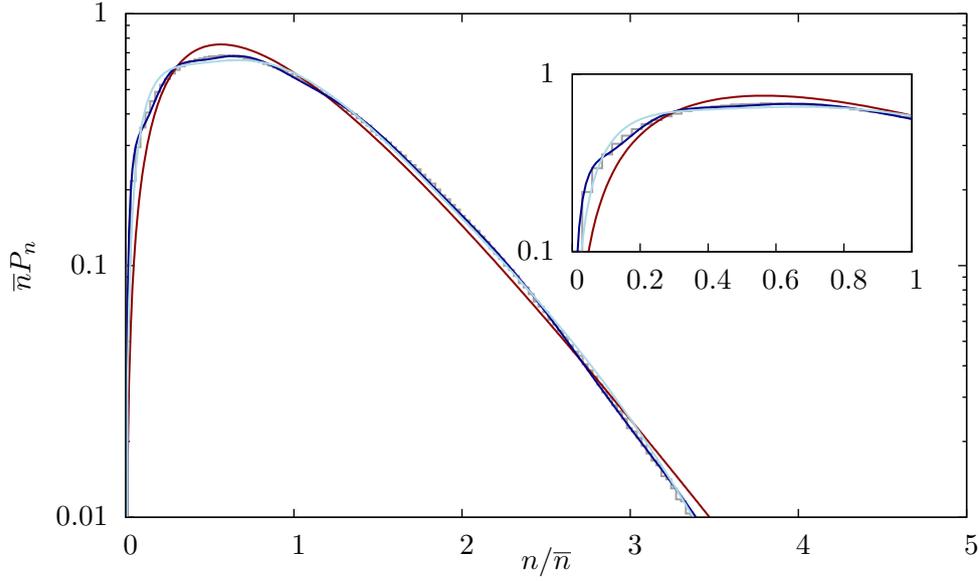
Figure 3.5. Approximations of Legler's "model gas" distribution (for $\alpha x_0 = 0.2$) obtained by truncating the series expansion (3.17) after 2 terms (red curve), 10 terms (light-blue curve), and 40 terms (dark-blue curve). The grey curve represents a histogram calculated using Monte Carlo simulation. A close-up of the region around the peak is shown in the inset.

according to Eq. (3.11) is considerably more challenging. Legler's model, for instance, leads to a so-called delay-differential equation, i. e. a differential equation which involves the function to be solved for at different values of the independent variable.

At first glance, reconstructing the distribution from its moments seems to be a promising approach. A possible method, which was explored within the framework of this thesis work, is based on an expansion of $\varphi(\nu)$ into a series of generalized Laguerre polynomials L_k^θ [73].

The generalized Laguerre polynomials,

$$L_k^\theta(\nu) = \sum_{i=0}^{k} \binom{k+\theta}{k-i} \frac{(-\nu)^i}{i!},$$

are orthogonal over $[0,\infty)$ with respect to the weighting function $\nu^\theta e^{-\nu}$,

$$\int_0^\infty d\nu\, L_m^\theta(\nu) L_n^\theta(\nu) \nu^\theta e^{-\nu} = \frac{\Gamma(n+\theta+1)}{n!} \delta_{mn}.$$

The avalanche size distribution $\varphi(\nu)$ can thus be expressed as

$$\varphi(\nu) = \frac{(\theta+1)^{\theta+1}}{\Gamma(\theta+1)} \nu^\theta e^{-(\theta+1)\nu} \sum_{k=0}^{\infty} c_k L_k^\theta((\theta+1)\nu), \tag{3.17}$$

where the coefficients c_k of the series expansion are given by

$$
\begin{aligned}
c_k &= \frac{\Gamma(\theta+1)\Gamma(k+1)}{\Gamma(k+\theta+1)} \int_0^\infty d\nu\, L_k^\theta((\theta+1)\nu)\, \varphi(\nu) \\
&= \sum_{i=0}^{k} \binom{k}{i} \frac{\Gamma(\theta+1)}{\Gamma(\theta+1+i)} (-1)^i (\theta+1)^i \mu_i.
\end{aligned}
$$

The idea is now to approximate the avalanche size distribution by including only polynomials up to an order $k_{\max}$. The variances of the approximative solution and the original function are matched if the parameter θ is chosen as $\theta = 1/(\mu_2 - 1) - 1$. As lowest order approximation ($k_{\max} = 2$), one then obtains a Pólya distribution with the same relative variance as $\varphi(\nu)$, which makes this approach potentially very attractive.

As can be seen from Fig. 3.5, the convergence of the series is rather slow however. Especially the shape of the peak is not correctly reproduced if only low order polynomials are taken into account. In the example shown in Fig. 3.5, a reasonable approximation is obtained by truncating the series after 40 terms. The oscillatory character of the generalized Laguerre polynomials leads to large distortions of the fitted distribution however, if polynomials of order greater than 60 or so are included and thus prevents the distribution to be evaluated to arbitrary precision. There is also no guarantee that the calculated distribution is positive definite.

The above method is, therefore, not well suited for accurate calculations of $\varphi(\nu)$ and, due to the sensitive dependence on $k_{\max}$, does not offer an easy-to-use fit function either. For the latter purpose, the Pólya distribution (or a superposition of Pólya functions) is in many cases sufficient, though. Monte Carlo integration, on the other hand, while by construction unsuitable for fitting purposes, represents a mathematically simple and accurate method for the numerical evaluation of toy model avalanche size distributions. This technique was used for producing Figs. 3.4a and 3.4b. In Legler's model, for instance, the step size Δx between successive ionizing collisions can be sampled using

$$\Delta x = x_0 - \frac{2\mathrm{e}^{-\alpha x_0} - 1}{\alpha} \ln u,$$

where $u \in (0, 1]$ is a uniform random variate.

3.2.3. Microscopic Simulation

The toy models discussed above have the merit of affording qualitative insight into the multiplication process. On the other hand, in order to arrive at a closed-form expression for the relative variance f (and higher moments), they inevitably involve a number of simplifying assumptions. In a microscopic Monte Carlo simulation such approximations can be avoided, since the electron collision rates (or mean free paths) are modelled directly as functions of the electron energy. This approach also allows scattering processes other than ionization such as inelastic collisions (e. g. molecular vibrations and rotations), excitations, and attachment to be included. Hence, given the complexity of real gas mixtures (and the computational power available today), Monte Carlo simulation is the most efficient method for quantitative predictions of gain spectra.

In this section, calculations of avalanche fluctuations by means of the microscopic tracking method are presented. Starting with a single electron at $z = 0$, the avalanche evolution in a constant electric field $(0, 0, E)$ is followed until all electrons have either reached the anode (i. e. they have crossed the scoring plane $z = z_+$) or are stopped because of attachment. The avalanche size spectrum is established by histogramming the number of electrons arriving at the electrode. For each gas mixture and field, the gap size z_+ was adjusted such that a mean size between 100 and 1000 electrons was obtained.

Systematic Uncertainties

Besides the statistical error, the accuracy of the calculation is limited by uncertainties in the electron-molecule cross-sections. The uncertainties in the cross-sections for vibrations, rotations
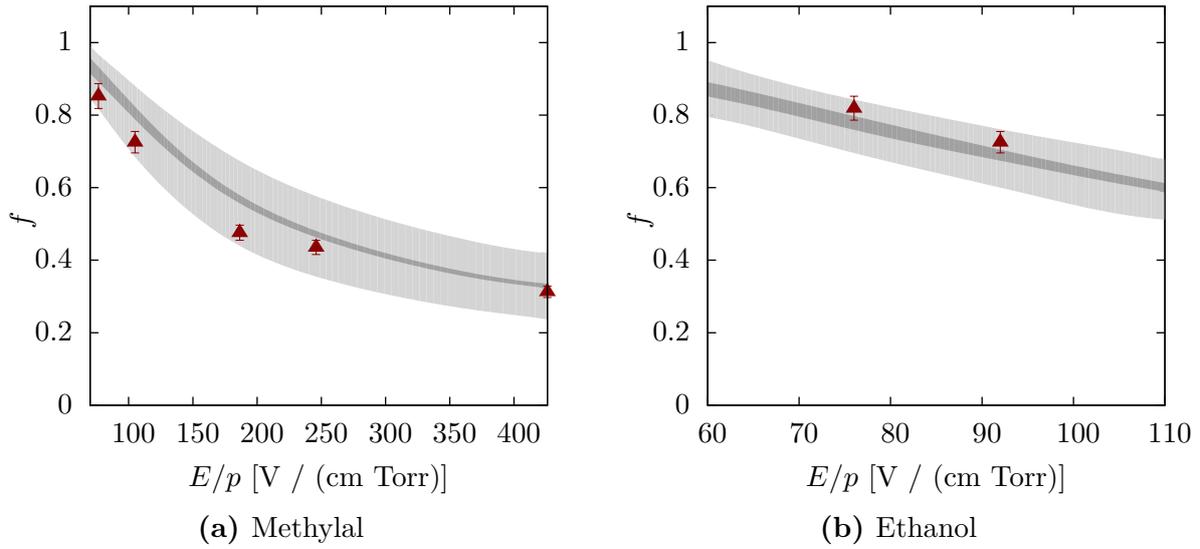
Figure 3.6. Relative variance f in methylal and ethanol as function of the reduced electric field E/p (at 20° C). The dark-grey band represents the (smoothed) calculated values, its width reflects the statistical error of the calculation. The light-grey band represents the estimated systematic uncertainty of f due to uncertainties in the electron-molecule cross-sections. In order to obtain this estimate, the excitation cross-sections were uniformly scaled by $\pm 30\%$ (methylal) and $\pm 20\%$ (ethanol). The triangles represent the relative variances of measured spectra [64] estimated from the fit parameters given in Ref. [69]. The error bars on the experimental data correspond to an uncertainty of ± 0.01 in the fitted shape parameter αx_0 [69].

and elastic scattering give no measurable contribution to the uncertainty in the Townsend coefficient [46]. For the calculation of gain spectra, ionization and excitation cross-sections are thus expected to constitute the dominant elements of uncertainty.

In order to estimate the uncertainty of the relative variance f, we calculate the upper and lower limits of f using two artificial sets of cross-sections where the excitation cross-sections are uniformly increased and decreased by a scaling factor A. For the well-known gases ("4*" and "5*"), the choice of A was guided by the constraint that the Townsend coefficient should not change by more than 3%. The value of A resulting from this constraint depends on the electric field since different energy ranges of the cross-sections are probed. For the "4*" and "5*" gases considered here (noble gases, CH_4, and CO_2), an uncertainty of $\pm 5\%$ in the excitation cross-sections was assumed, resulting in an estimated uncertainty in the calculated relative variance f of $< 5\%$. For the other two gases discussed below, the uncertainties in the electron-molecule cross-sections are significantly larger. The uncertainty in the excitation cross-sections for methylal ("2*" rating) might be as large as $\pm 30\%$ [46]. For ethanol ("3*" rating), where published total electron cross-section data are available, the cross-sections have a better accuracy (ca. $\pm 20\%$). The uncertainty in the cross-sections implies a large uncertainty in the calculated values of f in these gases as indicated by the light-grey shaded bands in Fig. 3.6.

In addition to the total cross-sections, we need to consider uncertainties in the differential cross-sections, in particular the energy partitioning between primary and secondary electron in ionizing collisions. Although based on fits to experimental data, the Opal-Beaty formula (2.27) does not reproduce the energy spectra of secondary electrons in full detail [48]. The impact of
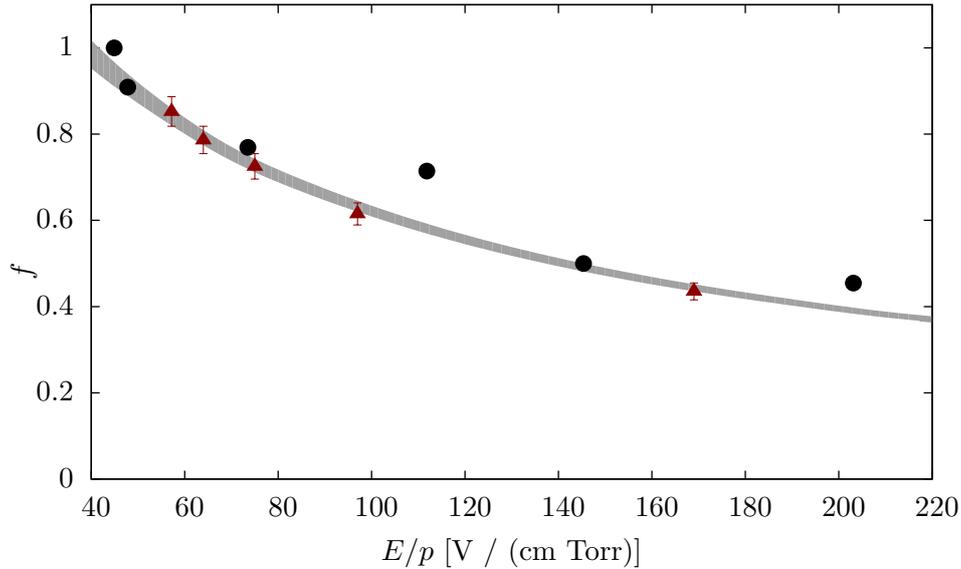
Figure 3.7. Relative variance in methane as function of the reduced electric field E/p (at 20°
   C). Triangles: relative variances of spectra measured by Schlumbohm [64], estimated from
   fits by Legler [69]. Full circles: fits by Cookson and Lewis [74] to measured spectra (no error
   estimates available). Smoothed dark-grey band: calculations (band width representing the
   statistical error).

this approximation on the calculated value of f is estimated in two ways: (1) by varying the
splitting parameter w, and (2) by using a flat distribution of ϵ' instead.

The simulation results are also biased by the initial energy ϵ_0 of the seed electron. The choice of ϵ_0
depends on the experimental setup to be studied in the simulation. In the following, calculation
results are compared with measurements where single electrons were released from the cathode
by illumination with a weak UV lamp. For the calculation, an initial energy of 1 eV was used.
The associated uncertainty was estimated by varying ϵ_0 between zero and the ionization potential.
The initial direction was sampled isotropically.

The relative variance was found to be insensitive to the shape of the differential ionization cross-
section and the initial electron energy. For methane, varying the splitting parameter w (originally
7.3 eV) between 2 and 15 eV, replacing the splitting function (2.27) by a flat distribution, or
varying the initial energy between 0.01 and 14 eV results in a change of f by only $1 - 2$ %.

Validation

In order to test the viability of the simulation method, we compare calculation results to published
gain spectra recorded with parallel-plate chambers.

Rounded avalanche size distributions in flat fields were first reported by H. Schlumbohm [64],
who performed systematic measurements of electron avalanche statistics for several gases over
a large range of reduced electric fields (at pressures between 10 Torr and 100 Torr) at a gain
of the order of $\bar{n} \lesssim 10^5$. Details of his results are available for methylal (dimethoxymethane),
ethanol vapour, acetone and methane. Since acetone is not included in the Magboltz database,
the corresponding spectra could not be used for validation purposes.

The relative variances of the measured methylal and ethanol spectra are shown in Fig. 3.6 together with the computed asymptotic values extrapolated using (3.7). The tendency of f to decrease with increasing E/p is reproduced by the simulation and the relative variances of the spectra are within the estimated systematic uncertainties of the calculation.

Gain spectra for methane ("5*" rating in Magboltz) are excellent references for benchmarking the simulation. Schlumbohm's results for methane are discussed in detail in an article by W. Legler [69], where the measured spectra are compared to theoretical avalanche size distributions according to Legler's model. By tuning the shape parameter αx_0 of the theoretical curve, Legler obtained good agreement between calculated and measured distributions. With the relative variance of Legler's "model gas" distribution being given by (3.13), the best–fit shape parameters αx_0 quoted by Legler can be used for estimating the relative variance of Schlumbohm's spectra.

The statistics of single electron avalanches in methane were also investigated experimentally by A. H. Cookson, T. J. Lewis, and B. W. Ward [74, 75], who found their spectra to be in good agreement with Pólya distributions. The relative variance of these spectra can be inferred from the fit parameters θ quoted by Cookson and Lewis using $f = 1/(1 + \theta)$. As can be seen from Fig. 3.7, Schlumbohm's data are reproduced by the simulation within the uncertainty of the fit parameters according to Legler. There is also agreement of the calculated relative variances with most of the values obtained by Cookson and Lewis, except for the points at $E/p \approx 112$ V cm^{-1} Torr^{-1} and $E/p \approx 203$ V cm^{-1} Torr^{-1} (at $20°$ C). As for the latter, the authors mention that the tail of this spectrum was modified by feedback processes. Cookson and Lewis make no statement concerning the uncertainty of their fit parameters. Estimating the error based on the plots included in their paper is also problematic due to the low resolution of the drawings.

Interpretation

Complementary to a detailed Monte Carlo simulation, toy models like the ones discussed above are useful for developing an intuitive understanding of the mechanisms which influence the gain spectrum. Such a toy model should reproduce basic features of the observed behaviour of f as a function of the reduced field (e. g. $f \approx 1$ at low E/p) and provide a qualitative explanation of the differences between gas mixtures regarding the avalanche spread. Using the example of methane, we show how such a model can help to interpret the simulation results.

First, we calculate the energy distribution of the electrons in the avalanche by histogramming the energy of an electron prior to each collision. Figure 3.8a shows that with increasing reduced field E/p the energy distribution gradually shifts towards higher energies. As a consequence, the probability for an electron to have an energy greater than the ionization threshold (12.65 eV in case of methane) increases. At energies close to the ionization threshold, the cross-section for ionization is still significantly smaller than the sum of the inelastic terms (including excitations). With increasing energy however, ionization gradually becomes the dominant process. Hence, one expects that increasing the reduced field E/p leads to an enhanced relative frequency of ionizing collisions. In the simulation, we can test this hypothesis by counting the number of ionizations N_{ion} and excitations N_{exc} occurring in an avalanche. As can be seen from Fig. 3.8b, the relative frequency of ionizing collisions (with respect to excitations) indeed grows with increasing E/p.

Conceptually, the influence of inelastic and ionizing collisions on the avalanche size distribution can be understood in terms of the "step model" discussed in Section 3.2.2. We recall that in this
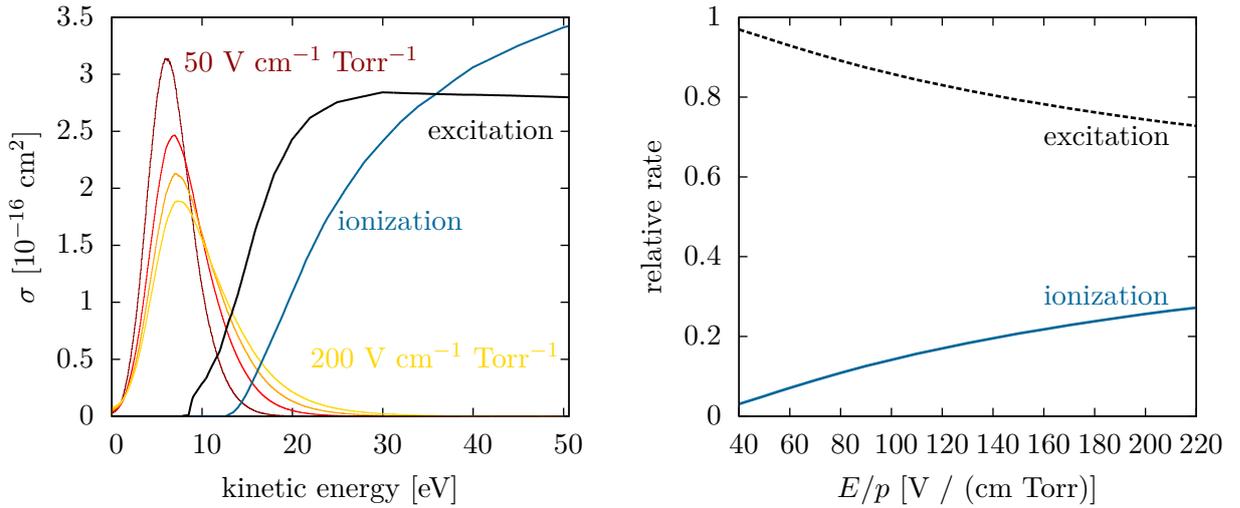
Figure 3.8. Left: calculated electron energy distribution (arbitrary scale of ordinate) in methane at reduced fields E/p of 50 V cm^{-1} Torr^{-1}, 100 V cm^{-1} Torr^{-1}, 150 V cm^{-1} Torr^{-1} and 200 V cm^{-1} Torr^{-1}, together with the total excitation and ionization cross-sections for scattering of electrons by methane (as implemented in Magboltz 8.9).
Right: number of ionizations N_{ion} (solid curve) and excitations N_{exc} (dashed curve) in methane, divided by the sum $N_{\text{ion}} + N_{\text{exc}}$, as a function of the reduced field E/p.

model the relative variance of the distribution is determined by the "ionization yield" p,

$$f = \frac{1-p}{1+p}. \tag{3.18}$$

Equating $p = N_{\text{ion}}/(N_{\text{ion}} + N_{\text{exc}})$, one sees that, consistent with the observed behaviour, the relative variance according to (3.18) approaches to $f = 1$ at low reduced field (small p) and falls with increasing reduced field. The toy model fails to reproduce the absolute value of f however. At 200 V cm^{-1} Torr^{-1}, for instance, one would expect from (3.18) a relative variance of $f \approx 0.59$, compared with a value of $f \approx 0.39$ calculated by means of the microscopic simulation (the latter being consistent with experimental data).

The reason for this discrepancy is that the "step" toy model is built on the assumptions that the thresholds for ionization and excitation are located energetically close to each other and that the corresponding mean free paths are of the same order of magnitude. This is a reasonable approximation for argon and other noble gases, but not for molecular gases like methane with significant inelastic absorption at energies well below the ionization threshold. This difference between atomic and molecular gases is reflected in the distribution of the distance ξ an electron travels between successive ionizing collisions. The corresponding histogram for Ar (Fig. 3.9) exhibits distinct bumps at regular intervals, as expected from the toy model (Fig. 3.3). For methane, the undulating structure of the inter-ionization distance distribution is less pronounced and becomes completely smeared out for large ξ. Nonetheless, the basic idea of the toy model, i. e. the interplay of ionization and excitation as a key factor determining the width of the gain spectrum, is consistent with the pieces of information extracted from the simulation.
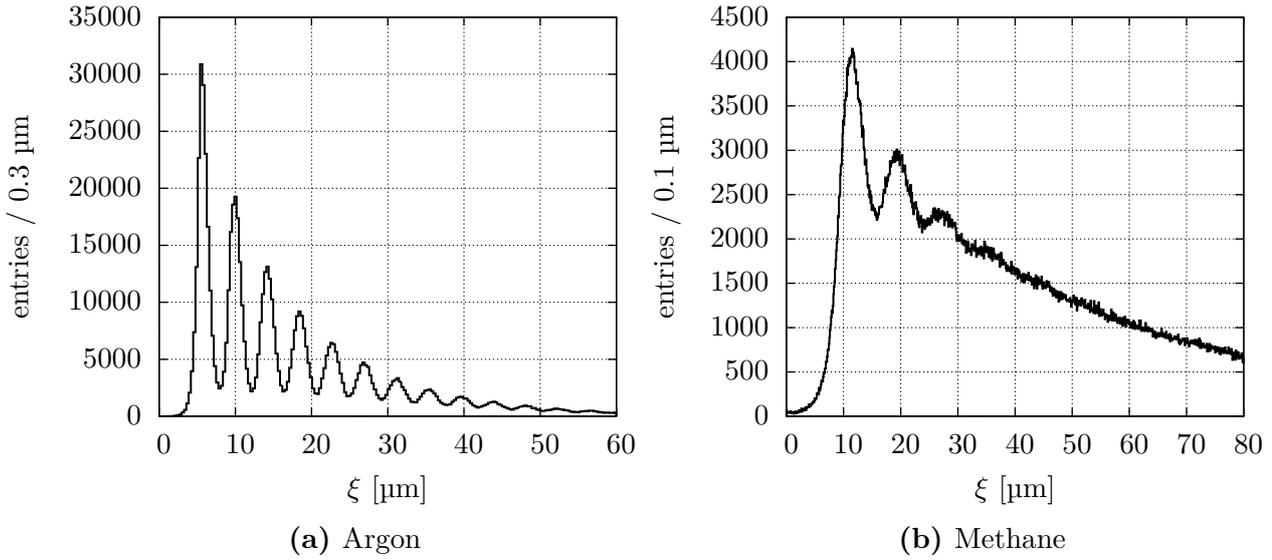
Figure 3.9. Histogram of the distance ξ between successive ionizing collisions for Ar (a) at $E = 30$ kV/cm (at atmospheric pressure and 20° C) and CH$_4$ (b) at $E/p = 78.9$ V cm^{-1} Torr^{-1} (0° C).

3.2.4. Comparison of Gases

As an application, we calculate the relative variance as a function of the electric field for a few typical noble gas based mixtures. Although rarely used in practice for amplification, pure noble gases represent a convenient theoretical playground due to their simple structure. In Fig. 3.10a, the calculated relative variances f for pure He, Ne, Ar, Kr, and Xe at atmospheric pressure are plotted as a function of the Townsend coefficient α. For helium, only values up to an applied field of 50 kV/cm are shown. At higher fields the electron mean free path becomes comparable to the gap size.

Comparing the relative variances at equal α, one sees that the lighter elements consistently have a lower value of f. This can be understood as a consequence of the higher ionization yield in the lighter gas (see Fig. 3.11). As an illustration, the cross-sections for ionization and excitation in Ne and Ar as functions of the electron energy are plotted in Fig. 3.12, together with typical electron energy distributions. Looking at the energy distributions in the two gases, one sees that neon is considerably "hotter" than argon. For example, at a field of 50 kV/cm the average electron energy in Ne is ≈ 20 eV, which is close to the ionization threshold of 21.56 eV, whereas the mean of the energy distribution in Ar (≈ 10.5 eV) is significantly lower than the ionization potential (15.76 eV). This may be understood as a consequence of the energetically lower threshold for excitations in Ar and the larger elastic cross-section.

So far, we have considered only pure gases. In order to achieve stable operation, a so-called quenching gas is usually added to the noble gas. Due to inelastic scattering at energies below the excitation and ionization thresholds, the energy distribution of the electrons in the gas mixture is "cooled" down and the ratio of inelastic vs. ionizing collisions is shifted in favour of inelastic scattering. As a consequence, one expects a broadening of the avalanche size distribution with respect to the pure gas. For many combinations of gases, this effect is mitigated, though, by Penning transfer.
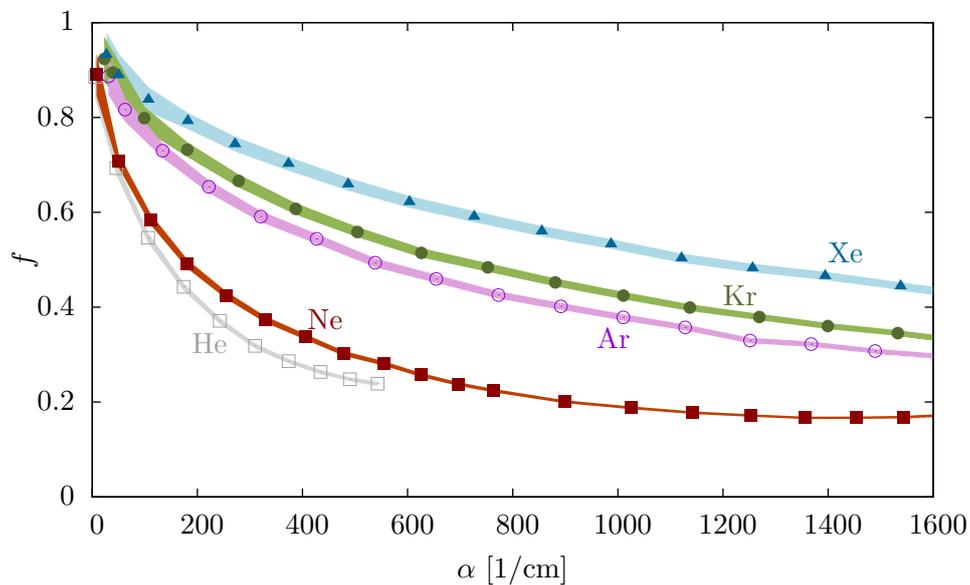
(a)
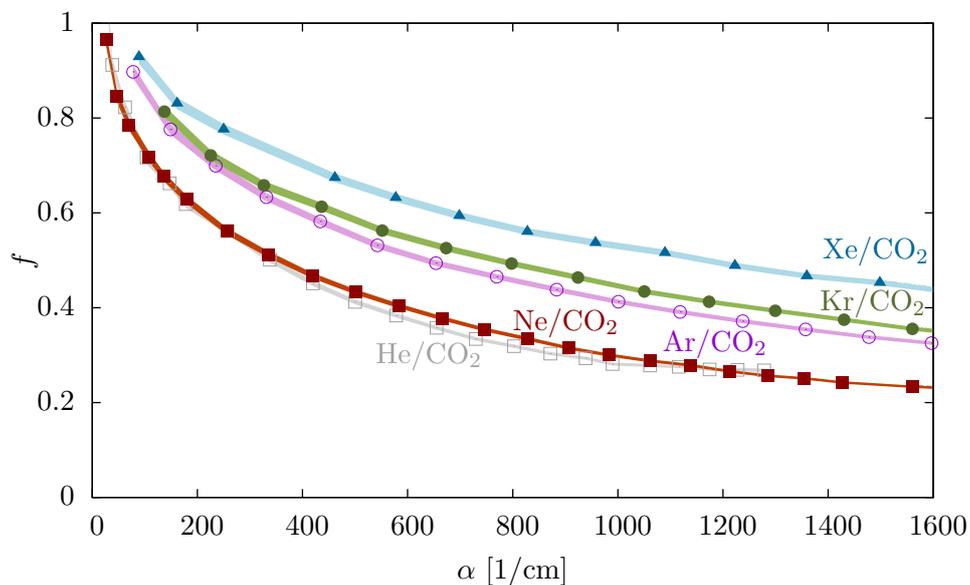
(b)

Figure 3.10. Relative width f as a function of the Townsend coefficient α (at atmospheric pressure and 20° C) in He (open squares), Ne (full squares), Ar (open circles), Kr (full circles) and Xe (triangles). Top: calculations for pure gases. Bottom: calculations (without Penning transfer) for an admixture of 10% CO_2 to the respective noble gas.

Figure 3.11 Ionization yield (fraction of ionizing collisions N_{ion} of the total sum of inelastic collisions $N_{\text{exc}} + N_{\text{ion}}$), as a function of the electric field (at atmospheric pressure and 20° C) for He, Ne, Ar, Kr, and Xe.
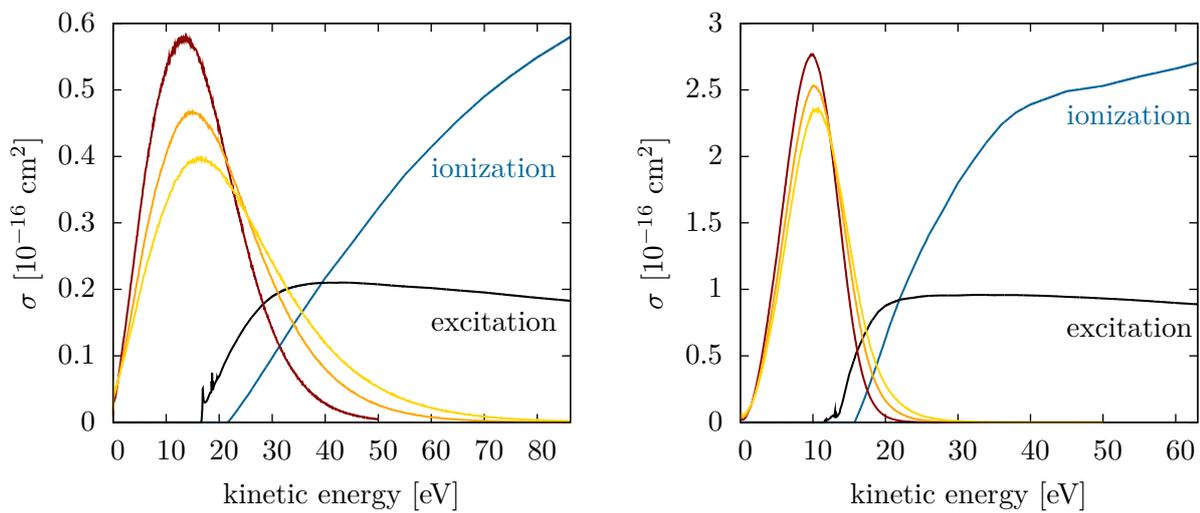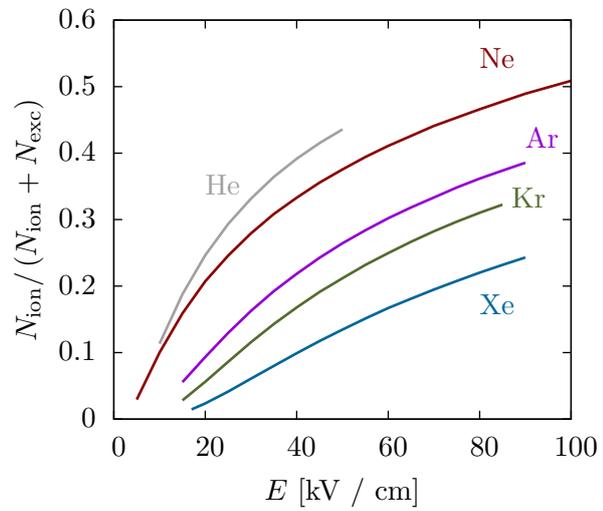
Figure 3.12. Electron scattering cross-sections for ionization and excitation in neon (left) and argon (right) as functions of the electron energy, and electron energy distributions in neon and argon at electric fields of 30 kV/cm, 50 kV/cm and 70 kV/cm (arbitrary scale of ordinate).
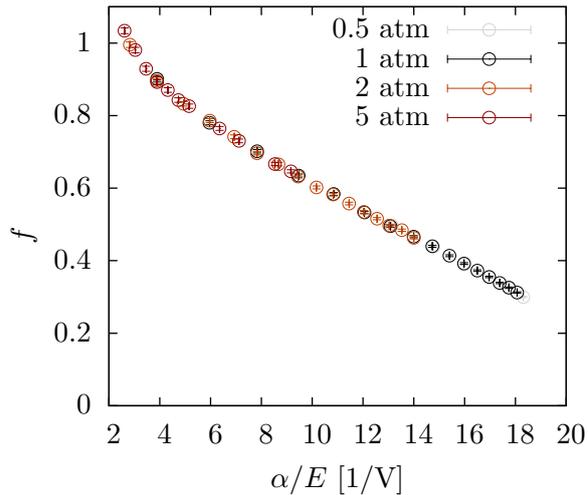
Figure 3.13 Relative width f in Ar/CO_2 (90:10) as a function of α/E at $p = 0.5$ atm, $p = 1$ atm, $p = 2$ atm, and $p = 5$ atm, calculated without Penning transfer.

As an example, we consider mixtures of noble gases with 10% CO_2. The relative variances calculated without Penning transfers are shown in Fig. 3.10b. The impact of the admixture on the relative variance is largest for the light gases. For instance, the relative variance in Ne increases by up to 50%. The effect is less pronounced in Ar (increase of f by max. $\approx 12\%$) and the values of f for Xe are only marginally altered (except at low α).

The dependence of f on the parameter αx_0 (with $x_0 \propto 1/E$) predicted by the toy models discussed above suggests that the relative variance is a function of α/E, and, consequently, the reduced electric field E/p. As can be seen from Fig. 3.13, which shows the relative variance in Ar/CO_2 (90:10) calculated at different pressures as a function of α/E (without Penning transfer), this scaling relation is also borne out by the simulation.

In a realistic calculation, Penning transfers need to be taken into account for He/CO_2, Ne/CO_2 and Ar/CO_2. For Ar/CO_2 (90:10), Şahin et al. [50] find an average transfer efficiency of $r \approx 0.48 \pm 0.01$ for the energetically eligible excitation levels. For Ne/CO_2 (90:10), the average transfer efficiency has been estimated as $r \approx 0.4$ [76], with an uncertainty of the order of $\pm 10\%$. In both cases, the transfer probabilities were inferred from gain measurements in cylindrical chambers.

The values of f for Ar/CO_2 and Ne/CO_2 calculated with these transfer efficiencies are shown in Fig. 3.14a. In both gases, the relative variance at $\alpha > 1400$ cm^{-1} is reduced by $\approx 12\%$ with respect to the values calculated without Penning transfer. The above uncertainties of the transfer efficiencies correspond to uncertainties in the relative variance of $< 1.5\%$ (for Ar) and $< 3\%$ (for Ne). In addition, the calculations are subject to a potential systematic bias: the transfer probabilities depend to some extent on the applied electric field, since they are average values, weighted by the frequencies with which the individual levels are excited.

Adding CH_4 to argon has a similar effect as in the case of CO_2 (see Fig. 3.14b). By adding 10% methane, the relative variance at $\alpha = 1000$ cm^{-1} (calculated without Penning transfer) increases by $\approx 8\%$ with respect to pure Ar. If a Penning transfer probability of $r = 0.212$ [50] is taken into account, the relative variance at $\alpha = 1000$ cm^{-1} is reduced to $f \approx 0.38$, which is only about 1% higher than (i. e. within the uncertainty of) the value in pure argon.

Penning effects can also be nicely incorporated in the toy model. Let p be the ionization yield in a scenario without Penning transfers and f the corresponding relative variance. With r being the average transfer probability, the effective ionization yield p' is given by

$$p' = p + r\,(1 - p)\,.$$
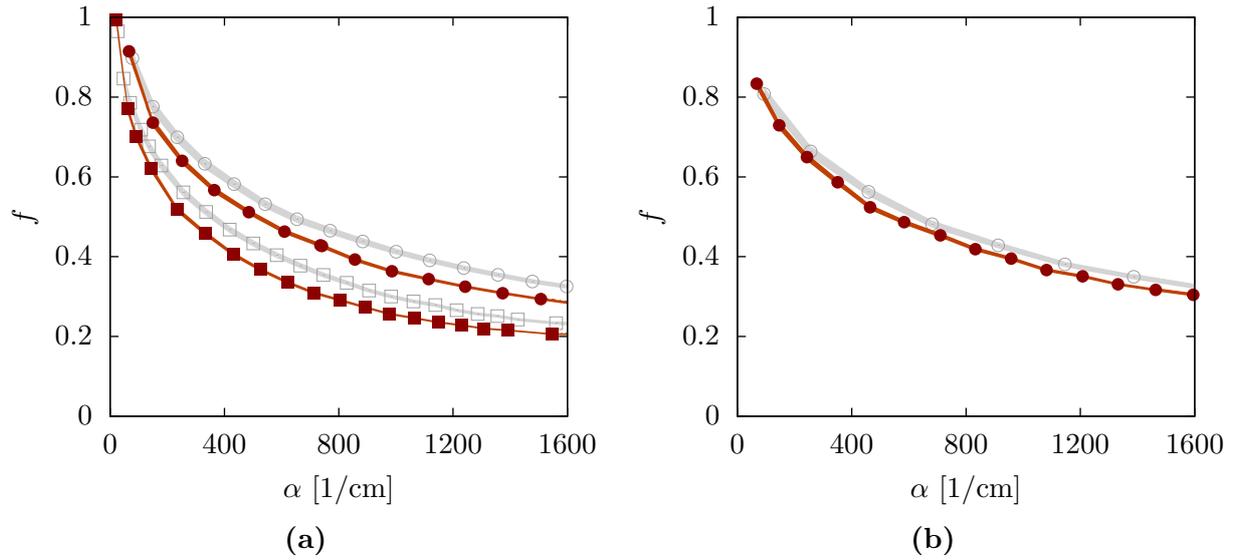
Figure 3.14. Relative width f as function of α (at atmospheric pressure and 20° C) with and without Penning transfer. Left: calculations for Ne/CO_2 90:10 (squares) and Ar/CO_2 90:10 (circles). Right: calculations for Ar/CH_4 (90:10). Open symbols represent the values calculated without Penning transfers, full symbols represent the values calculated with transfer efficiencies $r = 0.48$ for Ar/CO_2, $r = 0.4$ for Ne/CO_2, and $r = 0.212$ for Ar/CH_4.

For the relative variance f' with Penning transfers one then obtains

$$f' = f \frac{1-r}{1+rf},$$

which shows that $f' < f$.

3.3. Wire Chambers

The use of the Magboltz-based microscopic
tracking technique for gain calculations is not
restricted to uniform fields. In this section we
discuss the statistics of electron avalanches in
the vicinity of a wire.

3.3.1. Gain Fluctuations

We consider the array of wires schematically
depicted in Fig. 3.15. It consists of anode wires
(20 μm diameter) with periodicity $s = 4$ mm
in the horizontal direction, interleaved with
grounded field wires (75 μm diameter). The
wire grids are located at $y = s$, between two
ground planes at $y = 0$ and $y = 2s$.

Figure 3.15. Schematic layout of the wire cham-
ber configuration considered in Section 3.3.1.
Sense wires are marked by open circles, field
wires by full circles (wire diameters not
drawn to scale).

For the given geometry, the amplification prop-
erties depend on the gas density, the gas composition, and the voltage ϕ_s applied to the sense
wires. We first focus on the latter two aspects and consider the relative width f in two argon-based
gas mixtures at atmospheric pressure and room temperature (20° C).

The gain spectrum is further influenced by the initial position and energy of the seed electron.
For the calculations presented in the following, a set of initial conditions aimed at mimicking
electron amplification in a TPC readout chamber was chosen. The initial electron was released
0.4 mm below the upper cathode plane, its position along the horizontal axis was randomized. As
for the initial energy ϵ_0, two approaches were tried: using a fixed value $\epsilon_0 = 0.1$ eV, and sampling
ϵ_0 from the energy distribution in a uniform field of 100 V/cm. The results obtained using the
two methods agree within the statistical error.

As in the previous section, the initial electron and the secondary electrons produced in the
avalanche are traced until all electrons have either left the device or have been captured by a gas
molecule. The gain spectrum is calculated by histogramming the number of electrons which hit
the wire. Distortions of the electric field due to space charge are not taken into account.

The calculated relative width f as a function of the mean gain $\overline{n}$ (which in turn is a function of
the anode wire voltage ϕ_s) is shown in Fig. 3.16 for pure argon, methane, and carbon dioxide as
well as for mixtures of Ar with 10% CH_4 (also known as P10) and 10% CO_2, respectively. For
the Penning transfer efficiencies in the two gas mixtures, the same values as in Section 3.2.4 were
used ($r = 0.48$ for Ar/CO_2, $r = 0.212$ for Ar/CH_4).

In attaching gases, it is possible that the initial electron is lost before multiplication starts.
As can be seen from Fig. 3.16, this has a considerable effect on the relative width of the gain
spectrum, especially for CO_2. For instance, if events with $n = 0$ are included in the avalanche
size histogram, one obtains for $\overline{n} = 1000$ a relative variance $f \approx 1.03 \pm 0.02$. If only avalanches
with $n > 0$ are included in the histogram, the corresponding relative variance $f_{>0} \approx 0.76 \pm 0.02$
is substantially lower.

The simulation results for argon-methane are in agreement with calculations by Alkhazov [68],
who found the relative width for $\overline{n} > 100$ to be in the range $0.6 < f < 0.8$. The fact that the
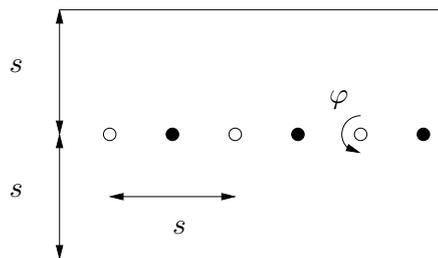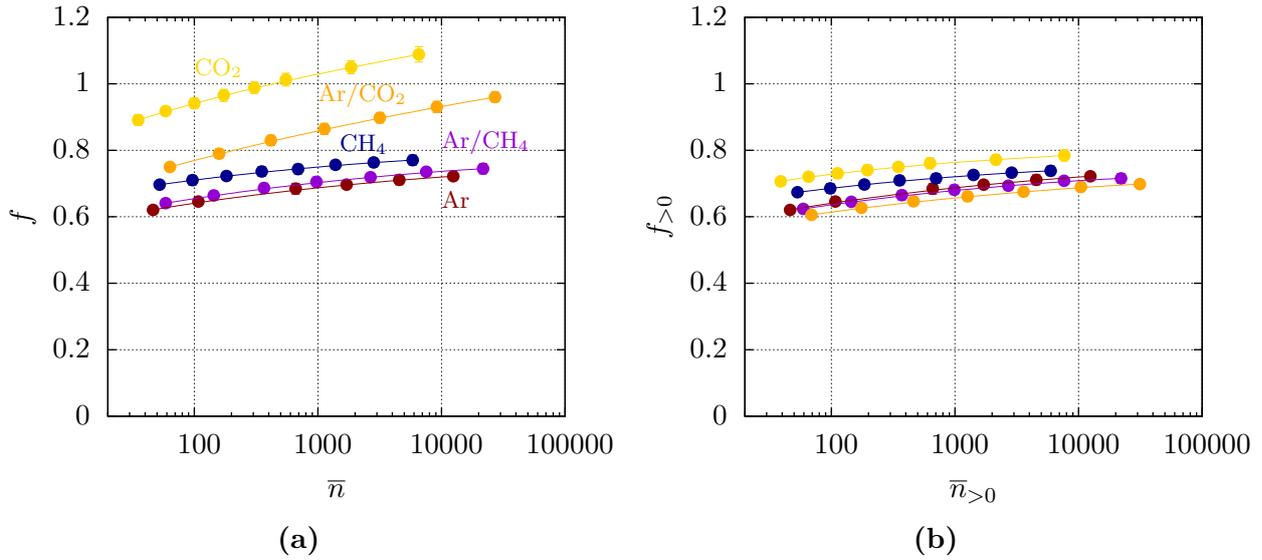
Figure 3.16. Relative variance of electron avalanches in the wire chamber configuration depicted in Fig. 3.15 as a function of the mean gain for Ar, Ar/CH$_4$ (90:10), Ar/CO$_2$ (90:10), CH$_4$, and CO$_2$ (at atmospheric pressure, 20° C). The error bars (which are in some cases inside the marker) indicate the statistical error (1 σ) of the calculation. The solid curves are drawn to guide the eye. Figure (a) shows the relative width f obtained by including events with zero electrons in the gain spectrum. For the calculation of the relative width $f_{>0}$ shown in Fig. (b) these events were not taken into account. In both plots, the same colour coding was used.

relative width increases with the mean gain deserves some explanation. Naively, one could expect f to be correlated with the maximum of the electric field (proportional to ϕ_s), which is higher at larger gain. Schlumbohm [77] and Alkhazov [68] pointed out however, that the fluctuations in the avalanche size are largely controlled by the electric field at which the multiplication process starts. This is confirmed by the simulation, as illustrated in Fig. 3.17 for the case of pure argon. Raising the sense wire voltage ϕ_s increases the mean gain $\overline{n}$ while E_2, i. e. the average electric field at which the first ionization occurs, decreases slightly. As can be seen from Fig. 3.17b, the value of f for Ar in the present field configuration as a function of E_2 follows closely the relative width in a uniform field of strength E_2.

Besides the gas composition, the pressure and the sense wire diameter are additional parameters which can be used for optimizing the detector performance. In this respect, the relative width tends to increase with higher pressure and larger wire diameter [68]. For instance, the calculated relative width in P10 at $\overline{n} \approx 1000$ increases from $f \approx 0.70$ at $p = 1$ atm to $f \approx 0.75$ at $p = 2$ atm (the latter value being calculated with a Penning transfer efficiency $r = 0.232$ [50]). Using sense wires with a diameter of 50 μm (instead of 20 μm), one obtains for $\overline{n} \approx 1000$ a relative width $f \approx 0.77$ (at atmospheric pressure).

Experimental Data

The experimental data on avalanche statistics in wire-based chambers available in the literature are less comprehensive and conclusive than in case of parallel-plate counters. The first measurement of gain spectra was published by Curran et al. [78]. Using a cylindrical counter with a wire radius
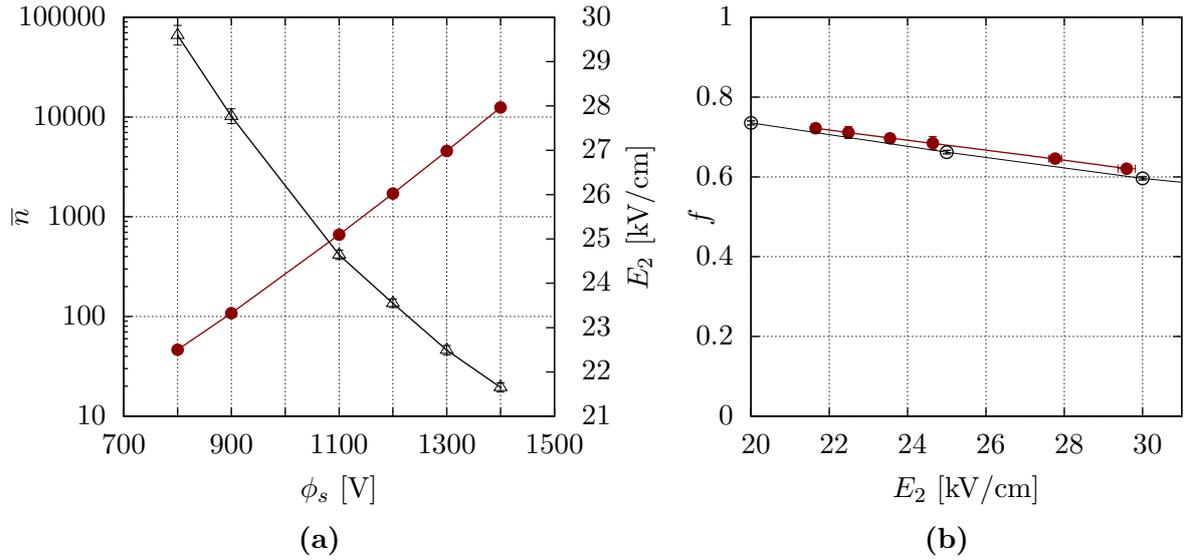
Figure 3.17. Left: mean gain $\overline{n}$ (red curve, left scale) and average electric field E_2 at which
multiplication sets in (black curve, right scale), as a function of the sense wire voltage ϕ_s
(calculation for pure argon in the wire chamber configuration shown in Fig. 3.15). Right:
relative width for Ar in the wire chamber configuration as a function of E_2 (red symbols),
and relative width for Ar in uniform fields as a function of the applied electric field (black
symbols).

of 76.2 μm (the outer diameter of the tube is not mentioned) filled with Ar/CH_4 (50:50), they
found at a mean gain of $\overline{n} \approx 1.5 \times 10^5$ a relative width $f \approx 0.68$. This value is roughly in line
with the above simulation results. A quantitative comparison is difficult however, because of
the high gain in the experiment, the unknown Penning transfer efficiency for this mixture, and
the uncertainty in the geometry of the device. Assuming a Penning transfer efficiency $r = 0.52$
(extrapolated from the fit function given in Ref. [50]), one obtains at $\overline{n} \approx 1.5 \times 10^4$ a calculated
relative width of about 0.8. Gold and Bennett [79] reported measurements in methane with an
admixture of 5% nitrogen, at pressures of 800 Torr and 400 Torr, using a proportional counter
with a wire diameter of 25.4 μm and an outer tube radius of ≈ 2.7 cm. The variation of the
relative width as a function of the mean gain found by these authors – for the counter operated at
800 Torr: decrease of the relative variance from $f \approx 1$ at $\overline{n} \approx 5 \times 10^3$ to $f \lesssim 0.55$ at $\overline{n} \approx 5 \times 10^5$ –
seems to be contradictory to the simulation results. The reason for this discrepancy is unclear. A
potential source of systematic error in the results given in Ref. [79] could be the extrapolation
procedure towards low avalanche sizes. The decrease of f towards high gain could also be caused
by space charge.

3.3.2. Angular Spread

In the wire chamber configuration shown in Fig. 3.15, ions created in the avalanche can drift
either towards the upper ($y = 2s$) or the lower ($y = 0$) ground plane, depending on the position
they are produced at, in particular the azimuthal angle φ (Fig. 3.15). On the lower plane, the
ion motion induces in the first case a bipolar signal with negative undershoot, whereas in the
second case the induced current has a positive sign.

The situation is similar in the readout chambers of the ALICE TPC [80], where the ions can end

up on the pad plane (below the sense wires), the cathode wires, or the gate wires. In a recent paper [81], S. Rossegger and W. Riegler showed that the shape of the average ion signal can be exploited for estimating the angular spread of avalanches in these chambers. Assuming that the ion starting points follow a Gaussian distribution in φ, they determined the value of the standard deviation σ_φ which gives the best agreement between the calculated and observed ion signal. In this way, an avalanche spread $\sigma_\varphi = 50 - 120$ degrees (increasing with the gain) was found [81].

We use this example for discussing the limitations of the present simulation technique with respect to the modelling of Penning transfer in terms of phenomenological transfer coefficients. The ALICE TPC is operated with $Ne/CO_2/N_2$ (85.7:9.5:4.8) which is a strong Penning mixture as all excited states of Ne are eligible for ionization of both CO_2 and N_2. Using an average transfer efficiency $r = 0.57 \pm 0.04$ (obtained from gain curve fits [67]) and assuming that excitation transfers happen "on the spot" (i. e. assuming that the distance between the point where an atom is excited and the point where a quencher molecule is subsequently ionized can be neglected), the microscopic tracking method gives a standard deviation $\sigma_\varphi \approx 33 - 37$ degrees of the angular distribution of ion starting points (with no significant dependence on the gain).

In order to explain the observed azimuthal spread, a spatial extent of Penning transfers, mediated by photons produced in the avalanche, would probably need to be taken into account. This conclusion is also supported by gain curve fits: best agreement is achieved by including a photon feedback term,

$$\overline{n} = \frac{\overline{n}_0}{1 - \beta \overline{n}_0},$$

with a feedback coefficient $\beta = 2 \times 10^{-5}$ [67].

An extended version of the microscopic tracking technique which includes coupled electron-photon transport is described in Chapter 5. Because of a lack of input data however, a detailed model capable of reproducing the measured spread in the above gas mixture could not be implemented yet.

3.4. Micropattern Gas Detectors

In the context of micropattern gas detector R&D, the topic of gas gain fluctuations has received renewed attention in recent years, in particular with respect to single electron detection applications.

3.4.1. Micromegas

Measurements of single electron spectra in a Micromegas with an amplification gap $d = 160$ µm have recently been published by T. Zerguerras et al. [82]. Neon, with an admixture of 5% isobutane, was used as filling gas (at a pressure of 1 bar). The relative width of the avalanche size distribution was determined by fitting the pulse height spectrum with a Pólya function. Results for different values of U_{mesh} – i. e. the potential difference between mesh and anode – are shown in Fig. 3.18. For $U_{\mathrm{mesh}} < 500$ V, a relative width $f \approx 0.31 \pm 0.02$ was measured. The increase of f observed for $U_{\mathrm{mesh}} \geq 500$ V was attributed to photon feedback [83].

The dominant source of uncertainty in the calculation of gain spectra for this gas mixture is given by the Penning transfer efficiency: as yet, no estimates for r in Ne/iC_4H_{10} from gain curve fits are available. As a first approximation, one can compute the relative width in a uniform
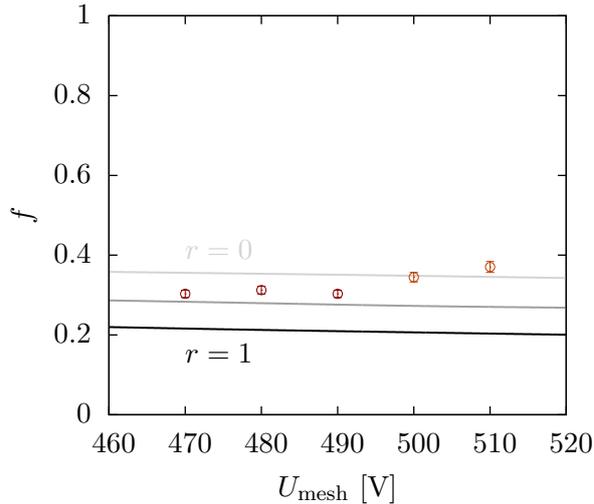
Figure 3.18 Relative width f of single electron gain spectra in Ne/iC$_4$H$_{10}$ (95:5). Circles: experimental results [82, 83], measured in a Micromegas with an amplification gap $d = 160$ µm, for different values of the mesh voltage U_{mesh} (at a drift field of 1 kV/cm). Lines: relative width in a uniform field $E_{\text{a}} = U_{\text{mesh}}/d$, calculated by means of microscopic tracking (using Penning transfer efficiencies $r = 0$, $r = 0.5$, and $r = 1$).

amplification field $E_{\text{a}} = U_{\text{mesh}}/d$. Compared to using a finite-element field map (which provides a more realistic representation of the electric field), this approach allows a much faster calculation and is thus more suitable for a "scan" of r.

Figure 3.18 shows the calculated values of f obtained using transfer efficiencies $r = 0$, $r = 0.5$, and $r = 1$. Since the electric field in the centre of the mesh hole is lower than E_{a}, one can expect the measured gain spectrum to be broader than predicted by the above calculation. Judging from Fig. 3.18, a transfer efficiency of about 50% seems plausible. With $r = 0.5$, a detailed simulation using a FEM field map (calculated with Ansys [36]) gives at $U_{\text{mesh}} = 470$ V a relative width $f \approx 0.34 \pm 0.04$, which is compatible with the experimental data.

The statistics of single electron avalanches in GridPix[1] detectors were investigated in the doctoral thesis of M. Chefdeville [85] and, subsequently, in the diploma thesis of M. Lupberger [86]. The latter effort was accompanied by simulations using Garfield++.

In both works, the same gas mixture, Ar/iC$_4$H$_{10}$ (95:5), was used. In Ref. [85], the relative width of the avalanche size distribution was estimated using an indirect method. Assuming that the gain spectrum can be described by a Pólya distribution, Eq. (3.6) allows one to determine the shape parameter θ from a measurement of the detection efficiency κ and the mean gain $\overline{n}$, provided that the threshold n_{t} and the electron transparency of the mesh are known.

In this way, an exponential shape (i. e. $\theta = 0$) of the avalanche size distribution could be excluded. The measured efficiency was stated to be compatible with a shape parameter $\theta \approx 2$. Using the same method, a similar result ($\theta > 0.5$) was found in Ref. [86]. In addition, a direct measurement of single electron spectra was attempted. The gain distribution measured at $U_{\text{mesh}} = 340$ V could be approximated by a Pólya function with shape parameter $\theta \approx 2.6$ (corresponding to $f \approx 0.28$). However, the result is subject to large systematic uncertainties. Sources of systematic uncertainty are the calibration curve relating "time-over-threshold" and charge (this function is non-linear at low gain and its parameters vary from pixel to pixel), charge sharing between pixels and a time-dependence of the gain (attributed to charging-up of the resistive layer [86]).

On the simulation side, the main source of uncertainty is the Penning transfer efficiency. For Ar/iC$_4$H$_{10}$ (90:10), Şahin et al. found $r = 0.40 \pm 0.01$ [50]. Adopting the same value for a 5%

---

[1] GridPix detectors are Micromegas-like devices (typically with an amplification gap of 50 µm, where a grid is deposited on top of a pixel chip by means of wafer post-processing techniques [84].
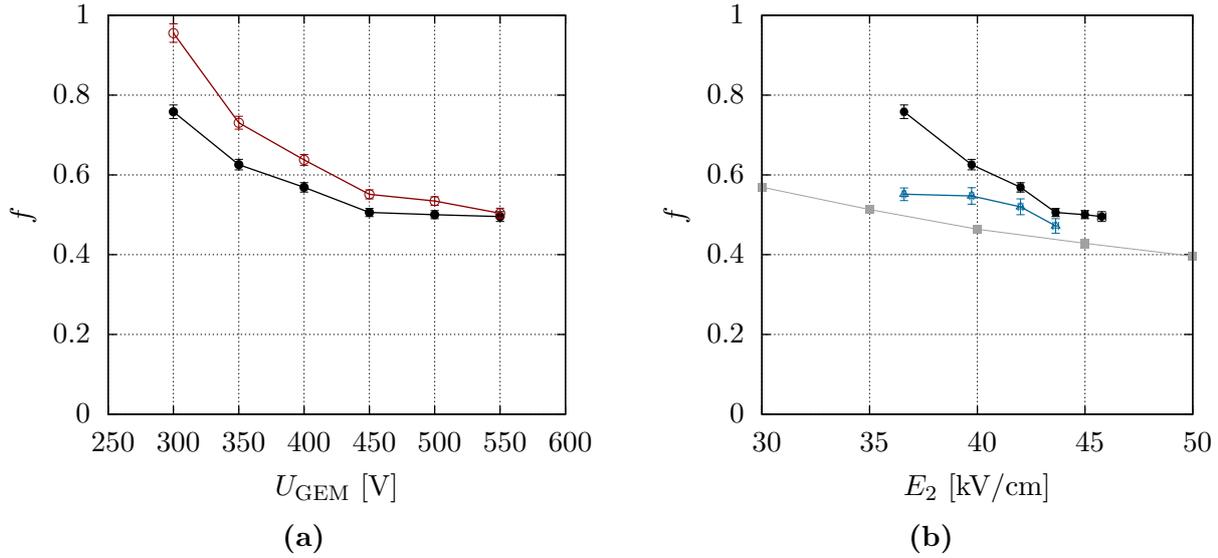
Figure 3.19. Relative variance in a standard GEM filled with Ar/CO_2 (90:10). Left: relative variance as function of the voltage difference U_{GEM} across the dielectric (full symbols: relative variance of the total gain; open symbols: relative variance of the effective gain). Right: relative variance as function of E_2 (mean electric field at which the first ionization occurs).

concentration of isobutane and using a finite element field map, one obtains at $U_{mesh} = 340$ V a calculated relative width $f \approx 0.24$.

3.4.2. GEMs

In this section, the statistics of single electron avalanches in a single GEM are discussed. For the following calculations the same simulation procedure as in Sec. 2.3.4 is used. As gas mixture we use Ar/CO_2 (90:10), assuming – as in previous calculations – a value of $r = 0.48$ for the Penning transfer efficiency.

We first consider the influence on the gain spectrum of the voltage difference U_{GEM} between the two electrodes of the foil. Fig. 3.19a shows the calculated relative variance as function of U_{GEM}, with the values of the drift field E_D and induction field E_I being kept fixed at $E_D = 1$ kV/cm, $E_I = 3$ kV/cm.

One usually distinguishes between the total gain $\overline{n}_{tot}$ which comprises all electrons produced in the avalanche and the effective gain $\overline{n}_{eff}$ which only includes electrons which traverse the GEM and arrive in the induction gap. The total and effective gain values corresponding to the GEM voltages covered by the simulation range from $\overline{n}_{tot} \approx 30.2$, $\overline{n}_{eff} \approx 11.7$ (at $U_{GEM} = 300$ V) to $\overline{n}_{tot} \approx 1.49 \times 10^4$, $\overline{n}_{eff} \approx 4.49 \times 10^3$ (at $U_{GEM} = 550$ V). Both the relative variance f_{tot} of the total gain spectrum and the relative variance f_{eff} of the effective gain spectrum decrease with increasing U_{GEM} (and thus increasing gain). At low gain f_{eff} is significantly higher than f_{tot}, but converges towards f_{tot} with increasing gain.

Based on the discussion in Sec. 3.3.1, one would expect the decrease of f as function of U_{GEM} to be paired with an increase of the mean electric field E_2 at which the first ionization occurs. This is indeed the case: according to the simulation E_2 increases from 36.6 ± 0.1 kV/cm at $U_{GEM} = 300$ V to 45.8 ± 0.2 kV/cm at $U_{GEM} = 550$ V. As can be seen from Fig. 3.19b, the relative

variance in the GEM is higher than in a uniform field of strength E_2 however. At $U_{\text{GEM}} = 450$ V (with corresponding $E_2 = 43.6$ kV/cm), for instance, one obtains $f_{\text{tot}} = 0.49 \pm 0.01$, compared to $f = 0.437 \pm 0.003$ calculated in a uniform field of 43.6 kV/cm. This is plausible as – unlike in parallel-plate or wire chambers – transverse diffusion plays a significant role for the avalanche evolution in a GEM.

- Losses of electrons to the dielectric, which can happen already at an early stage of the avalanche, give rise to additional size fluctuations. To quantify this effect we calculate the relative variance for avalanches in which no losses have occured in the upper cone of the GEM hole and compare it to the relative width obtained without such a cut. As can be seen from Fig. 3.19b the f value of avalanches without losses in the upper part is significantly closer to the relative variance in a uniform field of strength E_2.

- The region with highest ionization density in a GEM is in the vicinity of the interface between dielectric and lower metal layer [67], where the probability of losses to the dielectric is also high.

No systematic measurements of gain spectra in single GEMs could be found in the literature, such that a validation against experimental data is not possible in this case.

3.5. Summary

The microscopic tracking technique, introduced in Section 2.3.2, allows a quantitative prediction of gas gain fluctuations. Contrary to earlier avalanche models [68, 69], no simplifying assumptions concerning the shape of the ionization mean free path need to be made.

The impact of gas mixture and electric field on the avalanche size distribution (in particular the relative variance $f = \sigma^2/\overline{n}^2$) in uniform fields can be summarized as follows.

- As can intuitively be understood in terms of a simple toy model, the relative variance is to a large extent determined by the relative abundance of exciting and ionizing electron collisions. Molecular gases, characterized by significant inelastic absorption, tend to exhibit broader gain spectra compared to noble gases. Among noble gases, the relative variance is predicted to increase with the atomic number of the gas.

- Increasing the electric field and thus – at a fixed gap size – the mean gain, leads to an increase of the relative frequency of ionizing collisions and, therefore, a reduction of the relative variance.

- Penning transfer enhances the effective number of ionizing collisions and thus reduces the avalanche spread.

Within the systematic uncertainty of the calculation – which is determined mainly by uncertainties in the excitation cross-sections and the Penning transfer efficiencies – the simulation results are in agreement with measurements using parallel-plate chambers as well as recent experimental data for Micromegas-like detectors.

The simulation method can also be used for non-uniform field configurations. In wire chambers, the minimum value of f which can be achieved for a given gas mixture is larger than in homogeneous fields. Due to the specific shape of the electric field, the relative variance tends to increase with the mean gain. In GEMs the relative variance is predicted to decrease with increasing voltage difference across the foil.

4. Primary Ionization

In this chapter, we review some key parameters characterizing ionization fluctuations in gases and discuss the accuracy with which they can be computed from elementary physical data such as photoabsorption and electron scattering cross-sections.

4.1. Overview

A popular tool for the simulation of charged particle ionization in gas detectors is the program Heed[1] [88], written by I. Smirnov. The calculations in this chapter were done with the C++ version of Heed [89], to which an interface was made available in Garfield++. The previous (Fortran) version of Heed, which is integrated in (Fortran) Garfield, has been used for numerous detector studies in the past decade (some examples are given in Refs. [88, 90]).

As for the energy loss of the primary charged particle, Heed uses essentially the differential cross-section of the PAI model as formulated by Allison and Cobb [23] with a modification of the $1/E^2$ prefactor in the "Rutherford" term. By splitting the atomic photoabsorption cross-section into partial cross-sections for each subshell, simulating atomic relaxation effects (emission of fluorescence photons and Auger electrons), and tracking the emerging δ-electrons, the program allows a detailed calculation of ionization patterns.

The transport of δ-electrons in Heed is done in a phenomenological fashion: the number of "conduction electrons" (in this context: electrons with energy below the ionization threshold) generated at each step of a δ-track is sampled according to an algorithm (described in Ref. [88]) which reproduces the asymptotic W value and Fano factor F specified by the user. This approach has the merit of being generic, in that only the atomic composition of the material and the values of W and F need to be supplied. A drawback of this method, however, when used in conjunction with microscopic tracking, is that only the positions of the conduction electrons are provided, but not their energies. This limitation can be overcome by sampling the energy of the conduction electron from the equilibrium energy distribution at the local field. An alternative approach, which is explored here (Section 4.3), is to use the microscopic transport technique based on Magboltz directly for tracking the δ-electrons.

Combining energy loss sampling based on the PAI model and atomic relaxation simulation as implemented in Heed with microscopic transport of the emerging δ-electrons allows a full simulation of primary ionization in gases without free parameters other than photoabsorption cross-sections, atomic transition probabilities and electron scattering cross-sections.

---

[1] "**H**igh **E**nergy **E**lectro**d**ynamics"
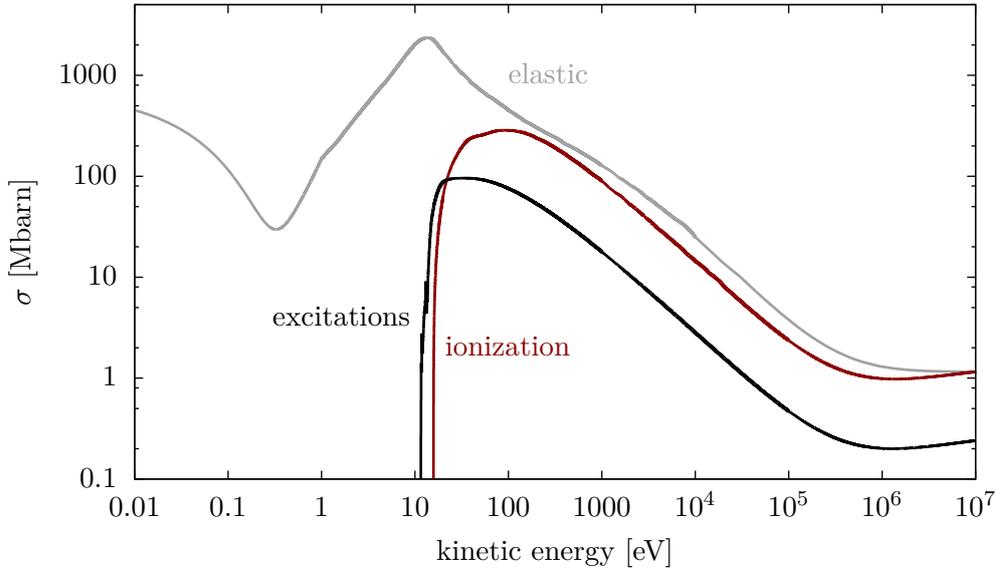
Figure 4.1. Elastic, ionization and total excitation cross-sections for electrons in Ar, as implemented in Magboltz 8.9. For the elastic cross-section at high energy ($\gtrsim$ MeV) values from Ref. [87] were added. Both ionization and excitation cross-sections exhibit a minimum around ≈ 1 MeV.

4.2. Cluster Density

The first observable we discuss is the so-called cluster density (sometimes also referred to as the "specific ionization"). It is equivalent to the inverse mean free path for ionization, $\lambda^{-1} = N\sigma_{\text{ion}}$. Unlike in case of the stopping power dE/dx, the measurement of λ^{-1} is independent of the energy calibration of the detector. The cluster density is, therefore, well suited for benchmarking purposes. Accurate calculations of λ^{-1} are also of practical importance. For instance, the probability $p_1 = 1 - \exp\left(-x/\lambda\right)$ for a particle to ionize at least once over a distance x sets an ultimate limit to the detection efficiency. This limit becomes relevant if the dimension of the detector is of the same order as the ionization mean free path λ. Let us consider, for example, a gas layer with a thickness of 1 mm, as in case of GOSSIP detectors [91]. In order to achieve an efficiency $p_1 > 0.99$, a cluster density $\lambda^{-1} > 46$ cm^{-1} would be required, which imposes a considerable restriction on the gas mixtures with which such a device can be operated.

4.2.1. Experimental Data

Total ionization cross-sections in the minimum-ionizing range can be measured by determining the inefficiency of a gas-filled counter operated at high gain ("0-counting method"). An extensive series of measurements based on this technique was conducted by Rieke and Prepejchal [92], using monoenergetic β rays with kinetic energies between 0.1 and 2.7 MeV. Their paper includes results for fourty counting gases, represented in the form of fit parameters M^2, C to the relativistic Bethe-Born cross-section

$$\sigma_{\text{ion}}\left(\epsilon\right) = 4\pi \left(\frac{\hbar}{m_e c}\right)^2 \frac{1}{\beta^2}\left[M^2\left(\ln\left(\beta^2\gamma^2\right) - \beta^2\right) + C\right]. \tag{4.1}$$

The parameters in this formula are the dipole moment (divided by a_0^2) M^2 and a constant C. These two variables are not mutually independent: according to theory [27], M^2 and C are

related by

$$C = M^2 \left(\ln \tilde{c} + \ln \frac{2 m_e c^2}{R} \right),$$

where both $\tilde{c}$ and M^2 are determined by the oscillator strength density.

The systematic error in the results, as estimated by Rieke and Prepejchal, is typically $3 - 5\%$ for M^2 and $\lesssim 0.5\%$ for C. Good agreement between experimental data and the Bethe-Born formula had already been found earlier by McClure [93], who measured ionization cross-sections in H_2, He, Ne, and Ar.

Results from more recent measurements for Ar and a number of organic gases, carried out by a group at Weizmann Institute, are reported in Ref. [94]. According to the authors, these data have an accuracy of -3/+5%, except for the measurement in Ar which has a larger systematic error.

4.2.2. Simulation Methods

In Magboltz/Imip[2] ionization cross-sections in the relativistic range are calculated using the Bethe-Born formula[3] (4.1). The parameters M^2 and C used in the program are based on a fitting procedure [46] matching experimental data in the keV range to the measurements of Rieke and Prepejchal [92] (within somewhat enlarged error bars) at MeV energies. For most gases, optical values given by Berkowitz [95, 96] have been used as a guide for adjusting the dipole moment M^2.

Given the transfer efficiencies r_j of each excitation level, the contribution of excitations to the cluster density in gas mixtures can be calculated using

$$\lambda_{\text{exc} \to \text{ion}}^{-1} (\epsilon) = N \sum_j r_j \sigma_j (\epsilon), \qquad (4.2)$$

where $\sigma_j (\epsilon)$ is the excitation cross-section for level j.

Excitation cross-sections for resonance transitions are calculated using

$$\sigma_j (\epsilon) = \sigma_j^{(\text{BB})} (\epsilon) \frac{\epsilon}{\epsilon + \epsilon_j + \epsilon_{\text{ion}}}; \qquad \sigma_j^{(\text{BB})} (\epsilon) = \frac{f_j}{\epsilon_j / R} 4\pi \left(\frac{\hbar}{m_e c} \right)^2 \frac{1}{\beta^2} \left(\ln \frac{m_e c^2 \beta^2 \gamma^2}{2 \epsilon_j} - \beta^2 \right).$$

At high energies, the excitation cross-section σ_j converges to the Bethe-Born cross-section $\sigma_j^{(\text{BB})}$. In this regime, the dipole-allowed excitation cross-sections scale essentially with f_j / ϵ_j, i. e. the oscillator strength divided by the excitation energy. Cross-sections for non-resonant excitations ($f_j = 0$) fall off more steeply with increasing energy and are thus negligible in the minimum-ionizing energy range. This is different from the situation in avalanches, where non-resonant transitions do constitute a sizeable fraction of the total excitation rate. In Ar/CO_2 (90:10), for instance, a simulation using the Magboltz cross-sections predicts that at a field of 60 kV/cm (atmospheric pressure) metastables contribute $\approx 13\%$ to the total excitation rate, 2p levels (Paschen notation) about 21%, and non-resonant 3d and 5s levels about 22%. It is, therefore,

---

[2]The "Imip" program is a spin-off of Magboltz, recently developed by S. Biagi. It is intended to be used for simulating electrons at minimum ionizing energy.

[3] The Bethe-Born expression can be extended to energies beyond the minimum-ionizing range by incorporating a density-effect correction in the transverse term,

$$\sigma_{\text{ion}} (\epsilon) = 4\pi \left(\frac{\hbar}{m_e c} \right)^2 \frac{1}{\beta^2} \left[M^2 \left(\ln \left(\beta^2 \gamma^2 \right) - \beta^2 - \delta_F \right) + C \right],$$

where the correction term δ_F is identical to the one appearing in the Bethe-Bloch formula (A.12).

not clear whether excitation transfer efficiencies determined from gain curve fits are directly applicable to cluster density calculations. Alternatively, the following estimates can be used.

- Assuming that excitation transfers proceed exclusively via photoabsorption, the transfer efficiency is given by

$$r_j = \eta\left(\epsilon_j\right), \tag{4.3}$$

  where η is the photo-ionization yield of the quenching gas.

- In the other limiting case that collisions constitute the only relevant deexcitation channel,

$$r_j = \eta\left(\epsilon_j\right)^{2/5} \tag{4.4}$$

  can be considered as an estimate for the upper limit of the transfer efficiency (see Sec. 5.2.3).

Based on the excitation cross-sections it is also possible to estimate the amount of primary scintillation produced in noble gases (at high pressure), assuming that each excited state gives rise to the emission of a VUV photon via excimer formation [47].

In Heed, the total ionization cross-section is calculated by numerical integration of $d\sigma/dE$ over the physically allowed range $\epsilon_{ion} < E < E_{max}$. The total cross-section depends sensitively on the underlying photo-ionization cross-section. By default, Heed relies for most elements on the compilation of atomic photoabsorption cross-sections by Henke et al. [17]. For hydrogen the parameterization given in Ref. [97] is used (with a modified scaling factor). The molecular photoabsorption cross-sections are approximated by the sum of the atomic cross-sections of the constituent elements. This approximation is justified at energies of the order of the inner shell binding energies and beyond but is rather problematic at low energies. Moreover, the molecular energy levels of the valence electrons are usually shifted with respect to the atomic levels. In order to correct for these effects, Heed allows the ionization thresholds ϵ_{ion} of the atomic photoabsorption cross-sections to be adjusted, depending on the molecule for which they are used. For example, carbon as a component of CF_4 is assigned a binding energy of 16.23 eV, while the binding energy of carbon in CO_2 is set to 13.79 eV. The choice of ϵ_{ion} is not straightforward, though, and represents a significant source of systematic bias in the calculation. For the present calculations, the original threshold values, as predefined by the author of Heed, were kept, except for N_2 where the outer shell binding energy was adjusted to 15.581 eV. An additional systematic error is introduced by approximating the photo-ionization cross-section by the total photoabsorption cross-section. Whereas the photo-ionization yield η of molecules is typically close to 100% from a few eV above the ionization threshold on, there is a significant difference between absorption and ionization in the near threshold region.

4.2.3. Results

For the purpose of comparison, the cluster density computed using Heed was fitted with the Bethe-Born formula in the range $1 < \beta\gamma < 6$. The values of M^2 and C extracted from the fit are presented in Table 4.1 for a number of frequently used gases[4], together with experimental data and the parameters used in Magboltz. Optical values for the dipole moment given in the books of Berkowitz [95, 96] are provided as well. The table also shows the number of clusters per cm for minimum ionizing electrons ($\beta\gamma = 3.5$), at room temperature (20° C) and atmospheric pressure, corresponding to the respective cross-section parameters.

---

[4] The table includes all gases for which at the time of writing high energy cross-sections were implemented in Magboltz.

For some of the gases (He, Ne, Ar, Xe, CO_2, CH_4), Rieke and Prepejchal [92] provide more than one set of fit parameters. In these cases, the values shown in Table 4.1 are those which were given the best "rating" (quality estimate) by the authors. For He, the values with H_2 as additive were adopted.

Noble Gases

As the photoabsorption cross-sections for the low Z atoms He and Ne are well known, the PAI model should give accurate results for these two gases. Both measurements in He were done with a small admixture of H_2. With an ionization threshold of 15.43 eV, H_2 is eligible for ionization by all excited states of He. According to Magboltz the total excitation cross-section in He at 1.4 MeV is ≈ 0.058 Mbarn, which is about 43% of the ionization cross-section calculated by Heed. Since at energies above ≈ 18 eV, the photo-ionization yield of H_2 is close to unity [95], the ionization efficiency in excitation transfers is also expected to be close to 100%. The result from Heed is thus consistent with the measurements if the measured cross-sections are interpreted as the sum of ionization and excitation cross-sections.

For Ne and Ar (and also H_2), the values reported by McClure are consistently higher than Rieke and Prepejchal's results which are corroborated by the spark-chamber measurement by Söchting [98], who found $n \approx 10.8 \pm 0.3$ for Ne, and the measurement by Malamud et al. [94], who found $n \approx 22.9 + 15\% / - 12\%$ for Ar. The reason for this discrepancy is unclear. In the case of Ne, the higher value measured by McClure might to some extent be due to Penning effects. A crude estimate[5] gives an upper limit for the increase of the cluster density due to excitations of about $1.1 - 1.2$ cm^{-1} for Ne/H_2. Excitation transfers are, however, not likely to play a role in Ar/H_2.

The Heed calculation for Ne agrees well with Rieke and Prepejchal's data. For Ar, two sets of Heed results are given, the first one being calculated with the (default) photoabsorption cross-sections [17], and the second one being calculated using the cross-sections compiled by Marr and West [100]. The cluster density according to Heed, $n \approx 25$, is close to McClure's result but larger than the experimental value of Rieke and Prepejchal ($n \approx 23$) which is reproduced by Magboltz. The Heed results for Kr and Xe are in agreement with the experimental data.

Molecular Gases

If the default photoabsorption cross-section is used, the cluster density for molecular hydrogen calculated by Heed (upper set of parameters in the table) exceeds the measured values by more than 60%. This is due the fact that in the default parameterization the (continuous) photoabsorption cross-section σ_γ is scaled by matching its integral to the TRK sum rule (A.8). In the case of H_2, however, this approach overestimates σ_γ substantially because of the large contribution to this sum ($\gtrsim 40\%$) from absorption below the ionization threshold. Using the original fit parameters given in Ref. [97] and extending this parameterization to the ionization threshold, one obtains the values given in the lower row. The calculation can be refined further by taking the detailed structure of σ_γ and η close to the threshold into account. Using the data compiled in Ref. [101] for the continuous photoabsorption cross-section, together with the photo-ionization yield from Ref. [99], and neglecting autoionization and discrete transitions above the ionization threshold, yields a cluster density of $n \approx 4$ cm^{-1}, which could be regarded as a lower bound to the calculation.

---

[5] $\sigma_{\mathrm{exc}} \left(\epsilon = 1.3 \text{ MeV} \right) = 0.0492$ Mbarn, $\sigma_{1s_2} \approx 0.64 \sigma_{\mathrm{exc}}$, $\eta \left(\epsilon_{1s_2} \right) \approx 0.9 - 0.95$ [99]

	He			Ne			Ar		
	M^2	C	n	M^2	C	n	M^2	C	n
Heed	0.505	5.829	3.4	1.65	18.17	10.5	3.86	43.945	25.5
							3.60	42.45	24.4
Magboltz	0.489	5.50	3.2	1.69	17.80	10.4	3.593	39.70	23
Rieke/Prepejchal	0.745	8.005	4.7	2.02	18.17	10.8	4.22	37.93	23
McClure	0.86	7.87	4.7	2.21	19.16	11.5	4.72	43.23	25.7
Berkowitz	0.4896			1.72			3.48		

	Kr			Xe			H_2		
	M^2	C	n	M^2	C	n	M^2	C	n
Heed	4.57	53.96	31	6.39	72.87	42.1	1.22	14.35	8.3
							0.857	10.1	5.8
Magboltz	5.50	56.90	33.3	8.04	75.25	44.6	0.642	8.30	4.7
Rieke/Prepejchal	6.09	52.38	31.5	8.04	72.35	43.2	0.695	8.115	4.7
McClure							0.706	8.64	5
Berkowitz	4.57			6.12			0.642		

	N_2			CO_2			CF_4		
	M^2	C	n	M^2	C	n	M^2	C	n
Heed	3.38	39.0	22.5	5.01	59.08	34	7.73	89.86	51.8
Magboltz	3.35	38.1	22	5.60	57.91	33.9	7.20	93.0	53
Rieke/Prepejchal	3.74	34.84	20.7	5.75	57.91	34	10.27	84.05	50.9
Berkowitz	3.36			5.42					

	CH_4			iC_4H_{10}		
	M^2	C	n	M^2	C	n
Heed	4.04	48.15	27.5	13.13	158.35	91
	3.46	41.79	24.0			
Magboltz	3.75	42.5	24.5	15.5	160.0	93.6
Rieke/Prepejchal	4.23	41.85	24.6	14.19	141.9	83.4
Berkowitz	3.76					
Malamud			25.9			91.5

Table 4.1. Measured and calculated parameters M^2, C of the Bethe-Born formula (4.1), and corresponding number of clusters per cm n at minimum ionizing energy ($\beta\gamma = 3.5$) and $T = 20°C$, $p = 760$ Torr.

In general, molecular photoabsorption cross-sections near the threshold exhibit a rather complicated structure with processes such as dissociation competing with photo-ionization. In this light, the close agreement for N_2, CO_2, and CF_4 between experimental data and Heed calculations (for which the atomic photoabsorption cross-sections were used), should be interpreted with a grain of salt. As an aside, it may be noted that the value for the specific ionization of CF_4 quoted in the PDG review [5], $n = 63$, is not corroborated by any of the calculations or measurements discussed here.

For the alkanes CH_4 and iC_4H_{10}, the Heed calculation is primarily biased by the choice of the hydrogen cross-section. The first set of values for CH_4 given in the table was calculated using the default settings. The set of parameters given in the second row was obtained by:

- modelling the hydrogen cross-section at low energies ($\epsilon < 80$ eV) as the difference between the molecular CH_4 cross-section (taken from Ref. [101]) and the atomic carbon cross-section,

- using the standard parameterization for hydrogen at higher energies, and

- scaling both carbon and hydrogen cross-sections by the ionization yield η (taken from Ref. [102]).

The cluster density resulting from this approach is in fair agreement with the measurement of Rieke and Prepejchal. It should be noted, though, that the experimental data also show significant scatter, with the cluster densities reported by Malamud et al. [94] being consistently higher than the measurements of Rieke and Prepejchal, not only in case of methane and isobutane but also for the other gases measured by both groups (C_2H_6, C_3H_8, and DME). The authors of Ref. [94] point out that for these gases the measurements by Rieke and Prepejchal were done in the proportional mode of amplification (as opposed to the Geiger mode), and that the detection efficiency could have been overestimated.

Gas Mixtures

Table 4.2 shows the cluster density in argon with 10% admixtures of carbon dioxide, methane, and isobutane as well as in neon with 10% admixtures of CO_2 and CH_4 calculated without and with excitation transfer. For the latter case, three values for λ^{-1} corresponding to different estimates of the transfer efficiencies are given. The values shown in column (a) were calculated with average transfer efficiencies extracted from gain curve fits ($r = 0.48$ for Ar/CO_2, $r = 0.212$ for Ar/CH_4, $r = 0.4$ for Ne/CO_2). For the calculation of the values given in columns (b) and (c), the transfer efficiencies were assumed to be given by Eqs. (4.3) and (4.4), respectively. In the above mixtures, the additional specific ionization due to excitation transfers represents a correction of order $\lesssim 10\%$.

4.3. Delta Electron Transport

4.3.1. Ionization Yield

The mean energy W required to produce an electron-ion pair and the Fano factor F for electrons are largely determined by the partitioning between exciting and ionizing collisions. While avalanche calculations (see Chapter 3) typically probe the excitation and ionization cross-sections up to a few tens of eV, W and F are sensitive to the cross-sections over the full energy range between the

Gas	λ^{-1} [cm^{-1}]			
	without excitation transfer	with excitation transfer		
		(a)	(b)	(c)
Ar/CO$_2$ (90:10)	24.1	25.6	26.2	26.6
Ar/CH$_4$ (90:10)	23.2	23.8	25.2	25.6
Ar/iC$_4$H$_{10}$ (90:10)	31.4	33.4		
Ne/CO$_2$ (90:10)	13.2	13.7	14.3	14.3
Ne/CH$_4$ (90:10)	12.3		13.4	13.4

Table 4.2. Calculated cluster density (at atmospheric pressure, 20° C) in argon and neon based mixtures.

ionization threshold and the primary electron energy, thus providing a complementary consistency check of the cross-section data.

The results presented in this section were obtained by tracing the primary δ-electron and the secondary electrons produced in the cascade by means of the microscopic tracking technique until the electron energy falls below the ionization threshold of the gas. The calculations were done at a uniform electric field of 100 V/cm (20° C, atmospheric pressure). Under these conditions, the Townsend coefficient is negligibly small such that the ionization cascade is unaffected by amplification in the electric field. Of the gases included in Magboltz, only the noble gases as well as the molecular gases H$_2$, N$_2$, CO$_2$, CF$_4$, CH$_4$, and iC$_4$H$_{10}$ (i. e. those already discussed in the previous section) are considered here. Since, on one hand, the ionization cross-sections for these gases used in Magboltz are consistent with measured cluster densities in the minimum-ionizing range, and, on the other hand, the Townsend coefficient (determined primarily by the excitation and ionization cross-sections) is supposed to be in good agreement with experimental data[6], a reliable description of the cross-sections also in the intermediate range can be expected.

After verifying that the calculated values of W and F for pure gases are consistent with experimental data, we discuss the influence of excitation transfer on ionization fluctuations in Penning mixtures.

Pure Gases

At primary electron energies ϵ_p in the keV range and above, W and F depend only weakly on ϵ_p. One, therefore, speaks of asymptotic W values and Fano factors. For most gases, these high energy values are fairly well established. A compilation of recommended average W values, based on experimental data until 1978, is given in ICRU report 31 [19]. Critical reviews of W values and Fano factors including also more recent data can be found in Ref. [103] and, with emphasis on noble gases, in Ref. [104]. The asymptotic W values for Ar, Kr, Xe, H$_2$, N$_2$, CO$_2$, CH$_4$, and iC$_4$H$_{10}$ recommended in Ref. [19] agree with the calculated values (between 1 keV and 10 keV) within about 3%. Systematic uncertainties in the calculation for CH$_4$, where the difference is largest, are discussed below. For He and Ne, the calculated W values are significantly higher than the experimental ones (calculated value for He at 5 keV: $\approx$ 46.3 eV, recommended experimental value [19]: 41.3 $\pm$ 0.1 eV). This is likely to be due to Penning effects [104]. No experimental data for the W value of electrons or photons in CF$_4$, and only one measurement for α particles

---

[6] With the exception of Kr, Xe, and isobutane, the gases under consideration are attributed a 5* rating in Magboltz. For this category, the Townsend coefficient is supposed to be reproduced within about 3% [46].

($W = 34.3$ eV [105], no error bars indicated) was found in the literature. A meaningful validation of the calculation ($W \approx 29.6$ eV at 5 keV) against experimental data is, therefore, not possible in this case. The value quoted in the PDG review [5], $W = 54$ eV, seems unrealistic.

Measurements of W as a function of the electron energy, especially at low energies ($\lesssim 1$ keV), allow the most direct validation of the calculations. Unfortunately, such measurements are scarce and, even worse, the existing data exhibit in many cases large differences. The lack of experimental data is, to some extent, probably due to the difficulties involved in the measurement which, for instance, requires a very high detection efficiency. For Ar, CH_4, N_2, and CO_2, where at least two independent sets of measurements were found in the literature, Fig. 4.2 shows a comparison of Magboltz based calculations (black bands) and experimental results:

- measurements by Combecher [106] (open circles),

- experimental data from Smith and Booz [107] (full circles),

- measurements by Waibel and Grosswendt [108–110] (open squares), and,

- for CH_4, W values inferred from measurements with photons by Krajcar-Bronić and coworkers [111] (triangles).

For comparison, the W values calculated with Heed are also included in the plot (grey bands). As mentioned above, the Heed algorithm is designed to reproduce a given asymptotic W value (for the present calculations the recommended ICRU values were used).

As can be seen from Fig. 4.2, Combecher's data do not converge towards the "canonical", asymptotic W values, which might be an indication for a systematic error in the measurement exceeding the quoted error bars. Below about 100 eV however, the W values measured by Combecher are in close agreement with the results obtained by Waibel and Grosswendt (where available). The latter data do exhibit the expected high-energy behaviour. We therefore consider these measurements as prime reference for the validation. The measurements by Smith and Booz are in clear disagreement with the other measurements, except at high energies. At low energies, these data are of limited significance because of the large error bars.

The calculated W value in Ar exhibits a bump around an energy of ≈ 1.7 times the ionization threshold, which is confirmed by Combecher's measurement. This feature can also be observed in the calculations for the other noble gases. The oscillatory structure in the calculated W value of methane is likely to be an artefact, though (see the discussion about systematic errors below).

Ignoring the low energy part of the data by Smith and Booz, one may conclude that for the above gases, given the spread of the experimental data and the estimated uncertainty in the calculation of about 5%, the sets of excitation and ionization cross-sections implemented in Magboltz allow a realistic calculation of the W value as function of the electron energy.

Little experimental data on the Fano factor for electrons, and virtually no measurements of its energy dependence, seem to exist [103, 104]. A validation of the calculations with respect to F is, therefore, difficult. For Ar, Kr, N_2, and CO_2 the values given in Refs. [103, 104] are higher than the high energy Fano factor calculated using the Magboltz cross-sections (see Fig. 4.3 for Ar), but are within the systematic uncertainty of the calculation ($\approx 10\%$).
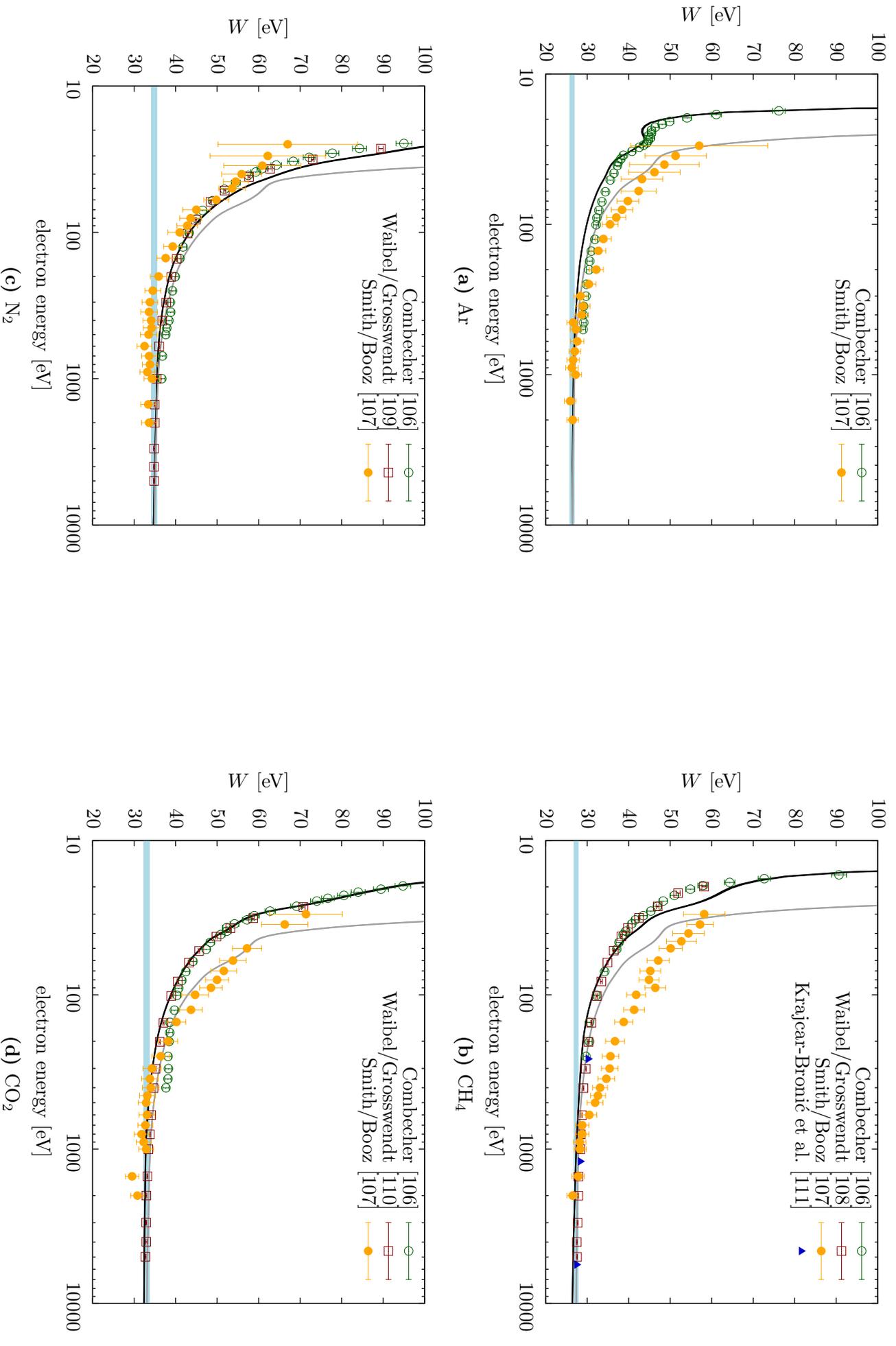
Figure 4.2. W values for electrons in Ar, CH$_4$, N$_2$, and CO$_2$ as functions of the electron energy. Light-blue bands: recommended asymptotic values from Ref. [19]; black lines: calculations based on Magboltz cross-sections; grey lines: calculations using Heed (W values taken from Ref. [19], $F = 0.19$). The line widths represent the statistical uncertainty of the calculations.
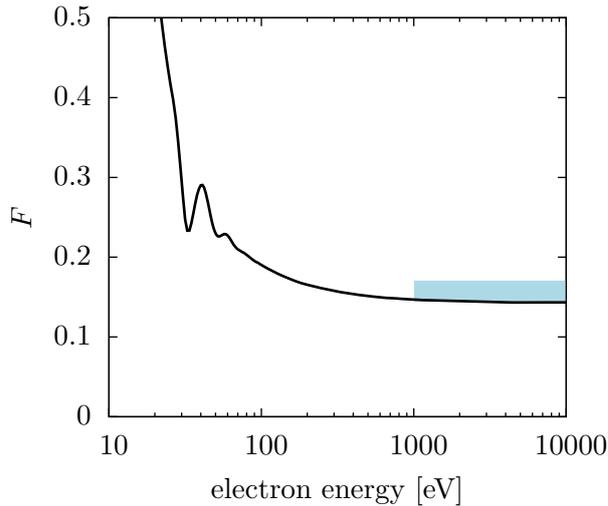
Figure 4.3 Fano factor as a function of the electron energy in argon. The black line represents calculated values based on the Magboltz cross-sections. The light-blue bar indicates the range of calculated and measured values for keV electrons ($0.145 \leq F \leq 0.17$) given in Refs. [103, 104].

Systematic Uncertainties

We try to quantify the systematic error in the calculation of W and F due to uncertainties in the excitation and ionization cross-sections and the approximations made in the modelling of these scattering processes exemplarily for the case of methane. We first estimate the effect of uncertainties in the total cross-sections by varying the excitation cross-sections which, in general, tend to be less accurately known than the ionization cross-section [46]. More precisely, we consider the dissociative excitation cross-sections. The sum of other excitation cross-sections included in Magboltz (such as those for light emission) amounts to less than 3% of the sum of the dissociative cross-sections.

The dissociative excitation cross-sections used in Magboltz are based on measurements of the total dissociation cross-section by Winters [112]. According to Fig. 6 in Ref. [112], these data have an uncertainty of about ±5% around 100 eV. Comparing the results of Winters with other measurements [113], one sees that the spread of the experimental data is of similar magnitude (typically $\approx 5 - 10\%$). We estimate the influence of an overall bias by applying a uniform scaling factor of ±10% to the excitation cross-sections above 30 eV. The cross-sections below this energy are left unchanged in order not to alter the Townsend coefficient. Such a scaling of the cross-sections leads to a change in W of $2 - 3\%$ and to a change in F above 100 eV of $\approx 5\%$.

In Magboltz, the dissociative excitation cross-section is subdivided into five levels with excitation energies of 8.55, 9, 10.5, 12, and 13.3 eV. The distribution of the cross-section among the invidual levels and the choice of the excitation energies is to some extent arbitrary and thus represents a further source of systematic bias. In addition, the energy loss of the electron should realistically be modelled by a continuous distribution. If – in order to obtain a crude estimate for the above effects – the energy loss in dissociative collisions is sampled uniformly between 8.55 and 13.3 eV (irrespective of the actual level hit by the electron), one observes at electron energies above 50 eV a reduction of the W value by between $\approx 2\%$ (at low energy) and $\lesssim 1\%$ (above 1 keV or so) and a reduction of the Fano factor by about $1 - 4\%$, Furthermore, the oscillations of the W value between 20 and 50 eV are considerably smoothed out.

The modelling of the differential ionization cross-section may also contribute to the systematic uncertainty. In order to estimate this effect we replace the Opal-Beaty formula (2.27) with the parameterization of the secondary electron energy distribution by Green and Sawada (2.28). While the difference in the resulting W value does not exceed the statistical fluctuations, the Fano factor in the keV range is altered by $2 - 3\%$.
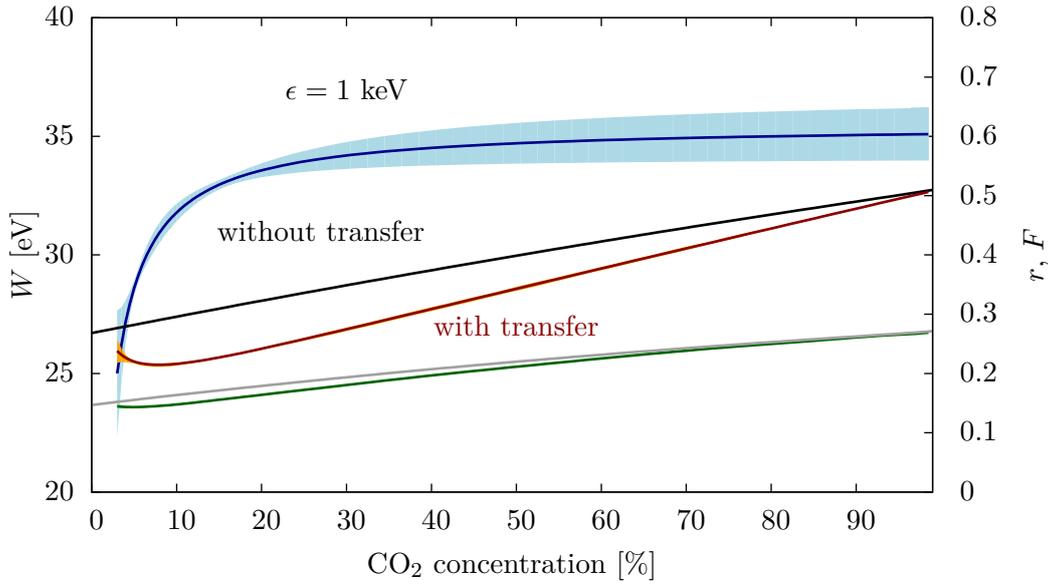
Figure 4.4. Calculated W value (left scale) and Fano factor (right scale) in Ar/CO_2 as functions of the CO_2 concentration. Black line: W value without Penning transfer, red line and orange band: W value with Penning transfer, band width indicating the uncertainty due to errors in the transfer efficiency. Grey line: Fano factor without Penning transfer, green line and error band: Fano factor with Penning transfer and its uncertainty due to errors in the transfer efficiency. Blue line and error band: transfer efficiency according to Ref. [50] and associated uncertainty (right-hand scale).

Excitation Transfer

In "regular" mixtures, i. e. gas mixtures without Penning transfers, the W value is, to good approximation, given by the mean of the W values in the pure gases, weighted by the respective concentrations. The same applies to the Fano factor.

In Penning mixtures however, excitation transfer can lead to a substantial reduction of W and F with respect to the pure gases. The lowering of W as a consequence of Penning transfers is known as Jesse effect [114]. It can be quantified as follows. Let W_0 be the hypothetical W value calculated without Penning transfers. If N_{ion} is the number of ionizing collisions occuring in the δ-electron cascade, $N_{\text{exc}}^{(j)}$ is the number of collisions leading to the excitation of a level j, and r_j is the associated transfer efficiency, the W value in the presence of Penning transfers, W', is given by

$$W' = W_0 \frac{1}{1 + \frac{1}{N_{\text{ion}}} \sum_j r_j N_{\text{exc}}^{(j)}}. \tag{4.5}$$

Hence, if the transfer efficiencies r_j are known (e. g. from gain fits), W' can easily be evaluated. Vice versa, if measurements of W' are available, the (overall) transfer efficiency can be extracted from (4.5).

We discuss the influence of Penning transfers on W and F exemplarily for the case of Ar/CO_2. This choice is motivated by two facts:

- as discussed above, the experimental W values for these gases are correctly reproduced by the Magboltz cross-sections;

- a fit formula for the overall transfer efficiency r as a function of the CO_2 concentration c extracted from gain measurements [50] is available,

$$r\left(c\right) = \frac{a_1 c + a_3}{c + a_2}. \tag{4.6}$$

Figure 4.4 shows the transfer efficiency r according to (4.6) with fit parameters $a_1 = 0.620 \pm 0.057$, $a_2 = 0.008 \pm 0.034$, $a_3 = -0.011 \pm 0.009$ [50, 67] and the resulting W value and Fano factor at a primary electron energy of 1 keV. The fit is based on gain measurements for CO_2 concentrations down to 5%. At smaller concentrations, the uncertainty of the above parameterization of the transfer efficiency diverges rapidly. The calculations were, therefore, restricted to $c > 0.03$.

As can be seen from Fig. 4.4, the W value displays a minimum $W_{\min} \approx 25.3 \pm 0.1$ at a concentration $c_{\min} \approx 0.08 \pm 0.005$. A minimum of W at low admixture concentrations is a typical feature of Penning mixtures since the transfer efficiency r tends to rise with increasing concentration [50] while the relative abundance of excitations with respect to ionizing collisions decreases.

The calculated Fano factor in the Ar/CO_2 mixture is also significantly reduced, with a minimum at $c_{\min} \approx 0.05$.

Systematic measurements of W in binary gas mixtures seem to have been published only for α particles. Experimental data for Ar/CO_2 (and a large number of other gas mixtures) were reported by Bortner and coworkers [115], who found a minimum W value of $W_{\min} = 26.05$ eV at a concentration of 4.5% CO_2 (no error estimate given). The larger value of $W_{\min}$ with respect to the calculation is not too surprising considering that the W value for α particles in pure CO_2 is also higher than the one for electrons or photons. The difference between this measurement and the above calculation might thus to some extent be explained by the different type of primary particle. One also has to keep in mind that the transfer efficiency used in the calculation is an average over the transfer efficiencies of several levels which might give rise to a systematic error inasmuch as the relative abundances of the individual excitation levels in high energy δ-electron cascades are different from those in avalanches. As the transfer efficiency is, in general, pressure-dependent, the lower pressure (500 Torr) used in the experiment might also play a role.

4.3.2. Range

The spatial distribution of the secondary ionization produced by a δ-electron is a key factor to be considered when assessing the position resolution of a detector. It can be characterized in terms of the electron range, i. e. the typical pathlength travelled by a δ-electron before its energy falls below the ionization threshold. In the literature, a number of different definitions of "range" exist. In the following, we consider the so-called fractional ionization range R^x, which is defined as the projected distance along the initial δ-electron direction within which the percentage x of the total ionization is produced (cf. Ref. [108]).

Figure 4.5a shows the 95% range in CH_4 as function of the primary electron energy according to measurements by Waibel and Grosswendt [108], together with calculated values using the Heed δ-electron transport algorithm and the microscopic tracking technique. The calculations were done by simulating 10^6 primary δ-electrons starting from $z = 0$ with initial direction $(0, 0, 1)$ and histogramming the z coordinates of the ionizing collisions in the energy degradation cascade. An example of the resulting distribution (for a 1 keV electron in methane) is shown in Fig. 4.5b. In line with the experimental setup described in Ref. [108], the tracking of an electron is stopped if it is backscattered behind the $z = 0$ plane.
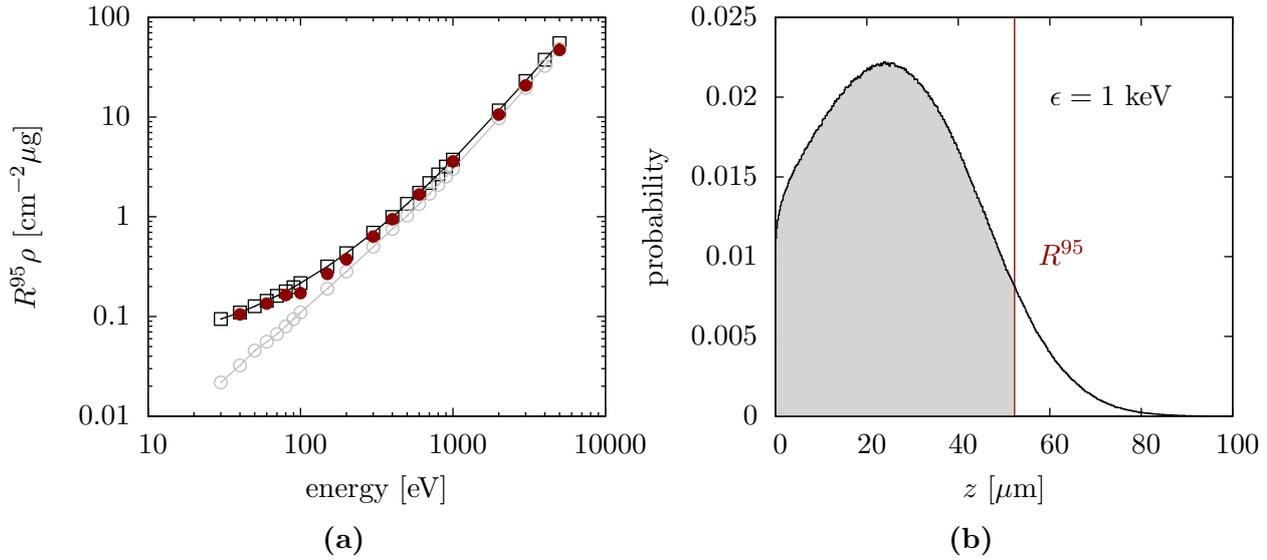
Figure 4.5. Left: fractional ionization range R^{95} scaled by the mass density ρ in methane (red symbols: experimental data [108]; black symbols: calculation based on Magboltz cross-sections; grey symbols: calculation using Heed). Right: distribution of the z-coordinates of ionizations created by a 1 keV δ-electron track (initial direction $\parallel$ z-axis) and its secondaries in methane (at atmospheric pressure), calculated using microscopic tracking. The red line indicates the 95% fractional ionization range.

Heed uses a multiple-scattering scheme [88]: the δ-electron is propagated in fixed distance steps, after each of which the trajectory is rotated. In the microscopic transport method, the direction is updated[7] after every collision. The latter technique, therefore, gives better agreement with experimental data at low energies. In particular, the energy dependence of R^{95} is correctly reproduced. The values calculated using microscopic tracking agree with the measurement to within 10%, except for the datapoints at 5 keV and between 100 and 200 eV. The agreement between experimental data and Heed results improves with increasing energy, for $\epsilon > 500$ eV the calculated values differ from the measured ones by $< 20\%$.

The Heed and Magboltz calculation results for N_2 and CO_2 exhibit a similar level of agreement with measurements [109, 110]. Experimental data for other counting gases – with an accuracy comparable to those by Waibel and Grosswendt – could not be found. Judging from the limited available data, both calculation methods (Heed and Magboltz-based microscopic tracking) seem to provide a realistic account of the spatial extent of ionization by δ-electrons.

---

[7]For most collision processes, the scattering angle is sampled from a screened Rutherford distribution,

$$\frac{\mathrm{d}\sigma}{\mathrm{d}\left(\cos\theta\right)} \propto \frac{1}{2}\frac{1-\chi^2}{\left(1-\chi\cos\theta\right)^2},$$

where the parameter χ is tuned based on the transport cross-section.

4.4. Summary

In atomic gases, the total ionization cross-section calculated by means of the PAI model as implemented in Heed is within the spread of the experimental data. In Sec. 4.2 it was shown that by taking molecular effects in the photoabsorption cross-section into account a similar level of accuracy can also be achieved for molecular gases. If the photoabsorption cross-section of complex gases is approximated by the sum of atomic cross-sections however, the predictive power of the calculation is limited and ad-hoc tuning (e. g. of binding energies) is necessary to obtain agreement with measurements.

Using the electron cross-sections for excitation and ionization available in the Magboltz database, the effect of excitation transfer on the cluster density in gas mixtures can be estimated.

The microscopic tracking technique allows a detailed calculation of δ electron transport properties (including their energy dependence) such as W value, Fano factor, and range. For pure gases, the uncertainty of the ionization yield calculations, dominated by uncertainties in the excitation and ionization cross-sections, is about $\pm 5\%$ for W and about 10% for F. The method is particularly valuable for Penning mixtures, where linear interpolation of W and F between pure gas values is not applicable.

5. Deexcitation Processes

In the calculations discussed above, we have modelled Penning effects in terms of an empirical transfer efficiency. In this chapter, we try to go a step further and explore the feasibility of simulating deexcitation processes on a microscopic level.

5.1. Overview

5.1.1. Motivation

The maximum gain achievable in a gas detector before breakdown occurs has so far eluded quantitative predictability. A plausible explanation for the onset of discharges is that VUV photons resulting from the decay of noble gas atoms escape the confinements of the "primary" avalanche and initiate a chain of secondary avalanches. A detailed deexcitation simulation could be useful for understanding the relevance of the above mechanism with respect to breakdown.

As shown in Ref. [50], determining the dependence of the average transfer efficiency r on the gas pressure p and the quencher concentration c from gain curves is possible but requires a large set of gain measurements. In a "microscopic" deexcitation simulation, the pressure and concentration dependence of Penning ionization should emerge naturally.

5.1.2. Description of the Model

For the purpose of simulating deexcitation processes, the microscopic tracking method was extended by: (1) modelling of the decay processes following the production of an excited state and (2) transport of the photons produced in the deexcitation cascade.

A schematic overview of the steps involved in the simulation is given in Fig. 5.1. Let us assume that, as a consequence of an electron collision, a noble gas atom has been promoted to an excited state k. The time Δt after which the excited level decays is exponentially distributed and thus sampled according to $\Delta t = -\tau_k \ln u$, where τ_k is the total lifetime of the level and $u \in (0, 1]$ is a uniform random variate. The competing deexcitation processes are (1) spontaneous decay under emission of a photon, and (2) excitation transfer induced by a collision of the excited atom with another atom or molecule.

If the final state of the radiative decay is another, energetically lower lying excited state, the energy $\hbar\omega \approx \epsilon_k - \epsilon_i$ of the emitted photon is (in case of argon) below the absorption threshold of all relevant quenching gases. These photons are, therefore, not tracked in the simulation. The deexcitation cascade then proceeds with the state ϵ_i.

If the excited level decays directly to the ground state, a photon with energy $\hbar\omega \approx \epsilon_k$ is emitted. After an (exponentially distributed) free flight step, the photon is absorbed either by the same resonance line of the noble gas atom or by a quencher molecule. In the latter case, with a probability given by the photo-ionization yield η, a new electron can be produced, which is added
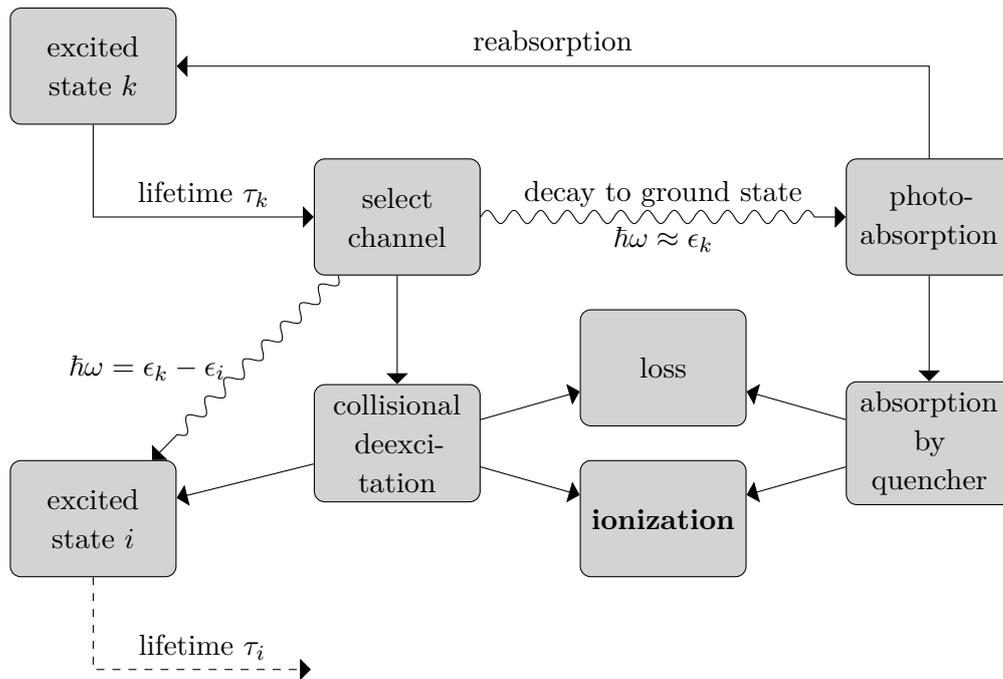
Figure 5.1. Schematic flowchart of the deexcitation model.

to the stack of electrons to be transported. In case of reabsorption, the deexcitation sequence is repeated (we assume that the directions of absorbed and emitted photon are uncorrelated). Since the photoabsorption cross-section of the resonance line typically exceeds the photoabsorption cross-section of the quencher, the cycle of emission and re-absorption may recur many times before the photon is eventually absorbed by the quencher or has diffused to the walls.

5.2. Atomic Data

In order to compile the data necessary for implementing the simulation method described above, a literature survey was conducted, the results of which are presented in this section. In the following, we consider mixtures of argon with the quenching gases methane, ethane, acetylene, and carbon dioxide. This selection is based on the availability of experimental data for transfer efficiencies [50].

5.2.1. Excitation Cross-Sections

The pathway towards a microscopic description of deexcitation processes in noble gases was opened up by recent upgrades of the Magboltz database with respect to the modelling of excitation cross-sections. As mentioned in Section 2.3.1, Magboltz includes since version 8.6 separate cross-sections for 44 Ar excitation levels, which had previously been lumped together to three terms. The energetically lowest levels, which are also the most frequently excited ones, are the four states with configuration $3p^5 4s$ (in Paschen notation: $1s_5$, $1s_4$, $1s_3$, and $1s_2$). Two of these levels, $1s_5$ ($J = 2$) at 11.55 eV and $1s_3$ ($J = 0$) at 11.72 eV, are metastable since electric dipole transitions to the ground state are forbidden. Of the radiative 4s states ($1s_4$ at 11.62 eV and $1s_2$ at 11.83 eV), the energetically higher level is the stronger one, as can be seen from Fig. 5.2.

The ten 4p levels (in Paschen notation: $2p_{10} - 2p_1$) have energies between 12.91 and 13.48 eV. For reasons of readability, Fig. 5.2 shows only the sum of their cross-sections.
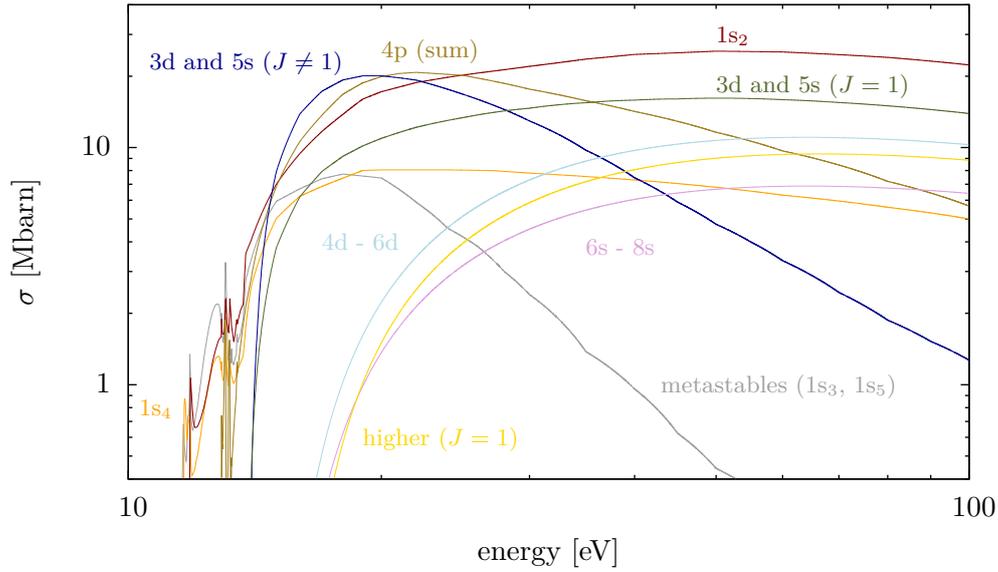
Figure 5.2. Electron excitation cross-sections in argon, as implemented in Magboltz 8.9.

The 3d levels, which have energies between 13.85 and 14.3 eV, overlap with the 5s levels at about 14.1 eV and 14.25 eV. In Fig. 5.2, the 3d and 5s cross-sections are grouped into resonant ($J = 1$) and non-resonant ($J \neq 1$) levels.

Of the higher excited states, Magboltz includes only resonant ns and nd levels. Up to 8s and 6d, respectively, separate cross-sections for the individual levels are implemented. The higher levels are combined to an artificial cross-section term with a threshold of 15.66 eV (labelled "higher" in Fig. 5.2).

5.2.2. Radiative Decay

The strength of an optical transition between two levels k and i is characterized by the transition rate A_{ki}, i. e. the probability per unit time for the level k to decay spontaneously to a lower level i. The total radiative lifetime τ_k is, consequently, given by

$$\tau_k = 1/\sum_i A_{ki},$$

where the sum extends over all allowed final levels. Another frequently used measure of the intensity of an atomic transition is the oscillator strength f_{ik}, which is related to A_{ki} by [116]

$$A_{ki} = \frac{2\alpha_f}{\hbar m_e c^2} \frac{g_k}{g_i} \left(\epsilon_k - \epsilon_i\right)^2 f_{ik},$$

with $g_{i,k} = 2J_{i,k} + 1$ being the statistical weights of the two levels involved.

Where available, we have adopted the A_{ki} values given in the NIST Atomic Spectra Database [117]. Theoretical values calculated by Zatsarinny and Bartschat [118] have been used for a number of 3d – 4p transitions not covered by the NIST compilation. For most of the resonance levels, the decay to the ground state is not included in the NIST database either. In these cases, transition rates corresponding to the f values recommended by Berkowitz [95], and, for the highest levels ($\epsilon > 15.3$ eV), where no other published data seem to exist, the oscillator strengths calculated by Lee and Lu [119], have been used.

Tables of the transition rates implemented in the simulation are given in Appendix A.3. For the Magboltz cross-section term with a threshold of 15.66 eV, a special sequence is followed. If this level is excited, the excitation is reallocated with equal probability to one of the five nearest states ($6d_2$, $5s_4$, $4s_2$, $5s_1'$, and $6d_5$) and the deexcitation cascade of the thus selected level is followed.

Emission and Absorption Lines

The integral photoabsorption cross-section σ_0 of a resonance line is given by [116]

$$\sigma_0 = \frac{2\pi^2 \alpha_f (\hbar c)^2}{m_e c^2} f,$$

where f is the oscillator strength of the respective line. For calculating σ_0 we use f values (listed in Table A.1) consistent with the transition rates for emission.

The absorption probability for a photon with energy $\hbar\omega$ is determined by the energy-dependent photoabsorption cross-section

$$\sigma (\hbar\omega) = \sigma_0 \phi (\hbar\omega),$$

where $\phi (\hbar\omega)$ denotes the so-called lineshape function with normalization

$$\int_{-\infty}^{\infty} \mathrm{d} (\hbar\omega) \, \phi (\hbar\omega) = 1.$$

The emission spectrum of a line is assumed to be described by the same lineshape function as the absorption probability. The shape of $\phi (\hbar\omega)$ depends on the physical processes which are responsible for the broadening.

- Natural broadening is a consequence of the finite lifetime of an excited state which, according to Heisenberg's uncertainty relation, implies an uncertainty in the energy of the level. The natural lineshape follows a Lorentzian

$$\phi_{\mathrm{nat}} (\hbar\omega) = \frac{1}{\pi} \frac{\Gamma_{\mathrm{nat}}/2}{(\hbar\omega - \hbar\omega_0)^2 + (\Gamma_{\mathrm{nat}}/2)^2},$$

  with a full width at half-maximum (FWHM) $\Gamma_{\mathrm{nat}} = \hbar/\tau$. For the $1s_4$ and $1s_2$ lines of Ar, the natural linewidth is of order 10^{-7} eV, which (under normal conditions) is negligibly small compared to the other broadening mechanisms discussed below. Natural broadening was, therefore, not taken into account in the simulation.

- Doppler broadening, caused by the relative motion of atoms in the gas, leads to a Gaussian lineshape [120]

$$\phi_D (\hbar\omega) = \frac{1}{\sqrt{2\pi\sigma_D^2}} \mathrm{e}^{-\frac{(\hbar\omega - \hbar\omega_0)^2}{2\sigma_D^2}}$$

  with standard deviation

$$\sigma_D = \hbar\omega_0 \sqrt{\frac{k_B T}{Mc^2}} \tag{5.1}$$

  and FWHM $\Gamma_D = 2\sigma_D \sqrt{2\ln 2}$. At room temperature, one obtains for Ar a linewidth (FWHM) of about $2 - 3 \times 10^{-5}$ eV.

- Pressure broadening is caused by collisions of an excited atom with its neighbours. For radiative lines, resonance broadening is in weakly ionized gases the dominant mechanism of this kind. It is caused by energy transfer between a resonant state and the surrounding ground state atoms of the same species [120]. The line profile due to pressure broadening is to good aproximation described by a Lorentzian. The full width at half maximum due to resonance broadening is of the form

$$\Gamma_{\text{res}} = 2k \frac{\alpha_f (\hbar c)^3}{m_e c^2 \hbar \omega_0} fN, \tag{5.2}$$

where N is the density of ground state atoms. The values of the prefactor k given in the literature exhibit some scatter. We adopt the value proposed by Ali and Griem [121, 122], $k = 1.92\pi/\sqrt{3}$. For pure Ar (at atmospheric pressure, $T = 20°$ C), one obtains for the $1s_2$ line a width $\Gamma_{\text{res}} \approx 4 \times 10^{-4}$ eV.

The combined effects of pressure broadening and Doppler broadening lead to a so-called Voigt profile, which is a convolution of a Gaussian and a Lorentzian. Let σ_D^2 be the variance of the (Gaussian) lineshape when only Doppler broadening is present, and Γ_{res} be the FWHM of the Lorentzian in case of pure resonance broadening. In terms of the reduced frequency $x = (\hbar\omega - \hbar\omega_0) / (\sqrt{2}\sigma_D)$, the Voigt lineshape is given by (see e. g. Ref. [123])

$$\phi_V(x) = \frac{a_V}{\pi} \int_{-\infty}^{\infty} du \frac{e^{-u^2}}{(x-u)^2 + a_V^2}, \qquad a_V = \frac{\Gamma_{\text{res}}/2}{\sqrt{2}\sigma_D}.$$

The shape of the profile is controlled by the Voigt parameter a_V. For the implementation in a Monte Carlo simulation, we need to be able to draw random numbers from this distribution. The following recipe (see e. g. Ref. [123] and references therein) is used: if x_L is a Lorentzian random variate with $\Gamma/2 = a_V$, and x_G is a Gaussian random variate with $\sigma = 1/\sqrt{2}$, the reduced frequency $x_V = x_L + x_G$ is distributed according to a Voigt profile with shape parameter a_V. For the evaluation of the Voigt function itself, which is needed for the calculation of the absorption mean free path, the implementation in ROOT [124], `TMath::Voigt`, is used.

In order to avoid unphysically large deviations of the emitted photon energy with respect to the line centre, the line shape function is cut off at the wings such that

$$\phi(\hbar\omega) = \begin{cases} \phi_V(\hbar\omega), & |\hbar\omega - \hbar\omega_0| < \Delta(\hbar\omega)_{\text{max}} \\ 0, & \text{else} \end{cases}.$$

Photoabsorption and Photoionization

The photoabsorption cross-sections for CO_2, CH_4, C_2H_6, and C_2H_2 (shown in Fig. 5.3) were taken from the compilation by Berkowitz [95] and a recent report by Sakamoto et al. [101] based thereon. Ionization yield data were taken from Ref. [102] (methane and ethane), Ref. [125] (acetylene), and Ref. [126] (carbon dioxide).

5.2.3. Collisional Deexcitation

Collisions with Quencher Molecules

A compilation of rate constants for 4s and 4p levels of argon used in the simulation is given in Table 5.1.

Figure 5.3 Photoabsorption cross-section σ_γ of carbon dioxide, methane, ethane, and acetylene [95, 101]. Grey lines indicate resonance levels of argon.
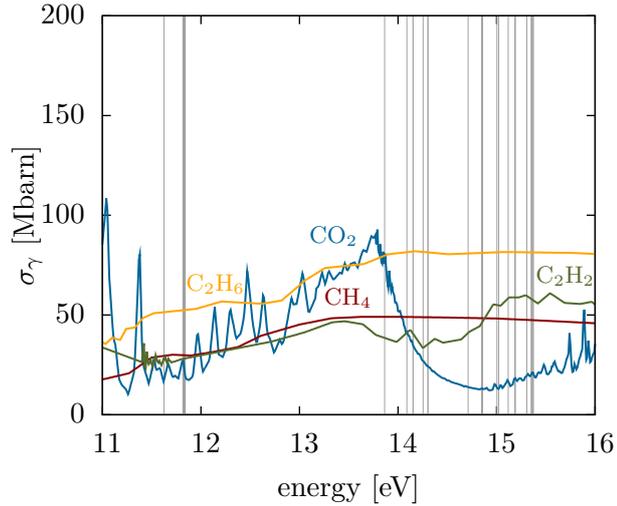
metastable 4s levels A comprehensive set of experimental data for a large number of quencher gases was published by Velazco et al. [127]. In addition to their own measurements, the authors also included a compilation of earlier results from other groups in their paper. The rate constants for CO_2 and C_2H_2 are taken from Table I of Ref. [127] (in case of acetylene, the value for the $1s_5$ level was adopted also for the $1s_3$ level).

For the quenching of $1s_5$ by isobutane, the rate constant given in Ref. [128] is used. Since this value is very close to the one for n-butane, we take the n-butane value for $1s_3$ given in Ref. [127] as an approximation for iC_4H_{10}.

For CH_4 and C_2H_6, the rate constants are taken from the set of measurements reported by Chen and Setser [129]. Except for methane, these values are in good agreement with the earlier data of Velazco et al. [127].

The uncertainty in the rate constants can be estimated to be about $10 - 20\%$ [127, 129].

radiative 4s levels The rate constants for CO_2, CH_4, C_2H_6, and C_2H_2 are taken from Table II in Ref. [127]. For iC_4H_{10} the values given in Table IV of Ref. [128] are used.

4p levels Measurements of quenching rate constants for $2p_8$, $2p_6$, $2p_5$, and $2p_1$ (Paschen notation) were reported by Sadeghi et al. [130]. For the other 4p levels, no experimental data seem to be available. We use the average of the experimentally known levels as an estimate for these rate constants.

For the higher levels, no measured rate constants could be found in the literature. In order to estimate the rate constants of resonance levels, the Watanabe-Katsuura formula [131],

$$k_M \left[\text{cm}^3/\text{s} \right] = 2.591 \times 10^{-10} \left(\frac{R^2}{\epsilon_i^2} f_i \frac{\sigma_\gamma \left(\epsilon_i \right)}{2\pi^2 \alpha_f a_0^2} \right)^{2/5} \left(\frac{T}{\mu_r} \right)^{3/10}, \tag{5.3}$$

can be used, where μ_r is the reduced mass of argon atom and quencher molecule. For the remaining (non-radiative) levels, an order-of-magnitude estimate of the rate constant can be obtained using

$$k_M = \sigma_{\text{HS}} \overline{v}, \tag{5.4}$$

where

$$\sigma_{\text{HS}} = \left(r_{\text{Ar}^\star} + r_M \right)^2 \pi,$$

label	level energy [eV]	rate constant [10^{-19} cm^3 ns^{-1}]				
		CO$_2$	CH$_4$	C$_2$H$_6$	iC$_4$H$_{10}$	C$_2$H$_2$
1s$_5$	11.548	5.3	4.55	5.29	7.1	5.6
1s$_4$	11.624	5.0	4.5	6.2	6.1	4.6
1s$_3$	11.723	5.9	5.30	6.53	8.5	5.6
1s$_2$	11.828	7.4	5.7	10.7	11.0	8.7
2p$_8$	13.095	6.4	7.4	9.2		5.0
2p$_6$	13.172	6.1	3.4	4.8		5.7
2p$_5$	13.273	6.6	6.0	9.9		6.0
2p$_1$	13.480	6.2	9.3	11.0		5.3

Table 5.1. Rate constants for collisional quenching of Ar excited levels by carbon dioxide, methane, ethane, isobutane, and acetylene [127–130].

gas	ionization threshold [eV]	diameter [pm]
CO$_2$	13.78	330
CH$_4$	12.65	380
C$_2$H$_6$	11.52	390
iC$_4$H$_{10}$	10.67	500
C$_2$H$_2$	11.0	330

Table 5.2 Ionization potentials and kinetic diameters [134] of quenching gases.

with r_M being the radius of the quencher molecule, is the "hard sphere" collision cross-section and

$$\overline{v} = \sqrt{\frac{8k_B T}{\pi \mu_r}}$$

is the average thermal (relative) velocity. For the radii of excited argon atoms we use calculated values given in Ref. [132]: $r_{3d} = 436$ pm, $r_{5s} = 635$ pm.

Ionization Yield

The above rate constants describe the total probability for collisional quenching, both ionizing and non-ionizing. Branching ratios for quenching of metastables by C$_2$H$_2$ have been reported in Ref. [133]. Two estimates are given: 0.61 ± 0.14 and 0.74 ± 0.07. For other levels and quenchers, one can estimate the fraction of deexciting collisions leading to ionization of the quencher molecule based on (5.3) as

$$k_{M^+}/k_M \approx \eta \left(\epsilon_i\right)^{2/5}.$$

Collisional Self-Quenching

Collisions with ground state Ar atoms can give rise to population transfer between levels of the same multiplet (collisional mixing) or to excitation transfer to an energetically lower lying excited state.

metastable 4s levels Kolts and Setser [135] reported two-body rate constants $k = 2.1 \pm 0.3 \times 10^{-24}$ cm^3 ns^{-1} for the deactivation of 1s^5 levels and $k = 5.3 \pm 0.9 \times 10^{-24}$ cm^3 ns^{-1} for the deactivation of 1s^3 levels.

4p levels Rate constants for collisional population transfers within 4p levels are taken from Ref. [136]. Rate constants for transfers to 4s states are given in Ref. [137]. The measurements do not resolve the "recipient" 4s state however. We assume equal probabilities for each of the four 4s states.

For levels with excitation energies above 14.7 eV, Hornbeck-Molnar ionization (2.31) was taken into account, using the rate constant given in Ref. [138].

5.2.4. Tuning

Not all parameters needed for a microscopic simulation are available from experimental data or can be calculated reliably. We, therefore, try to adjust the unknown parameters such that the average transfer efficiencies obtained from gain curve fits are reproduced. More precisely, we are interested in the parameters which minimize

$$\sum_i \left(r_i^{\text{(fit)}} - r_i^{\text{(sim.)}} \right)^2,$$

where r_i are the average transfer efficiencies for Ar with 5%, 10%, 15%, and 20% CO$_2$, 2%, 5%, and 10% CH$_4$, and 10% C$_2$H$_6$ (at atmospheric pressure). The reference values $r_i^{\text{(fit)}}$ are taken from Ref. [50]. The simulated values $r_i^{\text{(sim.)}}$ are calculated in a parallel-plate geometry with a gap of 50 μm at an electric field of 70 kV/cm.

In order to reduce the parameter space, the rate constants and ionization yields are assumed to be the same for all levels pertaining to one multiplet. Collisional mixing between 3d/5s levels and transfers from higher excited levels to 3d and 5s levels are neglected.

One is then left with the following set of free parameters related to collisional deexcitation:

- rate constant $k_{\text{3d,5s} \rightarrow \text{4p}}$ for collisional excitation transfer from Ar 3d and 5s levels to 4p levels;

- rate constant $k_{\text{high} \rightarrow \text{4p}}$ for collisional excitation transfer from higher excited Ar levels to 4p levels;

- rate constants and ionization yields for quenching of non-resonant 3d and 5s levels by CO$_2$, CH$_4$, and C$_2$H$_6$ (for resonant levels the Watanabe-Katsuura formula is used);

- ionization yields for quenching of 4p levels by CH$_4$ and C$_2$H$_6$;

- ionization yield for quenching of the metastable level 1s$_3$ by C$_2$H$_6$.

In addition, the cut-off energy $\Delta (\hbar \omega)_{\text{max}}$ of the line-shape profiles can be considered as a free parameter.

Initial estimates for the quenching rate constants are obtained from (5.4). Using a stochastic (simulated annealing-like) optimization procedure a possible set of parameters (Table 5.3) was found, which satisfactorily reproduces the Penning transfer efficiencies obtained from gain curve fits. The results are shown in Fig. 5.4. The set of parameters shown in Table 5.3 is clearly not a unique solution and probably needs to be revised if more measurements are included in the fit. For Ar/C$_2$H$_2$, two sets of transfer efficiency measurements (using gain measurements with

parameter	value
$k_{\text{3d,5s}\rightarrow\text{4p}}$ [10^{-20} cm^3 ns^{-1}]	10
$k_{\text{high}\rightarrow\text{4p}}$ [10^{-20} cm^3 ns^{-1}]	0.8
quenching of 3d levels by CO_2	
rate constant [10^{-19} cm^3 ns^{-1}]	12
ionization yield	0.8
quenching of 5s levels by CO_2	
rate constant [10^{-19} cm^3 ns^{-1}]	22
ionization yield	0.8
quenching of 3d levels by CH_4	
rate constant [10^{-19} cm^3 ns^{-1}]	1.8
ionization yield	0.2
quenching of 5s levels by CH_4	
rate constant [10^{-19} cm^3 ns^{-1}]	3.1
ionization yield	0.2
quenching of 3d levels by C_2H_6	
rate constant [10^{-19} cm^3 ns^{-1}]	1.5
ionization yield	0.8
quenching of 5s levels by C_2H_6	
rate constant [10^{-20} cm^3 ns^{-1}]	2.6
ionization yield	0.8
quenching of 4p levels by CH_4	
ionization yield	0.2
quenching of 4p levels by C_2H_6	
ionization yield	0.3
quenching of 1s$_3$ by C_2H_6	
ionization yield	0.8

Table 5.3 Possible set of tuning parameters which reproduces the transfer efficiencies (at atmospheric pressure) for Ar/CO_2, Ar/CH_4, and Ar/C_2H_6 obtained from gain curve fits.

Figure 5.4 Average transfer efficiencies as functions of the quencher concentration in Ar/CO_2, Ar/CH_4, Ar/C_2H_6, Ar/C_2H_2. Open symbols: r values extracted from gain curves [50], full symbols: results from microscopic calculation (see text).
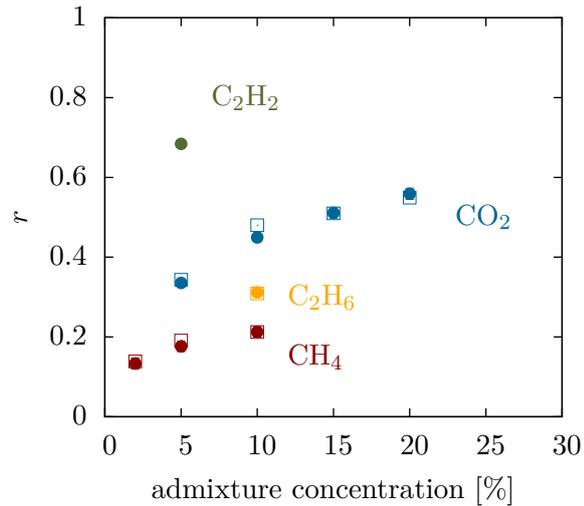
parallel-plate and cylindrical chambers, respectively) are given in Ref. [50]. At a concentration of 5% C_2H_2, the extracted transfer efficiencies are $r = 0.79$ (cylindrical chamber) and $r = 0.73$ (parallel-plate chamber). As can be seen from Fig. 5.4, the simulated transfer efficiency with the ionization yield of the metastable 4s levels set to 0.61 [133] and the ionization yield of the 4p levels adjusted to 0.3 is in the same range ($r = 0.68$).

5.3. Summary

Input data for the microscopic model of Penning transfer presented in Section 5.1.2 are

1. optical transition rates for the excited states of the noble gas and lineshapes of the resonance transitions;

2. photoabsorption cross-section and ionization yield of the quencher;

3. rate constants and ionization yield for collisional deactivation of excited noble gas atoms by quencher molecules;

4. rate constants for collisional transitions between noble gas levels.

For the considered gases, the data associated to radiative decay (items 1 and 2) are available from literature (except for isobutane for which no photoabsorption cross-section measurements could be found). Literature data on collision-induced deexcitation transfer are less abundant. A "first-principle" simulation is, therefore, not possible. By tuning the missing parameters however, agreement with measured transfer efficiencies could be achieved, as shown in Sec. 5.2.4. The model and the compilation of atomic data can be used as a basis for further investigations such as photon feedback studies.

6. Semiconductor Detectors

In this chapter, the implementation of silicon detector simulation methods in Garfield++ is described. Similarities and differences with respect to gas-based detectors are discussed.

6.1. Primary Ionization

As illustrated in Fig. 6.1, the absorption of photons with energies below ≈ 30 eV by solid, crystalline silicon differs from the photon interaction with isolated silicon atoms in the same energy range.

- Photo-ionization in solid silicon starts at the band gap energy (≈ 1.1 eV), whereas the ionization threshold of atomic silicon is about 8.15 eV [117].

- A dominant feature of the loss function $\text{Im}\left(-1/\varepsilon\right)$ of solid silicon is the so-called plasmon peak at ≈ 16.7 eV (see Section 2.1.3) which reflects the excitation of collective oscillations of valence electrons and is, consequently, not present in the atomic photoabsorption cross-section.

In order to examine to which extent solid-state effects are relevant for charged particle ionization, an implementation of the PAI model based on formula (2.14) – without the approximation (2.15) made by Allison and Cobb [23] – was developed. The dielectric function used in the simulation is based on experimental data for the complex index of refraction $\mathsf{n} + \mathsf{i}\mathsf{k}$ compiled in Ref. [139], complemented by the tabulation of semi-empirical atomic form factors by Henke et al. [17] and the compilation of optical data in Ref. [140]. The loss function, plotted in Fig. 6.1, satisfies the Thomas-Reiche-Kuhn sum rule (A.9) to within 1%. For energy transfers between 30 keV (i. e. the upper range of the Henke table) and the maximum allowed energy transfer, the appropriate differential cross-section for scattering off free electrons is used[1].

In terms of the level of detail with respect to the modelling of $\varepsilon\left(k, \omega\right)$, the above approach may be regarded as a compromise between Heed, which uses the atomic photoabsorption cross-section, and the more elaborate algorithm of Bichsel [141–143]. In the latter model (also called "Bethe-Fano" method), which is also based on dielectric theory, the differential inelastic cross-section is calculated as follows [141, 143]. For the transverse term, the same expression as in the PAI model is used. For the calculation of the longitudinal term, the integration over k is split into two domains. For low momentum transfers, $k < k_1$, the dipole approximation $\text{Im}\left(-1/\varepsilon\left(k, \omega\right)\right) = \text{Im}\left(-1/\varepsilon\left(\omega\right)\right)$ is used. For higher momentum transfers ($k > k_1$), numerical calculations of the generalized oscillator strength for the individual subshells are used. The parameterizations of the calculated generalized oscillator strength are matched to optical data in the low-k regime. For large energy transfers, the differential cross-sections for scattering of spin 0 particles by free electrons is used,

$$\frac{\mathrm{d}\sigma}{\mathrm{d}E} = \frac{\mathrm{d}\sigma}{\mathrm{d}E}^{(R)} \left(1 - \beta^2 \frac{E}{E_{\max}}\right),$$

---

[1] The relativistic cross-sections for scattering of spin 0, spin 1/2 and spin 1 particles with $m > m_e$, as well as of electrons and positrons are summarized in Ref. [24].
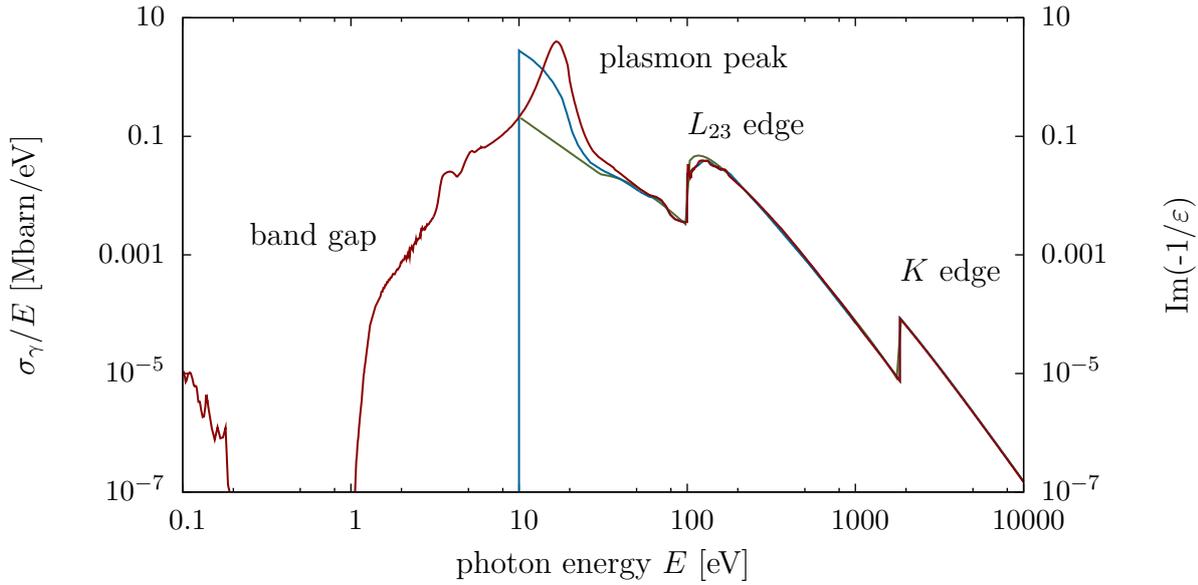
Figure 6.1. Optical data for silicon used in different implementations of the PAI model. Red
curve: loss function $\mathrm{Im}\,(-1/\varepsilon)$ of solid silicon (right scale) [17, 139, 140]. Blue curve: atomic
photoabsorption cross-section σ_γ divided by the photon energy, as used in Heed [17, 88].
Green curve: photoabsorption cross-section divided by the photon energy, as used in the PAI
model implementation of Geant4 (extracted from the file `G4StaticSandiaData.hh`).

where $\mathrm{d}\sigma/\mathrm{d}E^{(R)}$ is the Rutherford cross-section (A.3). Results for the stopping power $\mathrm{d}E/\mathrm{d}x$
and the inverse ionization mean free path λ^{-1} calculated by Bichsel, as well as tables of the
inverted cumulative differential cross-section for selected values of $\beta\gamma$ are available on a webpage
[144]. The extension of the Bichsel model to other materials is not trivial, and has not been
attempted so far. Unlike for the PAI model implementations discussed here, the source code for
calculating $\mathrm{d}\sigma/\mathrm{d}E$ is not publicly available.

Using the loss function depicted in Fig. 6.1, the stopping power calculated by means of the PAI
model is in agreement with Bichsel's results. For $0.316 \leq \beta\gamma \leq 31622.8$, i. e. the range covered in
the table provided by H. Bichsel [144], the difference between the two calculations is less than
0.5%. The difference in the inverse ionization mean free path is larger, with the values of λ^{-1}
according to the PAI model being about $4-5\%$ higher than the values calculated by Bichsel.
In order to estimate the effect of uncertainties in the optical data, we replace the loss function
in the vicinity of the L_{23} edge by the data of Henke [17] (green curve in Fig. 6.1). This results
in an increase of λ^{-1} by $1.1-1.7\%$ and an increase of $\mathrm{d}E/\mathrm{d}x$ by $1.4-2.4\%$ (with the larger
differences at low $\beta\gamma$).

The Heed results are also in agreement with Bichsel's calculations. In the considered range of $\beta\gamma$,
the difference of the calculated values is less than 2% for the stopping power and $< 5\%$ for the
ionization mean free path. The differences between the results increase towards smaller $\beta\gamma$.

The results for λ^{-1} should be taken with a grain of salt. According to all three models, the
ionization mean free path at $\beta\gamma = 3$ is about 250 nm, which is significantly smaller than the
typical dimensions of today's silicon sensors. No measurements of this quantity are available
which would allow a meaningful validation of the simulation.

In the next section, we shall discuss the impact of differences in the modelling of $\mathrm{d}\sigma/\mathrm{d}E$ on
the resulting energy loss spectra. In addition to the above models (Heed, PAI model based on

solid-state optical data, and Bichsel's model), calculations using the general-purpose transport codes Geant4[2] [11, 12] and Fluka[3] [145, 146] are also included in the comparison.

For simulating the ionization energy loss of swift charged particles, two options provided by Geant were explored.

standard electromagnetic package For thin absorbers, fluctuations of the continuous energy loss are simulated according to the model described in Ref. [147]. The atoms of the material are ascribed two discrete energy levels with excitation energies E_1, E_2 and oscillator strengths f_1, f_2. The energy E_2 is set to 10 eV $\times Z^2$ (corresponding roughly to the K shell energy), and the associated oscillator strength is set to $f_2 = 2/Z$. The energy E_1 and the oscillator strength f_1 representing loosely bound electrons are fixed by the constraints

$$f_1 + f_2 = 1, \qquad f_1 \ln E_1 + f_2 \ln E_2 = \ln I,$$

where I is the effective ionization energy of the material. Other parameters in the model cross-sections σ_1, σ_2 are adjusted such that the mean energy loss according to the Bethe-Bloch stopping formula is reproduced. The distribution of the energy loss due to ionization between 10 eV and the threshold E_{cut} for explicit δ-electron generation, is approximated by $g(E) \propto 1/E^2$. The number of energy loss events for each type of collision (i. e. excitations and ionization) within a step are sampled from a Poisson distribution.

PAI model As an alternative to the standard electromagnetic physics model, Geant4 provides an implementation of the PAI model [148]. For reasons of computational efficiency, the photoabsorption cross-section (shown in Fig. 6.1 for the case of silicon) is represented as a fourth-order polynomial in $1/\omega$.

For the present calculations, version 9.2 of Geant4 was used. The physics list was adapted from the one of novice example N03. The production threshold was set to 10 μm.

The algorithm for the simulation of energy loss fluctuations implemented in Fluka is described in Ref. [149]. Above a certain threshold, ionization is treated by means of explicit δ-electron production. For the continuous energy loss below, an atomic model similar to the one of Geant is adopted, considering two discrete energy levels (for elemental materials) and the appropriate differential cross-section for free electron scattering above a certain threshold. The cross-sections for "distant" collisions are assumed to be given by

$$\sigma_{1,2} = \frac{2\pi e^4}{\beta^2 m_e c^2} \frac{f_{1,2}}{E_{1,2}} \left[\ln \frac{2m_e c^2 \beta^2 \gamma^2}{E_{1,2}} - 0.577 - \delta_F^{(1,2)} \right],$$

with δ_F being the density effect correction.

The moments of the energy loss distribution for a single collision, $\langle \Delta E^m \rangle$, can be evaluated analytically. With the number of collisions n over a step being Poisson distributed, the cumulants K_m of the distribution of the total energy loss $E = \sum_{i=1}^{n} \Delta E_i$ are given by

$$K_m(E) = \langle n \rangle \langle \Delta E^m \rangle .$$

The energy loss is then sampled from a distribution which reproduces the first six cumulants. The present calculations were conducted with version 2008.3d.1 of Fluka, using the set of defaults `NEW-DEFA` (ionization fluctuations and δ-electron production – with a threshold of 100 keV –

---

[2] "**Ge**ometry **an**d **T**racking"
[3] "**Flu**ktuierende **Ka**skade"
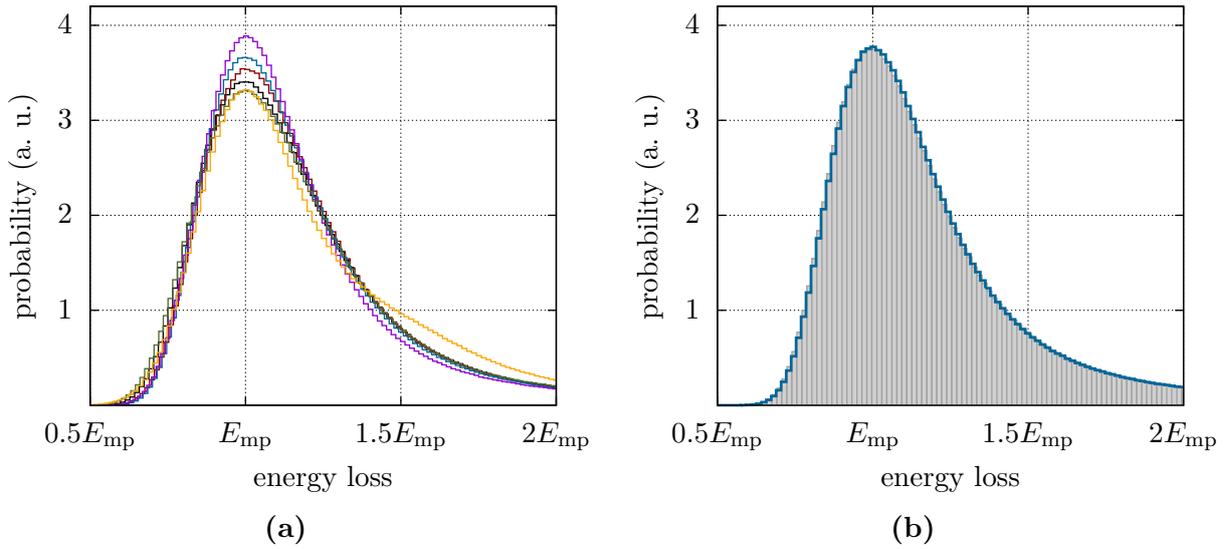
Figure 6.2. Energy loss spectra for pions ($\beta\gamma = 10$) traversing 100 µm of silicon. Left: calculations using the Bichsel model (black curve), the PAI model based on solid-state optical data (red curve), HEED (blue curve), the PAI model implemented in Geant4 (green curve), the standard electromagnetic model of Geant4 (orange curve), and Fluka (purple curve). Right: energy loss spectrum calculated using Heed (blue histogram) and distribution of the number of electrons (grey histogram) calculated using the subshell-separation and δ-electron transport algorithms in Heed and converted back to an energy loss spectrum (assuming $W = 3.6$ eV, $F = 0.11$).

switched on). The threshold for δ-electron production and transport can be set with the `DELTARAY` card. Varying the cut values was found to have no significant impact on the energy deposition spectrum. The `EVENTDAT` scoring option was used for retrieving the energy deposition in the target for each simulated event.

6.1.1. Energy Loss Straggling

We consider the distribution of the energy lost by a high-energetic charged pion crossing a silicon slab with a thickness of 100 µm. A pion was chosen as primary particle since in Bichsel's model (and also in Heed) the differential cross-section for large energy transfers is assumed to be given by the relativistic cross-section for spin 0 particles.

To lowest order, one can characterize energy loss spectra in terms of the most probable value E_{mp} and the full width at half maximum (FWHM) w. Absolute differences in E_{mp} and w between different models can to some extent be absorbed in a scaling constant (i. e. the W value) converting the theoretical energy loss distribution to an observable ionization spectrum. Hence, we use the relative width $\omega = w/E_{\mathrm{mp}}$ as a calibration-independent parameter characterizing the width of a spectrum.

A comparison of E_{mp}, w, and ω for 4 different values of $\beta\gamma$ is given in Table 6.1. For each value of $\beta\gamma$, 2×10^7 primaries were simulated. The same binning (200 bins between 0 and 80 keV) was used for each model. The overflow, i. e. the percentage of events with an energy loss greater than the upper range of the histogram, is also shown in Table 6.1.

	Bichsel	PAI (this work)	Heed	G4 PAI	G4 Standard	Fluka
$\beta\gamma = 1$						
E_{mp} [keV]	40.3	41.9	42.1	38.2	41.1	41.4
w [keV]	17.7	17.0	16.6	18.6	17.7	16.5
ω	0.44	0.42	0.39	0.49	0.43	0.40
overflow [%]	10.6	10.0	9.0	8.9	8.5	10.0
$\beta\gamma = 10$						
E_{mp} [keV]	24.4	25.3	25.0	24.4	24.2	25.1
w [keV]	11.5	11.0	10.8	12.0	10.7	10.4
ω	0.47	0.45	0.43	0.49	0.44	0.42
overflow [%]	4.0	3.6	2.7	2.6	2.6	3.5
$\beta\gamma = 100$						
E_{mp} [keV]	26.0	26.2	26.1	26.4	25.4	26.9
w [keV]	12.5	12.0	11.6	13.1	11.4	11.2
ω	0.48	0.46	0.45	0.50	0.45	0.42
overflow [%]	4.1	3.7	2.7	2.7	2.7	3.6
$\beta\gamma = 1000$						
E_{mp} [keV]	26.1	26.0	26.3	26.6	25.7	27.0
w [keV]	12.7	12.2	11.8	13.4	11.5	11.4
ω	0.49	0.47	0.45	0.50	0.45	0.42
overflow [%]	4.1	3.7	2.8	2.7	2.8	3.6

Table 6.1. Most probable energy loss E_{mp}, absolute (w) and relative ($\omega = w/E_{\text{mp}}$) full width at half maximum of the energy loss spectrum, and fraction of energy losses above 80 keV, for pions traversing 100 µm of silicon. The error in E_{mp} and w is ≈ 0.1 keV.
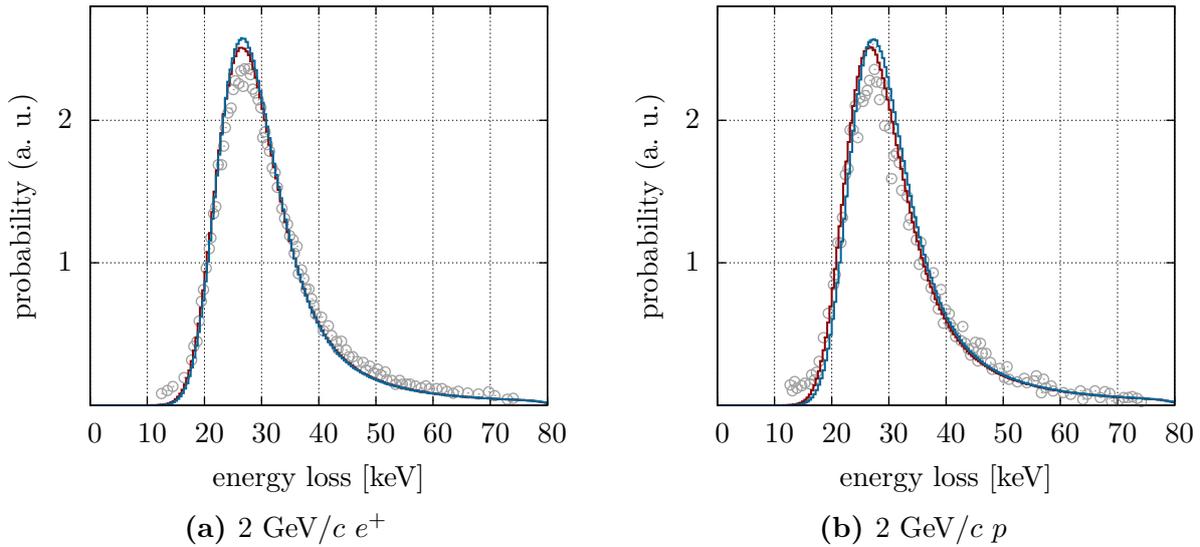
Figure 6.3. Energy loss spectra for positrons and protons in 100 µm silicon. The histograms represent distributions calculated using the dielectric loss function-based PAI model (red curve) and Heed (blue curve), smeared with a Gaussian ($\sigma = 2$ keV). The circles are experimental data reported by Bak et al. [150]. No scaling of the horizontal axis was applied.

The results are in the same "ballpark", with a standard deviation $\sigma \approx 6 - 8\%$ among the calculated values of ω. Non-negligible differences in the shape of the energy loss spectra do exist however. These are best illustrated with the help of a plot. Figure 6.2a shows the calculated energy loss distributions for $\beta\gamma = 10$. In order to align the peaks, the energy loss is normalized with respect to the most probable value E_{mp}. Of the four detailed models, Heed gives the narrowest distribution, followed by the loss-function based PAI model, the Bichsel model, and the G4 PAI model implementation. The same sequence is observed for the other values of $\beta\gamma$ considered here. Given the differences in the underlying photoabsorption cross-section (Fig. 6.1), the disagreement between the results from Heed and the G4 PAI model is plausible. With the settings described above, the shape of the energy loss spectrum calculated by means of the standard electromagnetic interaction model of Geant4 differs significantly from the other calculations. Bichsel model, loss-function based PAI model and Heed predict an increase of ω with increasing $\beta\gamma$ which is less pronounced in the Geant4 model and Fluka results.

In order to compare the calculations with measured spectra, it is necessary to convert the energy loss to a number of electrons. Possible changes of the spectrum due to this conversion can be conveniently estimated with Heed which – as mentioned in Chapter 4 – provides a generic algorithm for subshell separation, atomic relaxation, and δ-electron transport. Figure 6.2b shows two – virtually identical – energy loss distributions for $\beta\gamma = 10$ calculated using Heed. The blue histogram is identical to the one in Fig. 6.2a. The grey histogram represents the distribution of the number of electrons produced in the silicon layer, converted back to an energy loss spectrum using the same W value as used in the δ-electron transport procedure (cf. the discussion of the "PAIR" model in Ref. [88]). The close agreement between the two curves shows (1) that the ionization spectrum is, to good approximation, proportional to the energy loss spectrum, and (2) that δ-electron escape is insignificant for the considered detector thickness.

The set of experimental data reported by Bak and coworkers [150] seems to be a popular reference for validation purposes [141, 148, 149].
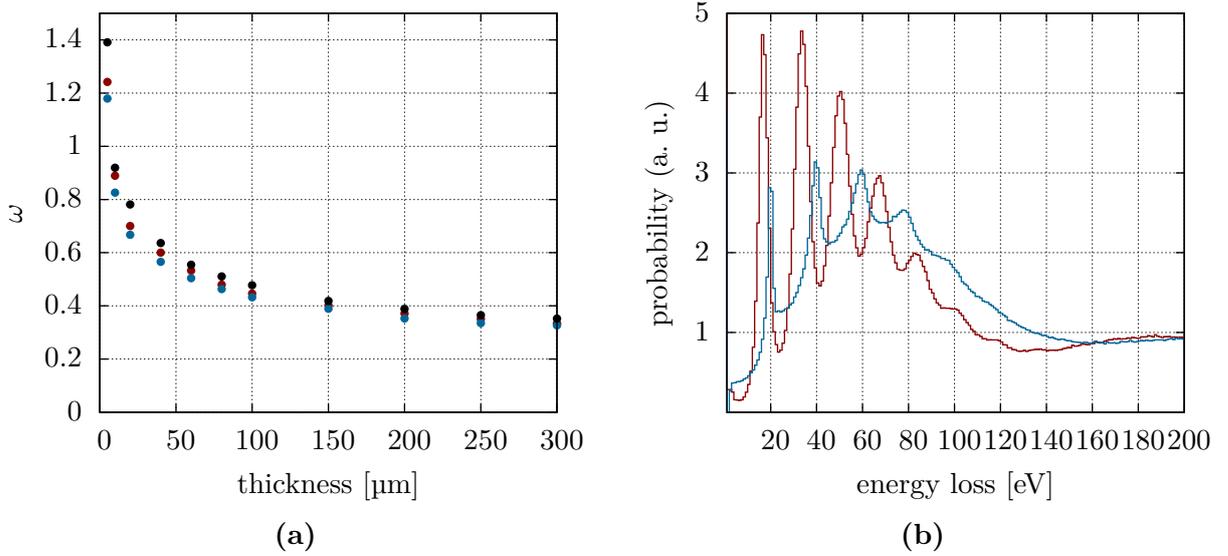
Figure 6.4. Left: relative peak width ω as function of the detector thickness calculated using Bichsel model (black symbols), Heed (blue symbols), and loss-function based PAI model (red symbols). Right: energy loss spectrum of pions ($\beta\gamma = 4$) in 1 µm of silicon, calculated using Heed (blue curve) and loss-function based PAI model (red curve). For producing these histograms 10^6 primaries were simulated.

- A systematic comparison of measurements and calculations is presented in Bichsel's paper [141]. Excellent agreement between experimental and theoretical distributions is found. Instrumental effects were accounted for by convoluting the calculated loss spectrum with a Gaussian (with a standard deviation $\sigma = 2$ keV in case of the 100 µm sensor).

- In Ref. [149], Bak's measurements for 2 GeV/c positrons and protons in 100 µm silicon are used for demonstrating the performance of the Fluka algorithm. Whether a broadening of the distribution due to the experimental resolution was taken into account is not indicated.

- Satisfactory agreement between calculations using the Geant4 PAI model implementation and experimental data by Bak for 2 GeV/c positrons in 32 µm silicon is reported in Ref. [148].

As shown in Fig. 6.3 for 2 GeV/c positrons and protons in a 100 µm thick sensor, calculations using Heed and the present implementation of the PAI model are also in reasonable agreement with measured ionization spectra.

In addition to the particle momentum, the shape of the energy loss spectrum also depends on the thickness of the silicon layer. Figure 6.4 shows the relative width $\omega = \text{FWHM}/E_{\text{mp}}$ as a function of the layer thickness. The differences between the calculations using Heed, the Bichsel model and the present implementation of the PAI model can be seen to increase towards smaller thicknesses. At typical thicknesses of planar sensors ($\approx 100 - 300$ µm) the different models produce very similar results for the relative width ω.

The differences between models become more pronounced in very thin layers since features of the differential cross-section such as the plasmon peak become visible. This can become relevant for monolithic sensors where the depletion depth can in some cases be only few µm. As an example, Fig. 6.4b shows the energy loss spectrum of a minimum-ionizing pion in a 1 µm thin silicon slab calculated using Heed and the PAI model based on the solid-state dielectric function,

respectively. The latter distribution exhibits pronounced maxima at multiples of the plasmon energy (≈ 16.7 eV). The differential cross-section calculated by Heed also features a peak in the same energy range, more specifically at about 20 eV, which is reflected in the energe loss spectrum. Of the two models, the PAI model based on the solid-state dielectric function is expected to provide a more reliable prediction of the energy loss spectrum at this thickness. Measured charge deposition spectra for depletion depths of few µm would be very useful for validating the PAI model. Unfortunately, no experimental data were found in the literature. At thicknesses above approximately 5 µm, the features visible in the spectra shown in Fig. 6.4b are largely "washed out" due to the large number of ionizing collisions the particle suffers during its passage through the detector.

6.2. Field Calculation

Due to the presence of mobile charges, electric field calculations for silicon sensors tend to be more complicated than for gas-based detectors. Whereas for the latter it is usually sufficient to solve the Laplace equation, the electric field in a silicon detector is determined by Poisson's equation

$$\nabla \cdot (\varepsilon \mathbf{E}) = \frac{\rho}{\varepsilon_0} = \frac{e}{\varepsilon_0} \left(p - n + N_D - N_A \right) + \frac{\rho_f}{\varepsilon_0}, \tag{6.1}$$

where p is the density of holes, n is the density of electrons, N_D, N_A are the densities of ionized donors and acceptors, respectively, and ρ_f accounts for a possible fixed charge density [8, 9, 151]. The temporal evolution of the electron and hole concentrations is described by the continuity equations

$$\frac{\partial n}{\partial t} = -\nabla \cdot \mathbf{j}_n + G_n - R_n, \qquad \frac{\partial p}{\partial t} = -\nabla \cdot \mathbf{j}_p + G_p - R_p, \tag{6.2}$$

where the terms $G_{n,p}$, $R_{n,p}$ describe the generation and loss of carriers. From a macroscopic viewpoint, the "driving forces" of the current densities $\mathbf{j}_{n,p}$ are (1) the electric field and (2) gradients in the respective concentrations,

$$\mathbf{j}_n = -n\mu_n \mathbf{E} - D_n \nabla n, \qquad \mathbf{j}_p = p\mu_p \mathbf{E} - D_p \nabla p, \tag{6.3}$$

with $\mu_{n,p}$ being the electron/hole mobilities and $D_{n,p}$ the diffusion coefficients[4]. To first approximation (drift-diffusion model), other driving forces such as temperature gradients are neglected.

Powerful device simulation (also referred to as TCAD[5]) programs dealing with the self-consistent solution of (6.1) and (6.2) are available. A popular commercial package is e. g. Synopsys Sentaurus Device [152]. While primarily geared towards microelectronics applications, the program also includes basic models for charge generation by ionizing radiation and can thus be used for investigating the behaviour of particle detectors (see e. g. Ref. [153]).

In the following, a "hybrid" approach is taken: only the electric field calculation is "outsourced" to TCAD while conventional detector simulation techniques are used for calculating primary ionization and induced currents. In Sentaurus Device, the drift-diffusion problem, given by Eqs. (6.1) and (6.2), is solved on a finite-element mesh [154]. As output of a simulation run, one obtains the values of the potential, electric field and other variables on the node points of the mesh. Sentaurus Device allows one to export these results to a file, from which they

---

[4] Note that the dimension of the diffusion coefficients $D_{n,p}$ appearing in Eq. (6.3) is different from the one of the longitudinal and transverse diffusion coefficients $D_{L,T}$ introduced in Section 2.3.

[5] **T**echnology **C**omputer-**A**ided **D**esign

can subsequently be imported in another program. Given the nodal solution, together with a description of the mesh[6], the field at any point inside the device can be evaluated by interpolation based on the values at the nodes belonging to the element in which the point is located. In Sections 2.3.4 and 3.4, we have used the same method for dealing with field maps calculated using the finite-element program Ansys [36].

In some cases it is also possible to find analytic expressions for the electric field. For instance, in an overdepleted, unsegmented planar diode of thickness d, the electric field in the n-type bulk is given by [8, 9]

$$E\left(x\right) = \frac{U - U_{\mathrm{dep}}}{d} + 2\frac{x}{d}\frac{U_{\mathrm{dep}}}{d}, \tag{6.4}$$

where U is the applied reverse bias voltage and U_{dep} is the voltage needed for full depletion.

For the calculation of weighting fields, the space charge distribution inside the device is not relevant. For fully depleted sensors, the same techniques as for gas-based detectors can, therefore, be used.

6.3. Charge Transport

6.3.1. Transport Parameters

The algorithm described in Section 2.3.2 for the stochastic integration of the first-order equation of motion (2.22) can be applied without changes to the calculation of electron and hole drift lines in silicon sensors. As input data the transport coefficients, in particular the drift velocity (or, equivalently, the mobility μ), need to be specified.

For device simulation purposes, elaborate mobility models have been devised, which provide empirical fit formulae for the dependence of μ on temperature, doping, impurity concentration, electric field and other parameters [151, 154–156]. The dependence of the lattice mobility μ_L – i. e. the mobility in pure silicon due to phonon scattering – on the temperature T is usually expressed in terms of a power law,

$$\mu_L\left(T\right) = \mu_L|_{T=T_0}\left(\frac{T}{T_0}\right)^{-\vartheta}, \qquad T_0 = 300 \text{ K}.$$

Most values for the lattice mobility at 300 K reported in the literature are in the range 1350 – 1500 cm^2 V^{-1} s^{-1} for electrons, and 450 – 500 cm^2 V^{-1} s^{-1} for holes [151]. In Section 6.4 the default parameters of Sentaurus Device ($\mu_0 = 1417$ cm^2 V^{-1} s^{-1}, $\vartheta = 2.5$ for electrons, $\mu_0 = 470.5$ cm^2 V^{-1} s^{-1}, $\vartheta = 2.2$ for holes) are used.

At high electric fields, the drift velocity in silicon approaches a saturation value v_{sat}. A popular parameterization for the mobility as a function of the electric field, proposed by Canali et al. [157], is given by

$$\mu\left(E\right) = \frac{\mu_L}{\left(1 + \left(\frac{\mu_L E}{v_{\mathrm{sat}}}\right)^{\beta}\right)^{1/\beta}}, \tag{6.5}$$

where both the saturation velocity v_{sat} and the exponent β are temperature-dependent. For the following calculations, the default models for v_{sat} and β implemented in Sentaurus Device were

---

[6] The coordinates of all nodes and the mapping between elements and nodes can be obtained from the output file of the mesh generator tool Mesh which is part of the Synopsys TCAD suite.

used. At 300 K, the values are $v_{\mathrm{sat}} = 107\ \mu\mathrm{m/ns}$, $\beta = 1.109$ for electrons and $v_{\mathrm{sat}} = 83.7\ \mu\mathrm{m/ns}$, $\beta = 1.213$ for holes.

In the presence of a magnetic field $\mathbf{B}$, the drift velocity can be calculated according to[7]

$$\mathbf{v}_{\mathrm{d}} = \mu\,|\mathbf{E}|\,\frac{1}{1 + \mu_H^2 B^2}\left(\hat{\mathbf{E}} + \mu_H B\left(\hat{\mathbf{E}} \times \hat{\mathbf{B}}\right) + \mu_H^2 B^2\left(\hat{\mathbf{E}} \cdot \hat{\mathbf{B}}\right)\hat{\mathbf{B}}\right), \qquad (6.6)$$

with $\mu_H = r_H \mu$ being the so-called Hall mobility. At room temperature, the Hall scattering factors are $r_H \approx 1.15$ for electrons, and $r_H \approx 0.7$ for holes [158]. For $\mathbf{E} \perp \mathbf{B}$, the angle θ_L (Lorentz angle) between the drift velocity vector and the electric field is given by $\theta_L = \arctan(\mu_H B)$.

In device simulation programs, the diffusion coefficients in (6.3) are usually modelled using the Einstein relation $D_{n,p} = \mu_{n,p} k_B T / e$. For the longitudinal and transverse diffusion coefficients $D_{L,T}$, as defined in Chapter 2, this corresponds to

$$D_L = D_T = \sqrt{\frac{2k_B T}{eE}}.$$

The probability for an electron or hole to be captured along its drift path by a defect state can be described in terms of an average trapping coefficient (analogously to the attachment coefficient η accounting for the loss of electrons in electronegative gases). In unirradiated sensors, charge trapping can to good approximation be neglected.

Charge multiplication due to impact ionization can, in principle, be calculated using the Yule-Furry like Monte Carlo method outlined in Section 3.1.4 – with the additional complication that (at very high fields) both electrons and holes are able to multiply. Empirical parameterizations[8] of the impact ionization coefficients for electrons and holes as functions of the electric field are available from literature (see e. g. Refs. [151, 159]).

In (small-scale) gas-based detectors the inhomogeneity of the electric field can be assumed to be the only relevant source of local variations in the transport coefficients. This is not necessarily true for silicon sensors, in particular after heavy irradiation. Defect accumulation, for instance, could cause a local increase of the trapping probability. If the field is calculated using Sentaurus Device, such inhomogeneities can be taken into account by exporting (in addition to the electric field) also the nodal solution for the mobilities (and other transport parameters). The mobility at a given point can then be obtained by interpolation in this "mobility map".

6.3.2. Microscopic Tracking

Semi-classical Monte Carlo simulation is an established method for electron transport in sub-micron semiconductor devices [160–162]. In this section, the relevance of this technique for the simulation of silicon detectors is discussed. We first review the key differences between gases and solids with respect to electron transport.

---

[7] Eq. (6.6) is to be understood with a negative sign of μ in case of electrons and a positive sign in case of holes.
[8] Interestingly, the standard parameterization ("Chynoweth law") for the impact ionization coefficient, $\alpha \propto \exp(-b/E)$, is virtually identical to the Rose-Korff formula for the Townsend coefficient in gases.

Semi-Classical Electron Transport in Semiconductors

The propagation of an electron wave packet – centred at a position $\mathbf{r}$ and a wave vector $\mathbf{k}$ – in a conduction band (index n) of a semiconductor can be described by the semi-classical equations of motion (see e. g. Ref. [163])

$$\hbar\dot{\mathbf{k}} = -q\left(\mathbf{E} + \mathbf{v}_n(\mathbf{k}) \times \mathbf{B}\right), \qquad \dot{\mathbf{r}} = \mathbf{v}_n(\mathbf{k}), \tag{6.7}$$

where

$$\mathbf{v}_n(\mathbf{k}) = \frac{1}{\hbar}\nabla_{\mathbf{k}}\epsilon_n(\mathbf{k})$$

is the group velocity. At low electron energies, the dispersion relation $\epsilon(\mathbf{k})$ can be approximated by a second-order Taylor expansion[9],

$$\epsilon(\mathbf{k}) \approx \frac{\hbar^2}{2}\left(\frac{k_t^2}{m_t^{\star}} + \frac{k_l^2}{m_l^{\star}}\right). \tag{6.8}$$

Eq. (6.8) is written with a view to the lowest conduction band of silicon (X valley), which has ellipsoidal equienergetic surfaces characterized by the longitudinal and transverse effective masses $m_l^{\star} = 0.916 m_e$, $m_t^{\star} = 0.191 m_e$. In order to account for the deviation of $\epsilon(\mathbf{k})$ from the parabolic shape (6.8), the expression [160]

$$\epsilon(1 + \alpha\epsilon) = \frac{\hbar^2}{2}\left(\frac{k_t^2}{m_t^{\star}} + \frac{k_l^2}{m_l^{\star}}\right), \tag{6.9}$$

is often used. In silicon, Eq. (6.9) – with a non-parabolicity parameter $\alpha = 0.5$ eV^{-1} – represents a reasonable approximation up to $\approx 1 - 2$ eV [164]. For a correct description of electron transport at higher energies so-called full-band simulations are necessary, which use numerical tabulations of $\epsilon(\mathbf{k})$ [161, 162].

Whereas the transport properties of electrons in gases are governed by collisions with atoms and molecules, the basic collision mechanisms of electrons in semiconductors are [160]

- scattering by phonons,

- scattering by defects (e. g. ionized impurities),

- scattering by other carriers.

Given the scattering rates $\tau_i^{-1}(\epsilon)$ for these processes, electrons can be tracked in a manner similar to the procedure discussed in Section 2.3.1.

Implementation

In the framework of this thesis, an extension of the microscopic tracking technique allowing for a basic simulation of electron transport in silicon was implemented. The band structure was approximated using (6.9). For calculating the scattering rates $\tau_i^{-1}(\epsilon)$, the semi-empirical formulae and parameters given in Ref. [160] were used. Figure 6.5a shows the collision rates (at 300 K) as a function of ϵ for the main scattering mechanisms of electrons in the X valley: acoustic phonon intravalley scattering, X-X intervalley scattering by phonon emission/absorption, and X-L intervalley scattering[10]. Impurity scattering and impact ionization are neglected.

The modified stepping algorithm proceeds as follows:

---

[9] In Eqs. (6.8), (6.9), $\mathbf{k}$ is measured with respect to the wave vector at the minimum of the band.

[10] The X-L scattering rates were calculated using the parameters given in Ref. [164].

- The duration Δt of a free flight step is sampled using the null-collision technique[11].

- The wave vector $\hbar \mathbf{k}'$ after the step is calculated in first order approximation,

$$\hbar \mathbf{k}' = \hbar \mathbf{k} + q\mathbf{E}\Delta t,$$

  and the electron energy is updated,

$$\epsilon(\mathbf{k}) \rightarrow \epsilon(\mathbf{k}').$$

- The new position in coordinate space is calculated,

$$\mathbf{r}' = \mathbf{r} + \frac{\Delta t}{2}(\mathbf{v} + \mathbf{v}').$$

- The type of collision to take place is selected based on the relative collision rates. The energy after the collision is updated,

$$\epsilon \rightarrow \epsilon \pm \hbar\omega.$$

  A new wave vector, which is consistent with the new energy and the angular distribution of the scattering process, is selected[12]. In the present implementation, all collision processes are assumed to be isotropic.

As can be seen from Fig. 6.5b, the calculated drift velocity is line with the empirical parameterization (6.5). The agreement is to be expected since the parameters given in Ref. [160] used for calculating the scattering rates are tuned to experimental data. For the range of fields considered here ($E < 100$ kV/cm), the mean electron energy remains below 0.5 eV, i. e. well within the scope of the non-parabolic band structure approximation (6.9). As an illustration, Fig. 6.5c shows the calculated electron energy distribution at 5 kV/cm, 10 kV/cm, and 20 kV/cm.

Possible Applications

As shown in Fig. 6.5d, the mean distance between successive collisions of an electron is about $10 - 50$ nm (to be compared with a mean free path of order 1 μm in gases at atmospheric pressure) which is significantly smaller than the the typical feature sizes of silicon sensors ($\gtrsim 1$ μm). In most cases, a macroscopic treatment of drift and diffusion is therefore sufficient.

In analogy to Magboltz, the microscopic simulation might be used for a calculation of transport coefficient tables however. This could be useful, for instance, for estimating the impact of defects on the transport properties. In its present form, the code can be used for calculating drift velocity, diffusion coefficients, and trapping rate. For the calculation of charge multiplication, a refined band structure model would need to be implemented.

The modelling of $\epsilon(\mathbf{k})$ is less critical for the simulation of δ-electrons since the main observables W and F are determined essentially by the scattering rates as functions of ϵ and the energy partitioning in ionizing collisions between the primary electron and the secondary electron and hole. When trying to simulate the energy degradation of high-energetic electrons, one is faced with other difficulties however. At energies above $\approx 40 - 50$ eV, the inelastic mean free path of electrons – which is obviously a key ingredient for the simulation – can be accurately calculated

(a) scattering rates

(b) drift velocity

(c) energy distribution

(d) mean free path
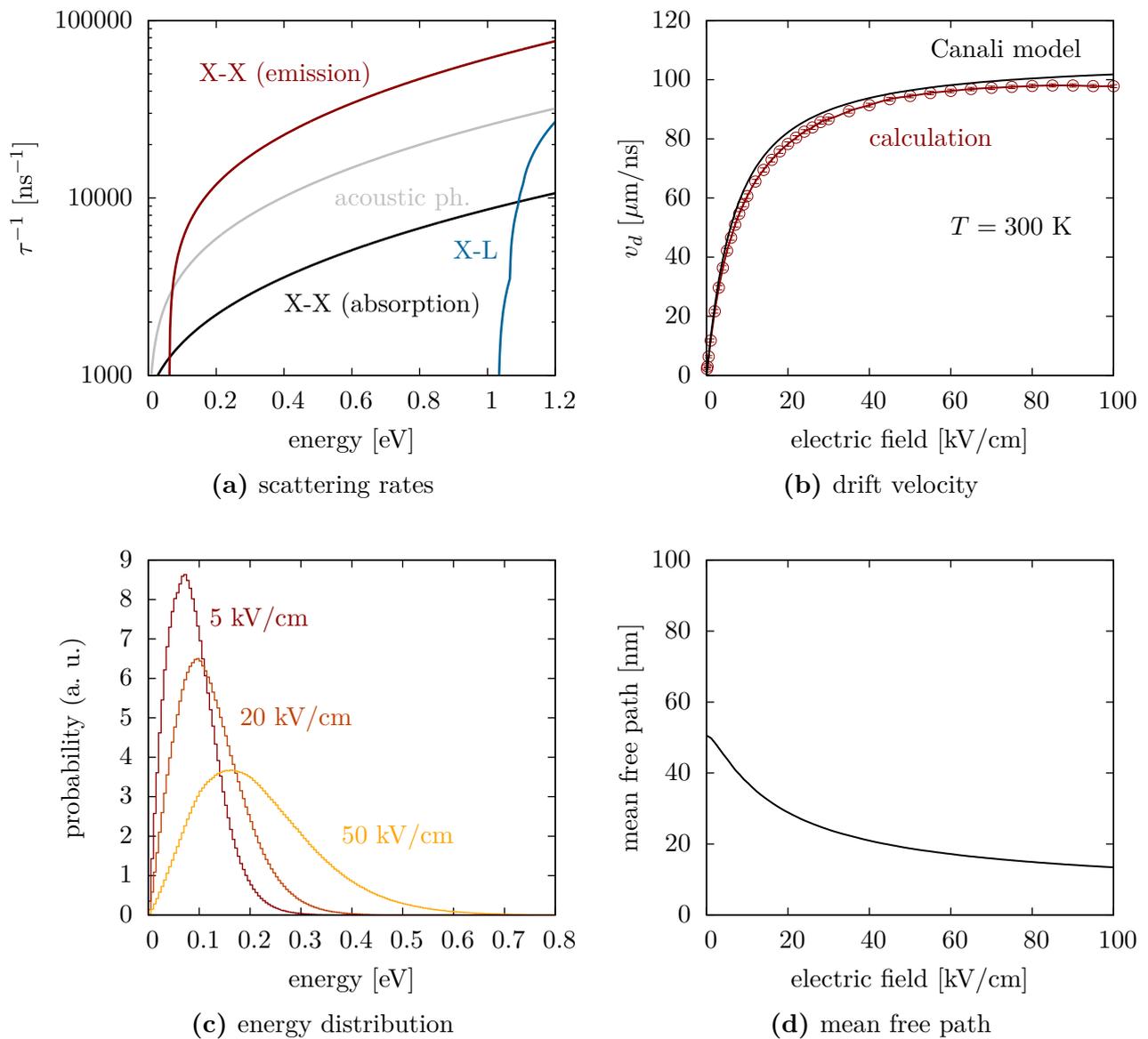
Figure 6.5. Monte Carlo simulation of electron transport in silicon (see text).
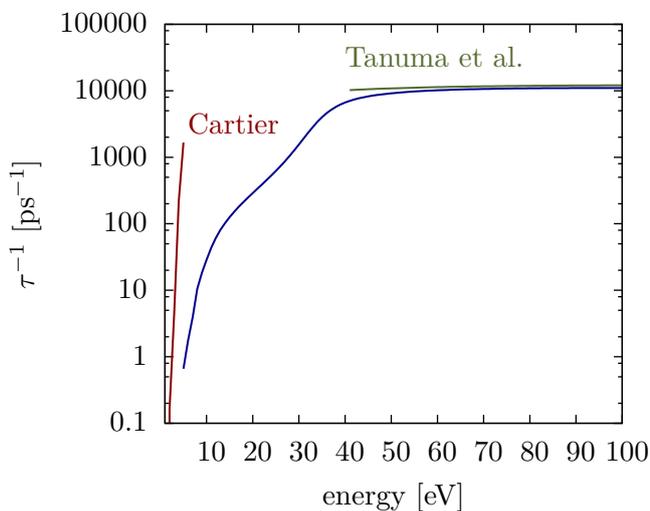
Figure 6.6 Electron impact ionization rate in silicon according to Cartier et al. [166] and inelastic scattering rate according to optical data models (green curve: fit formula given in Ref. [165], blue curve: calculation based on the Penn algorithm [167] using the same set of optical data as for the PAI model implementation discussed in Section 6.1).

(a) Contours of the electrostatic potential

(b) Drift lines from a charged particle track
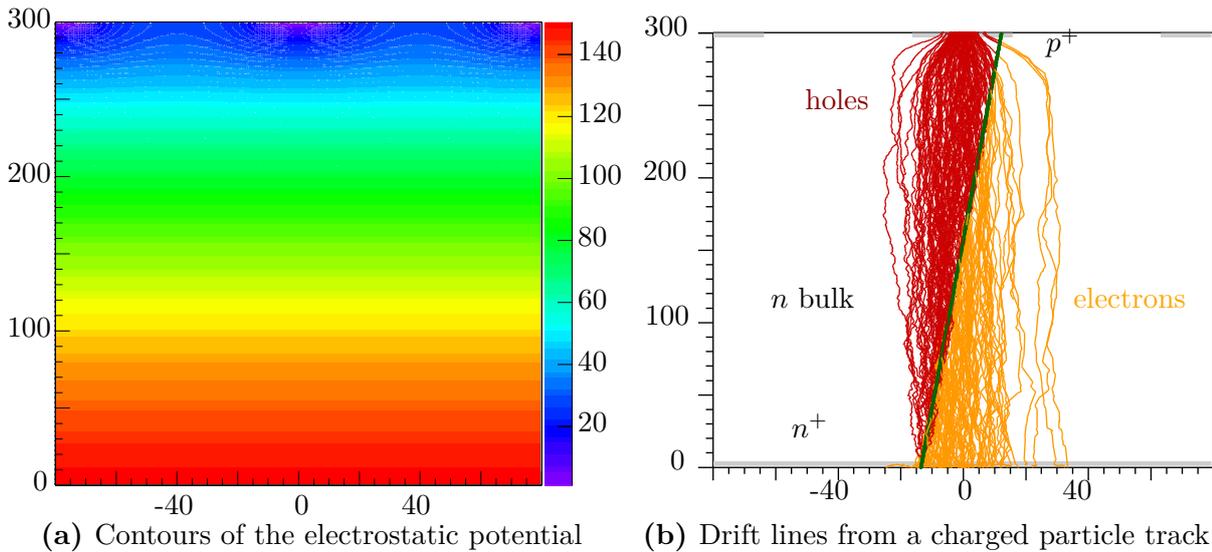
Figure 6.7. Left: contour plot of the electrostatic potential in a *p*-on-*n* silicon strip detector (150 V bias) as computed using Sentaurus Device [152]. Right: electron and hole drift lines from a charged particle track calculated using Heed [89] and Garfield++ [16]. Both plots show cross-sections (projection on the strip axis) through the sensor. The abscissae have tick marks in 5 µm intervals, the ordinates have tick marks in 10 µm intervals.

using optical data models based on dielectric theory (see e. g. Ref. [165]). The impact ionization rate at energies up to a few eV, on the other hand, can be calculated using semi-empirical models developed for device simulation purposes [166]. As can be seen from Fig. 6.6, the impact ionization rate according to Ref. [166] is not compatible with the inelastic scattering rate expected at low energies from optical data models. It is not clear how the scattering rate in the intermediate energy range (between about 5 and 40 eV) should be modelled. A microscopic simulation of *δ*-electron transport could, therefore, not be implemented within the framework of this thesis.

6.4. Simulation Chain

In this section, the assembly of individual components such as field calculation, energy loss simulation, and charge transport to a "full-chain" simulation is illustrated with the help of two examples for typical sensor geometries.

6.4.1. Strip Sensor

We consider an *n*-bulk sensor (thickness 300 µm) with 16 µm wide p^+ strip implants (pitch 80 µm). Since the strip width is considerably smaller than the detector thickness, the one-dimensional approximation (6.4) is not applicable here and the electric field needs to be calculated using numerical techniques. Figure 6.7a shows a contour plot of the electrostatic potential calculated using Sentaurus Device for a bias voltage $U_{\text{bias}} = 150$ V. For the field calculation, dopant concentrations of 1×10^{12} cm^{-3} in the *n*-bulk, 1×10^{19} cm^{-3} (peak value) in the p^+-implant,

---

[11] In the literature on Monte Carlo transport in semiconductors, this method is referred to as self-scattering algorithm.

[12] In case of full-band simulations, the search for an appropriate wave vector is a computationally very intensive step.

(a) Induced current
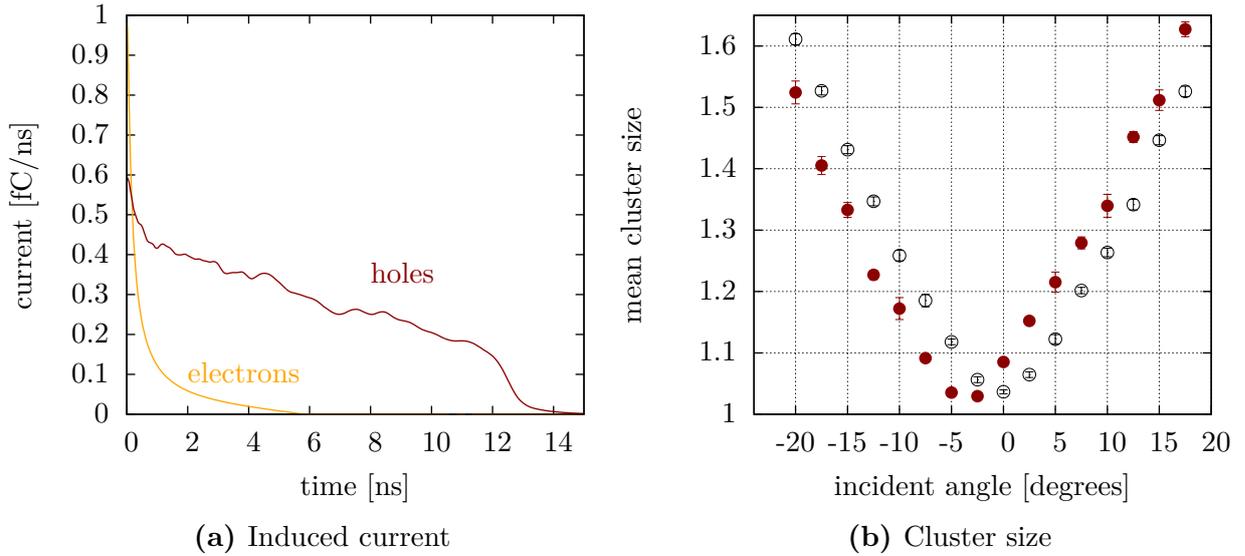
(b) Cluster size

Figure 6.8. Left: induced current on the central strip for tracks through the strip centre. Right: average cluster size as function of the track incident angle without magnetic field (open symbols) and in the presence of a magnetic field $B = 2$ T parallel to the strips (full symbols).

and 1×10^{18} cm^{-3} (peak value) in the n^+-implant were assumed. Surface charge at the interface between oxide and n-bulk was neglected.

Using Heed, the ionization pattern produced by a charged particle traversing the detector is simulated. For converting the energy loss in a collision to a number of "conduction" electrons, the phenomenological algorithm included in Heed is used (with $W = 3.6$ eV, $F = 0.11$).

The drift of electrons and holes (visualized in Fig. 6.7b) is calculated using the mobility and diffusion models discussed above (charge trapping is not taken into account). The drift line integration is performed in fixed-distance steps of 1 µm. For reasons of visibility, Fig. 6.7b shows only a small subset (0.1%) of the actual drift lines.

For the calculation of the weighting field of the strip electrode, the analytic expression (2.17) was used. Using the Shockley-Ramo theorem (2.34), the induced current at each drift line step is evaluated. The induced current, averaged over 500 charged particle tracks passing through the centre of a strip at perpendicular incidence, is shown in Fig. 6.8a. The hole current can be seen to constitute the dominant contribution to the total induced charge.

An example for a basic observable which can be calculated using this simulation chain, is the mean cluster size, i. e. the average number of strips with a signal above threshold upon the passage of a charged particle. For this calculation, a threshold of 1 fC was assumed. The simulation results are shown in Fig. 6.8b. In the presence of a magnetic field of 2 T parallel to the strips, the minimum of the cluster size can be seen to be shifted by the Lorentz angle θ_L.

6.4.2. Pixel Sensor (Time Resolution)

We consider a hybrid pixel detector with a sensor thickness of 200 µm and a pixel size of 300 µm×300 µm as used in the Gigatracker (GTK) of the NA62 experiment. The specification of the GTK requires the capability to timestamp tracks with an unprecedented precision of 150 ps RMS.

In this section we try to obtain a theoretical estimate of the single pixel hit time resolution. In order to achieve a short charge carrier drift time, the sensor (which is of *p*-on-*n* type) is operated in overdepletion at a bias of 300 V. To first approximation, the electric field in the sensor can, therefore, be assumed to be uniform. In order to identify the different contributions to the time resolution, we consider three combinations of simulation techniques for charge deposition and induced current.

1. The number of electron and hole pairs created by a charged particle is sampled using Heed but the positions of the electrons and holes are (re-)distributed uniformly along the track. Electrons and holes are drifted in a uniform electric field. For calculating the induced current, a constant weighting field (corresponding to an unsegmented readout pad) is used.

2. As in case 1, constant drift and weighting fields are assumed but spatial fluctuations in the ionization process as simulated by Heed are taken into account.

3. As in case 2, the spatial ionization profile calculated using Heed is used. For evaluating the weighting field, a field map (calculated using Ansys) for a pixel geometry is used. This is the most realistic case considered here.

The response of the front-end electronics can be described by the transfer function [168]

$$f(t) = \tau_{ac}\tau_r \left[f_1(t) + f_2(t) + f_3(t) + f_4(t) \right],$$

with

$$
\begin{aligned}
f_1(t) &= \frac{-\mathrm{e}^{-t/\tau_{ac}}\tau_{ac}}{(\tau_{ac} - \tau_i)^2 (\tau_{ac} - \tau_r)}, &\qquad f_2(t) &= \frac{t\mathrm{e}^{-t/\tau_i}}{(\tau_{ac} - \tau_i)\,\tau_i\,(\tau_i - \tau_r)}, \\
f_3(t) &= \frac{\mathrm{e}^{-t/\tau_r}\tau_r}{(\tau_{ac} - \tau_r)(\tau_r - \tau_i)^2}, &\qquad f_4(t) &= \frac{\mathrm{e}^{-t/\tau_i}\left(\tau_i^3 - \tau_{ac}\tau_i\tau_r\right)}{(\tau_{ac} - \tau_i)^2\,\tau_i\,(\tau_i - \tau_r)^2}, \\
\tau_r &= 5.6 \text{ ns}, &\qquad \tau_i &= 1.8 \text{ ns}, \qquad \tau_{ac} = 47 \text{ ns}.
\end{aligned}
$$

By convoluting the induced current with $f(t)$, we obtain the output signal of the preamplifier. As a next step, the pulse shape is compared against a threshold value and the threshold crossing times t_1 (leading edge) and t_2 (trailing edge) are determined. In the present calculation, the nominal discriminator threshold value, corresponding to 0.7 fC, was used. The time over threshold (ToT), $t_2 - t_1$, provides information about the deposited charge. Since t_1 is a monotonic function of the input charge, the ToT information can be used for a timewalk correction of t_1.

For each of the above-mentioned cases, a sample of 10000 tracks (10 GeV/c pions) with perpendicular incidence is simulated. Similarly to the procedure used in the experiment, a look-up-table (more precisely: a profile histogram) of ToT vs. t_1 is established. In a second pass, the distribution of the ToT-corrected arrival time t_1^{corr} is calculated. For the jitter of t_1^{corr}, we thus obtain $\sigma_1 = 71.0 \pm 0.5$ ps (statistical error) for case 1, $\sigma_2 = 105.7 \pm 0.7$ ps for case 2, and $\sigma_3 = 141.5 \pm 1.0$ ps for case 3. Assuming that the contributions to σ_3 due to ionization fluctuations and due to the variation of the weighting field add in quadrature, we obtain for the latter $\sqrt{\sigma_3^2 - \sigma_1^2} = 94.1$ ps. The contribution to the jitter due to the inhomogeneity of the weighting field can thus be seen to be of similar magnitude as the jitter due to ionization fluctuations.

In a beam test, the NA62 collaboration measured a single hit time resolution of ≈ 175 ps [169]. The difference between calculated and experimental results is qualitatively plausible considering that jitter due to electronic noise was neglected in the simulation.

6.5. Summary

The implementation of silicon detectors in Garfield++ profits from conceptual similarities with gas-based detectors, which exist in several areas of detector simulation such as the calculation of energy loss, the "macroscopic" transport of charge carriers in an electric field, and the evaluation of induced signals.

Energy Loss Two variants of the PAI model were made available: an interface to the Heed program (which uses the atomic photoabsorption cross-section) and an implementation based on the solid-state dielectric function, developed within this thesis work. For sensor thicknesses of the order of 100 µm and above, the calculated spectra according to both models are within the margin of experimental uncertainty. Using the phenomenological δ electron transport algorithm provided by Heed, spatial fluctuations of primary ionization which have significant impact on the spatial and time resolution (Sec. 6.4.2) can be simulated.

Field Calculation An interface to the device simulation program Synopsys Sentaurus Device was written which allows virtually arbitrary two- and three-dimensional field configurations to be simulated.

Charge Transport An extended version of the microscopic tracking method allowing for electron transport in silicon was implemented using literature data for scattering rates and band structure. For microscopic tracking with the currently implemented level of detail no obvious application could be identified yet. Since the mean distance between successive collisions of an electron (about $10 - 50$ nm) is small compared to typical feature sizes of silicon sensors, macroscopic simulation based on parameterized transport coefficients provides for most applications a sufficient approximation. It is possible however, that for novel detector structures with reduced feature size microscopic tracking will become relevant.

The implementation of silicon detector simulation in Garfield++ was not driven by a specific application but was intended as a "proof-of-principle" demonstration. For further developments, it would be beneficial to use the program embedded in a concrete R&D effort. The simulation methods mentioned above are not limited to silicon, but can also be extended to other semiconducting materials provided that the relevant material properties are known.

7. Software Aspects

This chapter outlines the motivations for developing Garfield++ and gives an overview of its design.

7.1. Motivation

"Classic" Garfield [15] is written in Fortran 77, which used to be the prevalent programming language in high-energy physics computing until the LHC era. Over the last 15 years or so, C++ has gradually replaced Fortran as the main language in this field. On the detector simulation side, Geant4 [11, 12] was developed as a successor of the Fortran based Geant3 program. The C++ based package ROOT [124] has emerged as a widely used framework for data analysis and other aspects of computing. Event generators like Pythia and Herwig have also been rewritten in C++ [10].

The dominance of C++ implicates that many physicists working in particle physics and related areas such as instrumentation have nowadays at least a basic knowledge of this programming language, while Fortran literacy is diminishing. In order to encourage users to look into the source code and add their own contributions, thus trying to steer the development process towards a more collaborative style, a migration of Garfield to C++ was initiated.

Making the procedures of Fortran Garfield accessible via wrapper classes would be a simple method to give the program a C++ appearance. Instead of executing a set of instructions in the native scripting language, users could include these wrapper objects in a C++ program and combine them at liberty with elements from other packages such as ROOT.

Such a merely "cosmetic" approach is unsatisfactory, though.

- Instead of making the algorithms used in the program more transparent to non-experts of Fortran, the parts of the code doing actual calculations are hidden from the user.

- The layout of the Fortran code imposes restrictions on the class structure of the wrapper. For instance, in a C++ program one would typically integrate all functionality pertaining to the handling of gas properties (e. g. specification of the gas composition, interpolation of gas tables) in a dedicated class. In the "wrapping" approach, the variables describing the gas properties are not encapsulated in the C++ class, but are stored in Fortran common blocks. As a consequence, all instances of the class would share the same data. In order to avoid inconsistencies, the class object should, therefore, be implemented as a singleton. The same is true for other aspects of the program like electric fields or signals. A genuine object-oriented design is not possible.

- Garfield uses a number of modules from the Cern program library (CERNLIB). This might lead to compilation problems in the future, because this library is no longer supported. In order to ensure the long-term maintainability of the program, dependencies on CERNLIB should thus be kept at a minimum.

material properties   detector description

- gas → Magboltz

- silicon   field calculation

    - analytic

    - field maps

    - neBEM

primary ionization   charge transport

- Heed   - microscopic

- ...   transport   - MC

                                                                       - RKF
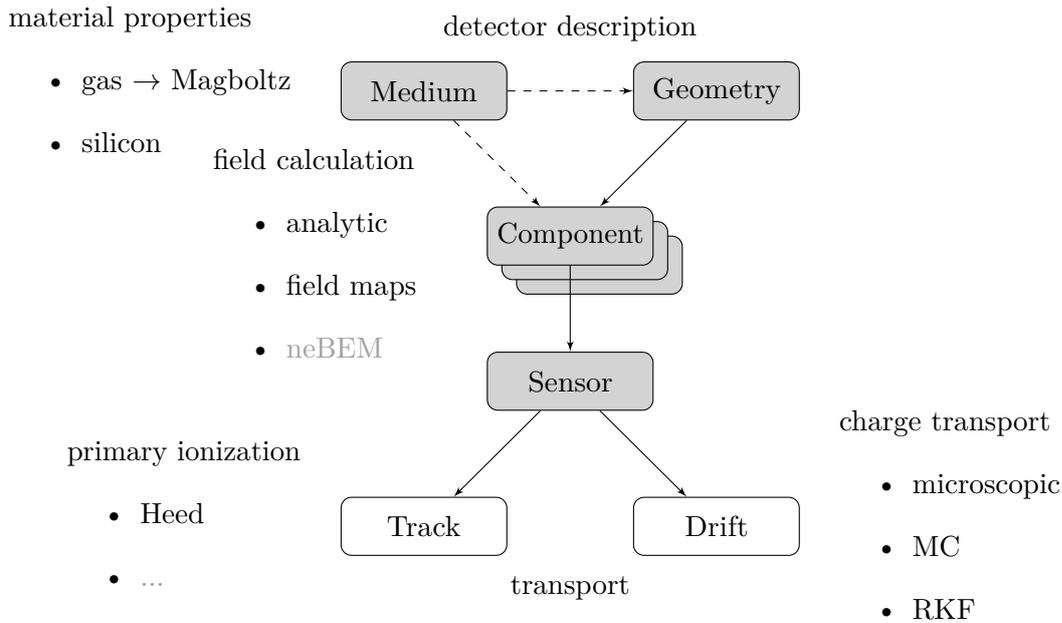
Figure 7.1. Overview of the main class categories in Garfield++ and their interrelations. A detailed explanation is given in the text.

Rewriting the program from scratch has the advantage that one can rethink its architecture and adapt it to the simulation needs of current detector development efforts. Since the source code of Garfield – not including Heed and Magboltz – comprises at present about 160000 lines of code[1], translating it to another language is not only a very time-consuming task but also introduces inevitably some bugs.

For the development of Garfield++ [16] a step-wise, application-driven approach was taken. By translating pieces of code only if their functionality is needed for a concrete simulation study, and by benchmarking calculations against the Fortran version, it is hoped that serious bugs can be detected and eliminated at an early stage. Since the start of the project (a first prototype was written at the end of 2009), the C++ version has steadily grown, currently counting about 60000 lines of code. As the development of Garfield++ was initiated in the context of the RD51 collaboration, it has been used mainly for MPGD simulations so far. A non-exhaustive list of examples can be found on the webpage [16].

7.2. Class Structure

The design philosophy of Garfield++ is to provide a collection of C++ classes to be used as building blocks of a detector simulation program.

An overview of the class structure is given in Fig. 7.1. Two main categories can be distinguished: (1) classes dealing with the transport of particles, and (2) classes providing a "static" description of the detector. The latter group comprises classes describing the relevant material properties (labelled `Medium` in Fig. 7.1), classes representing the geometry, and classes dealing with the calculation of fields (labelled `Component` in Fig. 7.1). More precisely, the main purpose of

---

[1] Even if obsolete parts of the code and subroutines dealing with graphics, histogramming, fitting etc. (i. e. functionality which can, to some extent, be outsourced to ROOT) are subtracted, one is left with an "irreducible" core of about 100000 lines of code.

`Component` classes is to provide, for a given point (x, y, z) inside the detector, the electric and magnetic field and a pointer to the `Medium` at this location. As schematically illustrated in Fig. 7.1, a detector can be described by several `Components`, which are also allowed to overlap. Combinations and superpositions of electric, magnetic and weighting fields calculated using different techniques are thus possible. The `Sensor` class, which is basically an assembly of `Component` objects, acts as a central interface to the transport classes and, in addition, takes care of signal calculations.

The class concept of Garfield++ was devised with a view to minimizing mutual dependencies between the individual objects. In Fig. 7.1, the class "hierarchy" is indicated by the directions of the arrows. For instance, a `Track` class requires a description of the detector in form of a `Sensor` object, whereas, casually speaking, the `Sensor` does not "know" about the transport classes in which it is used. Further, a `Track` class depends only on the `Sensor` but has no reference to the hierarchically subordinate `Component` class. As an illustration of the interrelations between the objects discussed above, consider the following minimal code example.

```cpp
// Setup the gas.
MediumMagboltz* gas = new MediumMagboltz();
gas->SetComposition("ar", 80., "co2", 20.);
// Create a field map component.
ComponentAnsys123* fm = new ComponentAnsys123();
fm->Initialise("ELIST.lis", "NLIST.lis", "MPLIST.lis", "PRNSOL.lis");
for (int i = fm->GetNumberOfMaterials(); i--;) {
  // The gas is identified by its dielectric constant.
  if (fabs(fm->GetPermittivity(i) - 1.) < 1.e-3) fm->SetMedium(i, gas);
}
// Assemble a sensor.
Sensor* sensor = new Sensor();
sensor->AddComponent(fm);
// Create a class for microscopic tracking.
AvalancheMicroscopic* aval = new AvalancheMicroscopic();
aval->SetSensor(sensor);
...
```

In this case, the geometry of the detector is fully determined by the field map. A separate `Geometry` object is thus not necessary; it is sufficient to associate the regions in the field map where charge transport is to be enabled with a `Medium` class (lines 7 – 10). In order to be able to transport electrons through the field map (in this case using the microsopic tracking technique), a pointer to a `Sensor` object is passed to the `AvalancheMicroscopic` class (line 16). The `Sensor` in turn holds a pointer (more generally, a list of pointers) to a `Component` object.

Some of the above class categories bear resemblance to "sections" in (Fortran) Garfield scripts. `Medium` classes, for instance, can be regarded as the counterpart of the `&GAS` section, `Component` classes are similar (but not identical) in scope to the `&CELL` section. These similarities might help users accustomed to Garfield to become familiar with the C++ version.

In addition to the classes discussed so far, Garfield++ also includes classes for visualization purposes such as plotting drift lines, making a contour plot of the electrostatic potential, or inspecting the layout of the detector. Whereas these auxiliary classes rely extensively on ROOT, the core framework shown in Fig. 7.1 was, as far as possible, decoupled from external software.

7.3. Summary

Garfield++ is an object-oriented toolkit for the simulation of ionization-based particle detectors. It shares functionality with and inherits many algorithms of the Fortran program Garfield, but has been rewritten from scratch in C++. The focus of applications is currently in the domain of micropattern gas detector R&D, for example for LHC upgrade studies.

Outlook

At present, the following methods for calculating electric fields are available:

- semi-analytic (two-dimensional) solutions for configurations of wires and planes;

- interpolation of field maps created with the finite element programs Ansys, Elmer, and CST;

- interpolation of field maps created with the device simulation program Synopsys Sentaurus [152].

In the near future, an interface to the (three-dimensional) neBEM field solver should be made available. This requires a geometry package which is capable of discretizing surfaces into rectangles and rectangular triangles (with consideration of overlaps). A third-party open-source software with this feature could not be found yet. In Garfield, the internal graphics library is used for this purpose. Porting this library to C++ (or wrapping it) seems at present the most promising (albeit cumbersome) solution.

Depending on demand, other procedures available in Fortran Garfield (e. g. additional interfaces to finite element programs, field optimization etc.) might also be translated or reimplemented. Otherwise, future work should focus on aspects which are complementary to the traditional scope of Garfield.

Finally, it should be mentioned that an interface between Garfield++ and Geant4 is in preparation [170]. This effort is primarily motivated by the idea of enabling detailed simulations of gas-based detectors within the Geant framework; such an interface is also attractive from the Garfield perspective however, since it provides access to the rich catalog of physics processes available in Geant.

8. Summary

Within the framework of the present thesis, an object-oriented version of the detector simulation program Garfield was developed. A key feature of this toolkit (Garfield++) is a refined treatment of electron transport: instead of calculating drift lines based on macroscopic transport parameters, electrons are traced through individual collisions with gas atoms or molecules. The viability of this so-called "microscopic" tracking method for modelling drift and diffusion in small-scale devices was demonstrated by comparing simulation results and measurement data from literature for the electron transparency of a single GEM.

Using the same technique the statistics of electron avalanches in gas detectors were examined. Up to now, gas gain fluctuations used to be modelled in terms of a phenomenological parameterization (Pólya distribution) or – in case of uniform fields – using toy models the physical basis and numerical evaluation of which were discussed in Section 3.2.2. Unlike these previous approaches, the "microscopic" simulation procedure allows a quantitative prediction of the relative variance of gain spectra. This was verified by comparing simulation results with experimental data for parallel-plate chambers from literature. For methane, which is the only gas for which two independent measurements are available, excellent agreement was found. The method was then used to investigate gain fluctuations in parallel-plate chambers, wire chambers, Micromegas and GEMs.

- A toy model providing an intuitive explanation for the impact of gas mixture and electric field on the relative variance in uniform fields was proposed and shown to be consistent with the simulation.

- A study of avalanche fluctuations in noble gas based mixtures was carried out. In line with the above mentioned model, neon mixtures were found to exhibit a lower relative variance than argon based mixtures (at the same Townsend coefficient) since exciting collisions are less abundant (compared to ionizing collisions) than in Ar.

- The relative variance in non-uniform field configurations is correlated with the mean field E_2 at which the first ionization occurs.

- In GEMs, E_2 increases with increasing potential difference U_{GEM} between the electrodes on the foil. The relative variance is lower than in a uniform field of strength E_2 due to losses.

- In wire chambers, E_2 decreases with increasing sense wire potential. For a given gas composition and density, the relative variance increases with increasing mean gain.

As demonstrated in Section 4.3, the "microscopic" transport method can also be used for simulating δ electrons. Unlike for phenomenological calculations, the energy dependence of the characteristic parameters such as W value, Fano factor, and range emerges naturally. The W value as function of the electron energy in Ar, N_2, CH_4, and CO_2 could be reproduced within the spread of experimental data.

For the calculation of both avalanche and primary ionization statistics in Penning gas mixtures, excitation transfer needs to be included in the simulation. Two approaches were explored: (1)

modelling excitation transfers in terms of an empirical average transfer efficiency and (2) a detailed simulation of the deexcitation processes on an atomic level. Using the former method, estimates for the impact of Penning transfer on cluster density, W value, Fano factor, and relative variance of gain spectra were made. For Ar/CO_2, for instance, it was found that

- the cluster density of minimum-ionizing electrons in Ar/CO_2 (90:10) is $6-10\%$ higher compared to a calculation without Penning transfer,

- the W value exhibits a minimum around a concentration of $\approx 8\%$ CO_2,

- the relative variance f of the avalanche size distribution in Ar/CO_2 (90:10) is $\approx 12\%$ lower compared to a calculation without Penning transfer.

A proof-of-principle demonstration of the viability of the second approach was given in Chapter 5. The average transfer efficiencies in Ar/CO_2, Ar/CH_4, Ar/C_2H_6, and Ar/C_2H_2 could be reproduced using a set of microscopic parameters based on literature data and fitted values.

While originally developed for the simulation of gas-based detectors, a number of calculation techniques available in Garfield can – with appropriate modifications – be applied to the simulation of silicon sensors. The PAI model, for instance, can be used for primary ionization calculations in both gases and semiconductors. The impact of the level of detail in the modelling of the photoabsorption cross-section on the ionization mean free path in gases and on energy deposition spectra in silicon was examined in Sections 4.2 and 6.1, respectively.

Using PAI model based simulation of primary ionization, electric field calculation using device simulation programs, and "macroscopic" transport of electrons and holes, Garfield++ allows one to simulate a broad class of silicon sensors.

A. Appendix

A.1. Inelastic Scattering of Charged Particles

We consider the scattering of a charged particle with mass M and charge ze by the Coulomb field of an atom within the framework of non-relativistic quantum theory. The following derivation of the stopping power is based on Refs. [171, 172].

In first order perturbation theory, the transition rate $w_{i \to f}$ between two eigenstates $|i\rangle, |f\rangle$ of the unperturbed Hamiltonian can be calculated using Fermi's "golden rule"

$$w_{i \to f} = \frac{2\pi}{\hbar} |\langle f| U |i\rangle|^2 \rho_f, \tag{A.1}$$

where ρ_f is the density of final states.

The particle is represented by a plane wave with incident wave vector $\mathbf{K}$ and outgoing wave vector $\mathbf{K}'$. As a result of the collision, the atom is promoted from its ground state $|0\rangle$ with energy ϵ_0 to an excited state $|j\rangle$ with energy ϵ_j. The interaction Hamiltonian is given by

$$U = ze^2 \left[\frac{Z}{r} - \sum_{i=1}^{Z} \frac{1}{|\mathbf{r} - \mathbf{r}_i|} \right].$$

Hence, we have to evaluate the matrix element

$$\langle j, \mathbf{K}'| U |0, \mathbf{K}\rangle = \int \mathrm{d}^3 r \int \mathrm{d}^{3Z} r_i \mathrm{e}^{\mathrm{i}\mathbf{k}\cdot\mathbf{r}} ze^2 \left[\frac{Z}{r} - \sum_{i=1}^{Z} \frac{1}{|\mathbf{r} - \mathbf{r}_i|} \right] \varphi_0(\mathbf{r}_i) \varphi_j^*(\mathbf{r}_i),$$

where $\mathbf{k} = \mathbf{K} - \mathbf{K}'$.

Because of the orthogonality of the atomic states, the first term ($\propto 1/r$) vanishes. The second term can be evaluated using a "trick" [171]. The electrostatic potential associated to a charge density $\rho(\mathbf{r})$ is given by

$$V(\mathbf{r}) = \int \mathrm{d}^3 r' \frac{\rho(\mathbf{r}')}{|\mathbf{r} - \mathbf{r}'|}.$$

For a point charge $\rho(\mathbf{r}) = \delta(\mathbf{r} - \mathbf{r}_i)$, the Fourier components $V_{\pm\mathbf{k}}$ of the potential are

$$V_{\pm\mathbf{k}} = \frac{1}{(2\pi)^{3/2}} \int \mathrm{d}^3 r \frac{\mathrm{e}^{\mp\mathrm{i}\mathbf{k}\cdot\mathbf{r}}}{|\mathbf{r} - \mathbf{r}_i|}.$$

By comparison with the Poisson equation,

$$V_{\pm\mathbf{k}} = \frac{1}{(2\pi)^{3/2}} \frac{4\pi}{k^2} \mathrm{e}^{\mp\mathrm{i}\mathbf{k}\cdot\mathbf{r}_i},$$

one obtains

$$\int \mathrm{d}^3 r \frac{\mathrm{e}^{\pm\mathrm{i}\mathbf{k}\cdot\mathbf{r}}}{|\mathbf{r} - \mathbf{r}_i|} = \frac{4\pi}{k^2} \mathrm{e}^{\pm\mathrm{i}\mathbf{k}\cdot\mathbf{r}_i}.$$

The matrix element is thus given by

$$\left|\langle j, \mathbf{K}'| \, U \, |0, \mathbf{K}\rangle\right|^2 = \frac{1}{V^2} \frac{4 \, (2\pi)^2 \, z^2 e^4}{k^4} \, |F_{j0}(\mathbf{k})|^2 \, ,$$

where F_{j0} denotes the form factor

$$F_{j0}(\mathbf{k}) = \left\langle j \left| \sum_{i=1}^{Z} e^{i\mathbf{k}\cdot\mathbf{r}_i} \right| 0 \right\rangle.$$

Inserting the density of final states,

$$\rho_f = \delta\left(\frac{\hbar^2}{2M} \left(K^2 - K'^2 \right) - (\epsilon_j - \epsilon_0) \right) \frac{V \mathrm{d}^3 p'}{(2\pi\hbar)^3}, \qquad \mathrm{d}^3 p' = \hbar^3 K'^2 \mathrm{d}K' \mathrm{d}\Omega,$$

and integrating over K' yields

$$\mathrm{d}w_j = \frac{1}{V} \frac{4z^2 e^4}{\hbar k^4} \, |F_{j0}(\mathbf{k})|^2 \, \frac{M K'}{\hbar^2} \mathrm{d}\Omega.$$

The transition rate w is the product of the scattering cross-section σ and the incident probability current density j_{in},

$$w = \sigma j_{\mathrm{in}}.$$

With $j_{\mathrm{in}} = \frac{1}{V} \frac{\hbar K}{M}$ the differential cross-section reads

$$\frac{\mathrm{d}\sigma_j}{\mathrm{d}\Omega} = \frac{4z^2 e^4 M^2}{\hbar^4 k^4} \frac{K'}{K} \, |F_{j0}(\mathbf{k})|^2 \, .$$

Using

$$k^2 = K^2 + K'^2 - 2KK' \cos\theta \to \mathrm{d}\Omega = \frac{2\pi k \mathrm{d}k}{KK'}$$

one obtains for the differential cross-section with respect to the momentum transfer k

$$\frac{\mathrm{d}\sigma_j}{\mathrm{d}k} = \frac{8\pi z^2 e^4 M^2}{\hbar^4 K^2} \frac{|F_{j0}(\mathbf{k})|^2}{k^3}. \tag{A.2}$$

For the scattering off free electrons, i. e. $|F_{j0}(\mathbf{k})|^2 = 1$, one obtains the Rutherford cross-section

$$\frac{\mathrm{d}\sigma}{\mathrm{d}E} = \frac{2\pi z^2 \, (\alpha_f \hbar c)^2}{m_e c^2} \frac{1}{\beta^2 E^2}, \qquad E = \frac{\hbar^2 k^2}{2m_e}. \tag{A.3}$$

The total cross-section is obtained by integrating[1] (A.2) over k and summing over all possible transitions,

$$\sigma = \sum_j \sigma_j = \frac{8\pi z^2 e^4 M^2}{\hbar^4 K^2} \sum_j \int_{k_{\mathrm{min}}}^{k_{\mathrm{max}}} \mathrm{d}k \frac{|F_{j0}(k)|^2}{k^3}.$$

In the non-relativistic case considered here, the maximum momentum which can be transferred to an electron by the primary particle is given by

$$\hbar k_{\mathrm{max}} = \frac{2m_e M}{m_e + M} \beta c,$$

---

[1] It is assumed here that the form factor is isotropic.

which for $M \gg m_e$ can be approximated by $\hbar k_{\max} \approx 2m_e \beta c$. For electrons, $\hbar k_{\max} = m_e \beta c / \sqrt{2}$. The minimum momentum transfer is given by

$$\hbar k_{\min} = \frac{\epsilon_j - \epsilon_0}{\beta c}. \tag{A.4}$$

For the stopping power

$$\frac{\mathrm{d}E}{\mathrm{d}x} = -\sum_j N \int \mathrm{d}k \frac{\mathrm{d}\sigma_j}{\mathrm{d}k} (\epsilon_j - \epsilon_0)$$

one obtains by inserting (A.2)

$$\frac{\mathrm{d}E}{\mathrm{d}x} = -\frac{8\pi z^2 e^4 M^2 N}{\hbar^4 K^2} \sum_j \int_{k_{\min}}^{k_{\max}} \mathrm{d}k \frac{|F_{j0}|^2}{k^3} (\epsilon_j - \epsilon_0). \tag{A.5}$$

A.1.1. Sum Rules

The following derivation is taken from Ref. [171], where also a more general discussion of sum rules can be found. The quantum mechanical expression for the stopping power derived in the previous section involves the sum

$$
\begin{aligned}
S &= \sum_j |F_{j0}(\mathbf{k})|^2 (\epsilon_j - \epsilon_0) = \sum_j \langle j| F |0\rangle \langle 0| F^* |j\rangle (\epsilon_j - \epsilon_0) \\
&= \sum_j \langle 0| F^* |j\rangle \langle j| [H_0, F] |0\rangle = \langle 0| F^* [H_0, F] |0\rangle.
\end{aligned}
$$

The potential part of the atomic Hamiltonian commutes with F,

$$
\begin{aligned}
[H_0, F] &= -\frac{\hbar^2}{2m_e} \left[\sum_j \Delta_j, \sum_i e^{i\mathbf{k}\cdot\mathbf{r}_i} \right] \\
&= \frac{\hbar^2}{2m_e} \sum_{i,j} e^{i\mathbf{k}\cdot\mathbf{r}_i} \delta_{ij} \left(k^2 - i\mathbf{k} \cdot \nabla_j \right) \\
&= \frac{\hbar^2}{2m_e} \sum_j e^{i\mathbf{k}\cdot\mathbf{r}_j} \left(k^2 - i\mathbf{k} \cdot \nabla_j \right).
\end{aligned}
$$

As the ground state is real ($\varphi_0^* = \varphi_0$), one can write

$$S = \frac{\hbar^2}{2m_e} \sum_{i \neq j} \int \mathrm{d}^{3Z} r_a e^{-i\mathbf{k}\cdot(\mathbf{r}_i - \mathbf{r}_j)} \left(k^2 - i\mathbf{k} \cdot \nabla_j \right) \varphi_0^2 (\mathbf{r}_a) + \frac{\hbar^2}{2m_e} \sum_i \int \mathrm{d}^{3Z} r_a \left(k^2 - i\mathbf{k} \cdot \nabla_i \right) \varphi_0^2 (\mathbf{r}_a).$$

Partial integration over the terms involving the gradients and discarding the surface terms shows that the two terms in the first integral cancel each other out and that the second term in the second integral vanishes. Hence, one obtains

$$\frac{2m_e}{\hbar^2 k^2 Z} \sum_j |F_{j0}(\mathbf{k})|^2 (\epsilon_j - \epsilon_0) = 1. \tag{A.6}$$

This is the Bethe sum rule. The quantity

$$\frac{2m_e}{\hbar^2 k^2 Z} |F_{j0}(\mathbf{k})|^2 (\epsilon_j - \epsilon_0)$$

is called the generalized oscillator strength.

In terms of the loss function, the Bethe sum rule reads

$$\int\limits_0^\infty \mathrm{d}\omega \, \mathrm{Im}\left(\frac{-1}{\varepsilon\left(k,\omega\right)}\right)\omega = \frac{2\pi^2 e^2 NZ}{m_e} = \frac{\pi}{2}\omega_p^2. \tag{A.7}$$

In the limit of small momentum transfer $\hbar k$, the exponential in the form factor can be approximated by an expansion to linear order (dipole approximation). The generalized oscillator strength then reduces to the optical oscillator strength

$$f_{j0} = \frac{2m_e}{3\hbar^2 Z}\left|\langle j|\sum_i \mathbf{r}_i\,|0\rangle\right|^2 (\epsilon_j - \epsilon_0)$$

which satisfies the Thomas-Reiche-Kuhn (TRK) sum rule

$$\sum_j f_{j0} = 1. \tag{A.8}$$

In terms of the optical loss function, the TRK sum rule becomes

$$\int\limits_0^\infty \mathrm{d}\omega \, \mathrm{Im}\left(\frac{-1}{\varepsilon\left(\omega\right)}\right)\omega = \frac{\pi}{2}\omega_p^2. \tag{A.9}$$

A.1.2. Stopping Power

Owing to the Bethe sum-rule (A.6), the evaluation of the stopping power (A.5) would be greatly simplified if the summation over the states j and the integration over k were interchangeable:

$$\frac{\mathrm{d}E}{\mathrm{d}x} = -\frac{8\pi z^2 e^4 M^2}{\hbar^4 K^2}N\int\limits_{\overline{k}_{\mathrm{min}}}^{\overline{k}_{\mathrm{max}}}\frac{\mathrm{d}k}{k}\sum_j \frac{|F_{j0}|^2}{k^2}(\epsilon_j - \epsilon_0) = -\frac{4\pi z^2 e^4}{\beta^2 m_e c^2}NZ\ln\frac{\overline{k}_{\mathrm{max}}}{\overline{k}_{\mathrm{min}}}.$$

Since the lower limit of the integral depends on ϵ_j, the above equation is strictly speaking not correct and represents an approximation.

Therefore, the minimum and maximum momentum transfers have been replaced by average values $\overline{k}_{\mathrm{min}}, \overline{k}_{\mathrm{max}}$. To obtain the effective minimum momentum $\overline{k}_{\mathrm{min}}$, an appropriate average of (A.4) needs to be taken. In terms of an effective ionization potential I, $\overline{k}_{\mathrm{min}}$ is expressed as

$$\overline{k}_{\mathrm{min}} = \frac{I}{\beta c}.$$

One then obtains the non-relativistic Bethe stopping formula

$$\frac{\mathrm{d}E}{\mathrm{d}x} = -\frac{4\pi z^2 e^4}{m_e c^2}NZ\frac{1}{\beta^2}\ln\frac{2m_e c^2 \beta^2}{I}. \tag{A.10}$$

In a relativistic treatment, not only the Coulomb potential but also the vector potential need to be considered. The relativistic version of the Bethe stopping formula is

$$\frac{\mathrm{d}E}{\mathrm{d}x} = -\frac{4\pi z^2 e^4}{m_e c^2}NZ\frac{1}{\beta^2}\left[\ln\frac{2m_e c^2 \beta^2 \gamma^2}{I} - \beta^2\right]. \tag{A.11}$$
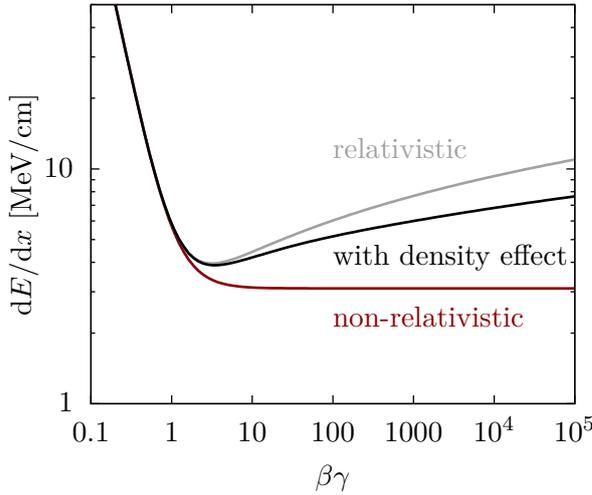
Figure A.1 Stopping power $\mathrm{d}E/\mathrm{d}x$ of Si ($I = 173$ eV) as a function of $\beta\gamma$ according to the non-relativistic expression (A.10), the relativistic expression (A.11) and the standard Bethe-Bloch formula (A.12) including the density effect correction δ_F (Sternheimer parameterization).

The derivation of this formula (see e. g. Ref. [22]) involves several approximations. In order to obtain a realistic description of the stopping power, additional correction terms are necessary. At high incident energies, the polarization of the medium reduces the energy loss. With a correction term δ_F accounting for this so-called density effect, the Bethe-Bloch equation for heavy particles reads [5]

$$\frac{\mathrm{d}E}{\mathrm{d}x} = -\frac{4\pi z^2 e^4}{m_e c^2} N Z \frac{1}{\beta^2} \left[\ln \frac{2 m_e c^2 \beta^2 \gamma^2}{I} - \beta^2 - \frac{\delta_F}{2} \right]. \tag{A.12}$$

A parameterization of δ_F and numerical values for various materials are given in [173]. For further refinement, additional correction terms can be taken into account.

- The above treatment of inelastic scattering was based on the assumption that the velocity of the incident particle is high compared with that of the atomic electrons. If this assumption is not valid, a further correction term (shell correction term) needs to be added.

- Measurements indicate that the stopping power of negative charged particles is lower than that of their anti-particles [28]. This so-called Barkas effect can be taken into account by a correction term $\propto z^3$.

A special treatment is required for electrons for which exchange effects and the Pauli principle need to be considered.

In Fig. A.1, the stopping power $\mathrm{d}E/\mathrm{d}x$ is plotted as a function of $\beta\gamma$. The $1/\beta^2$-dependence can be seen to dominate at low velocities. At $\beta\gamma \approx 3 \ldots 4$ the stopping power exhibits a minimum. Particles in this range are commonly referred to as minimum ionizing particles (mip). Beyond the minimum ionizing region the stopping power rises logarithmically. The relativistic rise is reduced by the density effect which leads to a saturation of $\mathrm{d}E/\mathrm{d}x$ at high energies.

A.1.3. Landau Distribution

If the total cross-section σ is constant, the number of collisions n over a distance x follows a Poisson distribution

$$w(n) = \frac{\overline{n}^n}{n!} e^{-\overline{n}}$$

around the mean $\overline{n} = N\sigma x$.

The probability of losing an amount of energy ϵ in a single collision is given by

$$f(\epsilon) = \frac{1}{\sigma}\frac{\mathrm{d}\sigma}{\mathrm{d}\epsilon}.$$

The probability of losing a total amount of energy E in n collisions follows from n-fold convolution of f. The probability $p(E,x)$ of losing a total amount of energy E over a distance x is then given by

$$p(E,x) = \sum_{n=0}^{\infty} w(n)\underbrace{f\otimes f\otimes\cdots\otimes f}_{n\text{ times}}(E).$$

In the Laplace domain one obtains

$$\begin{aligned}
P(s,x) &= \mathrm{e}^{-\bar{n}}\sum_{n=0}^{\infty}\frac{\bar{n}^n}{n!}F(s)^n \\
&= \exp\left[-Nx\int_0^{\infty}\mathrm{d}\epsilon\,(1-\mathrm{e}^{-s\epsilon})\frac{\mathrm{d}\sigma}{\mathrm{d}\epsilon}\right].
\end{aligned}$$

The following derivation is due to L. D. Landau [174]. The integral over ϵ is split into two parts:

$$\int_0^{\infty}\mathrm{d}\epsilon\,(1-\mathrm{e}^{-s\epsilon})\frac{\mathrm{d}\sigma}{\mathrm{d}\epsilon} = \int_0^{\epsilon_1}\mathrm{d}\epsilon\,(1-\mathrm{e}^{-s\epsilon})\frac{\mathrm{d}\sigma}{\mathrm{d}\epsilon} + \int_{\epsilon_1}^{\infty}\mathrm{d}\epsilon\,(1-\mathrm{e}^{-s\epsilon})\frac{\mathrm{d}\sigma}{\mathrm{d}\epsilon}.$$

The energy ϵ_1 is chosen such that $\epsilon_1 \gg \epsilon_0$ and $s\epsilon_1 \ll 1$, where ϵ_0 is of the order of the binding energy. Further, the maximum energy transfer $\epsilon_{\max}$ is assumed to satisfy $s\epsilon_{\max} \gg 1$. In the first integral the approximation $\mathrm{e}^{-s\epsilon}\approx 1-s\epsilon$ is used:

$$\int_0^{\epsilon_1}\mathrm{d}\epsilon\frac{\mathrm{d}\sigma}{\mathrm{d}\epsilon}(1-\mathrm{e}^{-s\epsilon}) \approx s\int_0^{\epsilon_1}\mathrm{d}\epsilon\frac{\mathrm{d}\sigma}{\mathrm{d}\epsilon}\epsilon.$$

The contribution to the stopping power by energy transfers exceeding ϵ_1 can be calculated from the cross-section for scattering of spin-0 particles by free electrons

$$\int_{\epsilon_1}^{\epsilon_{\max}}\mathrm{d}\epsilon\frac{2\pi z^2 e^4 Z}{m_e c^2\beta^2}\frac{1}{\epsilon^2}\left(1-\frac{\beta^2}{\epsilon_{\max}}\right) \approx \frac{2\pi z^2 e^4 Z}{m_e c^2\beta^2}\left(\ln\frac{\epsilon_{\max}}{\epsilon_1}-\beta^2\right).$$

Hence,

$$\int_0^{\epsilon_1}\mathrm{d}\epsilon\frac{\mathrm{d}\sigma}{\mathrm{d}\epsilon}(1-\mathrm{e}^{-s\epsilon}) \approx \frac{2\pi z^2 e^4 Z}{m_e c^2\beta^2}\left(\ln\frac{2m_e c^2\beta^2\gamma^2\epsilon_1}{I^2}-\beta^2\right) = \frac{2\pi z^2 e^4 Z}{m_e c^2\beta^2}\ln\frac{\epsilon_1}{\epsilon'}.$$

In the second integral, the Rutherford cross-section

$$\frac{\mathrm{d}\sigma}{\mathrm{d}\epsilon} = \frac{2\pi z^2 e^4 Z}{m_e c^2\beta^2}\frac{1}{\epsilon^2}$$

is used. Because of the rapid convergence of the integral for $s\epsilon \gg 1$, the upper integration limit can be extended beyond $\epsilon_{\max}$. Partially integrating and substituting $z = s\epsilon$ yields

$$\int_{\epsilon_1}^{\infty}\mathrm{d}\epsilon\frac{1-\mathrm{e}^{-s\epsilon}}{\epsilon^2} = \underbrace{\frac{1-\mathrm{e}^{-s\epsilon_1}}{\epsilon_1}}_{\approx s}+s\int_{s\epsilon_1}^{\infty}\mathrm{d}z\frac{\mathrm{e}^{-z}}{z} \approx s\left(1+\int_{s\epsilon_1}^{1}\frac{\mathrm{d}z}{z}+\underbrace{\int_0^{1}\mathrm{d}z\frac{\mathrm{e}^{-z}-1}{z}+\int_1^{\infty}\mathrm{d}z\frac{\mathrm{e}^{-z}}{z}}_{-C=-0.577215665...}\right).$$
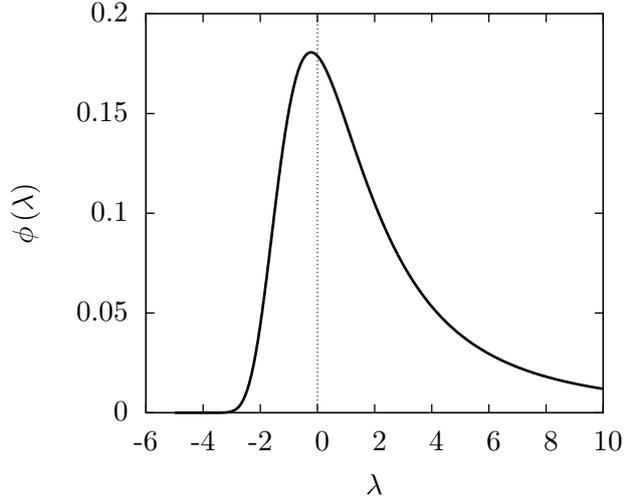
Figure A.2 Landau straggling function $\phi(\lambda)$, as implemented in ROOT [124].

For $P(s,x)$ one obtains

$$P(s,x) = \exp\left[-\xi s \left(1 - \ln s\epsilon' - C\right)\right],$$

where the variable

$$\xi = x\frac{2\pi z^2 e^4 N Z}{m_e c^2 \beta^2}$$

has been introduced. The original function $p(E,x)$ thus reads

$$p(E,x) = \frac{1}{2\pi i} \int\limits_{c-i\infty}^{c+i\infty} \mathrm{d}s\, \mathrm{e}^{sE - \xi s(1 - \ln s\epsilon' - C)}.$$

By substituting $u = \xi s$ and introducing the dimensionless variable

$$\lambda = \frac{1}{\xi}\left(E - \xi\left(\ln\frac{\xi}{\epsilon'} + 1 - C\right)\right),$$

$p(E,x)$ can be expressed as

$$p(E,x) = \frac{1}{\xi}\phi(\lambda)$$

where

$$\phi(\lambda) = \frac{1}{2\pi i} \int\limits_{c-i\infty}^{c+i\infty} \mathrm{d}u\, \mathrm{e}^{u\ln u + \lambda u}. \tag{A.13}$$

The function $\phi(\lambda)$, plotted in Fig. A.2, has a maximum at $\lambda \approx -0.222782$. The most probable energy loss is, therefore, given by

$$E_{\mathrm{mp}} = \xi\left(\ln\frac{\xi}{\epsilon'} + 0.2\right). \tag{A.14}$$

A.2. Avalanche Models

A.2.1. Yule-Furry Distribution

Let us assume that the distance between successive ionizing collisions of an electron is exponentially distributed with a mean free path $\lambda_{\mathrm{ion}} = \alpha^{-1}$ which depends only on the local electric field (not on the electron energy) and is, therefore, identical for all avalanche electrons (the spatial extent of the avalanche is neglected). The avalanche evolution can then be treated as a Yule-Furry process [175, 176]. The probability for an electron to produce a secondary electron while moving a step $\Delta x \ll \lambda_{\mathrm{ion}}$ along the electric field is given by $\alpha \Delta x$. For the probability that the avalanche has grown to a size of n electrons at a distance $x + \Delta x$ with respect to the initial electron's point of creation, one finds the equation [2]

$$P_n\left(x + \Delta x\right) = \left[1 - n\alpha\left(x\right)\Delta x\right] P_n\left(x\right) + \left(n - 1\right)\alpha\left(x\right)\Delta x P_{n-1}\left(x\right) + \mathcal{O}\left(\Delta x^2\right),$$

which in the limit $\Delta x \to 0$ becomes

$$\frac{\mathrm{d}}{\mathrm{d}x} P_n\left(x\right) = \alpha\left(x\right)\left(n - 1\right) P_{n-1}\left(x\right) - \alpha\left(x\right) n P_n\left(x\right). \qquad (A.15)$$

By means of the transformation $u = \int\limits_0^x \alpha\left(s\right)\mathrm{d}s$ [2] one obtains

$$\frac{\mathrm{d}}{\mathrm{d}u} P_n\left(u\right) = \left(n - 1\right) P_{n-1}\left(u\right) - n P_n\left(u\right). \qquad (A.16)$$

With the initial condition $P_n\left(0\right) = \delta_{n1}$, the solution of this differential equation is given by the geometric distribution

$$P_n\left(x\right) = \frac{1}{\overline{n}}\left(1 - \frac{1}{\overline{n}}\right)^{n-1} \qquad (A.17)$$

with mean

$$\overline{n} = \exp\left(\int\limits_0^x \alpha\left(s\right)\mathrm{d}s\right)$$

and variance $\sigma^2 = \overline{n}\left(\overline{n} - 1\right)$. For $\overline{n} \gg 1$, P_n is well approximated by the exponential distribution (3.2).

A.2.2. Pólya Distribution

In order to explain deviations of the avalanche size distribution from the exponential shape at large electric fields, Byrne [72, 177] and, independently, Lansiart and Morucci [70] proposed to amend the field-dependent Townsend coefficient by a factor depending on the instantaneous avalanche size n,

$$\alpha\left(x\right)\left(1 + \frac{\theta}{n}\right). \qquad (A.18)$$

The introduction of a size-dependent Townsend coefficient was originally motivated by the fact that electrons lose typically a large fraction of their kinetic energy in an ionizing collision and thus need to re-gain energy from the field before being able to ionize again. Consequently, a fluctuation towards larger n at a distance x would lead to a reduced fraction of electrons available for multiplication in the subsequent step $x + \mathrm{d}x$. This argument has been critized however, as being too simplistic [65]. An alternative, more plausible interpretation for (A.18) is that α is

reduced at high gain because of space charge. The following derivation of the Pólya distribution based on the ansatz (A.18) might rather be regarded as a model for the shape of avalanche size spectra at high gain than for the "rounding" effect observed in the proportional regime.

Inserting Eq. (A.18) into (A.15) leads to

$$\frac{\mathrm{d}}{\mathrm{d}u} P_n\left(u\right) = \left(n - 1 + \theta\right) P_{n-1}\left(u\right) - \left(n + \theta\right) P_n\left(u\right). \tag{A.19}$$

The solution of (A.19) is given by the negative binomial distribution

$$P_n = \binom{n - 1 + \theta}{n - 1} \left(\frac{\overline{n} - 1}{\overline{n} + \theta}\right)^{n-1} \left(\frac{\theta + 1}{\overline{n} + \theta}\right)^{\theta+1}, \tag{A.20}$$

with mean

$$\overline{n} = \left(\theta + 1\right) \exp\left(\int_0^x \alpha\left(s\right) \mathrm{d}s\right) - \theta$$

and variance

$$\sigma^2 = \frac{1}{\theta + 1} \left(\overline{n} + \theta\right) \left(\overline{n} - 1\right).$$

For large values of $\overline{n}$, the avalanche size can be treated as a quasi-continuous variable and (A.20) may be approximated by (3.4).

Assuming an ionization mean free path of the form $\alpha(x)/n$, leads to a Poisson distribution,

$$P_n = \frac{\overline{n}^n}{n!} \mathrm{e}^{-\overline{n}},$$

with variance $\sigma^2 = \overline{n}$.

Level	nl	Term	ϵ [eV]	f	Source
$1s_4$	4s	$^2[3/2]^o$	11.624	0.0609	NIST [117]
$1s_2$	4s	$^2[1/2]^o$	11.828	0.25	NIST [117]
$3d_5$	3d	$^2[1/2]^o$	13.864	0.0011	Berkowitz [95]
$2s_4$	5s	$^2[3/2]^o$	14.090	0.027	NIST [117]
$3d_2$	3d	$^2[3/2]^o$	14.153	0.0932	NIST [117]
$2s_2$	5s	$^2[1/2]^o$	14.255	0.0119	NIST [117]
$3s_1'$	3d	$^2[3/2]^o$	14.304	0.106	NIST [117]
$4d_5$	4d	$^2[1/2]^o$	14.711	0.0019	Berkowitz [95]
$3s_4$	6s	$^2[3/2]^o$	14.848	0.0144	Berkowitz [95]
$4d_2$	4d	$^2[3/2]^o$	14.859	0.048	Berkowitz [95]
$4s_1'$	4d	$^2[3/2]^o$	15.004	0.0209	Berkowitz [95]
$3s_2$	6s	$^2[1/2]^o$	15.022	0.0221	Berkowitz [95]
$5d_5$	5d	$^2[1/2]^o$	15.118	0.0041	Berkowitz [95]
$4s_4$	7s	$^2[3/2]^o$	15.186	0.0139	Berkowitz [95]
$5d_2$	5d	$^2[3/2]^o$	15.190	0.0426	Berkowitz [95]
$6d_5$	6d	$^2[1/2]^o$	15.308	0.00075	Lu and Lee [119]
$5s_1'$	5d	$^2[3/2]^o$	15.351	0.00051	Lu and Lee [119]
$4s_2$	7s	$^2[1/2]^o$	15.359	0.00074	Lu and Lee [119]
$5s_4$	8s	$^2[3/2]^o$	15.366	0.0130	Lu and Lee [119]
$6d_2$	6d	$^2[3/2]^o$	15.374	0.0290	Lu and Lee [119]

Table A.1. Oscillator strengths f for the Ar resonance levels included in Magboltz 8.9 [14].

A.3. Radiative Transition Rates

Unless indicated otherwise, the values for the transition rates given in Tables A.2, A.3, A.4, and A.5 are taken from the NIST atomic spectra database [117]. Theoretical values from Zatsarinny and Bartschat [118] are marked with a dagger (†). The values marked with a star (⋆) are calculated from the oscillator strengths recommended by Berkowitz [95]. Triangles (△) indicate that the respective value is based on the the oscillator strength calculated by Lee and Lu [119].

Level	Term	J	ϵ [eV]	Transition rate [ns^{-1}]
1s$_5$	$^2[3/2]^\circ$	2	11.548	
1s$_4$	$^2[3/2]^\circ$	1	11.624	0.119 (1p$_0$)
1s$_3$	$^2[1/2]^\circ$	0	11.723	
1s$_2$	$^2[1/2]^\circ$	1	11.828	0.51 (1p$_0$)

Table A.2. 3p^{5}4s levels of Ar and radiative transition rates of the 1s$_4$ and 1s$_2$ levels.

Level	Term	J	ϵ [eV]	Transition rate [ns^{-1}]	Lifetime [ns]
2p$_{10}$	$^2[1/2]$	1	12.907	0.0189 (1s$_5$), 5.43×10^{-3} (1s$_4$), 9.8×10^{-4} (1s$_3$), 1.9×10^{-4} (1s$_2$)	39.2
2p$_9$	$^2[5/2]$	3	13.076	0.0331 (1s$_5$)	30.2
2p$_8$	$^2[5/2]$	2	13.095	9.28×10^{-3} (1s$_5$), 0.0215 (1s$_4$), 1.47×10^{-3} (1s$_2$)	31.0
2p$_7$	$^2[3/2]$	1	13.153	5.18×10^{-3} (1s$_5$), 0.025 (1s$_4$), 2.43×10^{-3} (1s$_3$), 1.06×10^{-3} (1s$_2$)	29.7
2p$_6$	$^2[3/2]$	2	13.172	0.0245 (1s$_5$), 4.9×10^{-3} (1s$_4$), 5.03×10^{-3} (1s$_2$)	29.0
2p$_5$	$^2[1/2]$	0	13.273	0.0402 (1s$_4$)	24.9
2p$_4$	$^2[3/2]$	1	13.283	6.25×10^{-4} (1s$_5$), 2.2×10^{-5} (1s$_4$), 0.0186 (1s$_3$), 0.0139 (1s$_2$)	30.2
2p$_3$	$^2[3/2]$	2	13.302	3.8×10^{-3} (1s$_5$), 8.47×10^{-3} (1s$_4$), 0.0223 (1s$_2$)	28.9
2p$_2$	$^2[1/2]$	1	13.328	6.39×10^{-3} (1s$_5$), 1.83×10^{-3} (1s$_4$), 0.0117 (1s$_3$), 0.0153 (1s$_2$)	28.4
2p$_1$	$^2[1/2]$	0	13.480	2.36×10^{-4} (1s$_4$), 0.0445 (1s$_2$)	22.4

Table A.3. 3p^{5}4p levels of Ar and associated transition rates (from NIST Atomic Spectra Database [117]).

Level	nl	Term	J	ϵ [eV]	Transition rate [ns^{-1}]	Lifetime [ns]
3d$_6$	3d	$^2[1/2]^\circ$	0	13.845	8.1×10^{-3} (2p$_{10}$), 7.73×10^{-4} (2p$_7$) †, 1.2×10^{-4} (2p$_4$), 3.6×10^{-4} (2p$_2$)	106.9
3d$_5$	3d	$^2[1/2]^\circ$	1	13.864	3.06×10^{-3} (1p$_0$) *, 7.4×10^{-3} (2p$_{10}$), 3.9×10^{-5} (2p$_8$), 3.09×10^{-4} (2p$_7$) †, 1.37×10^{-3} (2p$_6$) †, 5.75×10^{-4} (2p$_5$) †, 3.2×10^{-5} (2p$_4$), 1.4×10^{-4} (2p$_3$), 1.7×10^{-4} (2p$_2$), 2.49×10^{-6} (2p$_1$)	76.4
3d$_3$	3d	$^2[3/2]^\circ$	2	13.903	4.9×10^{-3} (2p$_{10}$), 9.82×10^{-5} (2p$_9$) †, 1.2×10^{-4} (2p$_8$), 2.6×10^{-4} (2p$_7$), 2.5×10^{-3} (2p$_6$), 9.41×10^{-5} (2p$_4$) †, 3.9×10^{-4} (2p$_3$), 1.1×10^{-4} (2p$_2$)	118.0
3d$_4'$	3d	$^2[7/2]^\circ$	4	13.979	0.01593 (2p$_9$) †	62.8
3d$_4$	3d	$^2[7/2]^\circ$	3	14.013	2.29×10^{-3} (2p$_9$) †, 0.011 (2p$_8$), 8.8×10^{-5} (2p$_6$), 2.53×10^{-6} (2p$_3$)	74.7
3d$_1''$	3d	$^2[5/2]^\circ$	2	14.063	5.85×10^{-6} (2p$_{10}$) †, 1.2×10^{-4} (2p$_9$), 5.7×10^{-3} (2p$_8$), 7.3×10^{-3} (2p$_7$), 2×10^{-4} (2p$_6$) †, 1.54×10^{-6} (2p$_4$) †, 2.08×10^{-5} (2p$_3$) †, 6.75×10^{-7} (2p$_2$) †	74.9
2s$_5$	5s	$^2[3/2]^\circ$	2	14.068	4.9×10^{-3} (2p$_{10}$), 0.011 (2p$_9$), 1.1×10^{-3} (2p$_8$), 4.6×10^{-4} (2p$_7$), 3.3×10^{-3} (2p$_6$), 5.9×10^{-5} (2p$_4$), 1.2×10^{-4} (2p$_3$), 3.1×10^{-4} (2p$_2$)	47.1
2s$_4$	5s	$^2[3/2]^\circ$	1	14.090	0.077 (1p$_0$), 2.44×10^{-3} (2p$_{10}$), 8.9×10^{-3} (2p$_8$), 4.6×10^{-3} (2p$_7$), 2.7×10^{-3} (2p$_6$), 1.3×10^{-3} (2p$_5$), 4.5×10^{-4} (2p$_4$), 2.9×10^{-5} (2p$_3$), 3×10^{-5} (2p$_2$), 1.6×10^{-4} (2p$_1$)	10.2
3d$_1'$	3d	$^2[5/2]^\circ$	3	14.099	3.1×10^{-3} (2p$_9$), 2×10^{-3} (2p$_8$), 0.015 (2p$_6$) †, 9.8×10^{-6} (2p$_3$)	49.7
3d$_2$	3d	$^2[3/2]^\circ$	1	14.153	0.27 (1p$_0$), 1.35×10^{-5} (2p$_{10}$) †, 9.52×10^{-4} (2p$_8$), 0.011 (2p$_7$), 4.01×10^{-5} (2p$_6$) †, 4.3×10^{-3} (2p$_5$), 8.96×10^{-4} (2p$_4$) †, 4.45×10^{-5} (2p$_3$) †, 5.87×10^{-5} (2p$_2$) †, 8.77×10^{-4} (2p$_1$) †	3.5
3s$_1'''$	3d	$^2[5/2]^\circ$	2	14.214	7.51×10^{-6} (2p$_{10}$) †, 4.3×10^{-5} (2p$_9$) †, 8.3×10^{-4} (2p$_8$), 5.01×10^{-5} (2p$_7$) †, 2.09×10^{-4} (2p$_6$) †, 0.013 (2p$_4$), 2.2×10^{-3} (2p$_3$), 3.35×10^{-6} (2p$_2$) †	61.2
3s$_1''$	3d	$^2[3/2]^\circ$	2	14.234	1.89×10^{-4} (2p$_{10}$) †, 1.52×10^{-4} (2p$_9$) †, 7.21×10^{-4} (2p$_8$) †, 3.69×10^{-4} (2p$_7$), 3.76×10^{-3} (2p$_6$), 1.72×10^{-4} (2p$_4$) †, 5.8×10^{-4} (2p$_3$) †, 6.2×10^{-3} (2p$_2$)	82.4
3s$_1'''$	3d	$^2[5/2]^\circ$	3	14.236	7.36×10^{-4} (2p$_9$) †, 4.2×10^{-5} (2p$_8$) †, 9.3×10^{-5} (2p$_6$) †, 0.015 (2p$_3$)	63.0
2s$_3$	5s	$^2[1/2]^\circ$	0	14.241	3.26×10^{-3} (2p$_{10}$), 2.22×10^{-3} (2p$_7$), 0.01 (2p$_4$), 5.1×10^{-3} (2p$_2$)	48.6
2s$_2$	5s	$^2[1/2]^\circ$	1	14.255	0.035 (1p$_0$), 1.76×10^{-3} (2p$_{10}$), 2.1×10^{-4} (2p$_8$), 2.8×10^{-4} (2p$_7$), 1.39×10^{-3} (2p$_6$), 3.8×10^{-4} (2p$_5$), 2×10^{-3} (2p$_4$), 8.9×10^{-3} (2p$_3$), 3.4×10^{-3} (2p$_2$), 1.9×10^{-3} (2p$_1$)	18.1
3s$_1'$	3d	$^2[3/2]^\circ$	1	14.304	0.313 (1p$_0$), 2.05×10^{-5} (2p$_{10}$) †, 8.33×10^{-5} (2p$_8$) †, 3.9×10^{-4} (2p$_7$) †, 3.96×10^{-4} (2p$_6$), 4.2×10^{-4} (2p$_5$), 4.5×10^{-3} (2p$_4$), 4.84×10^{-5} (2p$_3$) †, 7.1×10^{-3} (2p$_2$), 5.2×10^{-3} (2p$_1$)	3.0

Table A.4. Transition rates for the Ar 3d and 5s levels. Bold: levels with dipole decay to the ground state (1p$_0$ in Paschen notation).

Level	nl	Term	ϵ [eV]	Transition rate [ns^{-1}]
4d$_5$	4d	$^2[1/2]^\circ$	14.711	0.006 (1p$_0$) *, 2.78×10^{-3} (2p$_{10}$), 2.8×10^{-4} (2p$_8$), 8.6×10^{-4} (2p$_6$), 9.2×10^{-4} (2p$_5$), 4.6×10^{-4} (2p$_3$), 1.6×10^{-4} (2p$_2$)
3s$_4$	6s	$^2[3/2]^\circ$	14.848	0.046 (1p$_0$) *, 4.21×10^{-4} (2p$_{10}$), 2×10^{-3} (2p$_8$), 1.7×10^{-3} (2p$_7$), 7.2×10^{-4} (2p$_6$), 3.5×10^{-4} (2p$_5$), 1.2×10^{-4} (2p$_4$), 4.2×10^{-6} (2p$_3$), 3.3×10^{-5} (2p$_2$), 9.7×10^{-5} (2p$_1$)
4d$_2$	4d	$^2[3/2]^\circ$	14.859	0.153 (1p$_0$) *, 1.7×10^{-4} (2p$_7$)
4s$'_1$	4d	$^2[3/2]^\circ$	15.004	0.068 (1p$_0$) *, 1.05×10^{-3} (2p$_{10}$), 3.1×10^{-5} (2p$_8$), 2.5×10^{-5} (2p$_7$), 4×10^{-4} (2p$_6$), 5.8×10^{-5} (2p$_5$), 1.2×10^{-4} (2p$_3$)
3s$_2$	6s	$^2[1/2]^\circ$	15.022	0.072 (1p$_0$) *, 2.85×10^{-4} (2p$_{10}$), 5.1×10^{-5} (2p$_8$), 5.3×10^{-5} (2p$_7$), 1.6×10^{-4} (2p$_6$), 1.5×10^{-4} (2p$_5$), 6×10^{-4} (2p$_4$), 2.48×10^{-3} (2p$_3$), 9.6×10^{-4} (2p$_2$), 3.59×10^{-4} (2p$_1$)
5d$_5$	5d	$^2[1/2]^\circ$	15.118	0.014 (1p$_0$) *, 2.2×10^{-3} (2p$_{10}$), 1.1×10^{-4} (2p$_8$), 7.6×10^{-5} (2p$_7$), 4.2×10^{-4} (2p$_6$), 2.4×10^{-4} (2p$_5$), 2.1×10^{-4} (2p$_4$), 2.4×10^{-4} (2p$_3$), 1.2×10^{-4} (2p$_2$)
4s$_4$	7s	$^2[3/2]^\circ$	15.186	0.046 (1p$_0$) *, 1.9×10^{-4} (2p$_{10}$), 1.1×10^{-3} (2p$_8$), 5.2×10^{-4} (2p$_7$), 5.1×10^{-4} (2p$_6$), 9.4×10^{-5} (2p$_5$), 5.4×10^{-5} (2p$_4$)
5d$_2$	5d	$^2[3/2]^\circ$	15.190	0.142 (1p$_0$) *, 5.9×10^{-5} (2p$_8$), 9×10^{-6} (2p$_7$), 1.5×10^{-4} (2p$_5$), 3.1×10^{-5} (2p$_2$)
6d$_5$	6d	$^2[1/2]^\circ$	15.308	2.5×10^{-3} (1p$_0$) $^\triangle$, 1.9×10^{-3} (2p$_{10}$), 4.2×10^{-4} (2p$_6$), 3×10^{-4} (2p$_5$), 5.1×10^{-5} (2p$_4$), 6.6×10^{-5} (2p$_3$), 1.21×10^{-4} (2p$_1$)
5s$'_1$	5d	$^2[3/2]^\circ$	15.351	1.7×10^{-3} (1p$_0$) $^\triangle$, 7.7×10^{-5} (2p$_5$)
4s$_2$	7s	$^2[1/2]^\circ$	15.359	2.5×10^{-3} (1p$_0$) $^\triangle$, 4.5×10^{-4} (2p$_{10}$), 2×10^{-4} (2p$_8$), 2.1×10^{-4} (2p$_7$), 1.2×10^{-4} (2p$_5$), 1.8×10^{-4} (2p$_4$), 9×10^{-4} (2p$_3$), 3.3×10^{-4} (2p$_2$)
5s$_4$	8s	$^2[3/2]^\circ$	15.366	0.044 (1p$_0$) $^\triangle$, 3.6×10^{-4} (2p$_8$), 1.2×10^{-4} (2p$_6$), 1.5×10^{-4} (2p$_4$), 1.4×10^{-4} (2p$_3$), 7.5×10^{-5} (2p$_2$)
6d$_2$	6d	$^2[3/2]^\circ$	15.374	0.1 (1p$_0$) $^\triangle$, 3.33×10^{-3} (2p$_7$) ‡

Table A.5. Transition rates for the higher radiative ($J = 1$) ns ($n \geq 6$) and nd ($n \geq 4$) excited levels of Ar included in Magboltz.

A.4. Optical Properties

Macroscopically, the optical properties of a material are described by the complex dielectric function $\varepsilon(\omega)$. The dielectric function and the complex index of refraction $\mathsf{n} + \mathsf{i}\mathsf{k}$ are interrelated by

$$\varepsilon(\omega) = \varepsilon'(\omega) + \mathsf{i}\varepsilon''(\omega) = (\mathsf{n}(\omega) + \mathsf{i}\mathsf{k}(\omega))^2 .$$

The real and imaginary parts of $\varepsilon(\omega)$ can, therefore, be expressed in terms of the (real) index of refraction n and the extinction coefficient k as

$$\varepsilon'(\omega) = \mathsf{n}^2 - \mathsf{k}^2, \qquad \varepsilon''(\omega) = 2\mathsf{n}\mathsf{k},$$

and, vice versa,

$$\mathsf{n} = \frac{1}{\sqrt{2}}\sqrt{\sqrt{\varepsilon'^2 + \varepsilon''^2} + \varepsilon'}, \qquad \mathsf{k} = \frac{1}{\sqrt{2}}\sqrt{\sqrt{\varepsilon'^2 + \varepsilon''^2} - \varepsilon'}.$$

Let us consider a monochromatic plane wave $\mathbf{E}(x,t) = \mathbf{E}_0 e^{\mathsf{i}(kx - \omega t)}$. The dispersion relation of electromagnetic waves in a medium is given by

$$k = \frac{\omega}{c}(\mathsf{n} + \mathsf{i}\mathsf{k}).$$

The intensity $I \propto |\mathbf{E}|^2$ of a monochromatic photon beam thus falls off exponentially when penetrating a layer of material with thickness d,

$$I(d) = I_0 e^{-\mu d}.$$

The linear absorption coefficient μ is given by

$$\mu = \frac{2\omega\mathsf{k}}{c} = N\sigma_\gamma(\omega),$$

where $\sigma_\gamma(\omega)$ is the photoabsorption cross-section. For $\mathsf{n} \approx 1$, the imaginary part $\varepsilon''(\omega)$ of the dielectric function can be approximated by

$$\varepsilon''(\omega) \approx \frac{Nc}{\omega}\sigma_\gamma(\omega).$$

The photoabsorption cross-section is proportional to the oscillator strength density $\mathrm{d}f/\mathrm{d}E$,

$$\sigma_\gamma(\omega) = \frac{2\pi^2 \alpha_f (\hbar c)^2}{m_e c^2} \frac{\mathrm{d}f}{\mathrm{d}E}.$$

Bibliography

[1] G. Charpak, R. Bouclier, T. Bressani, J. Favier, and Č. Zupančič, Nucl. Instr. Meth. **62**, 262 (1968).

[2] W. Blum, W. Riegler, and L. Rolandi, *Particle Detection with Drift Chambers*, Springer, 2008.

[3] F. Sauli, Nucl. Instr. Meth. A **386**, 531.

[4] Y. Giomataris, P. Rebourgeard, J. P. Robert, and G. Charpak, Nucl. Instr. Meth. A **376**, 29 (1996).

[5] K. Nakamura et al., J. Phys. G **37**, 075021 (2010).

[6] I. C. Group, The international large detector: Letter of intent, Technical Report arXiv:1006.3396. DESY-2009-87. FERMILAB-PUB-09-682-E. KEK-REPORT-2009-6, 2010.

[7] F. Hartmann, Nucl. Instr. Meth. A **628**, 40 (2010).

[8] G. Lutz, *Semiconductor radiation detectors: device physics*, Springer, 1999.

[9] H. Spieler, *Semiconductor detector systems*, Oxford Univ. Press, 2005.

[10] T. Sjöstrand, arXiv:hep-ph/0611247.

[11] S. Agostinelli et al., Nucl. Instr. Meth. A **506**, 250 (2003).

[12] J. Allison et al., IEEE Trans. Nucl. Sci. **53**, 270 (2006).

[13] S. F. Biagi, Nucl. Instr. Meth. A **421**, 234 (1999).

[14] S. F. Biagi, Magboltz 8, `http://magboltz.web.cern.ch/magboltz`.

[15] R. Veenhof, Garfield – simulation of gaseous detectors, `http://cern.ch/garfield`.

[16] H. Schindler and R. Veenhof, Garfield++ – simulation of tracking detectors, `http://cern.ch/garfieldpp`.

[17] B. L. Henke, E. M. Gullikson, and J. C. Davis, At. Data Nucl. Data Tables **54**, 181 (1993), data files available online at `http://henke.lbl.gov/optical_constants/`.

[18] D. A. Verner, D. G. Yakovlev, I. M. Band, and M. B. Trzhaskovskaya, At. Data Nucl. Data Tables **55**, 233 (1993).

[19] International Commission on Radiation Units and Measurements, Average energy required to produce an ion pair, 1979, ICRU Report 31.

[20] E. Fermi, Phys. Rev. **57**, 485 (1940).

[21] L. D. Landau, E. M. Lifshitz, and L. P. Pitaevskii, *Electrodynamics of Continuous Media*, Butterworth, 1984.

[22] U. Fano, Annu. Rev. Nucl. Sci. **13**, 1 (1963).

[23] W. W. M. Allison and J. H. Cobb, Annu. Rev. Nucl. Part. Sci. **30**, 253 (1980).

[24] B. Rossi, *High energy particles*, Prentice-Hall, 1952.

[25] D. Pines, *Elementary Excitations in Solids*, Perseus, 1966.

[26] H. Bethe, Ann. Phys. **397**, 325 (1930).

[27] M. Inokuti, Rev. Mod. Phys. **43**, 297 (1971).

[28] P. Sigmund, *Particle Penetration and Radiation Effects: General Aspects and Stopping of Swift Point Charges*, Springer, 2006.

[29] J. M. Ziman, *Prinzipien der Festkörpertheorie*, Verlag Harri Deutsch, 1999.

[30] J. Lindhard, Mat. Fys. Medd. Dan. Vid. Selsk. **28**, 1 (1954).

[31] J. Lindhard and A. Winther, Mat. Fys. Medd. Dan. Vid. Selsk. **34**, 1 (1964).

[32] V. A. Chechin, L. P. Kotenko, G. I. Merson, and V. C. Yermilova, Nucl. Instr. Meth. **98**, 577 (1972).

[33] F. Lapique and F. Piuz, Nucl. Instr. Meth. **175**, 297 (1980).

[34] G. Hall, Nucl. Instr. Meth. **220**, 356 (1984).

[35] R. Veenhof, Electrostatics, unpublished manuscript, available at `http://cern.ch/garfield/notes/`.

[36] Ansys, Inc., `http://www.ansys.com`.

[37] R. Veenhof, JINST **4**, P12017 (2009).

[38] N. Majumdar and S. Mukhopadhyay, Nucl. Instr. Meth. A **566**, 489 (2006).

[39] N. Majumdar and S. Mukhopadhyay, JINST **2**, P09006 (2007).

[40] M. R. Spiegel, *Schaum's outline of theory and problems of complex variables, with an introduction to conformal mappping and its applications*, McGraw-Hill, 1964.

[41] E. Durand, *Electrostatique. T.2: Problèmes géneraux; conducteurs*, Masson, 1966.

[42] E. Durand, *Electrostatique. T.3: Méthodes de calcul; diélectriques*, Masson, 1966.

[43] S. F. Biagi, Nucl. Instr. Meth. A **273**, 533 (1988).

[44] H. R. Skullerud, J. Phys. D **1**, 1567 (1968).

[45] G. W. Fraser and E. Mathieson, Nucl. Instr. Meth. A **247**, 544 (1986).

[46] S. F. Biagi, personal communication.

[47] C. A. B. Oliveira et al., Phys. Lett. B **703**, 217 (2011).

[48] C. B. Opal, W. K. Peterson, and E. C. Beaty, J. Chem. Phys. **55**, 4100 (1971).

[49] A. E. S. Green and T. Sawada, J. Atmos. Terr. Phys. **34**, 1710 (1972).

[50] Ö. Şahin, I. Tapan, E. N. Özmutlu, and R. Veenhof, JINST **5**, P05002 (2010).

[51] K. Nikolopoulos, P. Bhattacharya, V. Chernyatin, and R. Veenhof, JINST **6**, P06011 (2011).

[52] F. Sauli, L. Ropelewski, and P. Everaerts, Nucl. Instr. Meth. A **560**, 269 (2006).

[53] L. Ropelewski, personal communication.

[54] J. D. Jackson, *Classical electrodynamics; 3rd ed.*, Wiley, 1999.

[55] W. Shockley, J. Appl. Phys. **9**, 635 (1938).

[56] S. Ramo, Proceedings of the I.R.E. **27**, 584 (1939).

[57] G. F. Knoll, *Radiation detection and measurement*, Wiley, 2010.

[58] D. C. Arogancia et al., Nucl. Instr. Meth. A **602**, 403 (2009).

[59] L. Frommhold, Z. Phys. **144**, 396 (1956).

[60] L. Frommhold, Z. Phys. **150**, 172 (1958).

[61] H. S. Snyder, Phys. Rev. **72**, 181 (1947).

[62] R. Wijsman, Phys. Rev. **75**, 833 (1949).

[63] W. Legler, Z. Phys. **140**, 221 (1955).

[64] H. Schlumbohm, Z. Phys. **151**, 563 (1958).

[65] W. Legler, Brit. J. Appl. Phys. **18**, 1275 (1967).

[66] H. Schindler, S. F. Biagi, and R. Veenhof, Nucl. Instr. Meth. A **624**, 78 (2010).

[67] R. Veenhof, personal communication.

[68] G. D. Alkhazov, Nucl. Instr. Meth. **89**, 155 (1970).

[69] W. Legler, Z. Naturforschg. **16a**, 253 (1961).

[70] A. Lansiart and J.-P. Morucci, J. Phys. Radium (Supplément) **23/S6**, 102A (1962).

[71] G. Vidal, J. Lacaze, and J. Maurel, J. Phys. D **7**, 1684 (1974).

[72] J. Byrne, Nucl. Instr. Meth. **74**, 291 (1969).

[73] G. A. Wilson and A. Wragg, J. Inst. Maths. Applics. **12**, 165 (1973).

[74] A. H. Cookson and T. J. Lewis, Brit. J. Appl. Phys. **17**, 1473 (1966).

[75] A. H. Cookson, B. W. Ward, and T. J. Lewis, Brit. J. Appl. Phys **17**, 891 (1966).

[76] R. Veenhof, Choosing a gas mixture for the ALICE TPC, available at `http://cern.ch/rjd/Alice`.

[77] H. Schlumbohm, Z. Phys. **152**, 49 (1958).

[78] S. C. Curran, A. L. Cockroft, and J. Angus, Phil. Mag. **40**, 929 (1949).

[79] R. Gold and E. F. Bennett, Phys. Rev. **147**, 201 (1966).

[80] J. Alme et al., Nucl. Instr. Meth. A **622**, 316 (2010).

[81] S. Rossegger and W. Riegler, Nucl. Instr. Meth. A **623**, 927 (2010).

[82] T. Zerguerras et al., Nucl. Instr. Meth. A **608**, 397 (2009).

[83] T. Zerguerras, Single-electron response and energy resolution of a Micromegas detector, presentation given at the RD51 mini week, 22-25 February 2010.

[84] H. van der Graaf, Nucl. Instr. Meth. A **580**, 1023 (2007).

[85] M. Chefdeville, *Development of Micromegas-like gaseous detectors using a pixel readout chip as collecting anode*, PhD thesis, University of Amsterdam, Université de Paris Sud XI, 2009.

[86] M. Lupberger, *Avalanche statistics and single electron counting with a Timepix-InGrid detector*, diploma thesis, Albert-Ludwigs Universität Freiburg, 2010.

[87] R. Mayol and F. Salvat, At. Data Nucl. Data Tables **65**, 55 (1997).

[88] I. B. Smirnov, Nucl. Instr. Meth. A **554**, 474 (2005).

[89] I. B. Smirnov, Heed-C++, `http://ismirnov.web.cern.ch/ismirnov/heed`.

[90] R. Veenhof, Nucl. Instr. Meth. A **563**, 291 (2006).

[91] H. van der Graaf et al., Nucl. Instr. Meth. A **560**, 131 (2006).

[92] F. Rieke and W. Prepejchal, Phys. Rev. A **6**, 1507 (1972).

[93] G. W. McClure, Phys. Rev. **90**, 796 (1953).

[94] G. Malamud, A. Breskin, R. Chechik, and A. Pansky, J. Appl. Phys. **74**, 3645 (1993).

[95] J. Berkowitz, *Atomic and Molecular Photoabsorption: Absolute Total Cross Sections*, Academic Press, 2002.

[96] J. Berkowitz, *Photoabsorption, Photoionization, and Photoelectron Spectroscopy*, Academic Press, 1979.

[97] E. L. Kosarev and E. R. Podolyak, Nucl. Instr. Meth. A **261**, 161 (1987).

[98] K. Söchting, Phys. Rev. A **20**, 1359 (1969).

[99] C. Backx, G. R. Wight, and M. J. Van der Wiel, J. Phys. B **9**, 315 (1976).

[100] G. V. Marr and J. B. West, At. Data Nucl. Data Tables **18**, 497 (1976).

[101] N. Sakamoto et al., Oscillator Strength Spectra and Related Quantities of 9 Atoms and 23 Molecules Over the Entire Energy Region, NIFS-DATA-109, National Institute for Fusion Science, 2010, available online at `http://www.nifs.ac.jp/report/nifsdata.html`.

[102] K. Kameta, N. Kouchi, M. Ukai, and Y. Hatano, J. Electron Spectrosc. Relat. Phenom. **123**, 225 (2002).

[103] D. Srdoč, M. Inokuti, and I. Krajcar-Bronić, Yields of Ionization and Excitation in Irradiated Matter, in *Atomic and Molecular Data for Radiotherapy and Radiation Research*, 1995, IAEA TECDOC 799.

[104] I. Krajcar Bronić, Hoshasen: ionizing radiation **24**, 101 (1998).

[105] G. F. Reinking, L. G. Christophorou, and S. R. Hunter, J. Appl. Phys. **60**, 499 (1986).

[106] D. Combecher, Radiation Research **84**, 189 (1980).

[107] B. G. R. Smith and J. Booz, Experimental results on *W*-values and transmission of low energy electrons in gases, in *Sixth Symposium on Microdosimetry*, pages 759–775, 1978.

[108] E. Waibel and B. Grosswendt, Nucl. Instr. Meth. **211**, 487 (1983).

[109] E. Waibel and B. Grosswendt, Study of W-values, practical ranges, and energy dissipation profiles of low-energy electrons in N_2, in *Eighth Symposium on Microdosimetry*, pages 301–310, 1983.

[110] E. Waibel and B. Grosswendt, Nucl. Instr. Meth. B **53**, 239 (1991).

[111] I. Krajcar Bronić, D. Srdoč, and B. Obelić, Radiation Research **115**, 213 (1988).

[112] H. F. Winters, J. Chem. Phys. **63**, 3462 (1975).

[113] M. Hayashi, Bibliography of Electron and Photon Cross Sections with Atoms and Molecules Published in the 20th Century - Methane, NIFS-DATA-90, National Institute for Fusion Science, 2004, available online at `http://www.nifs.ac.jp/report/nifsdata.html`.

[114] W. P. Jesse and J. Sadauskis, Phys. Rev. **88**, 417 (1952).

[115] T. E. Bortner, G. S. Hurst, M. Edmundson, and J. E. Parks, Alpha particle ionization of argon mixtures – further study of the role of excited states, ORNL-3422, Oak Ridge National Laboratory, 1963.

[116] R. Hilborn, Am. J. Phys. **50**, 982 (1982).

[117] Y. Ralchenko, A. Kramida, J. Reader, and N. A. T. (2010), NIST Atomic Spectra Database (version 4.0), `http://physics.nist.gov/asd`.

[118] O. Zatsarinny and K. Bartschat, J. Phys. B **39**, 2145 (2006).

[119] C.-M. Lee and K. T. Lu, Phys. Rev. A **8**, 1241 (1973).

[120] A. Corney, *Atomic and Laser Spectroscopy*, Clarendon Press, 2006.

[121] A. W. Ali and H. R. Griem, Phys. Rev. **140**, A1044 (1965).

[122] A. W. Ali and H. R. Griem, Phys. Rev. **144**, 366 (1966).

[123] A. Molisch and B. P. Oehry, *Radiation trapping in atomic vapours*, Oxford University Press, 1998.

[124] R. Brun et al., ROOT: An Object-Oriented Data Analysis Framework, `http://root.cern.ch`.

[125] M. Ukai et al., J. Chem. Phys. **95**, 4142 (1991).

[126] D. A. Shaw et al., Chemical Physics **198**, 381 (1995).

[127] J. E. Velazco, J. H. Kolts, and D. W. Setser, J. Chem. Phys. **69**, 4357 (1978).

[128] L. G. Piper, J. E. Velazco, and D. W. Setser, J. Chem. Phys. **59**, 3323 (1973).

[129] X. Chen and D. W. Setser, J. Phys. Chem. **95**, 8473 (1991).

[130] N. Sadeghi et al., J. Chem. Phys. **115**, 3144 (2001).

[131] T. Watanabe and K. Katsuura, J. Chem. Phys. **47**, 800 (1966).

[132] H. Deutsch et al., International Journal of Mass Spectrometry **233**, 39 (2004).

[133] M. Jones, T. D. Dreiling, D. W. Setser, and R. N. McDonald, J. Phys. Chem. **89**, 4501.

[134] D. W. Breck, *Zeolite molecular sieves*, Robert E. Krieger Publishing Company, 1984.

[135] J. H. Kolts and D. W. Setser, J. Chem. Phys. **68**, 4848.

[136] T. D. Nguyen and N. Sadeghi, Phys. Rev. A **18**, 1388 (1978).

[137] R. S. F. Chang and D. W. Setser, J. Phys. Chem. **69**, 3885 (1978).

[138] P. Becker and F. Lampe, J. Chem. Phys. **42**, 3743 (1965).

[139] E. D. Palik and E. J. Prucha, *Handbook of optical constants of solids*, Academic Press, 1998.

[140] S. Adachi, *Optical constants of crystalline and amorphous semiconductors*, Kluwer Academic Publishers, 1999.

[141] H. Bichsel, Rev. Mod. Phys. **60**, 663 (1988).

[142] H. Bichsel, Nucl. Instr. Meth. A **562**, 154 (2006).

[143] H. Bichsel, Comparison of B-F and FVP inelastic collision cross sections, unpublished manuscript, 2008.

[144] H. Bichsel, `http://faculty.washington.edu/hbichsel/MCCsi.html`.

[145] A. Ferrari, P. R. Sala, A. Fassò, and J. Ranft, *FLUKA: a multi-particle transport code (program version 2005)*, CERN, Geneva, 2005.

[146] G. Battistoni et al., AIP Conf. Proc. **896**, 31 (2007).

[147] K. Lassila-Perini and L. Urbán, Nucl. Instr. Meth. A **362**, 416 (1995).

[148] J. Apostolakis et al., Nucl. Instr. Meth. A **453**, 597 (2000).

[149] A. Fassò, A. Ferrari, J. Ranft, and P. R. Sala, New developments in FLUKA modelling. Hadronic and EM interactions, in *Proc. 3rd Workshop on Simulating Accelerator Radiation Environments (SARE 3), 7-9 May 1997, KEK, Tsukuba (Japan). Ed. H. Hirayama. KEK-Proceedings 97-5*, pages 32–43, 1997.

[150] J. F. Bak et al., Nuclear Physics B **288**, 681 (1987).

[151] S. Selberherr, *Analysis and simulation of semiconductor devices*, Springer, 1984.

[152] Synopsys, Inc., Synopsys TCAD, `http://www.synopsys.com/Tools/TCAD/`.

[153] D. Pennicard, *3D Detectors for Synchrotron Applications*, PhD thesis, University of Glasgow, 2009.

[154] Synopsys, Inc., *Sentaurus Device User Guide Version D-2010.03*.

[155] Institute for Microelectronics, TU Vienna, *Minimos-NT Device and Circuit Simulator Release 2.1*.

[156] A. Strachan, Modelling equations and parameters for numerical simulation, in *Properties of crystalline silicon*, edited by R. Hull, EMIS Datareviews series, INSPEC, 1999.

[157] C. Canali, G. Majni, R. Minder, and G. Ottaviani, IEEE Transactions on Electron Devices **22**, 1045 (1975).

[158] R. Börnstein, K. H. Hellwege, and H. H. Landolt, *Landolt-Börnstein. Neue Serie. Gr. 3, Bd. 17*, Springer, 1982.

[159] W. Maes, K. de Meyer, and R. van Overstraeten, Solid-State Electronics **33**, 705 (1990).

[160] C. Jacoboni and L. Reggiani, Rev. Mod. Phys. **55**, 645 (1983).

[161] M. V. Fischetti and S. E. Laux, Phys. Rev. B **38**, 9721 (1988).

[162] K. Hess, editor, *Monte Carlo device simulation: full band and beyond*, Kluwer Academic Publishers, 1991.

[163] L. M. Roth, Dynamics and Classical Transport of Carriers in Semiconductors, in *Handbook on Semiconductors*, edited by P. T. Landsberg, volume 1, chapter 10, Elsevier, 1992.

[164] M. Lundstrom, *Fundamentals of carrier transport*, Cambridge University Press, 2000.

[165] S. Tanuma, C. J. Powell, and D. R. Penn, Surf. Interface Anal. **43**, 689 (2011).

[166] E. Cartier, M. V. Fischetti, E. A. Eklund, and F. R. McFeely, Appl. Phys. Lett **62**, 3339 (1993).

[167] D. R. Penn, Phys. Rev. B **35**, 482 (1987).

[168] G. Aglieri Rinella, personal communication.

[169] M. Noy et al., JINST **6**, C11025 (2011).

[170] A. Bellerive, personal communication.

[171] H. A. Bethe and R. W. Jackiw, *Intermediate quantum mechanics*, Benjamin, 1986.

[172] L. D. Landau and E. M. Lifshitz, *Quantum Mechanics: Non-Relativistic Theory*, Butterworth, 1977.

[173] R. M. Sternheimer, M. J. Berger, and S. M. Seltzer, At. Data Nucl. Data Tables **30**, 261 (1984).

[174] L. D. Landau, J. Phys. USSR **8** (1944).

[175] G. U. Yule, Phil. Trans. R. Soc. London B **213**, 21 (1924).

[176] W. H. Furry, Phys. Rev. **52**, 569 (1937).

[177] J. Byrne, Proc. R. Soc. Edinburgh A **66**, 33 (1962).

Lebenslauf

DI Heinrich Schindler,
Mechtlerstr. 15 – 17,
2100 Korneuburg

15. 07. 1983	Geburt in Wien
09/1989 – 06/1993	Volksschule Korneuburg
09/1993 – 05/2001	Bundesgymnasium Stockerau
10/2001 – 09/2002	Präsenzdienst (EF)
10/2002 – 03/2008	Diplomstudium "Technische Physik" an der Technischen Universität Wien
03/2007 – 05/2008	Diplomarbeit *Protecting the ALICE Experiment Against Beam Failures*
seit 05/2008	Doktoratsstudium an der Technischen Universität Wien
06/2008 – 05/2011	CERN Doktorandenprogramm (PH-DT Gruppe)
seit 08/2011	CERN Applied Fellow (LHCb Experiment)